University of Wollongong Thesis Collection 2017+

University of Wollongong Thesis Collections

2022

Development of non-prestressed fibre-reinforced concrete sleepers

Ashkan Shakeri

Follow this and additional works at: https://ro.uow.edu.au/theses1

DEVELOPMENT OF NON-PRESTRESSED FIBRE-REINFORCED CONCRETE SLEEPERS

Ashkan Shakeri

Supervisors:
Professor Alex Remennikov
A/Professor Neaz Sheikh

This thesis is presented as part of the requirement for the conferral of the degree:
Doctor of Philosophy

University of Wollongong

School of Civil, Mining and Environmental Engineering

June 2022

Abstract

Railway sleepers are one of the essential parts of the ballasted railway tracks that provide support to the rails, retain the track gauge, and transfer the rail-seat loads uniformly to the underlying ballast layer. Prestressed concrete (PSC) sleepers are currently the most well-known railway sleepers used by the railway industry. It is estimated that there are around 400 billion prestressed concrete sleepers used in railway tracks worldwide and this number is increasing rapidly. The manufacturing process of the PSC sleeper requires relatively spacious indoor area with expensive machinery. Additionally, this manufacturing process needs heat curing and, therefore, is energy-consuming and pollutes the atmosphere due to the emission of greenhouse gases. This research proposes the application of non-prestressed concrete sleepers as an alternative to the currently used PSC railway sleepers. For manufacturing non-prestressed concrete sleepers, ultra-high tensile strength concrete is needed to resist the significant flexural tensile stresses generated within the sleeper under the design wheel load. In this research study, the reactive powder concrete (RPC) material, also called ultra-high performance fibre-reinforced concrete (UHP-FRC), is utilised for manufacturing the proposed non-prestressed concrete sleeper.

In the first stage, the optimal UHP-FRC mix design is determined through experimental testing of trial concrete mixes and a mathematical optimisation algorithm. Then, the standard rail-seat positive moment and the cyclic/fatigue tests are carried out for the prototype UHP-FRC sleepers. The prototype sleeper satisfies the criterion to pass the standard rail-seat static test. However, the fatigue performance of the UHP-FRC sleeper needs further improvements. Indeed, the prototype UHP-FRC sleeper sample failed under fatigue (cyclic) loading after around 200,000 load cycles, while according to the Australian Standard, concrete sleepers are expected to resist at least 3 millions of load cycles.

Research studies have revealed that concrete sleepers are expected to sustain infrequent high-frequency dynamic (impact) loads of high magnitudes (higher than their design rail loads) over their service lives. These impact loads normally occur due to the abnormalities of the wheel, rails, and the track foundation. Hence, the performance of the UHP-FRC prototype sleepers under high impact loads is also investigated. Additionally, the influence of the railway track foundation on the impact resistance of the UHP-FRC sleepers is studied. The experimental results show that the UHP-FRC sleeper samples have acceptable impact resistance. It has been found that the prototype non-prestressed sleepers can satisfy the impact wheel/sleeper loads for interstate railway tracks with infrequent traffic and the train speeds up to 80 km/hr.

In this research, the effects of the GFRP reinforcing bars on the static performance of the prototype UHP-FRC sleepers are also studied. For this purpose, a few low-height UHP-FRC prototype samples with different reinforcement ratios are produced for the rail-seat positive moment testing. The results showed the significant positive contribution of the GFRP bars on the static performance of the prototype samples. The first cracking and the ultimate rail-seat loads of the low-profile prototype sleeper increased by 91% and 325%, respectively.

In this research, simple techniques for the finite element (FE) modelling of the conventional prestressed concrete sleepers and the non-prestressed UHP-FRC prototype sleepers are developed and validated against the experimental results. The commercial FE code, ABAQUS, and the concrete damage plasticity (CDP) material model are utilised in this study. The CDP models the concrete material by defining the unidirectional compressive and tensile behaviour of the concrete material separately. It also uses the compressive and tensile damage indexes for the concrete material instead of defining cracking criteria. Hence, using this material model, the main challenge is to define the correct compressive and tensile stress-strain data points as the input data for the concrete material.

First, a conventional PSC sleeper model is developed. For this purpose, six PSC sleepers are tested to extract the required experimental data for the concrete material model and to validate the FE model. Also, the existing prestressing forces of the prestressed tendons are determined by conducting a simple 3-point decompression tests for three of the sleepers. It is found that the sleepers have an average of 13% prestress loss. Also, 18 core samples are taken from three of the sleepers to determine the average compressive strength of the concrete material, which is 66.13 MPa. The other required characteristics of the concrete material are extracted from its mean compressive strength by using the empirical equations found in the literature. Inserting the unidirectional compressive and tensile concrete material data and the prestress value, it is shown that the FE and the experimental results, including the load-deflection curves and the failure modes, are in good agreement with each other.

In the next step, the prototype UHP-FRC prototype sleeper is modelled using the CDP material model. The compressive performance of the UHP-FRC material is determined and validated using the universal compression test results without difficulties. In order to extract the tensile performance of the UHP-FRC material, a direct tensile test (DTT) method is developed in this research. Comparing the FE and experimental results obtained from the rail-seat testing of the prototype sleeper, it is shown that the DTT test result cannot represent the flexural (bending) performance of the UHP-FRC material. Hence, a tensile material model is developed based on several trial analyses in order to reach the FE results in good agreement with the experimental rail-seat test results. It is shown that by using the CDP material model, including the proposed tensile stress-strain data points, the FE model is validated against the prototype sleeper rail-seat test result, both in terms of the load-deflection curve and the failure mode. The FE models of the PSC sleeper and the non-prestressed prototype UHP-FRC sleeper, developed in this research, can be used as a reference model for future numerical investigations.

In general, the experimental results proved that the prototype non-prestressed UHP-FRC sleepers manufactured in this research with the proposed optimal UHP-FRC mix design, can reach acceptable static and impact load resistance capacities while the fatigue resistance of the of the proposed sleepers need further improvements. Furthermore, it has been shown that the CDP material model used by the finite element program, ABAQUS, can simulate the performance of the UHP-FRC sleepers using the material characteristics obtained in this research.

Acknowledgement

Certification

I, Ashkan Shakeri, declare that this thesis submitted in fulfilment of the requirements for the conferral of the degree Doctor of Philosophy, from the University of Wollongong, is wholly my own work unless otherwise referenced or acknowledged. This document has not been submitted for qualifications at any other academic institution.

Ashkan Shakeri

20st June 2022

List of Publications

SHAKERI, A., REMENNIKOV, A. M. & SHEIKH, M. N. Development of fibre-reinforced concrete mix for manufacturing non-prestressed concrete sleepers. Structures, 2022. Elsevier, 588-599.

Table of Contents:

List of Figures

List of Tables:

CHAPTER 1

INTRODUCTION

1.1 Problem Statement

In recent years, due to population growth and industrial developments, transportation demands have increased. Rail transport is one of the primary methods of transferring people and goods on land. The increased requirements can be fulfilled by constructing railway tracks with high tonne axle load (TAL) capacities (heavy haul tracks) and/or tracks suitable for higher train speeds (high-speed railways). The application of heavy-haul and high-speed trains imposes more demands on rail track components, either the sub-structural elements (ballast, sub-ballast, and foundation) or the super-structural components (rails, rail pads, and sleepers). Railway sleepers are cross members which support the rails in the longitudinal, transverse, and vertical directions. Concrete railway sleepers are widely used in ballasted rail tracks due to their superior behaviour in many aspects and for being cost-effective. Having a relatively long service life (around 50 years) and low maintenance costs, providing tremendous position stability due to its heavyweight, and being manufactured in any desired size and shape, are amongst the advantages of concrete sleepers.

Since World War II, when the modern prestressed concrete (PSC) sleepers were developed and utilised due to the lack of hardwood timber resources, concrete sleepers have become widely accepted in the railway industry (Shokrieh and Rahmat, 2006). However, these sleepers also have some drawbacks. One issue is the process of manufacturing the prestressed concrete sleeper, which is relatively complex and time and energy demanding (Bezgin, 2017). The loss of the prestressing force within the sleepers (applied from the prestressed tendons) is another problem with the conventional PSC sleepers. It has been found that the prestress loss, which occurs gradually over time, may rise to 40% of the initial prestressing force (Remennikov and Kaewunruen, 2014a). As the moment resistance of the PSC sleeper is highly dependent on its prestress force, the prestress loss reduces the capacity of the PSC sleeper to sustain the rail loads. Furthermore, expensive manufacturing plants with sophisticated equipment are needed to produce PSC sleepers.

According to the above statements, it will be an advantage to produce an alternative concrete sleeper with no need for being prestressed. However, it should be noted that under rail loads, extreme moments will be generated within concrete sleepers, especially at the rail-seat and the centre regions causing significant tensile stresses (AS1085.14, 2019). Hence, as will be explained in Chapter 3, if the prestressing technique is neglected, the concrete material must have a sufficiently high tensile strength so that it does not crack under rail loads. Indeed, the development of alternative concrete material with ultra-high strength for manufacturing non-prestressed concrete sleepers is one of the main challenges of this project.

In the case of reinforced or prestressed concrete structures subjected to numerous repeated (cyclic) loads, such as bridge girders, bridge deck slabs, offshore structures, or railway sleepers, fatigue will be a concern that needs to be considered in the design procedure. Typically, these structures are supposed to undergo millions of load cycles within their design service lives, which shows the necessity of these structures to have high fatigue resistance (Barnes and Garden, 1999, Zhang et al., 2001). Numerous research projects have been conducted to improve the knowledge of the fatigue phenomenon in plain, reinforced, or prestressed concrete, both at material and structural levels (e.g. (Barnes and Garden, 1999, You et al., 2017, Zanuy et al., 2009, Zhang et al., 2001)). According to the obtained results, the fatigue behaviour of concrete structures can be associated with:

- Loss of stiffness and growth of deflections;
- Increase of width and length of cracks; and
- Escalation of permanent strains.

It is important to note that due to the lack of knowledge about the fatigue performance of prestressed concrete structures, Australian Standard (AS1085.14, 2019) has a conservative approach towards the fatigue life of prestressed concrete sleepers. According to this standard, the expected design life of the conventional prestressed concrete sleepers can be attained as long as no tensile strains occur within the concrete component. This approach neglects the tensile strength of concrete and results in a conservative design.

On the other side, recent studies have shown the significance of the high-frequency dynamic (impact) loads that occur occasionally within the service lives of the railway

sleepers. These impact loads are normally caused by the abnormalities/deficiencies of the wheels, rail, or the track foundations (Esveld, 2001). In contrast to the fatigue (cyclic) loads that are also referred to as low-frequency dynamic loads, the impact loads take place infrequently. However, these impact loads are normally of extreme magnitudes and can be as high as five times the static rail loads (Van Dyk et al., 2017). Hence, the limit states design method, which has been recently suggested for the design of concrete sleepers, deems these extreme impact loads as the ultimate limit state (Kaewunruen et al., 2012). Thus, it is concluded that in addition to the standard static tests, cyclic (fatigue) and impact tests are also required to confirm the acceptability of the concrete sleepers, especially, when an alternative concrete sleeper is proposed.

1.2 Project Aim

This study aims to investigate the possibility of developing an alternative concrete material with ultra-high compressive and tensile strengths as well as high fatigue and impact resistance, to produce alternative non-prestressed concrete sleepers. According to the literature (e.g. (Richard and Cheyrezy, 1995)), it is expected that the ultra-high performance fibre-reinforced concrete (UHP-FRC), also known as Reactive Powder Concrete (RPC), is capable of resisting the spectrum of stresses generated within the non-prestressed concrete sleeper due to the rail wheel loads. UHP-FRC is a special type of cement-based fibre-reinforced concrete that contains no coarse aggregates and is known for its very high compressive and tensile strength. UHP-FRC is also called ultra-high performance concrete (UHPC). Some of the commercial names of this material are DUCTAL, CERACEM, and CEMTEC, by Lafarge-Rhodia-Bouygues, Eiffage, and LCPC companies, respectively (Lei, 2006). In this research, UHP-FRC is adopted to refer to the aforementioned material.

It should be noted that no specific studies have been found in the literature demonstrating the minimum required compressive and tensile strengths of UHP-FRC for manufacturing non-prestressed concrete sleepers. Hence, one of the early steps of this research is determination of the minimum required concrete strengths.

1.3 Research Objectives

The main objectives of this study are:

1) to develop an ultra-high performance fibre-reinforced concrete (UHP-FRC) mix with satisfactory compressive and tensile strengths for manufacturing non-prestressed concrete railway sleepers;

2) to investigate the static and cyclic (fatigue) performance of the non-prestressed prototype sleepers made with the proposed alternative concrete mix;

3) to investigate the impact performance of the non-prestressed prototype sleepers with the realistic track foundation conditions;

4) to investigate the static performance of the UHP-FRC prototype sleepers reinforced with GFRP reinforcing bars and find out the enhancing effects of the GFRP reinforcing bars on the performance of the UHP-FRC prototype sleepers;

5) to develop finite element models to simulate the performance of the conventional PSC sleepers and the non-prestressed UHP-FRC prototype sleepers under the standard static rail-seat loading and validate the models against the experimental results;

6) to develop a simplified step-by-step approach to designing the proposed non-prestressed UHP-FRC sleepers.

1.4 Significance of the Work

As explained in Section 1.1, although the conventional prestressed concrete (PSC) sleepers have several advantages, there are still issues associated with these sleepers as listed below:

- The manufacturing process of these sleepers is cost-ineffective and energy-demanding;
- The need for expensive factories with large indoor spaces and exclusive equipment;
- The loss of the prestress applied to the tendons over time.

In order to solve the aforementioned issues, in this research, the application of ultra-high performance fibre-reinforced concrete (UHP-FRC) in manufacturing non-

prestressed concrete sleepers is investigated. For this purpose, an optimal UHP-FRC mix is developed. Subsequently, a number of prototype sleepers are produced with the developed material and tested under static, fatigue, and impact rail-seat loads. The obtained results, show the satisfactory strength of the proposed non-prestressed concrete sleepers. Moreover, a simple method for modelling the concrete sleepers with the commercial finite element code, ABAQUS, is developed.

1.5 Organisation of the Thesis

The thesis consists of 8 chapters as follows:

Chapter 1 presents a brief statement of the problem, project aim, and objectives of the study.

Chapter 2 presents a general background about the rail track systems and concrete sleepers, followed by a review of the rail loads and the sleeper design methods. The fatigue phenomenon and the manufacturing process of the conventional PSC sleepers are also discussed. Subsequently, the typical failure modes observed in PSC sleepers are briefly reviewed and the application of alternative concrete materials for preventing or controlling the common failure modes of the current PSC sleepers are discussed.

Chapter 3 presents the optimisation process of the ultra-high performance fibre-reinforced concrete (UHP-FRC) for manufacturing the alternative non-prestressed concrete sleepers.

Chapter 4 presents the performance of the non-prestressed prototype UHP-FRC samples under static and cyclic loading. Indeed, in this chapter, the adequacy of the proposed UHP-FRC mix for manufacturing the non-prestressed UHP-FRC sleepers is investigated.

Chapter 5 presents the behaviour of the non-prestressed prototype UHP-FRC samples under impact loading. In this study, the actual rail-sleeper fastening system and track foundation are considered to provide a more realistic simulation of the rail-seat performance under extreme impact rail loads.

Chapter 6 presents the performance of the low-profile UHP-FRC samples reinforced with longitudinal GFRP bars. In this study, a variety of GFRP reinforcement ratios are considered to investigate the influence of the GFRP bars on the static performance of the UHP-FRC prototype samples.

Chapter 7 presents the finite element modelling of the conventional PSC sleepers and the non-prestressed prototype segments under the rail-seat positive moment loading conditions.

Chapter 8 presents a summary of the main results presented in previous chapters. Then, based on the obtained results, a series of recommendations are provided for the design of the proposed non-prestressed concrete sleepers.

CHAPTER 2
LITERATURE REVIEW

2.1 Introduction

Railway lines are constructed to transport passengers and cargo either through short or long distances. Indeed, a rail track system is supposed to provide a safe, stable and efficient transportation line for the wheels of trains with various velocities and axle loads (Indraratna and Salim, 2005). For this purpose, the rail track system must be able to resist the vertical, longitudinal and transverse loads applied from the train wheels to the railway system.

There are generally two main types of rail track systems over the world. One is the ballasted rail track system which is the traditional type and is mostly used around the world. The second one is called the slab track system, which has become popular in recent years (Indraratna and Salim, 2005). Although the initial costs of the ballasted rail track system are lower, it has been found that the long-term costs of the slab track system can be lower than the traditional type when the other costs are taken into account such as those related to the life cycle of the railway, the repairs and maintenance, and the traffic disruptions due to the maintenance issues (Jeffs, 1989).

As mentioned in Chapter 1, this research is dedicated to ballasted rail track systems and, more specifically, to the manufacturing and performance of the non-prestressed UHP-FRC sleeper. Hence, in this chapter, a brief literature review about the ballasted rail track system and its components, as well as the fundamental concepts of railway engineering is presented.

2.2 Ballasted Railway Tracks

A typical ballasted rail track system consists of several components that can be categorised into two major groups, superstructure and substructure. The superstructure includes the rails, rail pads, rail-sleeper fastening systems, and sleepers. The substructure, on the other hand, includes the foundation components, which are ballast, capping layer (sub-ballast), and the formation layer (subgrade). The superstructure and

substructure components of a typical ballasted railway are illustrated in Figure 2.1. In the following sections, these components are briefly described.
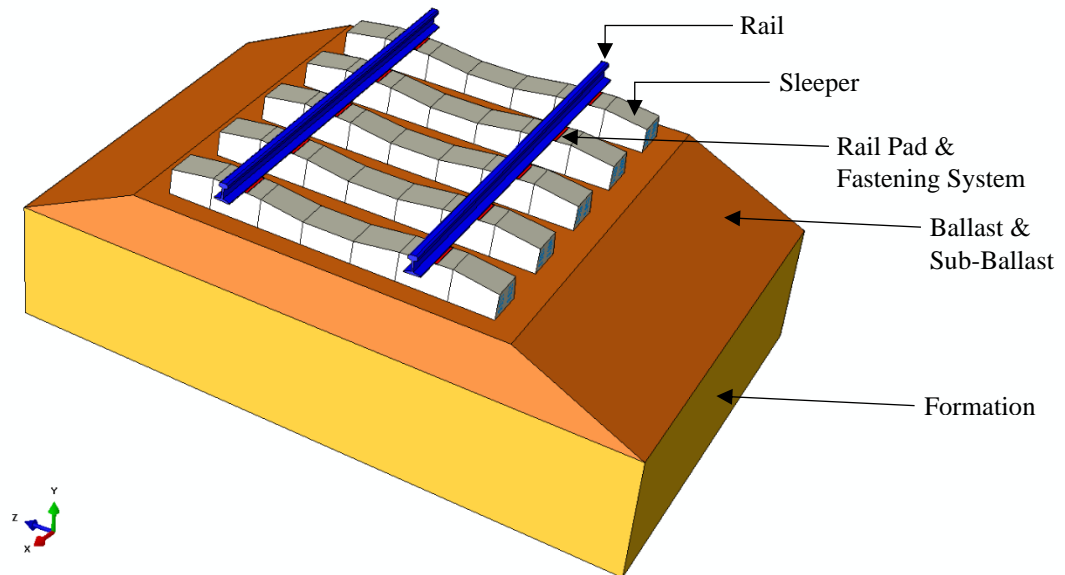
Figure 2.1 The 3D view of a typical ballasted rail track

2.2.1 Rails

As shown in Figure 2.1, rails are the longitudinal members that are expected to provide a guideway for the wheels and transfer the wheel loads to the sleepers through the fastening systems. Since the sleepers are placed at certain distances from each other, the rails must have sufficient stiffness to withstand the wheel loads with no significant deformations between the sleepers. Rails may also be used as electric signal conductors or electric power lines for electric trains (Selig and Waters, 1994, Indraratna and Salim, 2005).

Rail profiles are normally connected by bolted or welded connections. In the case of bolted connections, the two adjacent rail pieces are connected by fishplates which are a type of drilled plates. As will be explained in Section 2.3.2, the discontinuity (gap) between the two rail profiles in a bolted rail connection, which is considered as a rail defect, may cause extreme dynamic loads generated at the rail-wheel interface that may lead to severe damage to the rail track system. Therefore, in recent years, such bolted joints are replaced with continuously welded rails (CWRs) (Selig and Waters,

8

1994). CWRs provide continuous lines of rails that minimise the irregularity of the rails at the connections, which leads to lower maintenance costs and higher riding quality (Selig and Waters, 1994).

2.2.2 Fastening Systems

The fastening systems that are briefly called fastenings are used to connect the rails on top of the sleepers. Fastenings must be able to resist the vertical, lateral and longitudinal movements of rails with respect to sleepers. It is also expected that these systems absorb and dissipate the vibrations of the rails due to different causes such as the passage of trains or natural hazards.

Fastening systems can be categorized into two general types. One type, called the direct fastening system, is the older type and is widely used by the railway industry. In this type, the rail and baseplate are connected to the sleeper with the same fastener. In another type, i.e., the indirect fastening system, the rail is connected to the base plate with a fastener, and the baseplate is connected to the sleeper using a separate fastener. In Figure 2.2, a typical fastening system for concrete sleepers produced by Pandrol Pty Ltd. (Pandrol, accessed on 20/12/2021) is illustrated.

As can be seen in Figure 2.2, the fastening system consists of two main parts, namely, the fastener and rail pad. The fasteners resist the vertical, lateral and longitudinal movements of the rails. On the other side, the rail pads are utilised in order to filter the noises and transfer the loads from the rails to the sleepers. The rail pads have relatively high damping ratios that help in dissipating and reducing the high-frequency rail loads while they also provide sufficient flexibility at the rail-sleeper interface and reduce the possibility of cracks or abrasions at the rail seat areas of concrete sleepers.
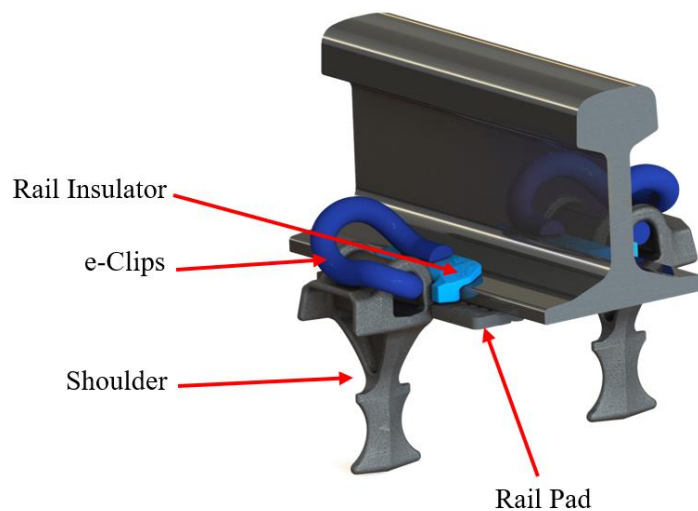
Figure 2.2 Components of a typical rail-sleeper fastening system (Pandrol, accessed on 20/12/2021)

2.2.3 Sleepers

The sleeper is deemed an important element of the railway track system. Railway sleepers are beams placed beneath the rails in order to support the system (Manalo et al., 2010). They transfer and dispense the rail loads to the ballast, keep the correct gauge (transverse position) of the rails and also provide support against vertical, lateral and longitudinal movements of the rails (Zhao et al., 2007). Currently, there are several types of railway sleepers used in ballasted rail tracks around the world. The most well-known types of railway sleepers are timber, concrete and steel sleepers. In recent years, other types of sleepers, such as composite sleepers, have been also introduced to the railway industry.

Amongst several types of railway sleepers, concrete sleepers are vastly used in the railway industry worldwide. Indeed, in recent decades, the railway industry is becoming more interested in concrete sleepers than sleepers made of timber or steel materials (Ferdous et al., 2015b). Various types of concrete sleepers are commonly used worldwide, as listed in the following (see Figure 2.3):

- Mono-block prestressed concrete (PSC) sleepers were initially used in France and have been adopted by other countries such as European countries, Mexico, Brazil, and India (Remennikov and Kaewunruen, 2005) (see Figure 2.3-a). These sleepers

have been utilized in Australia since 1970 and have been the most popular sleeper in recent decades (Kaewunruen, 2010).

- Twin-block concrete sleepers were first developed in the UK and have been used by Australia, the USA, the UK, Canada, China, and Japan (Remennikov and Kaewunruen, 2005), as well as Greece (Giannakos and Loizos, 2010). They consist of two concrete components connected by steel reinforcements (see Figure 2.3-b). The issue in the application of this type of sleeper is that it may be hard to handle and install twin-block sleepers because of their vulnerability to twisting when lifting (Manalo et al., 2010).

- Low-profile concrete sleepers with the same dimensions as timber sleepers are deemed as another ongoing progress (Stevens and Dux, 2008) (see Figure 2.3-c). It benefits the long life cycle of conventional prestressed concrete sleepers while can be easily used for the replacement of deteriorated timber sleepers due to similar dimensions as timber sleepers. However, it is only suitable for the replacement of mainline sleepers due to the fact that it has a special pattern to maintain the track gauge. They are also very stiff with a low damping ratio so they demand high-quality rails and ballast (Cope and Ellis, 2001).

- Wide sleepers: There is a direct contribution between the level of pressure applied from the sleeper to the sub-structure and the rate of track deterioration. Due to their bigger bottom surface, the application of wide sleepers leads to lower average pressure on the ballast, which reduces the rate of the track deterioration (see Figure 2.3-d). Also, they cover the track against rainwater and vegetation. The gap between adjacent wide sleepers is normally a few centimetres that can be covered by rubber substances. The track can be considered as a continuous slab of distinct components, and therefore, the tamping may be performed only at the sleeper ends. Other positive points about wide sleepers are listed in the following (Esveld, 2001):
    - Significant stability of the trackbed;
    - Marginal emissions of body noises;
    - Proper performance regarding the deformation (around 50 percent of the conventional ballasted tracks);
    - The manufacturing cost of this sleeper is higher than the conventional concrete sleeper (by around 10 to 20 percent). However, given its lower

maintenance demands, it has been predicted that in the mid- or long run, this extra cost will be compensated.

(a) mono-block PSC sleepers (You et al., 2017)
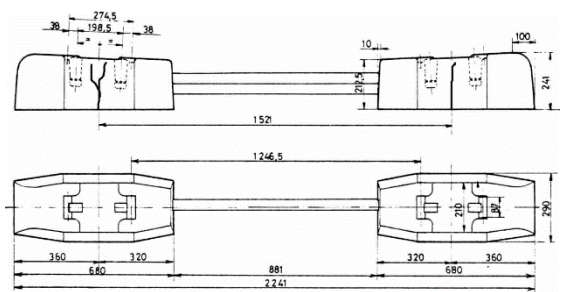
(b) twin-block concrete sleepers (Giannakos and Loizos, 2010)

(c) low-profile concrete sleeper (Gallery, 2010)

(d) wide sleepers (Auersch et al., 2014)

(e) ladder sleepers (Miura et al., 1998)
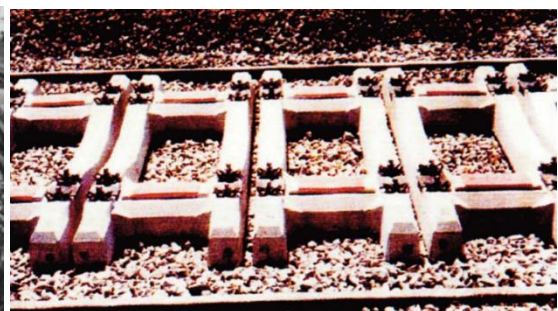
(f) frame sleepers (Pita, 2006)

Figure 2.3 Various types of concrete sleepers

- Ladder sleepers are considered as another promising development in the production of concrete sleepers, consisting of two parallel longitudinal prestressed reinforced concrete elements, each one 12 m long, bounded by steel tubes (Miura et al., 1998) (see Figure 2.3-e). One of the advantages of these sleepers is that they provide continuous support for the rails, which results in reducing the demands on the ballast and its maintenance.

- Frame sleepers: Combining the traditional load transferring system, cross-ties or sleepers, with continuous beams placed longitudinally under the rails, frame-sleeper is another successful approach for reducing the rate of ballast deterioration by decreasing the average pressure on the ballast layer (Zaragüeta, 2013) (see Figure 2.3-f). The fastening system consists of four fasteners per frame which provide considerable horizontal stiffness and buckling resistance of the rail track. Low settlements and more balanced settlements, and thereby, higher durability of the railway track geometry, are other merits of frame-sleepers compared with conventional sleepers (Esveld, 2001).

Advantages of concrete sleepers:

The advantages of concrete railway sleepers are summarized as (Manalo et al., 2010):

- Long life cycle (50 years);
- Lower costs of maintenance;
- Being relatively heavy, they provide satisfactory position stability, especially well for high traffic and speed railways;
- They are mostly tested and approved already.

Disadvantages of concrete sleepers:

The disadvantages of the concrete railway sleeper include:

- Due to its large weight, special equipment is required for the replacement and installation of it;

- It has different characteristics from timber sleepers, including higher stiffness as well as requiring more section height (except for the low profile concrete sleeper)

(Kohoutek, 1991), which makes it less suitable for partial replacement of timber sleepers;

- It is exposed to the corrosion of the rail seat in the absence of a resilient rail pad (Cope and Ellis, 2001).

2.2.4 Ballast

The term 'Ballast' in railway engineering represents a layer of free-draining coarse aggregates which is positioned on top of the capping layer (sub-ballast) in order to provide elastic support to the sleeper. The thickness of the ballast is normally around 200-350 mm. The ballast is typically made of crushed stones obtained from metamorphic, well-cemented sedimentary and igneous rocks resources. The ballast layer is supposed to fulfil the following functions (Esveld, 2001, Jeffs, 1989, Selig and Waters, 1994):

- To provide an even supporting layer for installing the sleepers in a line;
- To provide support to the railway sleepers against the vertical, longitudinal and transverse forces;
- To filter and dissipate the impact rail loads through the friction between the interlocked coarse aggregates;
- To transfer and alleviate the stresses over the sleeper-ballast interface to bearable stress levels for the sub-ballast layer;
- To sustain the minimum plastic deformation between the successive maintenances;
- To provide adequate permeability for fast water drainage;
- To provide sufficient empty spaces to accommodate the probable finer pieces from the failed aggregates or the interlocking abrasions of the coarse aggregates;
- To provide sufficient electrical insulation;
- To prevent the growth of weeds;
- To filter the noises; and
- To enable the maintenance measures.

2.2.5 Sub-ballast

The sub-ballast or capping layer is made of granular aggregates with finer dimensions in comparison with ballast. This layer normally consists of graded crushed aggregates or a mixture of sand and gravel. The main functions of the sub-ballast are as follows (Kaewunruen, 2007):

- To transfer and reduce the bearing stresses from the ballast/sub-ballast interface to bearable stress levels for the subgrade;
- To inhibit the penetration of the fine particles of subgrade into the ballast layer;
- To facilitate the water drainage as well as keeping the water away from ballast by shedding the water away;
- To inhibit the erosion of subgrade by preventing the direct contact of the subgrade with the ballast aggregates;
- To protect the subgrade against freezing and thawing issues.

2.2.6 Subgrade

The subgrade is indeed the ground base above which the railway system is constructed. Hence, it is also called formation. The formation is indeed the lowest support to the rail track system and may consist of natural soil and some structural waste materials. It must be able to withstand the bearing stresses at the sub-ballast/subgrade interface and dissipate the dynamic forces through its infinite depth. The failure of subgrade can lead to distortion and uneven settlements of the whole rail track structure, although the top layers, i.e., ballast and sub-ballast, are constructed from high-grade materials. In the case that the subgrade is made of soft soil, the subgrade may need to be strengthened using one of the ground improvement techniques, such as the vibratory compaction, prefabricated vertical drains (PVD) or the injection of cement/lime grouts (Indraratna and Salim, 2005).

2.3 Rail Loads, Ballast Contact Pressure, and Design Approaches

The railway loads mainly include the static loads, which are normally due to the weight of the train components, passengers, and freights, and the dynamic loads. The dynamic

loads are mainly generated through the interaction between rails and wheels, which can be classified into two groups, including low-frequency dynamic (cyclic) loads and high-frequency dynamic (impact) loads (Van Dyk et al., 2017). While the low-frequency dynamic load forms as a result of the normal wheel-rail interaction, the high frequency (impact) load is produced as a result of the irregularities of the rail, wheel or the track support (Kaewunruen and Remennikov, 2013, Kaewunruen and Remennikov, 2009c, Van Dyk et al., 2017). In the following, the two types of dynamic loads are briefly discussed.

2.3.1 Low Frequency Dynamic Loads

The low-frequency dynamic load, which is commonly referred to as dynamic or cyclic load, occurs due to the normal rail-wheel interaction when the train is passing through the track and mainly depends on the train speed as well as the static load. This type of load has been taken into account in the current design codes using the Dynamic Impact Factor (DIF), denoted by Φ, which multiplies the static wheel load, as shown in Equation (2.1) (Doyle, 1980):

$$P_d = \emptyset P_s \tag{2.1}$$

Where P_d and P_s are the dynamic wheel load and static wheel load, respectively. Numerous expressions have been recommended for calculating the value of DIF in different research studies or design codes around the world, most of which are dependent on the train speed (V) as the main parameter (Doyle, 1980, Van Dyk et al., 2017). A summary of the well-known suggestions for obtaining the DIF is presented in Table 2.1 (Doyle, 1980, Van Dyk et al., 2017). In Table 2.1, V and D represent the train speed (km/hour) and wheel diameter (mm), respectively. U is the track modulus (MPa) which is a parameter that defines the vertical stiffness of the rail foundation (Selig and Li, 1994). δ is a parameter that depends on the track condition and can be selected as 0.1, 0.2, and 0.3 for tracks of very good, good, and poor conditions, respectively. η is a factor that depends on the train speed and can be selected as 1.0 for

train speeds up to 60 (km/hour) while for the train speeds higher than 60 (km/hour) up to 200 (km/hour) it can be obtained from Equation (2.2):

$$\eta = 1 + \frac{V - 60}{140} \qquad (2.2)$$

Also, t is a parameter depending on the probability of exceedance from the upper confidence limits (UCL), and for various percentages of UCL can be determined using Equation (2.3):

$$\begin{cases} 0.0 \rightarrow UCL = 50\% \\ 1.0 \rightarrow UCL = 84.1\% \\ 2.0 \rightarrow UCL = 97.7\% \\ 3.0 \rightarrow UCL = 99.9\% \end{cases} \qquad (2.3)$$

Table 2.1 Suggested formulae for calculating the dynamic impact factor (Doyle, 1980, Van Dyk et al., 2017, You et al., 2017)

Expressions for calculating the Dynamic Impact Factor	Authors (references)
$\emptyset = 2.5$	Australian Standard (AS1085.14, 2019)
$\emptyset = 1 + 5.21\dfrac{V}{D}$	Talbot (Hay, 1982)
$\emptyset = 1 + \dfrac{V}{58.14U^{0.5}}$	Indian Railways (Srinivasan, 1969)
$\emptyset = 1 + \delta\eta t$	Eisenmann (Esveld, 2001)
$\emptyset = 1 + \alpha + \beta + \gamma$	Office of Research and Experiments of the International Union of Railways (ORE) (Birmann, 1965)
$\emptyset = 1 + \dfrac{V^2}{30,000}, if\ V \leq 100km/h$	German Railways (Schramm, 1961)

$\emptyset = 1 + \dfrac{4.5V^2}{10^5} - \dfrac{1.5V^3}{10^7}$, $if\ V > 100\ km/h$	
$\emptyset = 1 + \dfrac{8.784\ (\alpha_1 + \alpha_2)V}{P_S}\left[\dfrac{D_j + P_u}{g}\right]^{1/2}$	British Railways (Doyle, 1980)
$\emptyset = 1 + 4.92\dfrac{V}{D}$	South Africa (Doyle, 1980)
$\emptyset = 1 + \dfrac{19.65V}{D\sqrt{U}}$	Clarke (Doyle, 1980, Van Dyk et al., 2017)
$\emptyset = (1 + 3.86 \times 10^{-5}V^2)^{2/3}$	Washington Metropolitan Transit Authority (WMATA) (Prause et al., 1974)
$\emptyset = 1.098 + 8 \times 10^{-4}V + 10^{-6}V^2$	Sadeghi (Prause et al., 1974)
$\emptyset = 0.6 + 0.08V\ \ for\ 32 < V < 193$	AREMA (AREMA, 2013)
$\emptyset = (1 + \eta + \beta)f\ \ \ \ if\ V \leq 200$ $\emptyset = 2.5\ \ \ \ \ \ if\ 200 < V \leq 250)$ $\emptyset = 3.0\ \ \ \ \ \ \ \ \ \ \ if\ V > 250$	China (Q/CR-9130, 2015)

The coefficients α and β depend on the mean value of the DIF, while γ is related to the standard deviation of the DIF. The coefficient α is related to the track level, the vehicle suspension, and the speed of the vehicle. The coefficient β is related to the speed of the vehicle, the superelevation deficiency of the rail track, as well as the gravity centre of the vehicle. The coefficient γ depends on the speed and the design of the vehicle, the age of the track, the probability of hanging sleepers, as well as the maintenance situation of the train power units. $\alpha_1 + \alpha_2$ represents the total dip angle of the rail joints (in radians). D_j demonstrates the stiffness of the track at the joints (kN/mm), P_s represents the static load under the wheel (kN), P_u represents the unsprung weight per wheel, and g represents the gravity constant (9.81 m/s^2). Also, f is the coefficient of transverse force which relates to the radius of the rail curves. The latter parameter takes

into account the effects of the transverse forces, which are applied to the rails through the rail curves, on the vertical dynamic loads.

2.3.2 High-Frequency Dynamic (Impact) Loads

Impact loads, which are usually defined as high-frequency dynamic loads, are a class of dynamic loads applied within a short time frame. These transient loads are mostly caused by blasts and sudden loading. The main causes of impact loads in railway lines are irregularities over the interaction region of rails and wheels such as the track abnormalities, irregular stiffness of track because of varying material properties as well as the settlement of rail supports (ballast and formation layers), improper welds, joints or switches, vehicle imperfections such as wheel burns, wheel flats, hunting, or resonance vibrations, and the like (Esveld, 2001). During their short loading periods, the magnitudes of impact forces are significant (Lee et al., 2005), which considerably affects the design and application of concrete railway sleepers (Kumaran et al., 2002). It is necessary to take into account that the values of the impact loads are not only dependent on the train speed value but also the amount of irregularity (such as the amount of unevenness in the case of dipped rail connections) (Kaewunruen and Remennikov, 2013). In the following, the main causes of impact loads of the rail lines are briefly discussed.

2.3.2.1 Impact loads due to wheel-rail surface defects/irregularities

It has been found by Ahlbeck and Hadden (1985) that the magnitudes of the impact loads due to worn wheel profiles were around 214-312 (kN), varying with the surface profile roughness, within the short time duration of 2-5 milliseconds, respectively. Also, it was observed that the magnitudes of the impact loads are dependent on the train speed, in the way that the higher speeds result in bigger impact forces compared with the lower speeds. By contrast, the duration of the impulses is shorter at high speeds and longer at low speeds.

2.3.2.2 Impact loads due to wheel defects/irregularities

One of the reasons for impact loads on rail tracks is due to wheel defects such as wheel flats, out-of-roundness, and shells. A number of research projects have been conducted to investigate these wheel irregularities and their impact forces, as briefly summarised in the following paragraph.

Wheel abnormalities usually occur during braking (when the wheels slide on the rail) and they cause high impact loads depending on the defect dimensions and shapes, as well as the trainload (per axle) and speed (Remennikov and Kaewunruen, 2008a). It has been reported that the pattern of the impulses produced by both the wheel flats and wheel shells are similar despite their different appearances (Dukkipati and Dong, 1999). The full description of these types of irregularities can be found in the literature (Dukkipati and Dong, 1999, Knothe and Grassie, 1993, Newton and Clark, 1979, Sadeghi, 1997, Wakui and Okuda, 1997, Wu and Thompson, 2001). Also, out-of-round wheels can generate considerable impact forces, with magnitudes depending on the stiffness of the rail pads (lower rail pad stiffness can reduce the enormity of the impact forces) (Fermér and Nielsen, 1994, Johansson and Nielsen, 2003, Nielsen and Igeland, 1995, Wu and Thompson, 2004).

2.3.2.3 Impact loads due to rail defects/irregularities

This group of irregularities which is attributed to rail defects, mainly includes irregular rail connections such as improper rail welds, joints, and switches, as well as rail corrugations. In 1997, Sadeghi (1997) proved that even small weld abnormalities could result in huge impact loads. Also, it has been reported by different researchers (Esveld, 2001, Zhai and Cai, 1997) that the magnitude of the impact loads due to rail defects can intensely increase as the train speed goes up. Similarly, Rochard and Schmid (2004) showed that the impact loads due to dipped rail joints strongly depend on the train speed and vehicle types. An analogous trend was found by Cai (1992) in the case of rails corrugation, confirming the dependency of the magnitude and period of these impact loads on the speed of the train.

2.3.2.4 Impact loads due to sleeper sub-structure defects/irregularities

The voids and pockets beneath a railway sleeper can also cause considerable impact forces on a rail track. These support defects usually are generated due to the wet beds caused by water springs, extreme subgrade damage, or improper drainage capability of substructures (Kaewunruen and Remennikov, 2007, Lundqvist and Dahlberg, 2005, Rochard and Schmid, 2004). In extreme cases, these abnormalities may result in a situation that is called an *"unsupported or hanged sleeper"* (Remennikov and Kaewunruen, 2008a). It has been found that the worst scenario is when two unsupported sleepers surround a completely supported one (Lundqvist and Dahlberg, 2005).

It is important to note that during the service life of the sleeper, several issues such as surface abrasion may result in a decrease in the impact resistance of concrete sleepers (Ngamkhanong et al., 2017a, Ngamkhanong et al., 2017c, Ngamkhanong et al., 2017b).

Wakui and Okuda (1997) investigated the properties of the wheel/rail impact loads and found that the wheel/rail impact loads can be simulated simply as a shock pulse (impact load) with a duration ranging from 1 to 10 milliseconds.

Van Dyk et al (2017) extracted impact data from the North American track using an apparatus called wheel impact load detector (WILD). They found that DIF is dependent on the wheel load. Also, analysing the gathered impact data, they found that impact load can be very high and can exceed five times the wheel load (DIF>5), which shows the significance of impact loads.

Another fundamental research on the impact load data was conducted by the Queensland University of Technology in 2004 (Leong, 2007). The impact load applied by roughly six million passing wheels of heavy haul tracks, with static axle loads ranging between 26 (t) and 28 (t), were recorded. Using the limit state methodology, the author proposed Equation (2.4) for the prediction of the design wheel/rail force (F^*) taking into account the impact force:

$$F^* = 1.2F_s + F_i \tag{2.4}$$

Where F_s and F_i are the static wheel load and the wheel/rail impact force, respectively. While the static wheel load (F_s) is determined by the owner of the rail track based on the maximum allowable load limit (e.g., 20 t/axle), the wheel/rail impact force must be determined based on the wheel defects or the rail interface defects, but not both of them. This is because these two cases are independent of each other. Leong (2007) only investigated the case of the impact load due to the wheel defects and suggested a revised version of the latter equation for estimating the design wheel/rail force ($F_{t,w}$) by taking into account the impact force due to merely the wheel defects ($F_{i,w}$) using Equation (2.5):

$$F_{t,w} = 1.2F_s + F_{i,w} \qquad (2.5)$$

Where the impact force due to the wheel defects ($F_{i,w}$) can be obtained using Equation (2.6):

$$F_{i,w} = F_{imp}k_{wm}k_I k_{IFF} \qquad (2.6)$$

In which F_{imp} represents the allowable wheel impact force which is normally determined by the owner of the rail track and is utilized as a base case for the calculation of the design rail track forces. For instance, according to the interstate network in Australia (Australasian Railway Association, 2002), the maximum allowable impact force per wheel (F_{imp}) is 230 kN for freight vehicles.

Also, k_{wm} is the wheel maintenance factor and takes into account the frequency and the standard level of wheel maintenance used for the vehicle. It takes different magnitudes of 0.9 for the very high standard of maintenance (Group 1), as well as 1.0 and higher than 1.0 for lower standards of maintenance, Groups 2 and 3, respectively.

Besides, k_I is the track importance factor that reflects the level of acceptable commercial risk of the specific rail track. According to this definition, the rail tracks

are classified in four different categories, with Category 1 (representing the rail tracks of the highest importance) taking the unit (1.0) magnitude, while the three other categories including Category 2 to Category 4 take the lower magnitudes of 0.95, 0.90, and 0.85, respectively.

The impact force factor (k_{IFF}) is mainly dependent on the return period (R) and the train speed (V). The higher return period and higher vehicle speeds lead to higher values of k_{IFF}. Analysing the recorded data and considering the return period of the impact loads, Equation (2.7) has been proposed by Leong (2007) for estimating the impact load factor (k_{IFF}):

$$k_{IFF} = 0.00278R + 0.029V - 0.73 \qquad (2.7)$$

Where R and V are the return period (years) and the velocity (km/hour), respectively. Also, Equation (2.8) described the relation between R and the impact load ($F_{t,w}$) in kN:

$$\frac{1}{R} = 10^{-0.0191F_{(t,w)}+5.92} \qquad (2.8)$$
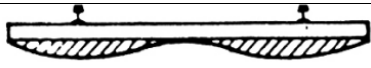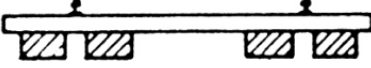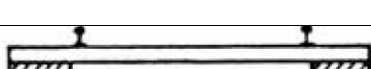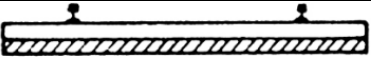
2.3.3 Ballast Contact Pressure

In ballasted railway tracks, the wheel and the self-weight loads applied to the sleeper lead to contact pressure at the sleeper-ballast interaction area. Before the evaluation of the moments generated within the sleeper under the rail-seat load, the support condition of the sleeper and its influence on the distribution of the sleeper-ballast contact pressure must be determined (Thompson and Tayabji, 1976).

The contact pressure distribution at the interface of the sleeper and ballast mainly depends on the compaction level of the ballast underneath the sleeper (Sadeghi and Youldashkhan, 2005). In the case of a well-tamped track, the contact pressure between the ballast and the sleeper is mainly developed around the rail-seat areas. However, when the track is under service, voids are developed in the ballast over time, leading

to a more uniform contact pressure distribution underneath the sleeper (Sadeghi and Barati, 2010). Some of the hypothetical patterns for the ballast contact pressure are listed in Table 2.2 based on a review study conducted by Sadeghi and Youldashkhan (2005). In Section 2.3.4.1, it will be shown that the current codes use an assumed contact pressure pattern to evaluate the design moments developed inside the sleepers under the rail-seat loads (Grassie, 1984).

Table 2.2 Theorretical patterns of ballast contact pressure (Sadeghi and Youldashkhan, 2005)

Contact pressure pattern	Remarks
	Based on laboratory tests
	Tamped ballast at the sides of the rail
	Tamped ballast at the sades of the sleeper
	Stabilised ballast around the rail-seat and sides
	Unifror pressure distribution
	Maximum ballast intensity around the sleeper centre

2.3.4 Current Design Methodologies of Concrete Sleepers

2.3.4.1 Permissible Design Method:

The design methodology of the current design codes can be summarized in the following steps (Grassie, 1984):
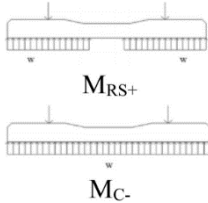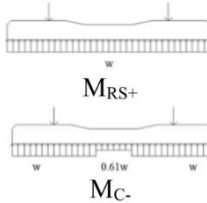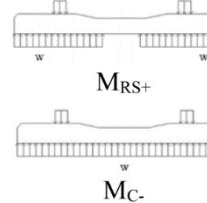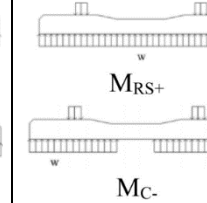
- To calculate the dynamic impact factor (DIF);

- To calculate the loads applied at the sleeper rail seats;

- To assume the sleeper support characteristics;

- To calculate the bending moment magnitudes at the rail seats and the mid-span sections of the sleepers.

In recent years, different countries have developed a series of provisions for the rail track design (especially railway sleepers) according to their requirements, such as Australian Standard (AS1085.14, 2019), Chinese Railway (Q/CR-9130, 2015), American Railway Engineering and Maintenance-of-way Association (AREMA, 2013), Euro Norm (EC2, 2005), International Union of Railways (UIC-713R, 2004). In Table 2.3, a comparison between the approaches of different codes for the concrete sleeper design is presented. In order to have a better view of the stress distribution pattern under the sleeper, a numerical case study is presented in Appendix B. In Table 2.3, P is the vertical wheel load. DF is the distribution factor, which takes into account the effects of the adjacent sleepers in carrying a portion of the wheel load and depends on the sleeper spacing. For example, according to the Australian Standard (AS1085.14, 2019), the value of DF can be obtained from Figure 2.4. Also, B, V, and T are the positive un-factored bending moment at the rail seat, the velocity of the train, and tonnage factors, respectively. L, g, f and h are the sleeper length, centre to centre spacing of rails, rail base width, and sleeper height, respectively. In addition, γ_p and γ_v are coefficients depending on the train speed and the impact attenuation, respectively. γ_i is a coefficient that depends on the irregularities of the sleeper support in the longitudinal direction of the rail line and the coefficient γ_r depends on the support faults of the sleeper.

2.3.4.2 Limit states design method:

As explained above, the "*permissible design*" approach considers the dynamic load by using a dynamic impact factor (DIF). However, such a method is not accurate. Besides, it underestimates the material strength (You et al., 2017). Therefore, in recent years, some researchers have worked on the development of the "*limit states design*" approach for concrete sleepers (Gustavson, 2002, Wakui and Okuda, 1997, Wang, 1996). This approach uses a number of coefficient factors for the load resisting capacity of the sleeper (strength) and loads based on a probabilistic model, taking into account reliable distribution statistic data (Remennikov et al., 2012).

Table 2.3 Comparison between different approaches for design of concrete sleepers (You et al., 2017)

Name of the code	AS 1085.14 (AS1085.14, 2019)	AREMA (AREMA, 2013)	UIC 713 (UIC-713R, 2004)	Q/CR 9130 (Q/CR-9130, 2015)
DIF (Φ)	≥ 2.5	2.0	$(1 + \gamma_p\gamma_v)\gamma_i\gamma_r - 1$	High speed railway: 2.0 Heavy haul railway: 1~1.5 Others: 1.0
Stress distribution	M_{RS+} M_{C-}	M_{RS+} M_{C-}	M_{RS+} M_{C-}	M_{RS+} M_{C-}
Rail-seat load (R)	$DIF \times P \times DF$	$P \times DF(1 + DIF)$	$P(1 + \gamma_p\gamma_v) \times DF \times \gamma_i\gamma_r$	$P \times DF(1 + DIF)$
Rail-seat positive (M_{RS+})	$\dfrac{R(L - g)}{8}$	$B \times V \times T$	$\dfrac{R(L - g - f - h)}{8}$	$\dfrac{R(L - g - f - h)}{8}$
Rail-seat negative (M_{RS-})	$0.67 M_{R+}$	A fraction of M_{RS-}	$0.5 \times M_{RS+}$	-------
Centre negative (M_{C-})	$\dfrac{R(2g - L)}{4}$	A fraction of M_{RS-}	$\dfrac{R}{2}\left(g - \dfrac{2L^2 - b^2}{2(2L - b)}\right)$	$\dfrac{R(2g - L)}{4}$
Centre positive (M_{C+})	$0.05R(L-g)$	A fraction of M_{RS-}	$0.7 \times M_{C-}$	-------

The concrete sleepers can be designed according to three different limit states as follows (Kaewunruen et al., 2012, Kaewunruen et al., 2014, Leong, 2007):

Ultimate limit state:

Caused by a single unrepeated load due to a rare condition such as the derailment or an extreme flat wheel (causing an extreme impact load). This situation can cause the ultimate failure of the concrete sleeper. The ultimate limit state failure includes intensive cracking at the rail seat or the middle part of the sleeper such that the sleeper cannot retain the rail gauge.
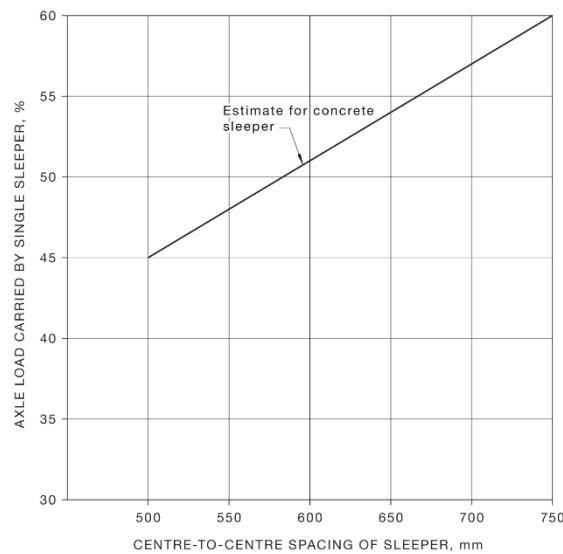
Figure 2.4 Distribution factor (DF) (AS1085.14, 2019)

Fatigue (damageability) limit state:

This limit state is time-dependent in which the accumulative damage develops within the concrete sleeper through the time until it meets the failure criterion. There are different forms of time-dependant limit state failure, such as rail seat abrasion or cracking, due to the cyclic loads caused by the normal wheel-rail interaction.

Serviceability limit state:

This limit state contains several limitations on the performance of the track, such as sleeper deformations, rail displacement, etc. This limit state usually does not turn into a crucial operational restriction due to the failure of a single sleeper in meeting the

criteria of this limit state, while in the case of many sleepers failing in meeting the requirements, the problem can apply considerable restrictions to the rail track.

In the current limit states design practice, prestressed concrete sleepers are designed based on the ultimate limit state (Kaewunruen et al., 2012). This is mainly due to the fact that on one side, the application of prestressed wires minimises the fatigue damages under regular track conditions, and on the other side, the dimensions and configuration of this type of sleeper normally satisfy the serviceability limit states. The limit states design of concrete sleepers consists of three steps (Kaewunruen et al., 2012):

- To calculate the design loads from Equation 2.5;
- To carry out the dynamic analysis and obtain the design moment magnitudes, that can be conducted using the commercial dynamic analysis packages such as D-TRACK;
- To perform the structural design and optimisation of the concrete sleeper.

2.4 Fatigue Phenomenon

A simple description of the fatigue phenomenon is a type of failure that happens at a stress level lower than the ultimate strength of the material due to the repeated loads (Thun, 2006). This type of failure was first observed in steel structures. The origin of the investigations on the fatigue behaviour of concrete at the level of material and structure dates back to the 19th century, and since then, numerous research work in this area has been carried out worldwide (Gylltoft, 1983). In the following, the fatigue assessment of concrete sleepers is briefly discussed.

2.4.1 Fatigue Assessment Methods for Prestressed Concrete Sleepers:

Cracking can occur in concrete sleepers due to intensive bending, shear or bond stresses (Hawkins and Shah, 1982). However, the propagation of these cracks until the total failure of the concrete sleepers is due to fatigue (low-frequency dynamic) loads and the fatigue resistance of these elements (Van Dyk et al., 2017). The hypotheses explained above are suitable for the fatigue life evaluation of bridges, while as the rail

loads are of periodic impact nature, they cannot model the fatigue life of the concrete sleepers accurately. Hence, the need to develop a fatigue assessment model for concrete sleepers, under cyclic wheel/rail loads, has been found.

Using the field data and experimental results and based on the prestressed steel rupture under impact loads, Wakui and Okuda (1997) proposed a model for the fatigue life assessment of prestressed concrete sleepers, as follows:

- To conduct a cumulative frequency distribution figure of the wheel loads;
- To calculate the flexural moments of the sleeper to obtain the cumulative frequency figure of the loading;
- To assess the fatigue life of the sleeper using Miner's model and the data obtained from the fatigue resistance and the frequency distribution figure of the prestressed steel stress values.

Furthermore, based on the concept of damage accumulation and using the data obtained from the concrete sleepers under impact loads, Kaewunruen and Remennikov (Kaewunruen and Remennikov, 2009b, Kaewunruen and Remennikov, 2009c) proposed a model for the prediction of the residual fatigue life of concrete sleepers under repeated impact loads.

The relation between the cumulative damage index and the repeated impact loads, for either soft or hard tracks, are presented in Figure 2.5 (Kaewunruen and Remennikov, 2009c). In this figure, the ratio of the maximum crack length due to flexural stress to the sleeper depth is called the damage index and is used as an indicator of the damage of the sleeper due to the repeated impact loads. According to the test results, this index can also be adopted for the calculation of the residual fatigue life of the concrete sleeper (You et al., 2017).

Based on the fatigue data reported by the previous researchers, You et al. (2017) proposed an approach to assess the service performance and calculate the fatigue life of prestressed concrete sleepers. This approach can be used for the design of concrete sleepers as well as maintenance considerations. However, the authors admitted that in order to achieve a thorough fatigue life prediction of prestressed concrete sleepers, further laboratory tests and field data plus an intensive theoretical investigation are required.
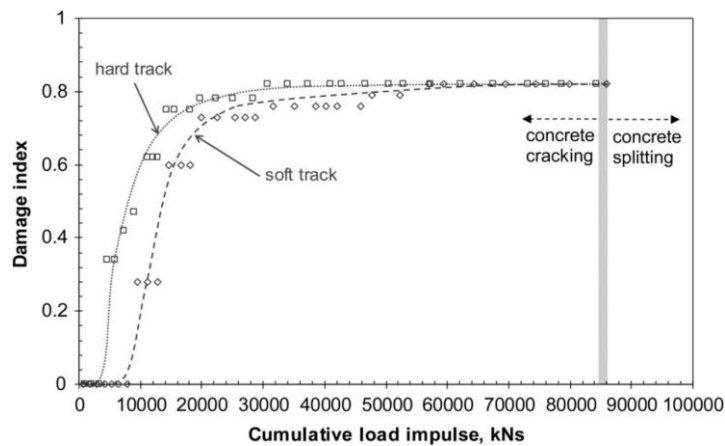
Figure 2.5 Damage index of concrete sleepers in two different track conditions (Kaewunruen and Remennikov, 2009c)

You and Kaewunruen (2019) carried out the fatigue life assessment of prestressed concrete sleepers. Based on the field-test results, they found that within the service life of concrete sleepers, the repeated impact loads and material degradation are the two important factors that affect the material properties. They found that within the first two years, the loss of prestressing force due to the strands was about 24%, and after that, the rate of prestress loss will be marginal. As shown in Figure 2.6, the authors found that around 96.7% of the impact loads cannot cause the decompression moments and more than 99.5% of the loads cannot lead to the positive flexural cracking at the rail seat section of the tested concrete sleeper, as shown in Figure 2.6.

Herein, it is important to note that according to the Australian Standard (AS1085.14, 2019), there has been relatively limited research work conducted on fatigue loading and fatigue life of prestressed concrete sleepers. Hence, this standard only relies on a conservative provision indicating that the design fatigue life of prestressed concrete sleepers will be achievable as long as the resultant strain in the sleeper due to pre-compression, static and dynamic loads is not tensile, i.e., no tensile stress occurs inside the sleeper.
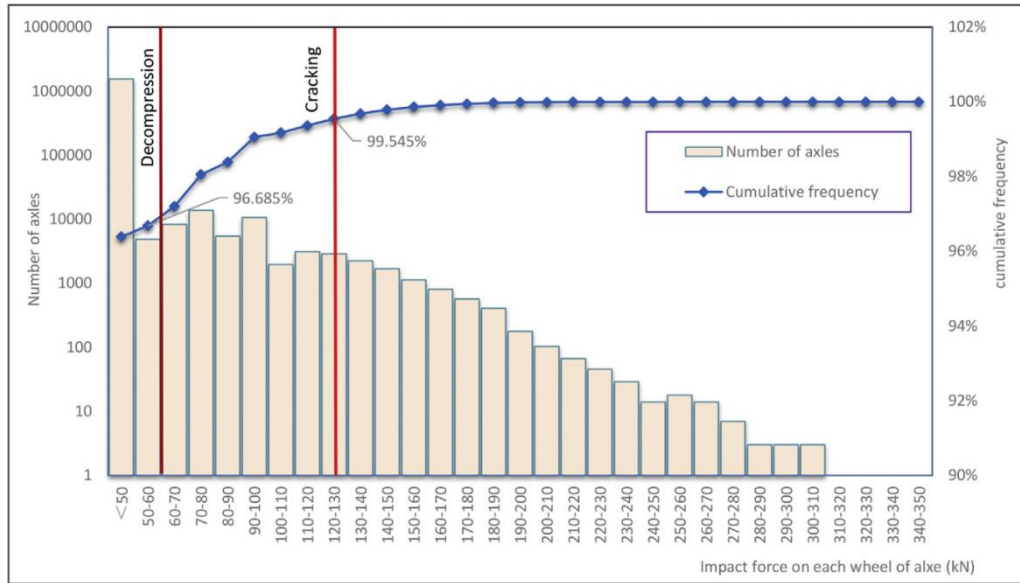
Figure 2.6 Impact loads causing the decompression and cracking moments (MR+) at the rail seat (You and Kaewunruen, 2019)

2.5 Production of Prestressed Concrete Sleepers for High-Speed and Heavy Haul Rail Tracks

Before the introduction of Shinkansen in Japan in 1964, the service speed of railways was limited to a maximum of 160 km/hour. Afterwards, Shinkansen extended this limit to 200 km/hour, which implied the reassessment of the railway characteristics. The significance of the extra 40 km/hour can be understood knowing the fact that it imposes 56% higher kinematic energy, which is applied to the rail track. High-speed rail track requires continuous rails, which necessitates increased lateral track stiffness (Esveld, 2001).

Since the 1950s, several countries have designed their desired configurations of prefabricated high-performance concrete sleepers. For example, in Germany, a series of concrete sleepers such as B58, B70 and B90 was developed. The letter "B" represents the word "beton" and the two following digits denote the year of production (Bezgin, 2017). Subsequently, several studies on the sleeper-ballast interaction and the demonstration of stress distribution patterns underneath the sleeper (through the sleeper-ballast interface) resulted in variable cross-section configuration of sleepers (Hay, 1982, Zakeri and Abbasi, 2011, AREMA, 2013). These investigations proved

that different values of bending moments generate within the sleeper over its length, which allows the designers to optimise the shape of the sleepers by reducing the cross-sections in some areas. In this manner, the non-prismatic prestressed concrete sleepers were produced (refer to Figure 2.3).

Due to the fact that railway sleepers are in continuous contact with the outdoor environment, the designers must make sure that the concrete sleepers do not experience cracking under the service loads due to the tensile stress. This condition imposes strict limitations on the concrete sleepers, which require the sleepers remain free of cracks under service loads (13230-1, 2009, UIC-713R, 2004). Also, as indicated earlier, according to Australian Standard (AS1085.14, 2019), in order to secure the expected fatigue life of the concrete sleeper, it is required that no tensile strain generates within the concrete sleeper (refer to Section 2.4.1). This requirement can be satisfied through the application of prestressing process (Bezgin, 2017).

2.5.1 Prestressing Methods

The approach by which the prestressing force is applied to the concrete sleeper has a crucial impact on the production and design requirements. The cast concrete needs to achieve a certain amount of early strength such that it can receive the loads from the prestressed wires that have been supported by the anchorage blocks at the two ends of the moulds. Different prestressing methods are separated according to the way the prestressing forces are released. Currently, two methods are widely used for the production of prestressed concrete sleepers: "line method" and "carousel method" (Bezgin, 2017). In the line method, the tensioning loads are transferred to the concrete material from the surface of the wires and are resisted through the wire-concrete interaction forces. On the other side, in the carousel method, the prestressing forces are carried by the concrete through the bearing plates installed at the two ends of the sleepers. The latter approach provides a faster production rate and needs smaller indoor factory space. However, it requires higher early strength of the concrete, and thereby, a more sophisticated curing procedure must be considered (Bezgin, 2017).

2.5.2 Loss of Prestress

When designing the prestressed concrete, the loss of the prestressing force must be taken into account. This is mainly due to the relaxation of the prestressing wire, shortening of concrete under the prestressing force transfer, as well as the creep and shrinkage of concrete. Several factors such as the prestressing force, the design elastic modulus of the concrete, the design relative humidity, as well as the prestressing relaxation class of the wire material affect the long-term loss of the prestressing forces (Bezgin, 2017). For instance, the loss of prestressing forces in 40 years, under the different relative humidity values of 80% and 50% are 18% and 28%, respectively (Bezgin, 2014, Bezgin, 2015). Moreover, You et al. (2019) suggested assuming the initial prestress loss of 12% (before the sleeper is transferred to the construction site) for the sake of numerical simulation. It is expected that the prestressing loss is the same for both of the production methods, i.e., line method and carousel method, under constant relative humidity and loading conditions (Bezgin, 2017).

2.5.3 High-speed Rail Tracks

As explained earlier, both the low-frequency (cyclic) and the impact loads applied to the rails are speed-dependent and increase with the speed magnitude. The effect of the train speed is usually taken into account using dynamic impact factor (Φ) in case of low-frequency dynamic (or cyclic) loads or impact load factor (k_{IFF}) in case of transient dynamic (impact) loads (refer to Section 2.3 for more information). The influence of the high cyclic and impact loads on the long-term behaviour of high-speed rail tracks has been investigated through several research projects either considering the total behaviour of the whole track system (e.g. (Fu and Zheng, 2014)), the ballast-sleeper interaction (e.g. (Abadi et al., 2019, Le Pen and Powrie, 2011)), the wheel-rail and rail-sleeper interactions (e.g. (Zhu, 2006)), or merely considering the noise emission of high-speed rail tracks (e.g. (Choi et al., 2004)). However, there has been little work considering the suitability of concrete material and the construction of sleepers for high-speed railways.

In 2017, Bezgin (2017) conducted a case study on the production of prestressed concrete sleepers for being used in high-speed rail tracks. In this case study, Bezgin

demonstrated the production steps of prestressed concrete sleepers for a 212-km rail track of 250 km/hr design speed. The carousel method was used in the production of the sleepers as it allows a fast and automated process and requires less indoor production area compared with the long-line method (see Figure 2.7). On the other side, the carousel method needs a concrete material with high early strength. The author suggested that the minimum early strength and the 28-day compressive strength values of the concrete must be of C40 and C60, respectively. Besides, the author highlighted two important issues to be considered in the massive production of prestressed concrete sleepers, including the rate and the duration of vibration after casting the moulds, and that the curing conditions must be such that the early strength of the material is sufficient while the "delayed ettringite formation" is prevented.

(a) the details of the dimensions   (b) the prestressing end plates
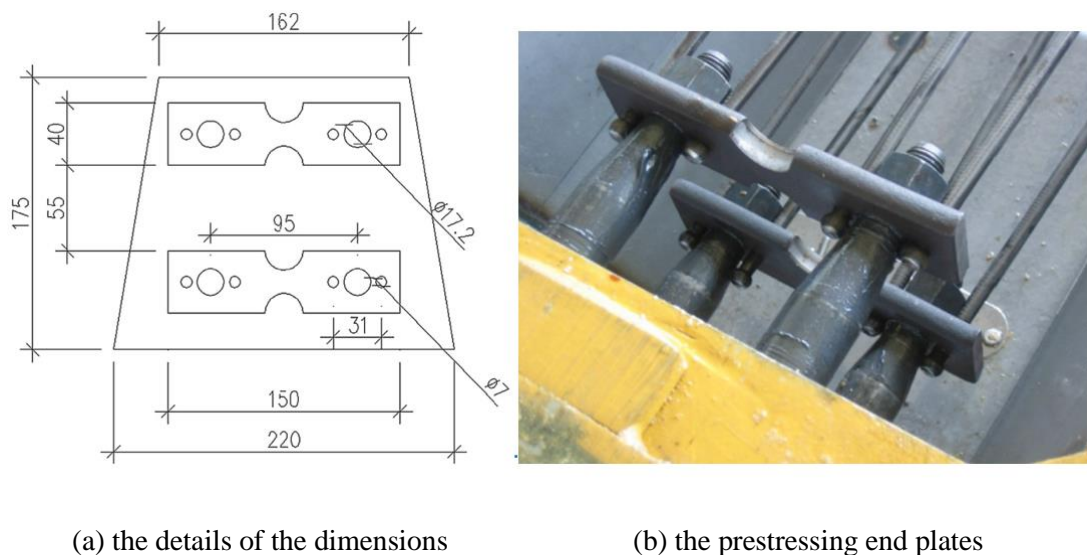
Figure 2.7 The prestressing mould (Bezgin, 2017)

2.5.4 Heavy-haul Tracks

Similar to the high-speed tracks, most of the research papers about the heavy-haul tracks are dedicated to the rail behaviour (e.g. (Grassie et al., 2002, Zhong et al., 2011, Sun et al., 2018)), the behaviour of the sub-structure (e.g. (Cai et al., 2019)) or the total behaviour of the track system (e.g. (Shi et al., 2019)). However, there has been little work dedicated to the production of concrete sleepers and their behaviour under heavy train loads.

In 2013, Bian et al (2012) carried out a numerical investigation on the effects of the wheel flat defects on the sleeper in heavy-haul rail tracks. Developing a numerical model using the commercial package, ANSYS, they studied the response of the prestressed concrete sleepers under the impact loads due to various dimensions of wheel defects in a heavy haul track of 28-tonne axle load. One of the most important achievements of this research was the nonlinear nature of the relationship between the sleeper impact force and the wheel flat dimension as shown in Figure 2.8. It can be seen that the relationship of the sleeper force and wheel flat dimension can be roughly considered linear. Similarly, it was found that the relationship between the wheel/rail impact and the impact force on the sleeper as well as the relationship between the wheel/rail impact and the sleeper bending moment at the rail seat, are nonlinear.
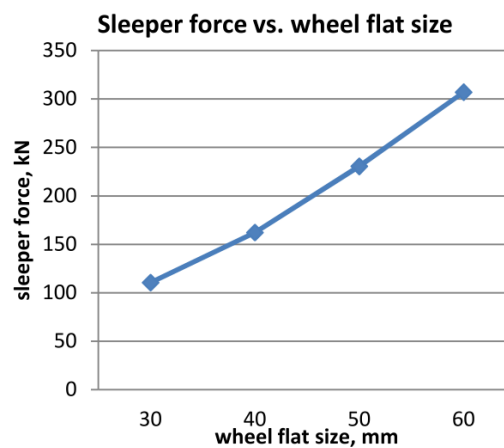
Figure 2.8 Relationship between the sleeper impact load at the rail seat and the wheel flat dimension (Bian et al., 2012)

Although the research study carried out by Bian et al. (2012) revealed important information (as mentioned above), it had a number of shortcomings. Only the vertical impact load was considered herein, while the conical shape of the wheel and also the variety of the wheel/rail characteristics were neglected. The effects of the ballast friction against the lateral walls of the sleepers and the contribution of the sleeper fasteners at the rail seat are other essential issues that have been ignored in this research.

Through another numerical study, Bian et al. (2013) found that by increasing the static wheel load, at any assumed train speed, the impact load due to the wheel flat increases, as shown in Figure 2.9-a. It can also be seen that for the lower train speeds, the increase of the impact load corresponding to the wheel static load has a nonlinear trend. On the other hand, Bian et al. (2013) found that for various static wheel loads, the maximum impact loads due to a specific wheel flat occurs at an optimum train speed which is not necessarily the maximum speed (see Figure 2.9-b). It is important to notice that wheel flat is only one source of the impact loads and it is expected that the impact forces due to other sorts of wheel-rail irregularities (such as dipped rail connection) increase with the increase of the train speed. Based on the obtained results, the authors suggested that for a specific rail track, in order to achieve higher safety, both the train static load and the critical speed must be taken into account.

(a) sleeper impact force vs. static wheel load

(b) sleeper impact force vs. vehicle speed
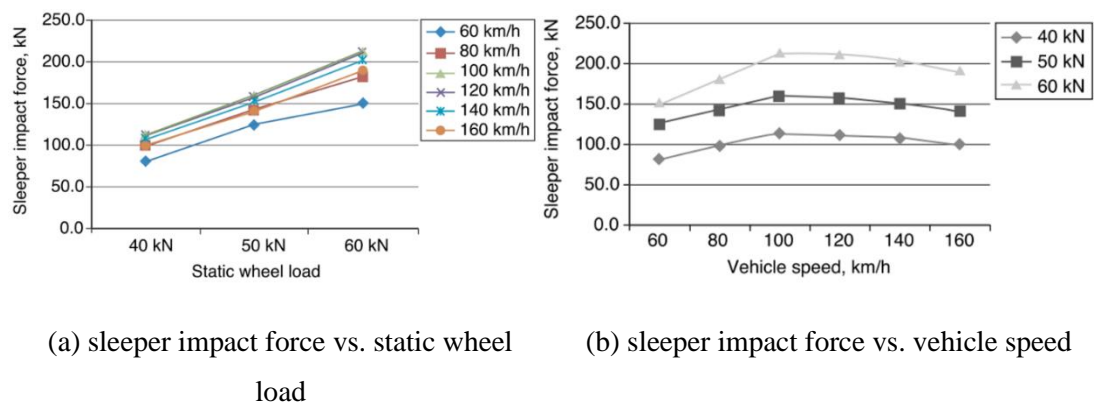
Figure 2.9 Sleeper impact force values due to wheel-flat (Bian et al., 2013)

Another significant research on the heavy-haul rail tracks has been the field experiment carried out by Shi et al. (2019). They studied the dynamic performance of a heavy-haul track under various heavy wheel loads ranging between 21 and 30 (t) at various speeds varying between 10 and 75 (km/hour). They found that the increase of the train speed (in a rail without irregularities) significantly increases the lateral wheel-rail force, although it does not affect the vertical force considerably (see Figure 2.10). The opposite trend was observed in the case of various axle loads where the vertical wheel-rail force increases corresponding to the axle loads while the lateral load does not

change considerably (see Figure 2.11). The authors also reported a linear relationship between the train speed and the axle load with the rail track dynamic vibration.

(a) lateral force   (b) vertical force
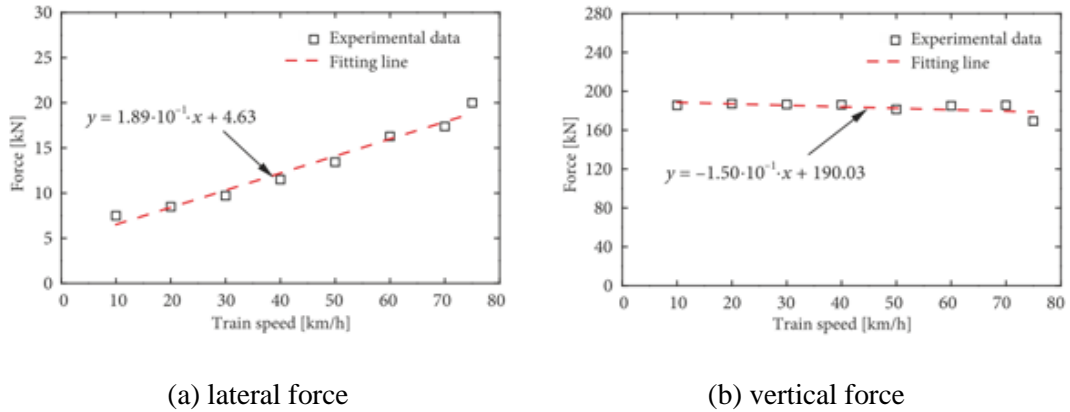
Figure 2.10 Peak values of the wheel-rail force vs. train speeds (Shi et al., 2019)

(a) lateral force   (b) vertical force
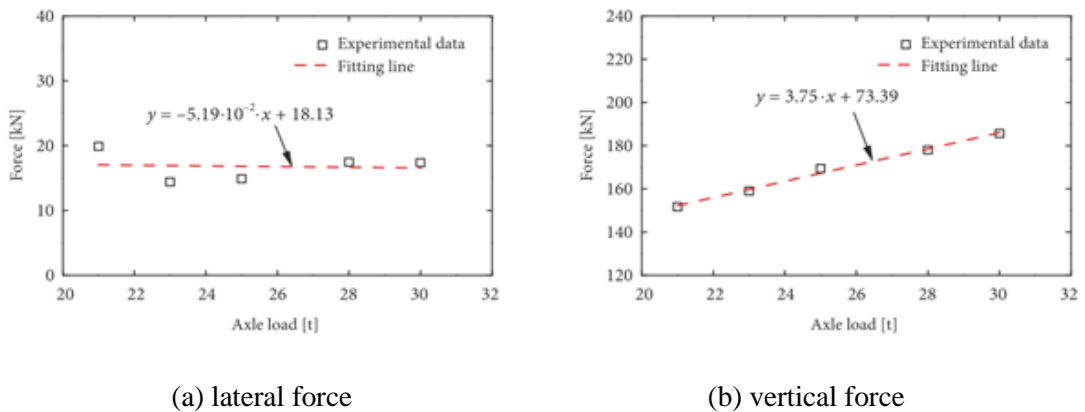
Figure 2.11 Peak values of the wheel-rail force vs. axle loads (Shi et al., 2019)

2.6 Failure Modes of Prestressed Concrete Sleepers

Prior to any approach towards the development of alternative concrete sleepers, it seems necessary to study the performance and especially the issues attributed to the conventional prestressed concrete sleepers. Therefore, in this section, various failure modes of conventional concrete sleepers are discussed. This section is mainly based on a comprehensive literature review carried out by Ferdous and Manalo (Ferdous and Manalo, 2014).

2.6.1 Deterioration at Rail-seat

There are a number of reasons for the rail-seat deterioration of PSC sleepers, such as abrasion at the rail-seat, hydro abrasive corrosion, chemical degradation, and cracking due to hydraulic pressure or freeze and thaw (Bakharev, 1994). Amongst the causes of rail-seat deterioration mentioned above, the most common and crucial factor is rail-seat abrasion which is caused by the relative movement in the interface of rail pad and concrete sleeper, which results in the removal of the concrete paste from the surface of the sleeper at the rail-seat. Two research reports in 2009 (Zeman et al., 2009) and in 2011 (Kernes et al., 2011) revealed that a shear force is activated through the interface of the rail-pad and concrete sleeper when the load is transferred from the rail to the sleeper. When this shear force exceeds the frictional resistance of the interface, the relative movement happens, which results in a marginal shear strain on the surface of the sleeper. Through time, this strain increases and eventually results in the loss of the concrete surface.

Many researchers have tried to enhance the resistance of the rail seat region of concrete sleepers against deterioration. Peters and Mattson (Peters and Mattson, 2004) investigated the application of cast-in-steel plates in order to protect the rail seat region. They observed that no rail seat deterioration (RSD) occurred after 10 million cycles at a frequency of 2.5 hertz. However, this method imposes high manufacturing costs, plus the water may intrude between the rail seat plate and the concrete sleeper and can deteriorate the concrete. Peters (2007) used a sort of epoxy coating material to cover the sleeper rail seat region. But this method is not practical as it requires significant labour work and the rail line closures during the application of the epoxy and its curing process, in addition to the fact that the epoxy cover wears away through time. A more practical solution is to add silica fume and fly ash to the concrete mix in the rail-seat regions of the sleeper (Shurpali et al., 2013). This approach aims at using a type of concrete with higher compressive and tensile strengths in order to limit the cracking and permeability of concrete in the rail seat area. Another approach is to use steel fibre reinforced concrete (SFRC) in the rail-seat region of the concrete sleeper during the manufacturing process (Peters and Mattson, 2004, Takahashi et al., 2008).

2.6.2 Damage at the Centre-bound

González-Nicieza et al. (2008) investigated the failure mechanism of a heavy-haul railway line that was expected to carry heavy dynamic loads from freight trains. The track was designed to support two classes of trains that were different in terms of loads and speeds. They observed that some vertical cracks occurred on a sleeper because of tensile failure in the middle of the element at the upper part. Eventually, that crack crossed the centre of the segment and developed into an "X" form prior to the total failure, as shown in Figure 2.12-a. It has been found that heterogeneity of the sleeper foundation due to the deterioration of the sub-structure and uneven maintenance activities through the years cause the unbalanced stress distribution underneath the sleepers and eventually resulted in this type of failure.

It was concluded that the un-even ballast maintenance, especially in heavy-haul tracks, can result in uneven stress distribution underneath the sleepers, causing the failure of these track elements (González-Nicieza et al., 2008). Besides, the final shape of the centre-bound crack is not vertical (see Figure 2.12-a), which indicates that the huge shear forces developed within the sleeper at the mid-span have contributed to the failure. Since the tensile and shear forces are responsible for this type of failure, the application of an alternative concrete with high tensile and shear strength can be a potential solution to prevent this type of failure.

2.6.3 Longitudinal Crack

Rezaie et al. (2012) observed severe longitudinal cracks which occurred even before the installation of the sleepers. It initiated from the fastening holes because of the huge concentration of tensile stress around these areas in the transverse direction caused by pre-tension forces. Also, additional forces such as water freezing force or the ones applied from the fine rocks (from inside the rawlplug holes) can deteriorate the situation and result in the general failure of the sleeper because of longitudinal cracks through the length of these segments (Figure 2.12-b). The authors also performed numerical simulation and proved that the tensile stress with its maximum occurring between the two fastening holes causes this type of failure in concrete sleepers. This conclusion was confirmed later on by Ma et al. (2010), who found that the

concentration of shear stress around the rawlplug holes is responsible for the longitudinal fracture.

Since the initiation of the longitudinal crack is due to the development of tensile stress around the fastening holes (as mentioned above), it is expected that the use of alternative concrete materials with high tensile strengths can significantly curtail this sort of failure.

(a) excessive tensile stress (González-Nicieza et al., 2008)

(b) longitudinal crack (Rezaie et al., 2012)

(c) derailment (Zakeri and Rezvani, 2012)

(d) high impact loads (Kaewunruen and Remennikov, 2009a)

Figure 2.12 Failure of concrete sleepers

(e) delayed ettringite formation (DEF)
(Hime, 1996)

(f) alkali-aggregate reaction (AAR) (Fertig
et al., 2013)

(g) bar corrosion (Mohammadzadeh and
Vahabi, 2011)

(h) ice forming (Zi et al., 2012)

Figure 2.12 Failure of concrete sleepers

2.6.4 Derailment

This type of failure is deemed as the ultimate failure since it makes the rail track unusable and is mainly caused by labour faults and invisible defects of the tracks. Zakeri and Rezvani (2012) investigated the derailment failures of the Iranian rail tracks supported by B70 concrete sleepers and found that those sleepers with the ultimate failure must be replaced while it imposes vast maintenance costs on the industry (Figure 2.12-c). Also, the authors stated that the manpower faults and existing deficiencies of the tracks were responsible for the derailment of the railway line.

2.6.5 High-impact Loading

Flexural cracks, which occur at the mid-span of concrete sleepers and result in the dramatic reduction of flexural stiffness in railway sleepers, are mainly caused by intensive but infrequent rail loads applied within a short time frame (Murray and Cai, 1998, Remennikov and Kaewunruen, 2007). It was reported that these impact loads are usually applied due to abnormalities in wheels (e.g., flat wheels) or rails (e.g., dipped rails). Some field inspections have revealed examples of this type of failure that happened in the suburban rail lines of Wollongong in the form of cracks either at the mid-span of the sleepers or near the rails (Ferdous and Manalo, 2014, Kaewunruen and Remennikov, 2008). Another collapse of the same kind was observed by Kaewunruen and Remennikov (2009a) in a rail line designed for huge loads of 30 tons per axle (Kaewunruen and Remennikov, 2009b) which is shown in Figure 2.12-d. A rail joint defect was deemed to be the cause of this failure. In 2011, Kaewunruen and Remennikov (2011) carried out an experimental investigation in order to find the ultimate capacity of a pre-stressed concrete sleeper. They observed the same failure pattern as the one found in the real rail track.

It is expected that the application of alternative concrete materials with high tensile strength and energy absorption capacities can intensely limit this type of failure.

2.6.6 Delayed Ettringite Formation (DEF)

There is a possibility that either soil, aggregates, or groundwater have some minerals such as calcium, magnesium, sodium or potassium that can react with cement when mixed during the process of making the concrete (Narayanan and Beeby, 2005). This sort of reaction leads to the expansion of the concrete, resulting in cracks and thereby deterioration of sleepers made from it. The DEF, which is a special case of sulphate attack, has been found responsible for the deterioration of concrete sleepers in Finland, which has happened within the relatively short time frame of 10 years from when they were manufactured, initiated by the micro-cracks formed during the heat treatment process of the concrete (Tepponen and Eriksson, 1987).

Heinz and Ludwig (1986) found that no DEF generates in low heat-curing temperatures (below 75 degrees) even during relatively long heat-treatment

procedures, which was confirmed by Hime (1996). Indeed, Hime (1996)suggested limiting the curing temperature of the concrete to the low magnitude of 70° C (preferably lower than 60° C). However, Sahu and Thaulow (2004) found that the heat-treatment temperature is not the only effective parameter in the occurrence of DEF, and in some circumstances, it may occur even during low temperature curing processes (lower than 70° C). They reported that the application of high alkali cement materials with high surface area, concrete with a high amount of C_3S, as well as concrete with a high amount of cement and with a low water-cement ratio are other issues that can cause DEF. Also, both the latter reports by Hime (1996) and Sahu and Thaulow (2004) suggested that the long-term water-exposure cycles can increase the occurrence likelihood of DEF.

Beyond that, in cement-based concrete, there is a chance that sulphate ions react with the calcium aluminate hydrate and form calcium sulfoaluminate or react with calcium hydroxide and form gypsum, while both the cases lead to DEF (Ferdous and Manalo, 2014). Amongst the factors mentioned above, the curing temperature is an issue that must be controlled during the manufacturing process of concrete sleepers, and especially heat curing is an inevitable part of the process of manufacturing prestressed concrete sleepers.

2.6.7 Alkali-Aggregate Reaction (AAR)

The major source of alkali in the concrete mixture is Portland cement; however, unwashed aggregates may contain sodium chloride. There is a possibility that aggregates that contain silica, such as chert, opal, and quartzite, react to hydroxyl ions in a mixture of alkaline concrete, causing a considerable expansion. Shayan and Quick (1992) observed some longitudinal cracks on the upper face of the prestressed concrete sleeper as well as a sort of map cracking at the sleeper ends, as shown in Figure 2.12-f. They found these cracks occurred due to alkali-aggregate reaction (AAR), which is also called alkali-silica reaction. This observation was also confirmed by other researchers (e.g. (Qinhua et al., 1996)).

2.6.8 Acid Attack in Concrete

It has been found that the concrete made with Portland cement is vulnerable to acid attacks (Gourley and Johnson, 2005, Hobbs, 2001). For instance, if the cement hydrate, $Ca(OH)_2$, has contact with a sort of acid, it will be converted to calcium salts (Narayanan and Beeby, 2005, True, 1993). Hence, acid rains are deemed to be a potential cause of deterioration to uncovered concrete structures such as prestressed concrete sleepers.

2.6.9 Bar Corrosion

In 2011, Mohammadzadeh and Vahabi (2011) investigated the effect of the environment on the deterioration of B70 PC sleepers, focussing on the adverse influence of chloride ion diffusion. They found that the mid-span area of concrete sleepers is more exposed to diffusion deterioration than the rail seat region. In their field observations, they found a significant quantity of fine-graded soil which, due to the low humidity of that area, could easily be distributed over the sleepers. In the long-term, due to rain and moisture, an ideal condition for the bar corrosion of the PC sleepers due to chloride diffusion could occur. This type of failure is shown in Figure 2.12-g. One apparent solution to the bar corrosion can be to replace the steel bars with GFRP bars.

2.6.10 Ice Forming Failure

Zi et al. (2012) investigated the failure of concrete sleepers in a high-speed rail track in Korea and observed that roughly one sleeper per 300 (m) length of the track was damaged due to conical cracks, as shown in Figure 2.12-h. Eventually, they found the considerable ice pressure of 40 MPa caused by the freezing of water that penetrates the sleeper, which is responsible for this sort of failure. The application of an alternative concrete mix with low permeability can be a good solution to this issue.

2.6.11 Summary of the Failure Modes of Concrete Sleepers

In Table 2.4, a summary of different failure types of concrete sleepers is presented. Based on the rigorous review of the literature, the demands for avoiding or at least limiting these failure modes are briefly stated, as well. It is important to note that most of these failure scenarios are expected to be more critical on high-speed and heavy haul rail tracks. According to the literature (e.g. (Shi et al., 2019, Bian et al., 2013)), in heavy haul tracks, higher static vertical loads are expected, while in high-speed rail tracks, significant impact loads (due to wheel-rail abnormalities), as well as higher lateral loads are predicted.

Table 2.4 Summary of the concrete sleeper failure modes

Mode of failure	Reason	Demands
Rail seat deterioration	Shear force between the rail and the sleeper	High strength material at the rail seat region
'X'-shaped fracture	Tensile & shear stresses	High tensile and shear strengths
Longitudinal cracking	Tensile stress	High tensile strength
Ultimate failure	Derailment	More accurate labour work
Cracking	High impact loads	High impact resistance & high residual strength
Micro-cracking	DEF	Control of heat curing
Cracking	AAR	Not using alkali aggregates in the concrete mix
Cracking	Acid attack	High chemical resistance
Mid-span damage	Bar corrosion	High resistance of the concrete against cracking
Conical cracking	Ice expansion	Low permeability

2.7 Selection of the Alternative Concrete Materials for Manufacturing Sleepers

As presented in Table 2.4, the most important requirements of the concrete sleepers for avoiding various modes of failure are related to the concrete material. These demands are listed together in the following:

- High compressive strength;
- High tensile strength;
- High shear strength;
- High impact resistance;
- High residual strength;
- Low permeability; and
- High resistance against chemical attacks.

In the following sections, various alternative concrete materials to satisfy the demands are briefly reviewed. Herein, the advantages and disadvantages of these alternative concrete materials are compared with the conventional high-performance concrete (HPC) currently used for manufacturing railway sleepers.

2.7.1 Geopolymer Concrete:

The well-known Australian supplier of concrete railway sleepers, Rocla, has adopted fly-ash based geopolymer concrete for producing prestressed geopolymer concrete sleepers. Through field inspections, Rocla has shown this sleeper type works well in mainline the rail track since 2002 (Gourley and Johnson, 2005, Cheema, 2012). Also, Palomo et al. (2007) proposed that the application of alkali-activated fly ash based concrete can be suitable for manufacturing concrete sleepers without demonstrating the details of their behaviour. Similarly, Uehara (2010) investigated the use of fly ash as the binding component of an environment-friendly concrete mix for producing prestressed geopolymer concrete sleepers, which showed satisfactory performance under static loading. Palomo and Fernández-Jiménez (2011) also used the alkali-activated fly-ash based geopolymer concrete for producing prestressed concrete sleepers to be experimentally tested, and again these sleepers proved well.

Herein, it is important to state that Nu-Rock materials produced by Nu-Rock Technology Pty Ltd, the industry partner of this PhD project, are special types of fly ash-based concrete with similar characteristics to those of the fly ash-based geopolymer concrete. Therefore, the advantages of the geopolymer concrete reported herein, are also applicable to Nu-Rock material.

Besides, Ferdous et al. (2013) carried out an experimental program in order to study the structural performance of the geopolymer concrete-filled composite beams in order to replace timber sleepers, as shown in Figure 2.13. They have proved the satisfactory performance of this composite sleeper, especially regarding its flexural strength. From Figure 2.13-a, it can be understood that the proposed sleeper has a brittle flexural failure as the experimental figures suddenly drop. From Figure 2.13-b, it can be found that this sleeper has a higher modulus of rupture than the hardwood timber sleeper and, therefore, can be a suitable choice for replacing timber sleepers (Ferdous et al., 2013). However, the brittle post-crack performance will be a challenge in the application of geopolymer concrete-filled composite sleepers.
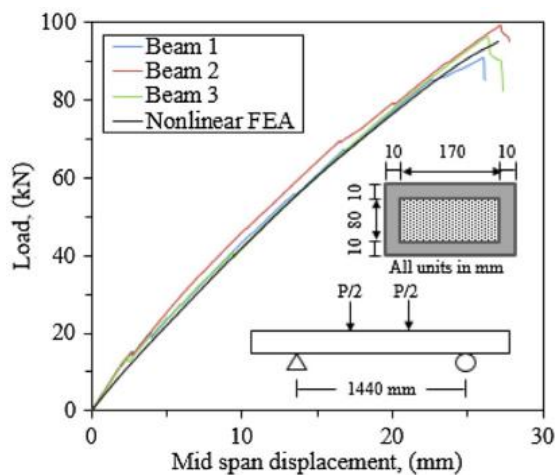
(a) load displacement behaviour   (b) comparison of the rupture modulus
                                                                    with other sleeper types
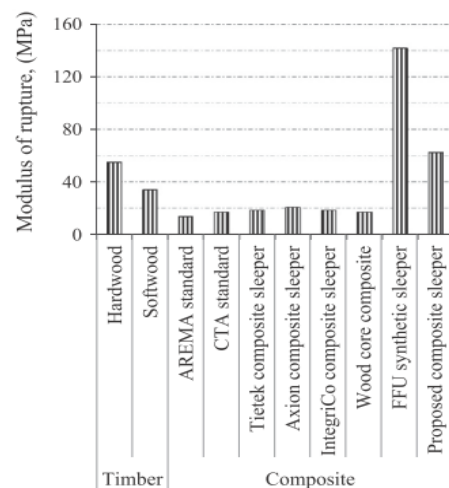
Figure 2.13 Flexural tests of the composite beam (Ferdous et al., 2015a)

2.7.2 Fibre-Reinforced Concrete:

By adding steel fibres into the plane concrete material, the compressive strength will change marginally, but the tensile strength of the concrete will increase roughly by 40 %, plus around 8% of rising in the elastic modulus (Thomas and Ramaswamy, 2007). Previous research works have shown the superior behaviour of concrete beams with steel fibres (Altun et al., 2007, Kovács and Balázs, 2003, Okay and Engin, 2012).

Furthermore, the addition of composite fibres to concrete can enhance the life cycle of railway sleepers by increasing their load-bearing and energy absorption capacity (Sadeghi et al., 2016), while their dynamic behaviour, including mode shapes and natural frequencies, as well as damping ratio, is not shifted from that of the conventional concrete sleepers. Also, it has been proved that the use of steel fibres in concrete, has a significant effect on the fatigue (cyclic) behaviour of prestressed reinforced concrete sleepers (Parvez, 2015). Indeed, the prestressed concrete (PSC) sleepers containing 5% fibres exhibited more static load-carrying capacity and better fatigue performance, as well as smaller deflections and lower crack widths, compared with the conventional PSC sleepers (without fibres) (Parvez and Foster, 2017). Therefore, it has been concluded that the minimum percentage of fibres (around 5%) is crucial in order to secure the superior performance of PSC sleepers.

2.7.3 Rubber Concrete:

The replacement of aggregates with rubber particles, either fine or coarse particles, and mostly in the forms of shredded or crumb pieces, has been practised since more than 40 years ago (Raj et al). It has been proved that the size of rubber particles affect strongly the behaviour of concrete both in fresh and hardened phases (Su et al., 2015). The concrete mixture containing coarse rubber particles has better workability but lower strength and water permeability in comparison to the one with finer rubber aggregates. In general, the best performance was obtained when using a variety of rubber particle dimensions, especially in terms of strength and water permeability, and they had more enhancing effects on the dynamic behaviour of the concrete rather than the single size rubber aggregates. Although it is undeniable that adding the rubble aggregates reduces the compressive strength and tensile resistance of the concrete, the

use of adhesive for the pre-treatment of the rubber aggregates increases the concrete-rubber bond and alleviates this negative effect. Furthermore, it has been found that the use of rubber aggregates made of waste tires improves the impact resistance of concrete (Shu and Huang, 2014). Hammed and Shashikala (2016) experimented on the application of rubber concrete in the production of railway sleepers and found that although adding fine crumb rubber aggregates results in a decrease in elastic modulus and compressive strength of the concrete, better fatigue behaviour and around 60% higher impact resistance is obtained compared with the conventional prestressed concrete sleepers (without rubber particles).

Kaewunruen et al. (2018a) studied the dynamic characteristics of high-strength rubberised concrete. Indeed, they investigated the effects of replacing fine aggregates with fine crumb rubber and performed several material tests to determine the compressive, tensile and flexural strengths of 20 different concrete mixes, as well as the conductivity and damping properties of these trial mixes. The authors have found that the mixes, including 10% of silica fume plus 5% of fine rubber particles, with the dimensions of either 75 microns or the mix of 180 and 400 (micron), attained compressive strengths higher than 55 (MPa) and therefore are acceptable for manufacturing PS concrete sleepers. They also found that the use of fine rubber particles in the concrete mix can enhance the damping ratio of the mix up to 100%. According to the results, the authors suggested the application of 10 % silica fume and 5% of fine crumb rubber (mix of 180 and 400 microns) in the concrete mix for manufacturing PS sleepers.

2.7.4 Ultra-high Performance Fibre Reinforced Concrete (UHP-FRC)

Ultra-high performance fibre reinforced concrete (UHP-FRC), also called reactive powder concrete, was first proposed by Richard and Cheyrezy (1995). It is a special type of fibre reinforced concrete (FRC) with excessively high compressive and tensile strengths. Two main differences distinguish UHP-FRC from other types of fibre-reinforced concrete (FRC). The first difference is in the contents of UHP-FRC. This material does not include coarse aggregates and normally contains silica fume and a high proportion of cement (800-1000 kg/m3). The second difference is the significantly high strength of the UHP-FRC material. Indeed, the compressive and

flexural strengths of this material under specific heat treatments can be up to 230 MPa and 60 MPa, respectively (Richard and Cheyrezy, 1995). Afterwards, in 1996, a foot-bridge was constructed in Sherbrooke, Canada, by using UHP-FRC material (Aitcin and Richard, 1996). Afterwards, this material has been widely used in construction over the world (Graybeal et al., 2020).

The typical components of UHP-FRC are cement, silica fume, sand, and fibres, as well as water and a high-range water reducer (also called superplasticiser) (Richard and Cheyrezy, 1995). In recent years several research studies have investigated the replacement of cement, and silica fume with waste industrial materials such as ground granulated blast furnace slag (GGBFS), fly ash (FA), and/or glass powder, and have proposed cheaper and more environmental-friendly UHP-FRC mixes, such as the research works performed by Yazici et al. (Yazıcı et al., 2009, Yazıcı et al., 2010, Yazıcı et al., 2008). Since there are no coarse aggregates included in the mix design of UHP-FRC material, this type of concrete material is well-known as reactive powder concrete (RPC).

The key characteristics of UHP-FRC or RPC are its extremely high compressive and flexural tensile strengths (Richard and Cheyrezy, 1995). In recent years, several researchers have examined the performance of this alternative concrete material under different loading conditions and have revealed further information about its mechanical performance. For example, Shaheen and Shrive (2007) investigated the fatigue performance of UHP-FRC samples of 40x40x160 (mm) under cyclic flexural loading. In their experiments, they used a commercial UHP-FRC mix, which included cement, silica fume, sand, micro-silica, high-range water reducer and Polyvinyl Alcohol (PVA) fibres. Four-point bending loads with a support span of 120 (mm) were applied to UHP-FRC samples. Interestingly, they found that the stress-strain curves under low cycle fatigue tests (with the applied strain range of 150-250 $\mu\varepsilon$) of the samples remained linear as shown in Figure 2.14, which proves the extremely high fatigue resistance of the UHP-FRC material. Even under greater fatigue loads (with more significant applied strains), no ultimate failure was observed in the UHP-FRC samples although the samples were cracked. This was due to the high fatigue strength of the fibres and the strong bond between the UHP-FRC matrix and fibres.

Regarding the performance of the UHP-FRC material under impact load, it should be noted that the UHP-FRC material without fibre is so brittle. However, the application of fibres can increase its fracture energy under impact loading up to around four times (Banthia et al., 1998). Research studies investigated the performance of UHP-FRC at the material level by using the split Hopkinson press bar (SHPB) testing technique. For example, Ju et al. (2010) found that samples of UHP-FRC including steel microfibers grasp significantly higher deformability under impact loading and can sustain higher applied strain rates (impacts). According to the test results, the maximum compressive strength was achieved with the fibre volume fraction of 1.75%. However, the maximum total dissipated energy of the UHP-FRC samples under impact loading as well as the highest dissipated energy until the peak impact load was obtained with the fibre volume fraction of 2%. Indeed, they have found that the fibre volume fraction of the UHP-FRC mix controls its stress-strain response under dynamic loading (using the SFPB technique).
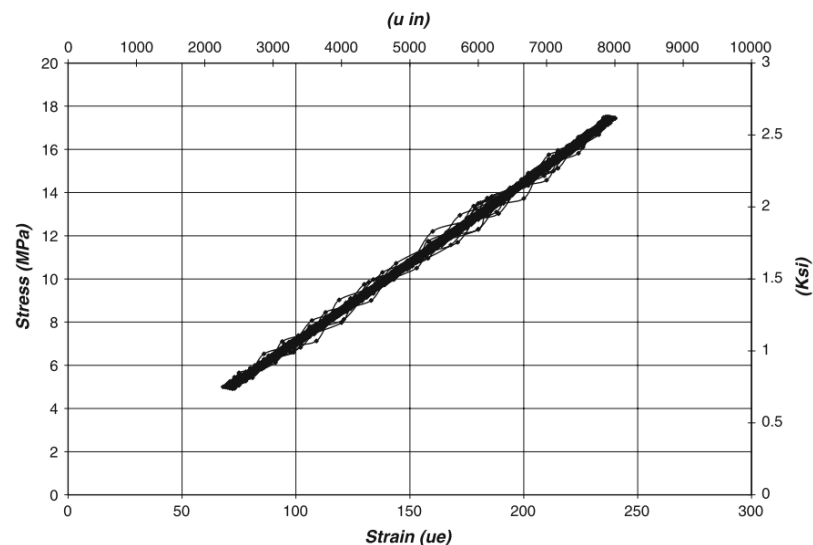
Figure 2.14 Flexural stress vs. strain curve under low cycle fatigue loading (150-250 με) (Shaheen and Shrive, 2007)

Jiao and Sun (2015), using the SHPB testing technique, confirmed that the UHP-FRC mixes with steel fibres have significantly higher dynamic strength and toughness compared with the plain UHP-FRC mix. They have also noticed that the UHP-FRC samples with high volume fractions of fibres (up to 4%) faced x-shaped cracks under impact loading while the plain UHP-FRC samples broke into small pieces. Based on

51

the results, they concluded the steel fibre reinforced UHP-FRC is an ideal alternative concrete material for structures under high impact loads. An example of such concrete elements is railway sleepers that are prone to intensive impact rail loads (Remennikov and Kaewunruen, 2008b).

An experimental and analytical investigation of the performance of UHP-FRC concrete beams under impact loads was performed by Fujikake et al. (2006b). They used a drop hammer test rig to apply the impact loading. They found that the UHP-FRC beams with only longitudinal bars (no shear reinforcement) had very ductile performance under impact loading with several minor flexural cracks rather than shear cracks. The same cracking pattern was observed by Yoo et al. (2015) under the first impact load (the first drop). They also proved that as the longitudinal reinforcement ratio increases, the impact load resistance of the UHP-FRC beam enhances. Indeed, the increase in the reinforcement ratio not only decreased the initial deformation of the UHP-FRC beams under the first impact load but also improved the deformation recovery of the samples.

Previous studies have proved that UHP-FRC has high durability. For instance, it has been found that the water permeability of UHP-FRC is significantly low compared with ordinary concrete. The reason for the marginal permeability of UHP-FRC is its low porosity due to the great compaction and homogeneity of this material (Tam et al., 2012). In this regard, it has been also found that the proper dosage of superplasticiser (water reducer) highly reduces the porosity of the UHP-FRC mix by facilitating the workability and compatibility of the mix and thereby leads to lower permeability (Anwar et al., 1993). Also, research studies have shown that the chloride diffusion of UHP-FRC is considerably low compared with the high-performance concrete (HPC) which is currently used for manufacturing PSC sleepers (Jooss and Reinhardt, 2002). Also, it has been found that optimal use of minerals, such as fly ash, in UHP-FRC can greatly increase the resistance of this material against chloride diffusion.

As it was explained earlier, ice forming is one of the failure types of the conventional PS concrete sleepers similar to other concrete structures subjected to cold weather. Studies have proved the high freezing-thawing resistance of UHP-FRC (Wang et al., 2015). Indeed, a study by Anwar et al. (1993) showed that after 600 cycles of freezing and thawing, the mass loss of the UHP-FRC samples were nearly zero. Another study

showed that after 1000 cycles of freezing and thawing, the reductions in the compressive strength of normal concrete, high strength mortar, and UHP-FRC, were 57%, 16%, and 6%, respectively (Lee et al., 2007). This study proved the great freezing and thawing resistance of UHP-FRC compared with normal concrete and high-strength mortar.

2.8 Conclusions

In this chapter, a general review of various components of ballasted rail track systems was provided, including a brief review of different types of concrete sleepers. It was shown that the conventional prestressed concrete (PSC) sleepers are amongst the most desirable types of sleepers due to their superior performance compared with other materials. However, there are yet some concerns about the manufacturing and performance of PSC sleepers. As explained in this chapter, the manufacturing process of PSC sleepers is relatively slow, energy-consuming and cost-inefficient. Another issue about PSC sleepers is the loss of prestressing, which exacerbates gradually over time and results in a significant loss of the load-bearing capacity of the old railway sleepers. Additionally, it has been stated in this chapter that the PSC sleepers may incure various failure modes due to the chemical reactions or mechanical actions. Thus, to avoid these potential failure modes, the application of alternative concrete materials for manufacturing alternative concrete sleepers has been reviewed. It has been found that ultra-high performance fibre reinforced concrete (UHP-FRC), that is also called Reactive Powder Concrete (RPC), is a promising material for manufacturing alternative non-prestressed concrete sleepers.

Furthermore, a review of various rail loads, including static, fatigue (cyclic), and dynamic loads, has been reported in this chapter. According to the literature, dynamic (impact) loads which are normally generated due to the irregularities of wheels and/or rails, can go up to 5 times the static train loads. Also, fatigue phenomenon can occur during the service life of sleepers. Hence, to confirm the adequate performance of a railway sleeper during its service life, any proposed alternative concrete sleeper is needed to be comprehensively tested, under static, cyclic (fatigue) and impact loads.

In light of the concerns about the chemical and mechanical failures of the conventional PSC sleeper, the application of the UHP-FRC material for manufacturing alternative non-prestressed concrete sleepers is investigated. For this purpose, several material tests and structural tests under static, cyclic (fatigue), and impact loads, are performed. In addition to the experiments, analytical and numerical (finite element) studies are also included in this thesis.

CHAPTER 3

DEVELOPMENT OF UHP-FRC MIX WITH OPTIMISED CHARACTERISTICS

3.1 Introduction

Ultra-high performance fibre-reinforced concrete (UHP-FRC) is well-known for its very high compressive and tensile strength. UHP-FRC is widely called reactive powder concrete (RPC) due to the fact that there are no coarse aggregates in the mix design of this material. In order to use UHP-FRC for producing modular non-prestressed concrete sleepers, it is needed to optimise the concrete mix design at the first step. In this chapter, a UHP-FRC material with optimum mechanical characteristics for concrete sleepers is developed. For this purpose, the plain UHP-FRC mix is optimised through a number of trial mixes and by applying the Taguchi method (Taguchi et al., 2005). Subsequently, the optimal content of steel fibres is determined using additional trial mixes.

3.2 History of UHP-FRC

Ultra-high performance fibre-reinforced concrete (UHP-FRC), commonly called reactive powder concrete (RPC), was first proposed by Richard and Cheyrezy (1995). In their paper, Richard and Cheyrezy showed that this material could reach the extremely high compressive and flexural strengths of 170 to 230 (MPa) and 30 to 60 (MPa), respectively, when the heat curing is applied. Within a short time, a footbridge was constructed in Sherbrooke, Canada, using UHP-FRC material (Aitcin and Richard, 1996). Afterwards, this material was utilised in the construction of numerous structures worldwide (Graybeal et al., 2020).

UHP-FRC is mainly made of cement, silica fume, sand, water reducer, water and fibres, without coarse aggregates (Richard and Cheyrezy, 1995). Indeed, UHP-FRC is cement-based concrete with a cement content of around 800-1000 (kg/m^3). The quantities (weights) of other components are normally described as fractions or percentages of the cement weight. However, the quantity of water is sometimes

described as a fraction weight of the binder components (which includes cement and silica fume). In recent years, several researchers have worked on partial replacement of cement and/or silica fume with other environment-friendly minerals such as fly ash (FA), ground granulated blast furnace slag (GGBFS), and glass powder, in which cases, the weights of these components will be also considered when calculating the binder weight (Yazıcı et al., 2009, Yazıcı et al., 2010, Yazıcı et al., 2008).

In recent years, several research studies have investigated the performance of UHP-FRC and have proposed different mix proportions for the optimal behaviour of this material. Table 3.1 summarises a number of UHP-FRC mix proportions suggested by different researchers. It is worthy to note that for the sake of brevity, only the mixes, including the original components, i.e., cement (C), silica fume (SF), sand, water (W), and superplasticiser (SP), are shown in Table 3.1 and the mix designs containing other minerals such as FA and GGBFS are not considered in this research. From Table 3.1 it is deduced that the typical UHP-FRC mix proportions can be drastically different. For instance, the ratio of sand to cement (Sand/C) by weight varies from 1.0 to 1.8. Such a significant divergence can be due to the variance in the chemical composition of each component, such as cement and silica fume. The optimisation target or the application of the UHP-FRC mix may also affect the quantities of the mix design components. For example, an UHP-FRC mix may be optimised according to the mechanical test results to achieve the highest compressive strengths in some cases, while in other cases, the highest resistance against chemical attacks may be the main target for optimisation (Ozbay et al., 2009).

From Table 3.1 and the above statements, it can be deduced that there is no certain mix design with optimum characteristics for various structural applications, and the optimisation process must be performed for any specific purpose. In this research, an UHP-FRC mix is of interest for manufacturing non-prestressed concrete sleepers. Hence, it is needed to perform an optimisation process to determine an optimal UHP-FRC mix design that satisfies the demanded flexural/tensile strength of non-prestressed sleepers. Herein, the primary step for developing such an optimal UHP-FRC mix design is to quantify the target flexural/tensile strength of non-prestressed concrete sleepers. In the following section, an estimation of the target flexural strength of non-prestressed concrete sleepers for the optimisation process is demonstrated.

Table 3.1 Typical proportion of reactive powder concrete

Authors	C	SF/C	Sand/C	W/Binder	SP/C	Fibre (by volume)
Richard and Cheyrezy (1995)	1	0.25	1.1	0.17	0.016	1%
Gao et al. (2006)	1	0.25	1.8	0.15	0.09	2%
Cwirzen et al. (2008)	1	0.25	0.8	0.18	0.05	3%
Yazıcı et al. (2008) Yazıcı et al. (2009) Yazıcı et al. (2010)	1	0.35	1.2	0.13	0.07	3%
Kim et al. (2011)	1	0.25	1.1	0.20	0.05	2%
Ipek et al. (2011)	1	0.30	1.0	0.19	0.03	4%
Tam et al. (2012)	1	0.325	1.7	0.20	0.025	No fibres
Wang et al. (2017)	1	0.23	1.8	0.14	0.105	2%
Al-Tikrite and Hadi (2017)	1	0.23	1.0	0.13	0.06	2-4%
Abdulraheem and Kadhum (2018)	1	0.22	1.11	0.15	0.03	2%
Visintin et al (2018)	1	0.27	0.99	0.14	0.04	3%
Tuama et al.(2020)	1	0.25	1.1	0.13	0.035	2%
Kim et al.(2021)	1	0.25	1.4	0.2	0.05	No fibres
Xu et al.(2021)	1	0.25	1.1	0.16	0.05	2%

3.3 Target Flexural Strength of Concrete Sleepers

First, it is important to determine what concrete strength characteristics (tensile, compressive, or shear strength) are required for the satisfactory performance of the non-prestressed concrete sleeper made with the UHP-FRC mix. According to the Australian Standard (AS1085.14, 2019), pre-stressed concrete (PSC) sleepers must be designed to resist the positive and negative design moments developed at their rail-seat and centre sections due to the vertical design rail-seat loads, i.e., the sleepers are designed for flexure. In the absence of a guideline for the analysis and design of non-prestressed concrete sleepers, the provisions of the Australian Standard (AS1085.14, 2019) are adopted as the basis in this research.

In general, under flexure (bending moment), both flexural compressive and tensile stresses are normally generate within the element. However, in the special case of non-prestressed concrete sleepers, the compressive strength of UHP-FRC is high and will usually exceed the concrete strength required for the concrete sleeper design. Therefore, the flexural tensile strength of the optimal UHP-FRC mix is selected as the target parameter for the optimisation process.

To predict the flexural tensile stresses formed inside the non-prestressed concrete sleepers due to the wheel/rail loads, the target axle loads, train speed, the dimensions and spacing of the sleepers are required. In the following, the assumptions for the analysis of the concrete sleepers are presented.

In this investigation, two different tonne axle loads (TALs) are considered, 25 TAL and 40 TAL, reflecting the normal and heavy-haul rail track conditions, respectively. The typical dimensions of the sleepers under the two TALs have been assumed in this study, as shown in Figure 3.1. The standard gauge distance (G = 1435 mm) has been assumed in this study for the proposed sleepers. Indeed, except for the cross-sections, other dimensions are assumed identical in both of the proposed non-prestressed sleepers.

The Australian Standard for prestressed concrete sleepers (AS1085.14, 2019) is based on the allowable stress design (ASD) method and assumes a constant uniformly distributed pressure under the rail-seat area of the sleeper, which represents the ballast pressure, as shown in Figure 3.2. As can be seen in Figure 3.2, the concentration of

ballast pressure around the rail-seat areas under the sleepers (refer to Sections 2.3.3 and 2.3.4 for further information about the contact pressure distribution between the sleeper and the ballast).
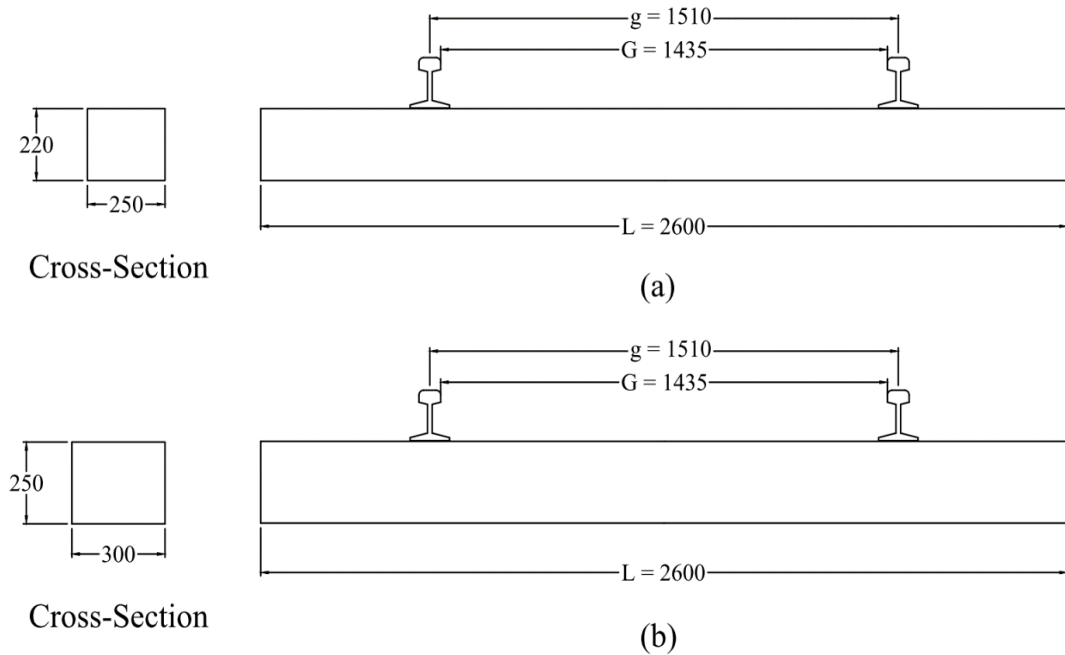
Figure 3.1 Dimensions for the non-prestressed UHP-FRC sleepers used in concrete mix optimisation study: (a) 25 TAL; (b) 40 TAL
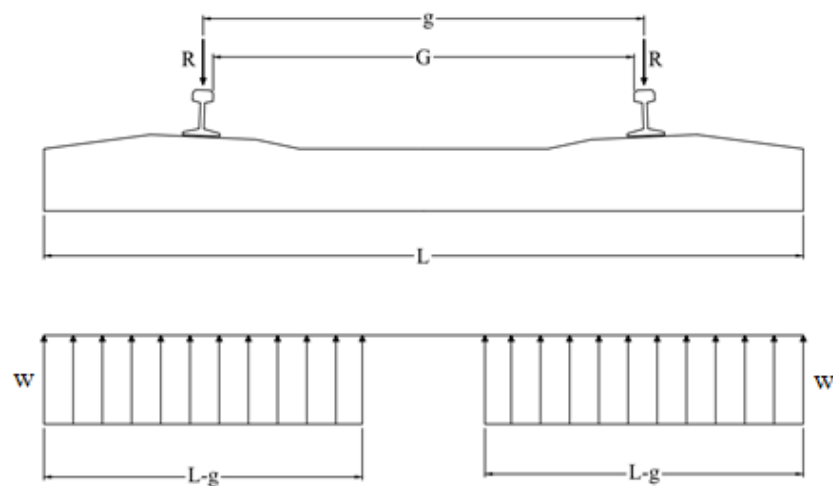
Figure 3.2 Simplified model for ballast pressure underneath the sleeper (AS1085.14, 2019)

The design rail-seat loads (R) and design moments as the rail seat and mid-span sections of the proposed sleepers, according to the Australian Standard (AS1085.14, 2019) are reported in Table 2.1. In Table 2.1, the dynamic impact factor (DIF) is a coefficient that takes into account the effects of the dynamic wheel loads. According to the Australian Standard (AS1085.14, 2019), the DIF is taken as 2.5 to consider the dynamic effects of various train speeds, up to 200 km/h. A comparison between various equations for obtaining the DIF magnitude has been presented in Table 2.1. The distribution factor (DF) is a coefficient that takes into account the effects of sleeper spacing on the distribution of the wheel loads over the adjacent sleepers, as explained in the previous chapter (refer to Figure 2.4 for determining the magnitude of DF according to the centre-to-centre sleeper spacing magnitude). According to the Australian Standard (AS1085.14, 2019), the vertical design rail-seat load is calculated as the vertical design wheel load (half of the TAL) multiplied by the DIF and the DF factors. Subsequently, the design moments can be calculated based on the design rail-seat load, as demonstrated in Table 3.2. The maximum design flexural stresses generated within the proposed non-prestressed UHP-FRC sleepers can be calculated using the design moments and the cross-section width (b) and height (h) as shown in Table 3.2.

Table 3.2 Calculation of the design loads, design moments and the required flexural strength of the proposed non-prestressed UHP-FRC sleepers

The ASD Approach	AS 1085.14-2019 Provisions	25 TAL	40 TAL
Dynamic impact factor (DIF)	2.5 (for high-speed railways up to 200 km/h)	2.5	2.5
Axle load distribution factor (DF)	0.45 ~ 0.6 (refer to Figure 2.4)	0.54	0.54
Design rail-seat load (R)	$DIF\left(\times \dfrac{TAL}{2} \times 9.81\right) \times DF$	165 (kN)	265 (kN)
Stress distribution (w) (see Figure 3.2)	$\dfrac{R}{(L-g)}$	152 (kN/m)	243 (kN/m)

Design ballast pressure (P_{ab})	$\dfrac{R}{b(L-g)}$	608 (kPa)	810 (kPa)
Rail-seat positive (M_{RS+})	$\dfrac{R(L-g)}{8}$	22.6 (kN.m)	36.1 (kN.m)
Rail-seat negative (M_{RS-})	$0.67 M_{R+}$	15.1 (kN.m)	24.2 (kN.m)
Centre negative (M_{C-})	$\dfrac{R(2g-L)}{4}$	17.4 (kN.m)	27.8 (kN.m)
Centre positive (M_{C+})	$0.05\,R\,(L-g)$	9.02 (kN.m)	14.4 (kN.m)
Width	b	250 (mm)	300 (mm)
Height	h	220 (mm)	250 (mm)
Maximum design flexural stress	$\dfrac{Max(M_{RS\pm}\,\&\,M_{C-})}{\dfrac{bh^2}{6}}$	11.2 (MPa)	11.6 (MPa)

As can be seen in Table 3.2, the design flexural stresses are 11.2 MPa for the 25 TAL and 11.6 MPa for the 40 TAL non-prestressed UHP-FRC sleepers with typical dimensions. Hence, the maximum magnitude of flexural stress, i.e., 11.6 (MPa), is deemed as the target flexural strength for the optimisation process. In other words, the optimal UHP-FRC mix must attain a flexural tensile strength equal to or higher than 11.6 MPa to satisfy the requirements for manufacturing non-prestressed UHP-FRC sleepers with the typical dimensions depicted in Figure 3.1. It should be noted that UHP-FRC mixes are generally expected to satisfy the criteria listed below (ASTM C1856/C1856M, 2017):

- A 28-day compressive strength of 120 MPa or higher;
- The aggregate dimensions equal or below 5 mm;
- The flow table results within the range of 200-250 mm.

3.4 Optimisation of the Plain UHP-FRC Mix Design

3.4.1 Materials

In this study, the ingredients of the UHP-FRC are the conventional components presented in Table 3.1. No additional minerals such as ground granulate blast furnace slag (GGBFS) or fly ash (FA) are used in this research. The cement (C) type is the general-purpose cement produced by Bastion Building Materials, Australia (Bastion, accessed on 04/04/2021). The silica fume (SF) with the commercial name of Sika Fume, produced by Sika Australia Pty Ltd (SikaFume, accessed on 04/04/2021) is utilized. The sand used in this study is a type of river silica sand with a maximum grain size of 3 mm. Clean water with ambient temperature is used for all the mixes. Also, a high-range water reducer (also called superplasticiser) with the commercial name of Sika Viscocrete PC HRF-1 produced by Sika Australia Pty Ltd (Sika-ViscoCrete-HRF-1, accessed on 04/04/2021) is utilised herein. The steel fibres with the commercial name of Dramix4D-65/35BG are provided by BOSFA, Australia (Dramix4D-65/35, accessed on 04/04/2021). Dramix4D-65/35BG is a type of macro steel fibres with hooked ends. The characteristics of the fibre are reported in Table 3.3.

Table 3.3 Characteristics of the macro steel fibre selected in this research

Commercial name	Shape	Length (mm)	Diameter (mm)	Tensile strength (MPa)
Dramix® 4D-65/35		35	0.55	1600

3.4.2 The Optimisation Plan Based on the Taguchi Method

In general, the optimisation of UHP-FRC needs several trial mixes and numerous samples (Gao et al., 2006). For instance, in the case that four UHP-FRC mix design parameters and three different amounts for each of the parameters are selected for the optimisation procedure, 81 trial tests (mixes) will be needed in total to perform the optimisation process ($3^4 = 81$). Thus, an effective optimisation method will be required

in order to decrease the number of trial mixes while retaining the significance of the optimisation process. To fulfil this goal, an efficient method was put forth in the 1950s, which is known as the Taguchi method after the name of its inventor, Genichi Taguchi (Taguchi et al., 2005).

The Taguchi method applies orthogonal arrays (OAs) in the optimisation procedure, which enables this method to investigate a large number of variables in the process with a few trials (tests). As an instance, in the example of four control parameters and three different values for each of the parameters, using the OAs, the number of examines (trials) will be 9 instead of 81. Despite the significantly fewer number of trials (9<<81), the optimisation outcome based on those few trials is valid over the whole space of trials generated by the control factors and their proportions (81 trials) (Phadke, 1989).

The Taguchi method is based on a model which is called a noise factor and applies a signal-to-noise (S/N) ratio to perform the optimisation. Noise factors are deemed responsible for the inconsistent behaviour of the products. Indeed, the noise factor is defined as something that makes a quantifiable process diverge from its aimed magnitude (Fowlkes and Creveling, 1995). This target magnitude can be defined as either of the following options:

- Bigger is better, i.e. the target is to attain the maximum response. In this case, the S/N ratio is obtained using Equation (3.1):

$$S/N = -10 \log_{10} \left(\frac{1}{n} \sum_{i=1}^{n} \frac{1}{Y_i^2} \right) \tag{3.1}$$

Where Y_i is the quantified magnitude of each response.

- Smaller is better, i.e., the target is to reach the minimum response. In this case, Equation (3.2) is used to calculate the S/N ratio:

$$S/N = -10\log_{10}\left(\frac{1}{n}\sum_{i=1}^{n}Y_i^2\right) \tag{3.2}$$

- Nominal magnitude is better, i.e., the aim is to achieve the closest response to a target magnitude (denoted by Y_0). In such a case, the minimum standard deviation is the goal which can be obtained from Equation (3.3):

$$S/N = -10\log_{10}\left(\frac{1}{n}\sum_{i=1}^{n}(Y_i^2 - Y_0^2)\right) \tag{3.3}$$

The inconsistency of the responses is attributed to the changes in the environment or any divergence from the original design (Taguchi, 1987). The noise factor can be categorised in one of the three classes:

- External noises, which are variabilities due to external causes;
- Unit-to-unit noise, which is based on the fact that no successive products are identical;
- Internal noises, which include ageing and deterioration during the storage and operation.

In the optimisation process, it is important to take the proper arrangement of the optimisation parameters in order to minimise the influence of the noise factors (Unal and Dean, 1990). In this study, the Taguchi method is applied to optimise the mix design of UHP-FRC with a few trial mixes for attaining the highest flexural strength. For this purpose, the well-known software, called Qualitek-4 (Roy, 1996), is utilised as it has been recommended by other researchers (Hadi et al., 2017).

Four important parameters are considered for the optimisation process in this research. These parameters are the ratio of silica fume to cement (SF/C), the ratio of sand to cement (Sand/C), the ratio of superplasticiser to cement (SP/C), and the ratio of water to the binder (W/Binder). It is important to note that all four ratios are measured by the weights of the components. Three proportions are selected for each of these parameters

(ratios), as presented in Table 3.4. According to the Taguchi method and considering the L9 orthogonal array (OA), nine trial UHP-FRC mixes are required to be tested for the optimisation process. The details of these nine trial mixes are summarised in Table 3.5.

Table 3.4 The important parameters in the UHP-FRC mix design and their various proportions

Parameters	Proportion 1	Proportion 2	Proportion 3
SF/C	0.25	0.30	0.35
Sand/C	1.00	1.10	1.20
SP/C	0.03	0.04	0.05
W/Binder	0.18	0.20	0.22

3.4.3 Preparation of the UHP-FRC mixes and the testing procedures

A Hobart mixer with a maximum capacity of 20 litres is used for preparing the UHP-FRC mixes, as shown in Figure 3.3. The mixer has three mixing speeds of 197, 317, and 462 rpm. The mixing procedure can be divided into three steps. The first step is the dry mixing part, through which the dry ingredients, cement, silica fume, and sand are mixed for about 2 minutes. Subsequently, two-thirds of the water and superplasticiser (mixed) are added to the dry materials gradually. This step takes around 3 minutes. Afterwards, the remaining amounts of water and superplasticiser are added to the mix. The mixing process will continue until the whole mixture turns into a homogenous mix by visual inspection.

Table 3.5 Mix design of the trial mixes using the L9 orthogonal array

Name	C	SF	Sand	SP	W	W/Binder
T1	1	0.25	1.0	0.03	0.225	0.18
T2	1	0.25	1.1	0.04	0.25	0.20
T3	1	0.25	1.2	0.05	0.275	0.22
T4	1	0.30	1.0	0.04	0.286	0.22
T5	1	0.30	1.1	0.05	0.234	0.18
T6	1	0.30	1.2	0.03	0.26	0.20
T7	1	0.35	1.0	0.05	0.27	0.20
T8	1	0.35	1.1	0.03	0.297	0.22
T9	1	0.35	1.2	0.04	0.243	0.18

Figure 3.3 The Hobart mixer used for mixing the trial UHP-FRC mixes

Table 3.6 presents the total mixing time for each of the nine trial mixes. From Table 3.6, it can be deduced that the mixing time is 12-13 minutes for the trial mixes except for three mixes, T1, T5 and T9. These mixes have the lowest water to binder ratio (W/Binder) of 0.18 amongst the nine trial mixes. Amongst these three mixes, T5 with the maximum superplasticiser to cement (SP/C) ratio of 0.05 has the lowest mixing time (14 minutes), while T1 with the lowest SP/C ratio of 0.03 requires the longest

mixing time of 18 minutes to turn into a homogeneous UHP-FRC mixture by visual inspection.

To evaluate the workability of the UHP-FRC mixes, flow table tests are conducted for each trial mix congruent with ASTM C230/C230M (C230/C230M, 1998), as shown in Figure 3.4. Table 3.6 presents the results of the table tests for each of the trial UHP-FRC mixes. It is observed that the trial mix T1 has the lowest percentage of flow, which is 178%. The relatively low percentage of flow can be attributed to the fact that the T1 mix has the lowest W/Binder and SP/C ratios amongst the trial mixes, i.e., 0.18 and 0.03, respectively. According to ASTM C230/C230M (C230/C230M, 1998), the flow table test result must be equal to or more than 125% to deem the mortar mix appropriate. Hence, all the trial mixes (including T1) satisfy the workability criterion. The trial mixes with the highest W/Binder ratio are highly workable and overpass the flow table testing equipment, and therefore, their table test results are recorded as +250% in Table 3.6.

Table 3.6 Characteristics of the trial UHP-FRC mixes

UHP-FRC Mixes	Mixing Time (min)	Flow Table (%)	Compressive strength (MPa)		28-day Flexural Strength (MPa)
			7-day	28-day	
T1	18	178	102.8	121	10.5
T2	12	192	102.4	112	11.2
T3	13	+250	86.9	101	10.2
T4	13	+250	100.4	124	10.3
T5	14	194	106.3	117	11.0
T6	13	181	109.4	132	11.5
T7	12	218	106.8	113	8.75
T8	13	+250	112.7	136	9.07
T9	17	182	103.8	115	9.69

Figure 3.4 Flow table testing of the UHP-FRC mixes in congruence with ASTM C230/C230M (C230/C230M, 1998)

In order to evaluate the compressive strengths of the trial UHP-FRC mixes, compression tests are performed for cubic samples with the dimensions of 50x50x50 (mm) in congruence with ASTM-C109M (Committee, 2002), as shown in Figure 3.5. The compression tests are performed on the 7th and the 28th days after casting for each of the trial mixes. In order to determine each of the 7-day and 28-day compressive strengths for each UHP-FRC mix, three samples are needed. Then, the mean compressive strength of the three test results is recorded as the compressive strength of the material by the specific day (either 7th or 28th day), as presented in Table 3.6. It should be noted that the differences between the three test results are within 10% of the mean values.

In order to determine the flexural strengths of the trial UHP-FRC mixes, the 28-day 3-point bending test in accordance with the British Standard (EN, 2005) is conducted for each of the mixes. For each mix, the three-point bending (flexural) tests are carried out for three samples with the dimensions of 40x40x160 (mm), as shown in Figure 3.6, and the average magnitude is considered as the flexural strength of that specific mix. The average flexural strengths of the trial mixes are listed in Table 3.6. Similar to the compressive test results for each trial mix, the flexural test results obtained from the three tests are within 10% of the average magnitude.

(a) cube samples of 50x50x50 (mm)

(b) 3000 kN MATEST test rig for compression testing of the UHP-FRC samples

Figure 3.5 Determination of the compressive strength of the trial UHP-FRC mixes according to ASTM-C109M (Committee, 2002)

(a) prismatic UHP-FRC sample of 40x40x160 (mm) for flexural testing

Figure 3.6 Determination of the flexural strength of UHP-FRC trial mixes according to the British Standard (EN, 2005)

(b) the 30 kN Instron test rig for flexural testing of the UHP-FRC samples

Figure 3.6 Determination of the flexural strength of UHP-FRC trial mixes according to the British Standard (EN, 2005)

According to the literature, the optimisation target for concrete mix designs is normally selected as the greatest compressive strength (Hadi et al., 2017, Gao et al., 2006). In other words, the optimisation process is performed based on the compression test results of the trial mixes. However, in this research, the optimisation target is to reach an UHP-FRC mix design with the flexural strength equal to or higher than the minimum required strength which is 11.6 MPa. In order to retain this research comparable with other optimisation results reported by various researchers, the optimisation is performed two times, once based on the compressive strengths of the trial UHP-FRC mixes and once based on the flexural strengths of the mixes. Eventually, the optimal UHP-FRC mix design based on the flexural strength is used for further studies in this research.

3.4.4 Determination of the Optimal UHP-FRC Mix Design

In this research, the optimisation process is carried out two times: once based on the 7-day compressive strengths of the trial mixes, and once based on their flexural (bending) test results, separately. Indeed, once the optimisation process is conducted

to reach the highest compressive strength and once to attain the highest flexural strengths.

The compression and flexural (bending) test results of the trial mixes are compared in Figure 3.7. It can be seen that samples of the T8 trial mix attained the highest 7-day and 28-day compressive strengths. The proportions of SF/C, Sand/C, SP/C and W/Binder, in T8, are 0.35, 1.1, 0.03, and 0.22, respectively. The lowest 7-day and 28-day compressive strength belong to the T3 trial mix with the ratios of SF/C, Sand/C, SP/C and W/Binder, equal to 0.25, 1.2, 0.05, and 0.22, respectively. It is observed that the mixes with the maximum (T8) and minimum (T3) compressive strengths are different in the proportions of SF/C and Sand/C, as well as SP/C, while they have the same W/Binder ratio.

It is worthy to note that the trial UHP-FRC mix, T8, shows a relatively small flexural strength, although it has the highest compressive strength (see Figure 3.7). It demonstrates that there may not be a direct relationship between the compressive and flexural (bending) strengths of UHP-FRC.

Figure 3.7 shows that the samples of the T6 trial mix have the highest flexural (bending) strength amongst the trial UHP-FRC mixes, with the proportions of SF/C, Sand/C, SP/C and W/Binder equal to 0.3, 1.2, 0.03, and 0.2, respectively. It is also found that T7 with SF/C of 0.35, Sand/C of 1.0, SP/C of 0.05, and W/Binder of 0.2, has the lowest compressive strengths. Analogous to the trial mixes with the maximum and minimum compressive strengths, the two mixes with the extremum flexural strengths. i.e. T6 and T7, are different in the ratios of SF/C, Sand/C, and SP/C, with similar W/Binder proportions.
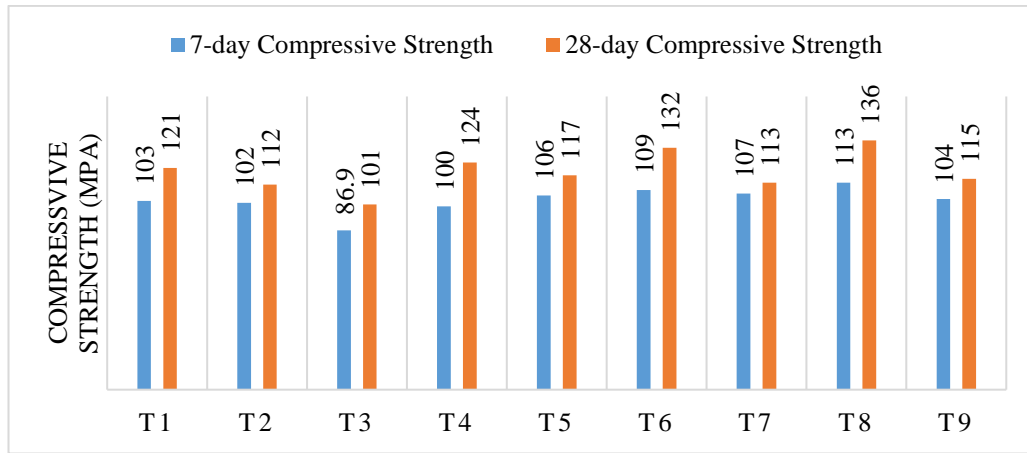
a) compressive strength of the trial mixes
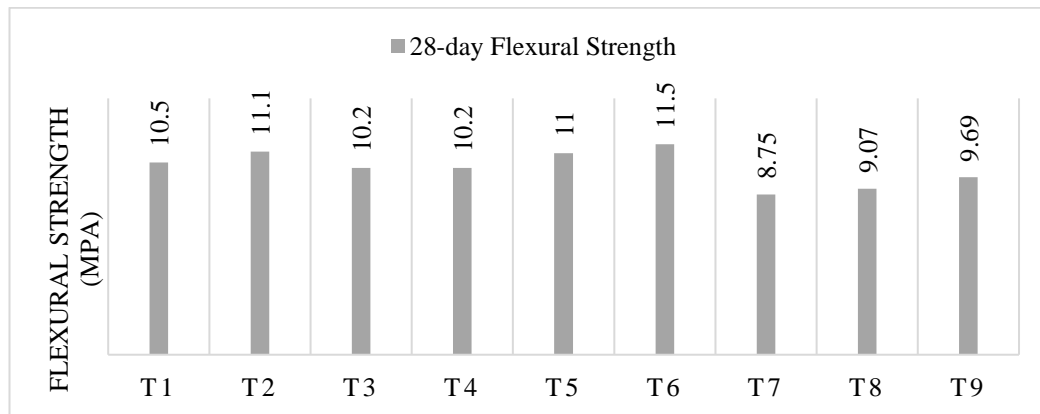
b) flexural strength of the trial mixes

Figure 3.7 Comparison of the compressive and flexural (bending) strengths of the trial mixes

The influence of different proportions of the important parameters on the compressive strength of UHP-FRC is illustrated in Figure 3.8. Indeed, Figure 3.8 illustrates the response indexes (RIs) which are calculated for each proportion (ratio) of each parameter separately, based on the 7-day compressive strengths of the trial mixes. The RIs are calculated according to S/N ratios and by applying the averaging method (Ross, 1996). In view of that, for each of the four parameters, three RIs are determined where each of the three RIs is the average of the 7-day compressive strengths of all the trial mixes that contain a specific proportion of that parameter. For example, the RI is calculated manually for the second proportion of the parameter SF/C, i.e. the SF/C ratio of 0.3. Three trial mixes, T4, T5, and T6, contain an SF/C ratio of 0.3, with the 7-day compressive strength of 100.4, 106.3, and 109.4 (MPa), respectively. Thus, the

RI for the SF/C ratio of 0.3 is determined as the average of the three compressive strengths which is 105.5 MPa. Accordingly, the RI values for the SF/C ratios of 0.25 and 0.35 are obtained as 97.4 MPa and 107.8 MPa (see Figure 3.8-a).

As can be seen in Figure 3.8, as the SF/C increases from 0.25 to 0.35, the 7-day compressive strength of UHP-FRC increases. The rate of increase (the angle of the curve) decreases from SF/C of 0.3 to 0.35. Similar relationships between Sand to cement (Sand/C) and Water to Binder (W/Binder) ratios with the 7-day compressive strength of UHP-FRC can be observed in Figure 3.8. As the Sand/C ratio increases from 1.0 to 1.1, the compressive strength goes up and then from the Sand/C ratio of 1.1 to 1.2, a downward trend in the compressive strength is observed. Similarly, the compressive strength reaches its peak compressive strength at the W/Binder ratio of 0.2, and then, from the Water/Binder ratio of 0.2 to 0.22, the compressive strength goes down. It can also be seen that when the superplasticiser to cement (SP/C) ratio rises from 0.03 to 0.05, the compressive strength drops. The optimal proportion of each parameter is listed in Figure 3.8.
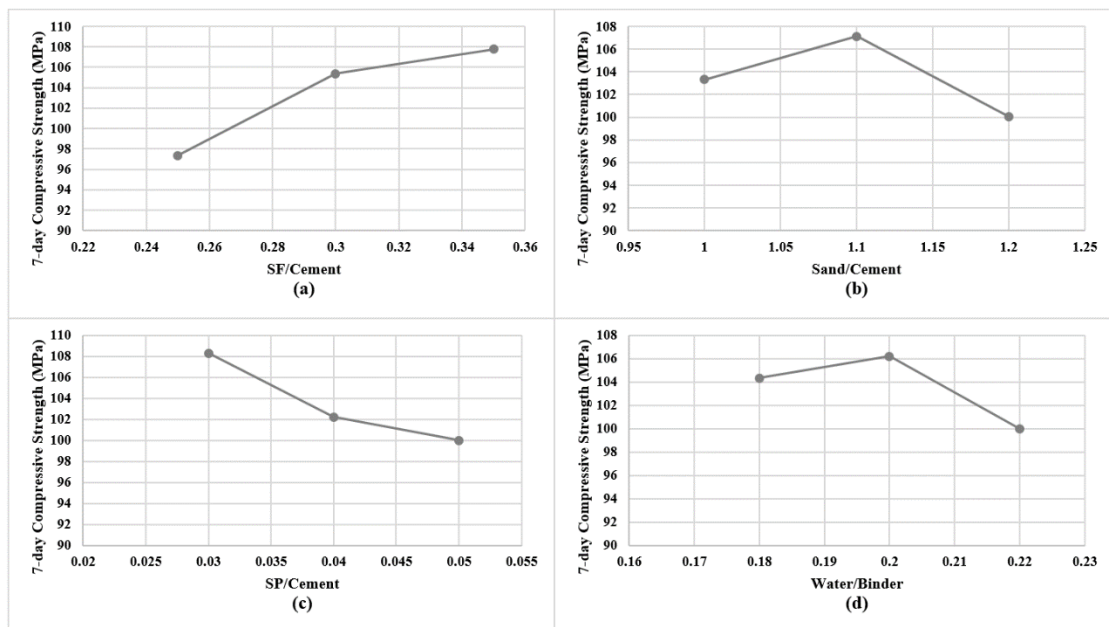
Figure 3.8 The influence of various proportions of the important mix design parameters on the 7-day compressive strength of UHP-FRC: (a) SF/Cement parameter; (b) Sand/Cement parameter; (c) SP/Cement parameter; (d) Water/Cement parameter

Figure 3.9, shows the influences of different proportions of the important design parameters on the 28-day flexural (bending) strength of UHP-FRC. It is observed that the increase of the silica fume to cement (SF/C) ratio from 0.25 to 0.3 increases the flexural strength of UHP-FRC. However, from the SF/C ratio of 0.3 to 0.35, a significant drop is observed in the Flexural strength. When the ratio of sand to cement (Sand/C) increases from 1.0 to 1.2, the flexural strength rises, but the rate of increase is less considerable from the Sand/C of 1.1 to 1.2. The two remaining parameters, i.e., the ratios of superplasticiser to cement (SP/C) and water to binder (W/Binder) have roughly similar influences on the flexural strength of UHP-FRC. The increase of these two ratios from the first proportions to the second proportions has minor influences on the flexural strength. However, when these ratios increase from the second to the third proportions, a considerable drop is observed in the flexural strength. Indeed, the SP/C and W/Superplasticiser ratios of 0.04 and 0.2 are observed as the optimal proportions in regard to the 28-day flexural strength of UHP-FRC. The optimum proportions of the important UHP-FRC mix design parameters and the percentage of participation of each parameter are presented in Table 3.7.

Table 3.7 The optimal proportions of the important UHP-FRC mix parameters and their participation percentages

Optimum mix	Optimisation Goal	Proportions / Participations	Important Parameters			
			SF/C	Sand/C	SP/C	W/Binder
T10-C	Greatest compressive strength	Optimal Proportions	0.35	1.1	0.03	0.20
		Participation (%)	75.2	10.2	3.99	10.6
T10-F	Greatest flexural (bending) strength	Optimal Proportions	0.30	1.2	0.04	0.20
		Participation (%)	41.9	17.7	26.2	14.3

As can be seen in Table 3.7, two optimal UHP-FRC mix designs have been determined to reach the highest compressive and highest flexural strengths, namely T10-C and T10-F, respectively. At this stage, in order to confirm the optimal strengths of these two UHP-FRC mixes and thereby verify the optimisation procedure, the proposed

UHP-FRC mixes are tested. The compressive and flexural strengths of the two PRC mixes (T10-C and T10-F) are summarised in Table 3.8. It is observed that the T10-C UHP-FRC mix, which has been optimised for reaching the highest 7-day compressive strength, reaches the high 7-day compressive strength of 118 (MPa), which is greater than the highest 7-day compressive strength of all the trial mixes (113 MPa). Also, it can be seen that the T10-F UHP-FRC mix, which has been optimised with the target of greatest flexural strength, attains the flexural strength of 12.6 (MPa), which is higher than the greatest flexural strength of the trial mixes (11.5 MPa). It is important to note that although T10-F reaches the highest flexural strength, it does not attain a significantly high compressive strength.
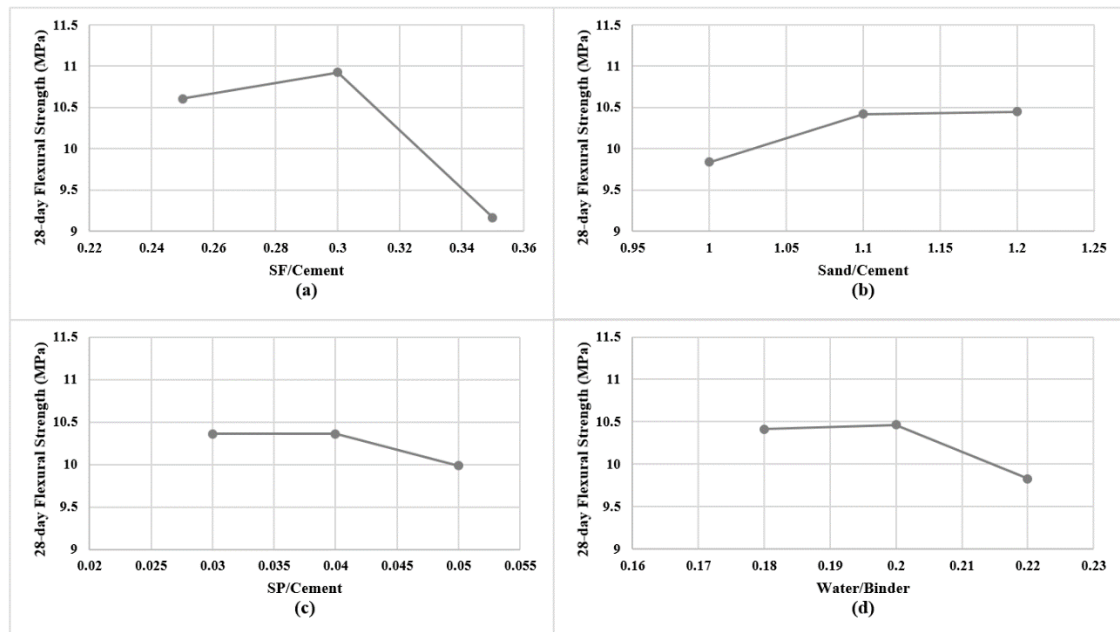
Figure 3.9 The effects of different proportions of the main mix design parameters on the 28-day compressive strength of UHP-FRC: (a) SF/Cement ratio; (b) Sand/Cement ratio; (c) SP/Cement ratio; (d) Water/Cement ratio

Table 3.8 Compressive and flexural strengths of the optimal UHP-FRC mixes

Optimal Mix	Target of Optimisation	Compressive Strength (MPa)		28-day Flexural Strength (MPa)
		7-day	28-day	
T10-C	Maximum compressive strength	118	142	11.2
T10-F	Maximum flexural strength	98.5	120	12.6

3.5 Optimum Content of Macro Steel Fibres

When the optimal plain UHP-FRC mix design (without fibres) is determined, the influence of macro steel fibres on the performance of the UHP-FRC mix is investigated. For this purpose, several trial mixes with optimal plain UHP-FRC with the highest flexural strength (T10-F) and various contents of fibres including 0.0%, 1.0%, 2.0%, and 3.0%, are considered. A 120-litre pan mixer is used for mixing these UHP-FRC mixes.

An issue that may occur during the mixing of the UHP-FRC with macro-fibres which leads to non-homogenous dispersal of fibres within the concrete mix is called "balling" (Al-Tikrite and Hadi, 2017). Balling happens when the fibres twist together tightly such that they cannot be simply disentangled by the paddles of the mixer. In order to avoid this problem, it is necessary to add the fibres gradually into the mix. In this way, the mixing process of the UHP-FRC mixes will be as follows:

- Dry mixing of cement, silica fume, and sand for about 2 minutes;
- Adding 2/3 of water and superplasticizer to the mix and mixing for about 3 minutes;
- Adding the remaining liquids (water and superplasticizer) and mixing for about 5 minutes;
- Adding fibres and continuing mixing until the mix becomes homogenous.

The total mixing process is around 15-18 minutes. The mixing time for the fibre-reinforced UHP-FRC is slightly longer than most of the trial mixes (T1-T9), presented in Table 3.6. The longer mixing process is mainly due to the larger quantity of the

UHP-FRC mixes compared to the plain UHP-FRC mixes and also the excess time required for the fibres to evenly mix with the plain UHP-FRC.

To study the mechanical performance of the UHP-FRC mixes with various amounts of fibres, several material tests must be carried out. For each mix, mass per unit volume, compressive strength, and ultimate flexural strength (modulus of rupture) are determined. The compressive strengths of the mixes are determined in congruence with the AS 1012.9 (AS-1012.9, 1999). For each trial mix, three cylindrical samples with the diameter and height of 100 mm and 200 mm, respectively (as shown in Figure 3.10), are utilised and the mean magnitudes are recorded. It should be noted that high-strength plaster is used for capping the cylindrical samples, in accordance with the AS 1012.9 (AS-1012.9, 1999), as can be seen in Figure 3.10. Indeed, high-strength plaster is found adequate for capping the UHP-FRC cylindrical samples for the compression tests according to the literature (e.g. (Al-Tikrite and Hadi, 2017, Algburi et al., 2019)). The capping procedure is as follows:

- The plaster powder is mixed with water until a smooth mix is obtained. The ratio of water to plaster (by weight) is 0.7;
- The mix is poured into the mould and the cylindrical sample is placed in the mould such that its unsmooth (top) face is inserted into the wet plaster;
- The sample is fixed and kept in the mould for about an hour;
- The plaster cap is unmoulded and kept for another hour before the compression testing to let the plaster hardens.

The same samples are also used for the determination of the mass per unit volume for each of the mixes in accordance with the rapid measuring technique recommended by AS 1012.1 (AS-1012.12.1, 2014). To obtain the ultimate flexural strength (modulus of rupture), three prismatic samples with the dimensions of 100x100x350 (mm) are tested in accordance with AS 1012.11 (AS-1012.11, 2000), as shown in Figure 3.11.
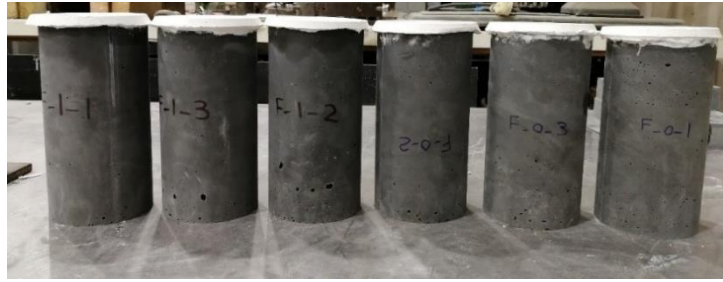
Figure 3.10 Cylindrical samples of 100mm x 200mm (diameter x height) for compression testing in accordance with (AS-1012.9, 1999)

(a) prismatic samples of 100x100x350 (mm) for flexural testing

(b) 100 kN MATEST test rig for flexural testing of UHP-FRC samples

Figure 3.11 Determination of the flexural strength of UHP-FRC samples in accordance with AS 1012.11 (AS-1012.11, 2000)

The 7-day characteristics of the UHP-FRC mixes with various volumes of fibres are presented in Table 3.9. The UHP-FRC mixes are named according to their optimal

plain UHP-FRC mix and the volume of fibres. As an example, T10-F-01 specifies a UHP-FRC mix which includes the optimal UHP-FRC mix with the highest flexural strength (T10-F) and 1.0% fibres (01). It can be deduced from Table 3.9 that the mass per unit volume of UHP-FRC increases as the volume of fibres increases. In order to observe the variation in the 7-day compressive and flexural strengths of the UHP-FRC mixes due to the change of fibres content, these test results are compared in Figure 3.12. From Figure 3.12, it can be deduced that the influences of fibre content on the compressive and flexural strength of the UHP-FRC are roughly analogous. In both cases, an upward trend is observed as the fibre content increases from 0.0% to 2.0%. From 2.0% to 3.0% of fibres, the compressive strength slightly reduces while the flexural strength shows a marginal rise. Since in both cases, marginal variations in the strength are observed from the fibre volume of 2.0 % to 3.0%, it is concluded that the optimal volume of fibres is 2.0%.

Table 3.9 7-day characteristics of UHP-FRC mixes with different volumes of fibres

UHP-FRC Mix Name	Fibres volume	Mass per unit volume (kg/m^3)	Compressive Strength (MPa)	Modulus of Rupture (MPa)
T10-F-00	0.0 %	2247	93.3	8.09
T10-F-01	1.0 %	2316	97.3	13.5
T10-F-02	2.0 %	2430	103	19.4
T10-F-03	3.0 %	2493	102	20.5
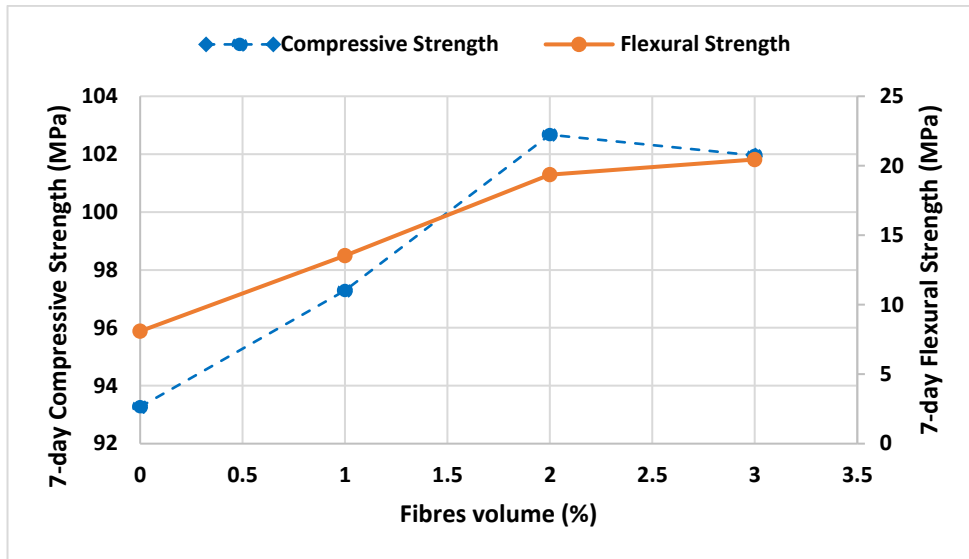
Figure 3.12 Compressive and flexural strengths versus fibre content of the UHP-FRC

After determining the optimum content of fibres (2% by volume), the 28-day material tests are performed for the optimal UHP-FRC mix with the optimum content of fibres (T10-F-02). The modulus of elasticity is determined by testing three cylindrical samples with the diameter and height of 150 mm and 300 mm, respectively, according to AS 1012.17 (AS-1012.17, 1997), as shown in Figure 3.13. Compressive strength and ultimate flexural strength (modulus of rupture) are determined per AS 1012.9 (AS-1012.9, 1999) and AS 1012.11 (AS-1012.11, 2000), respectively. Herein, the cracking strength of the UHP-FRC mix is also recorded during the flexural testing. The importance of flexural cracking strength in this research is due to the fact that the optimal UHP-FRC mix is developed for manufacturing non-prestressed concrete sleepers and the sleepers are designed such that they will not crack under the design rail loads. Therefore, the cracking strength of the material must be used for the design of the non-prestressed concrete sleepers rather than the ultimate flexural strength (modulus of rupture).

Figure 3.13 Determination of the modulus of elasticity of the optimal UHP-FRC mix in congruence with 1012.17 (AS-1012.17, 1997)

The 28-day test results of the optimal UHP-FRC mix are presented in Table 3.10. It can be deduced from Table 3.10 that the average 28-day compressive and flexural strengths of the optimal UHP-FRP mix (T10-F-02) samples are considerably higher than the 7-day strengths of the same mix reported in Table 3.9. The compressive strength shows a 13% of increase from the 7th day (103 MPa) to the 28th day (116 MPa). Also, the flexural strength (modulus of rupture) of the UHP-FRC mix shows a 10.3% of increase from the 7th day (19.4 MPa) to the 28th day (21.4 MPa).

Flexural cracking stress, which has been determined during the ultimate flexural test (modulus of rupture), is a critical test result that is presented in Table 3.10. Flexural cracking stress indicates the stress at which the flexural cracking is initiated. The minimum and average flexural cracking stresses are 13.2 and 13.3 (MPa). As will be explained in Chapter 8, the flexural cracking stress is a key parameter in the design of the non-prestressed UHP-FRC sleepers. Hence, in order to reach a safe design, the minimum flexural cracking strength, i.e., 13.2 (MPa) needs to be used for the design of the non-prestressed sleepers rather than the average value.

Table 3.10 28-day characteristics of the optimal UHP-FRC mix (T10-F-02)

Results	Modulus of Elasticity (MPa)	Compressive Strength (MPa)	Flexural Cracking Stress (MPa)	Modulus of Rupture (MPa)
Minimum magnitudes	37,568	112	13.2	20.2
Average magnitudes	38,694	116	13.3	21.4

3.6 Summary

In this chapter, the viability of utilising ultra-high performance fibre-reinforced concrete (UHP-FRC) for manufacturing non-prestressed concrete sleepers was studied. First, assuming typical dimensions of the non-prestressed concrete sleepers, under two different axle loads 25 TAL and 40 TAL, the minimum required flexural strength of the UHP-FRC mix was determined through a preliminary analysis according to the Australian Standard (AS1085.14, 2019). The cross-sections presumed for the two non-prestressed sleepers under axle loads of 25 TAL and 40 TAL were 250 x 220 and 300 x 250 (mm), respectively. It was found that in order to be able to manufacture non-prestressed concrete sleepers with these typical dimensions, the UHP-FRC material must have a flexural (cracking) strength of 11.6 MPa or higher.

After determining the minimum required flexural strength of the UHP-FRC (11.6 MPa), the optimisation process was carried out to attain plain UHP-FRC mixes with the highest compressive and highest flexural strengths. Four important design parameters (ratios) and three proportions for each of the parameters were considered in this study, which would normally require 81 trials (3^4=81). However, using the Taguchi method and the L9 orthogonal arrays (OAs), the number of trials was reduced to 9. In this manner, two separate optimisation processes were carried out based on the 7-day compressive and 28-day flexural strengths obtained from samples of the 9 trial mixes. The Qualitek-4 software (Roy, 1996) was used for the optimisation analysis. Two optimal UHP-FRC mixes with the highest compressive and flexural strengths were proposed, namely T10-C and T10-F, respectively. It was proved that the optimal UHP-FRC mix with the largest flexural (bending) strength can satisfy the minimum

required flexural strength for manufacturing the non-prestressed UHP-FRC sleepers with dimensions comparable to those of the conventional PSC sleepers (the flexural strength of T10-F is 12.6 MPa which is higher than 11.6 MPa). Subsequently, the optimum volume of macro steel fibres was determined. A number of trial mixes with the optimum UHP-FRC mix with the highest flexural strength (T10-F) and various volumes of Dramix4D-65/35BG steel fibres were investigated. It was found that 2% of Dramix4D-65/35BG fibres by volume is the optimal content regarding both the 7-day compressive and ultimate flexural strength (modulus of rupture).

Eventually, the 28-day properties of the optimal UHP-FRC mix with the optimum content of fibres (T10-F-02) were determined, as shown in Table 3.11. It was demonstrated that according to the Australian Standard (AS1085.14, 2019), concrete sleepers should not experience cracks under the design moments. Hence, the design of the proposed non-prestressed UHP-FRC sleepers must be based on the flexural cracking strength of the optimal UHP-FRC rather than the ultimate flexural strength (modulus of rupture). Hence, the flexural cracking strength of the optimal UHP-FRC mix was determined during the flexural testing. The minimum flexural strength obtained from the tests was 13.2 MPa which will be the key factor in the design of the non-prestressed UHP-FRC sleepers, as will be demonstrated in Chapter 8.

Table 3.11 The mix proportions of the optimal UHP-FRC Mix (T10-F-02)

Optimal mix	SF/C	Sand/C	SP/C	W/Binder	Fibre content by volume
T10-F	0.30	1.2	0.04	0.20	2%

CHAPTER 4
PERFORMANCE OF NON-PRESTRESSED UHP-FRC SLEEPERS UNDER STATIC AND CYCLIC (FATIGUE) LOADS

4.1 Introduction

In the previous chapter, it has been shown that a UHP-FRC material with a minimum cracking flexural strength equal to or higher than 11.6 MPa is required for manufacturing non-prestressed concrete sleepers with typical dimensions. Subsequently, a UHP-FRC material with a minimum flexural cracking strength of 13.2 MPa was developed. In this chapter, the performance of the non-prestressed UHP-FRC prototype sleepers under static and fatigue loading is investigated. For this purpose, standard static testing is performed for two prototype sleeper samples according to the Australian Standard (AS1085.14, 2019). Afterwards, the fatigue performance of the proposed UHP-FRC sleepers under cyclic loading is studied.

4.2 Manufacturing of the Prototype Non-prestressed UHP-FRC Sleepers

In order to verify the performance of the proposed non-prestressed UHP-FRC sleepers under rail-seat static and cyclic (fatigue) loading, two pairs of prototype sleepers are produced. These sleeper prototypes are of simple prismatic shapes, with the cross-section dimensions (width x height) of 250 x 220 (mm) that are close to the typical dimensions of 25 TAL prestressed concrete sleepers. According to the Australian Standard (AS1085.14, 2019), the support span for the rail-seat bending tests of sleepers must be 660 mm, as shown in Figure 4.1. Hence, the length of these samples is 1060 mm to accommodate the 200 mm overhanging length on each side of the sample (660 mm + 200 + 200 = 1060 mm).
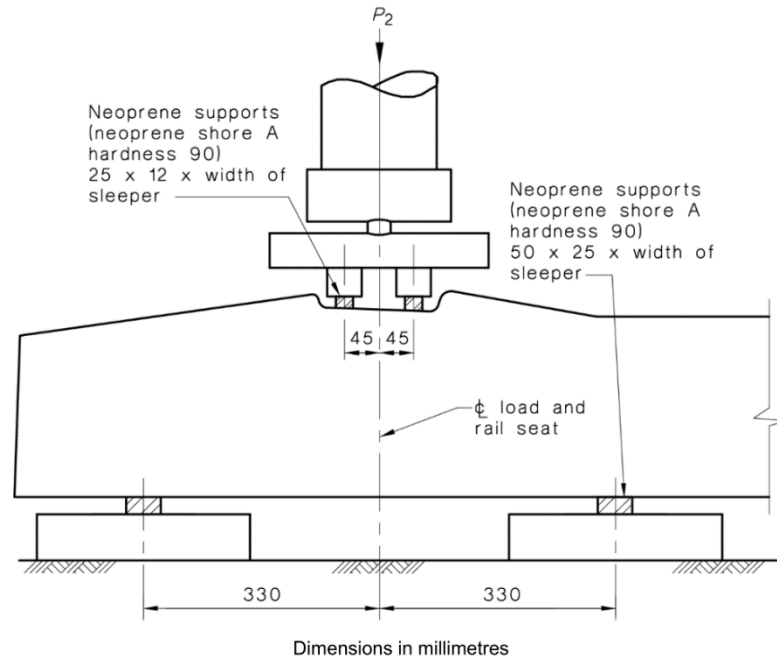
Figure 4.1 Details of the rail-seat positive moment test (AS1085.14, 2019)

In order to mix the relatively large amounts of UHP-FRC, a 300-litre pan mixer is utilised, as shown in Figure 4.2. It should be noted that prior to each mixing process, the mixer was cleaned thoroughly. Then, the inner surface of the mixer pan and the paddles were made slightly wet using a wet rag. Four prototype samples are produced in two batches, i.e. two prototype samples per batch. From each batch, three of the cylinder samples of 100 x 200 (mm) (diameter x height) and three prismatic flexural samples of 100x100x350 (mm) are taken for the 28-day compression and flexural (modulus of rupture) tests, respectively. The compression material tests have been performed according to AS1012.9 (AS-1012.9, 1999) and the flexural (modulus of rupture) tests are conducted in congruence with AS1012.11 (AS-1012.11, 2000). Also, the mass per unit volume magnitudes of the hardened UHP-FRC mixes are determined using the three samples, according to AS1012.12.1 (AS-1012.12.1, 2014). In addition to the necessary samples mentioned, four additional samples are taken from the batches in the case of inconsistency in the material test results. The newly poured UHP-FRC beams and the material samples are shown in Figure 4.3.

Figure 4.2 The 300-litre pan mixer for producing the UHP-FRC mixes
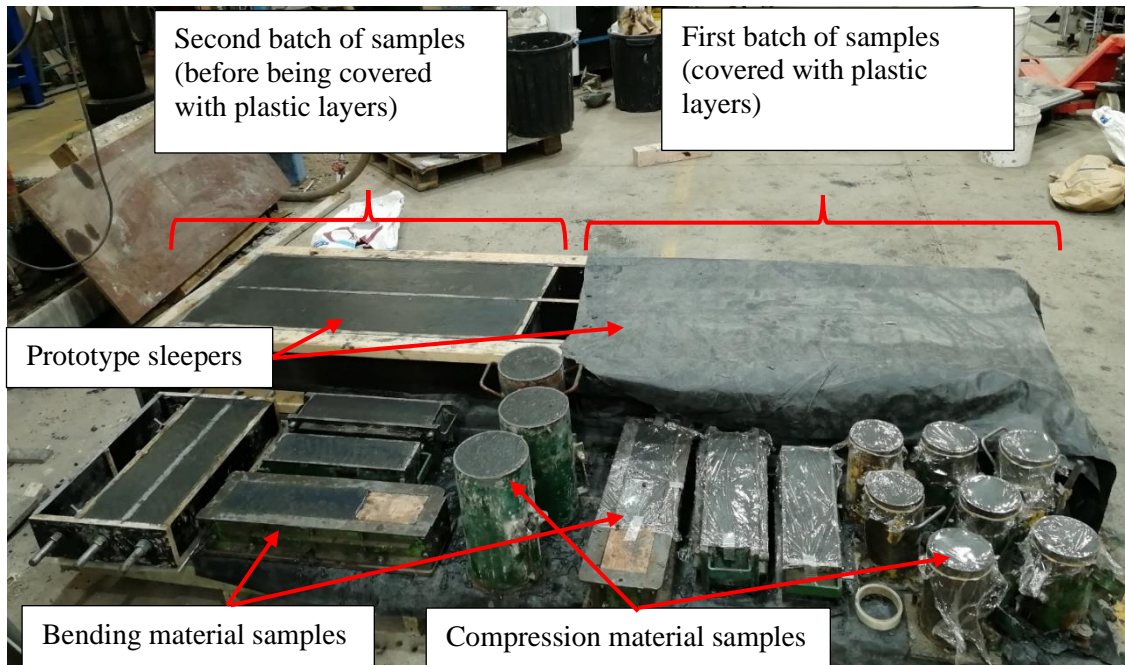
Figure 4.3 The UHP-FRC prototype beams and material samples for static and cyclic testing

The curing process for the material samples is described in Chapter 3. The prototype sleeper samples are kept in their moulds and covered with plastic sheets for 24 hours and then covered with wet hessian until the 28th day, when they are unmoulded and prepared for testing.

Although the quantity of each batch is slightly less than half of the maximum capacity of the mixer (around 140 litres), the mixer paddles stopped a few times when mixing the first batch, as the UHP-FRC mix becomes sticky before turning into a soft and wet mix. Such an issue was not observed when mixing the smaller amounts of UHP-FRC, as reported in Chapter 3. So, it is concluded that the mixing quality must be monitored thoroughly in the case that larger quantities of UHP-FRC material are needed. With more consideration, the second batch is mixed properly in congruence with the mixing steps stated in Chapter 3. Accordingly, it is expected that the samples from the first batch grasp less strength compared with those from the second batch.

One prototype sleeper sample from each batch is used for the static testing and one for the cyclic/fatigue testing, as shown in Table 4.1. The samples are named according to their batch number, test type and number. For instance, S1-S1 is the prototype sample from batch 1 and selected for static test #1, while S2-F2 is the sample from batch 2 and used for fatigue test #2.

Table 4.1 The prototype non-prestressed UHP-FRC sleeper samples for the static and fatigue testing

Sample name	Batch No.	Test type and number
S1-S1	Batch 1	Static Test #1
S1-F1		Fatigue Test #1
S2-S2	Batch 2	Static Test #2
S2-F2		Fatigue Test #2

The standard material test results are summarised in Table 4.2. As can be seen, the first batch has slightly lower strength in comparison with the second batch. This marginal

difference can be attributed to the better mixing quality of the second batch. Hence, it is also expected that the prototype UHP-FRC sleeper samples from the second batch, have a better performance under static and cyclic (fatigue) loads.

Table 4.2 Mechanical properties of the UHP-FRC mixes (batch 1 and batch 2)

Results	Mass per unit volume (kg/m^3)		Compressive Strength (MPa)		Modulus of Rupture (MPa)	
	Batch 1	Batch 2	Batch 1	Batch 2	Batch 1	Batch 2
Minimum properties	2379	2402	108	113	18.2	19.8
Average properties	2394	2418	113	117	19.6	21.0
Standard Deviation	14.2	19.5	4.77	4.15	1.70	1.05
Coefficient of Variation (%)	0.6	0.8	4.2	3.5	8.7	5

4.3 Rail-seat Positive Moment Static Test

In this research, the rail-seat positive moment test is performed for the proposed prototype non-prestressed UHP-FRC sleeper segments, according to the Australian Standard (AS1085.14, 2019). The test setup is shown in Figure 4.4. As can be seen, the support span is 660 mm, while the loading span is relatively small (90 mm). In order to verify the performance of the proposed non-prestressed UHP-FRC sleepers, two prototype sleeper samples are being tested under rail-seat static loading. In Figure 4.4, the steel/metal components of the test set-up are shown in blue. The sample rests on two prismatic bars with 50x50 (mm) cross-sections as supports. Also, two metal bars with a square cross-section of 25x25 (mm) are used for applying the static load. Thin sheets of rubber belts are placed between the sample and bars, shown in red in Figure 4.4, to assure the proper load distribution and avoid considerable stress concentration at the interface of the supports and loading bars. As can be seen, three

LVDT gauges have been utilised in the test setup. LVDT 1 is horizontally installed to capture the nonlinear tensile deformations of the samples under the static rail-seat loading. The distance between the two ends of this LVDT extensometer (the gauge distance) is 200 mm. On the other side, the other two LVDT gauges, i.e., LVDT 2 and 3, are vertically installed on top of the samples at the supports to capture the vertical settlement of the supports. Also, a laser displacement gauge is used to capture the vertical deflection of the sample at the mid-span. On the other (front) side of the sample, two dots are put at a horizontal distance of 150 mm from each other (each dot 75 mm off the mid-span of the sample) and a vertical distance of 10 mm from the bottom of the sample. A 2D video extensometer system MERCURY RT DIC was used to capture the relative movement of the two dots and thereby show the deformations at the centre zone of the sample. The reason to use this camera instead of an LVDT gauge is the need to have a clear face of the sample on the front side to observe the crack occurrence and propagation, whereas the LVDT gauge blocks the side face of the sample around the area that cracks are expected to initiate, i.e., the mid-span area close to the bottom. Also, two 60 mm strain gauges are attached to the top and bottom faces of the prototype sleeper sample, near the front side, to record the maximum compressive and tensile strain magnitudes, respectively, at the mid-span area. Indeed, the tensile strain of the prototype sample is recorded in three ways, using the LVDT1, DIC camera, and strain gauge. A comparison between the strain magnitudes recorded by these three tools will be presented in Section 4.3.2.
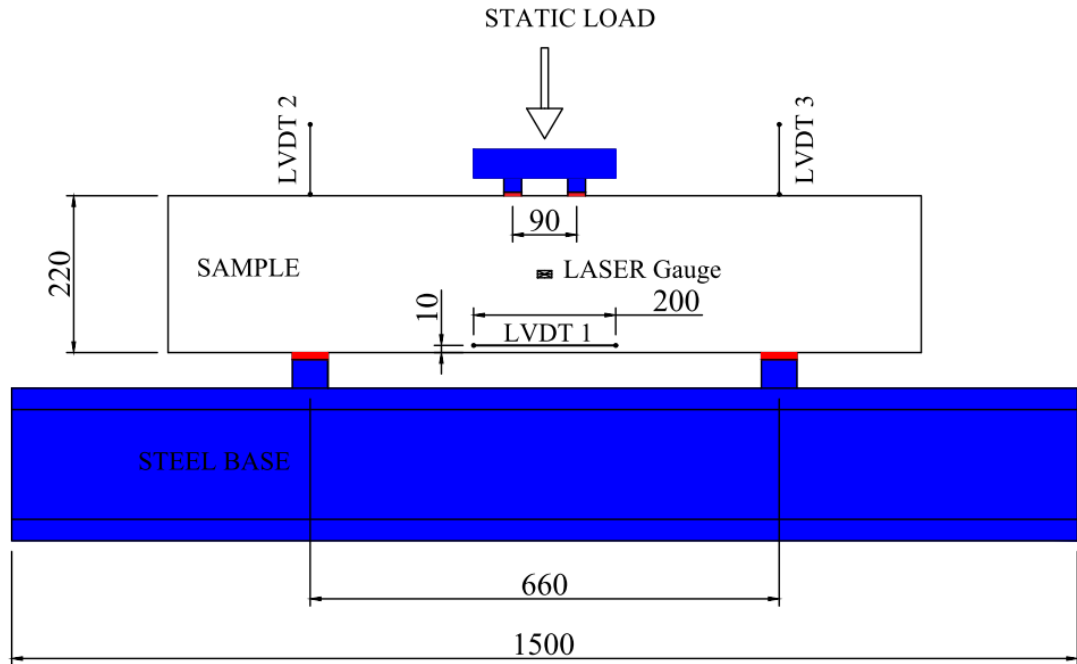
Figure 4.4 Rail-seat positive moment test set-up (rear side) (dimensions in mm)

The testing procedure for a PSC sleeper per AS 1085-14 (AS1085.14, 2019) is described as follows. The static load is applied at a load rate not higher than 25 kN/min until the defined test load required to cause the required first cracking moment (M^{cr}), called P_2, is reached. Then, the sleeper must be inspected for any structural cracks. If the sleeper does not incur any structural cracks under or at the load magnitude P_2, the sleeper is deemed approved. The magnitude of P_2 can be calculated using Equation (4.1):

$$P_2 = \frac{2M^{cr}}{(0.33 - 0.045)} \tag{4.1}$$

where M^{cr} is the cracking moment which can be calculated according to Equation (4.2) for a prestressed concrete sleeper:

$$M^{cr} = Z\left(f'_{ct.f} + \frac{P}{A_t}\right) + eP \tag{4.2}$$

where Z and A_t are the transformed section modulus and transformed section area of the sleeper at the rail seat, respectively. P is the prestressing force of the sleeper applied

90

from the prestressed tendons. It should be noted that the magnitude of P is equal to zero in non-prestressed sleepers. Also, $f'_{ct.f}$ can be calculated for normal-strength and high-performance concrete using Equation (4.3):

$$f'_{ct.f} = 0.6 \, (f'_c)^{0.5} \tag{4.3}$$

where f'_c is the characteristic 28-day compressive strength of concrete.

For calculating the magnitude of M^{cr} for the non-prestressed UHP-FRC samples ($P =$ 0), as there are no prestressing tendons in these samples, Equation 4.2 can be converted into a simple form using Equation (4.4):

$$M^{cr} = \frac{bh^2}{6} \left(f'_{ct.f} \right) \tag{4.4}$$

where b and h are the width (250 mm) and the height (220 mm) of the UHP-FRC samples, respectively. The magnitude of the flexural (cracking) strength, $f'_{ct.f}$, is selected as 13.2 MPa. This magnitude has been obtained as the minimum flexural cracking strength of the optimal UHP-FRC mix as described in Chapter 3 (refer to Table 3.10). In this manner, the magnitudes of M^{cr} and P_2 can be simply calculated according to Equation 4.4 and Equation 4.1, and will be equal to 26.6 (kN.m) and 161 (kN), respectively. Hence, the UHP-FRC samples will pass the rail-seat positive moment test if they do not incur structural cracks during the loading process until 161 kN as a minimum requirement.

Figure 4.5 and Figure 4.6 show the test set-ups of the UHP-FRC samples S1-S1 and S2-S2, respectively. It can be seen that the horizontal LVDT(s) and the laser displacement gauge are installed on the rear side of the samples, and the DIC camera captures the extension of the two points at a marginal distance (10 mm) from the bottom of the samples. For a better distinction of the two dots, as shown in Figure 4.5-a and Figure 4.6-a, the lower part of the mid-span of the front sides is coloured white. It will also help to find the cracks when they appear.
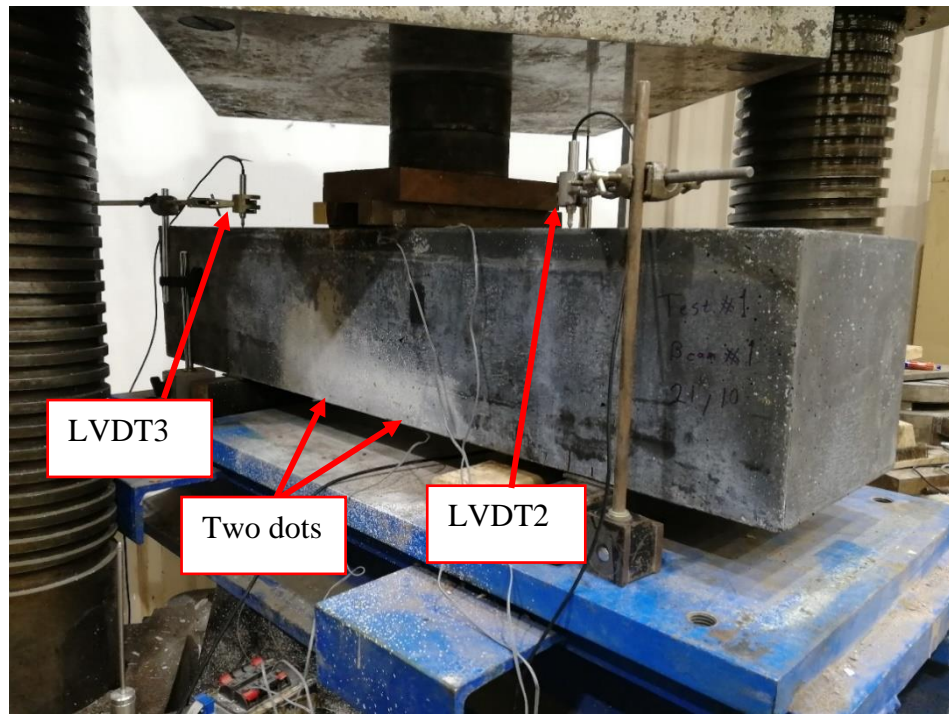
(a) front side
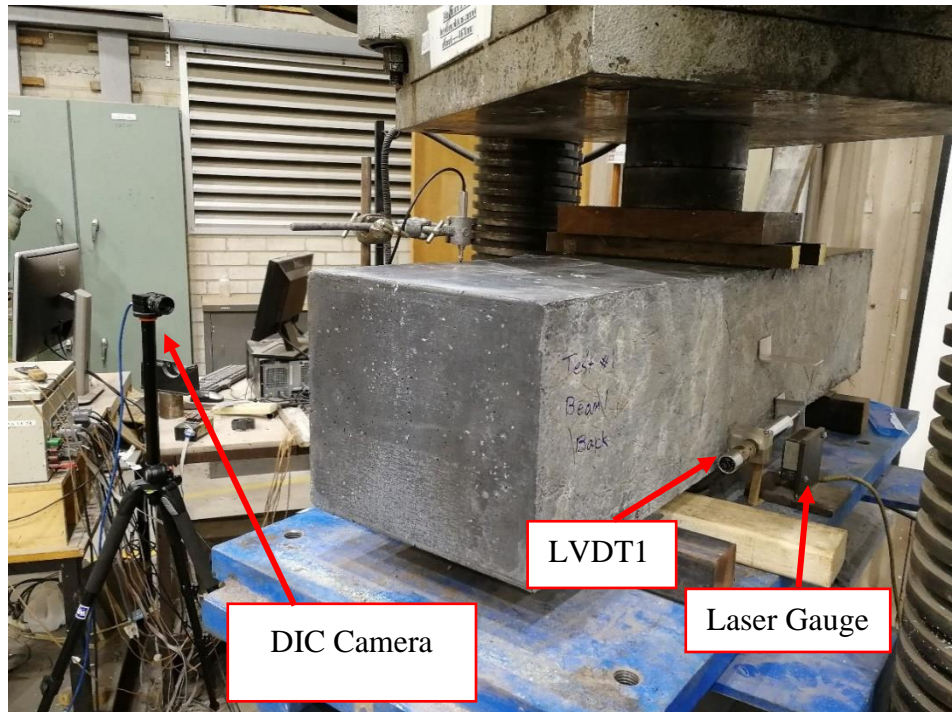
(b) rear side

Figure 4.5 The set-up for static testing of the UHP-FRC sample S1-S1
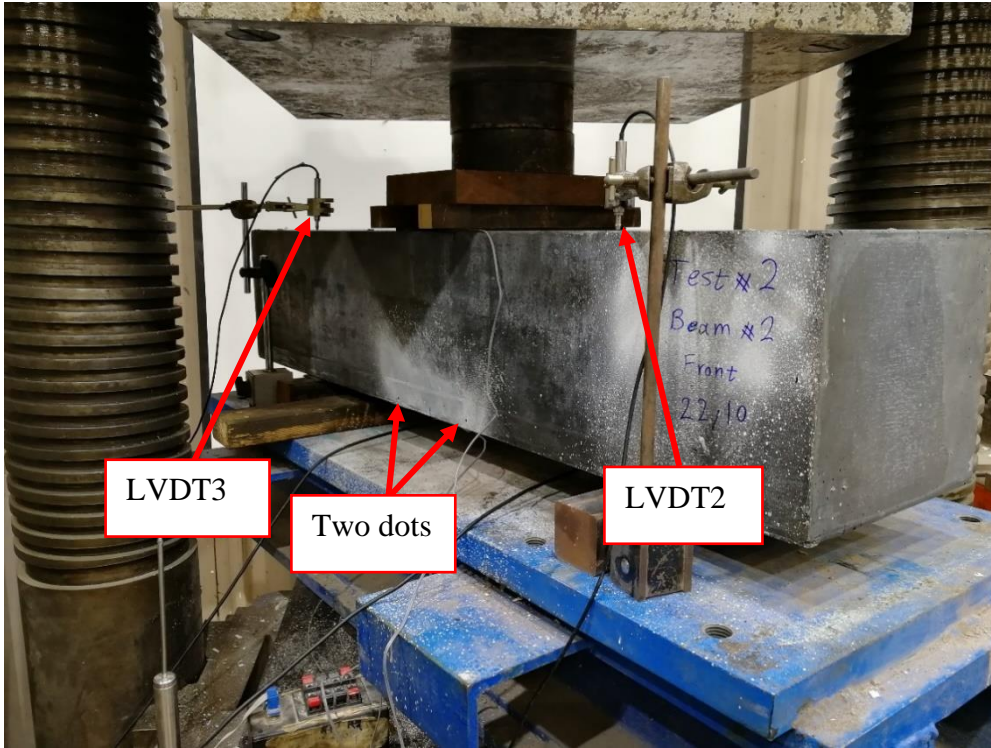
(a) front side
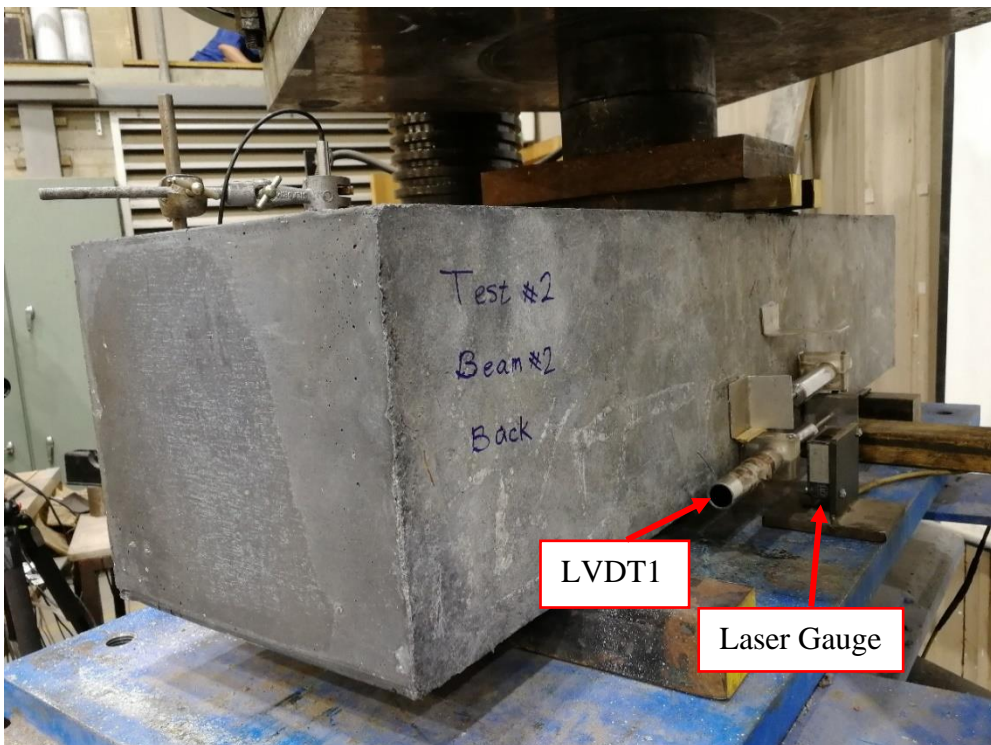
(b) rear side

Figure 4.6 The set-up for static testing of the UHP-FRC sample S2-S2

4.3.1 Load-Deflection Relationship

The load-deflection curves of the UHP-FRC prototype sleepers, S1-S1 and S2-S2, obtained from the static tests are shown in Figure 4.7. It can be deduced from these figures that sample S1-S1 has very weak performance compared with sample S2-S2. Indeed, even the linear part of the load-deflection curve of sample S1-S1 is significantly lower than S2-S2.

The structural cracks can be traced from the load-deflection curve, as each crack causes a slight drop in the curve. As can be seen, sample S1-S1 performed linearly at a relatively lower slope until the first minor drop (structural crack) occurred under the vertical load of 111 MPa. However, sample S2-S2 performed significantly stiffer in the linear zone, followed by a slope change until the first drop (structural crack) occurred under the vertical load 189 kN. The first cracking load of 189 kN agrees with the visual inspection during the testing process.
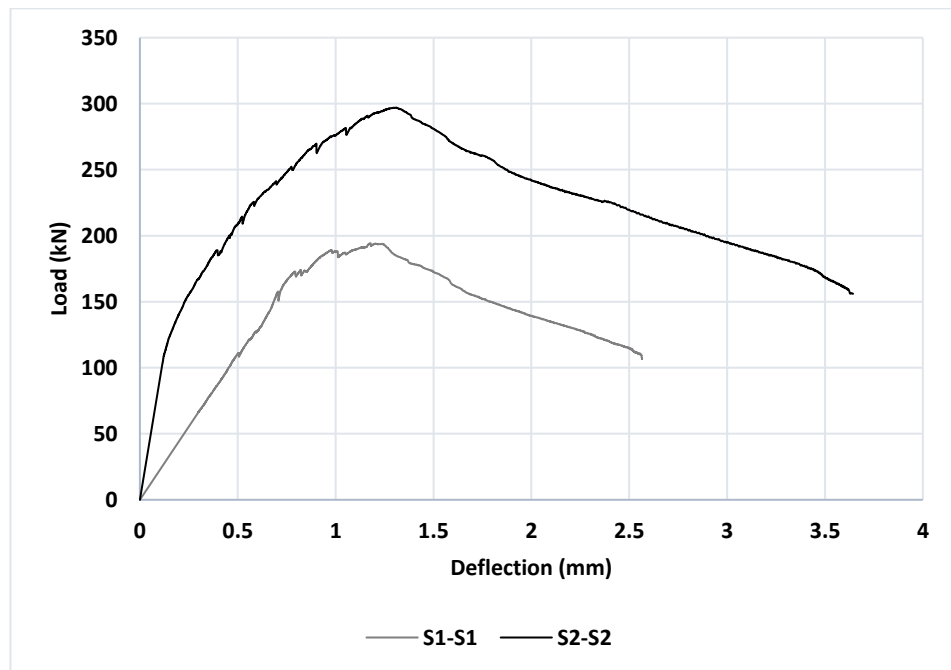
Figure 4.7 Load-deflection diagram of the prototype samples S1-S1 and S2-S2

Comparing the load-deflection curves of S1-S1 and S2-S2, and considering the weak performance of sample S1-S1 through the visual inspection, sample S1-S1 is regarded

as a failed sample and therefore is excluded from this study. This failure is attributed to the issues during the first batch mixing process, as reported in Section 4.2.

4.3.2 Load-Strain Relationship

In this section, the load-strain relationship of the prototype sleeper, S2-S2, under the rail-seat positive moment loading is studied. Figure 4.8 shows the Load versus the flexural tensile strain diagram of the prototype sleeper S2-S2 at the rail-seat section. The "LVDT gauge" shows the evolution of the tensile surface strain on the rear side, while the 60-mm electro-resistive "stain gauge" and the data recorded by the "Mercury camera" (DIC camera) show the tensile surface strain values recorded on the front side of the sample. It is observed that the strain values recorded by the LVDT extensometer and the strain gauge are more analogous than the ones recorded by the Mercury Camera. The divergence of the data recorded by the DIC camera from the ones recorded by the strain gauge and the LVDT extensometer is attributed to the vibrations (noises) generated from the 5000 kN hydraulic testing machine that has affected the performance of the DIC camera. According to the data recorded by the LVDT extensometer and the strain gauge, the tensile flexural strains at the peak load point on the front and rear sides of the UHP-FRC sample are equal to 0.0016 and 0.0011, respectively.

Figure 4.9 shows the relationship between the rail seat load and the compressive strain of the prototype sleeper S2-S2. The strain has been recorded using a 60-mm electro-resistive strain gauge attached to the top face of the sample close to the rear face. It is observed that there is a jump in the magnitude of the compressive flexural strain, which is attributed to a micro crack on the bottom of the sample. The compressive strain magnitude at the peak load point is around 0.00044, which is considerably below the crushing strain of concrete, which is typically about 0.0035 (AS-3600, 2018). Hence, it is deduced that the concrete crushing does not happen for a non-prestressed UHP-FRC prototype sleeper at the ultimate strength point, and the tensile fracture is the mode of failure. Even by the end of loading, the compressive strain reaches 0.001, which is still below the concrete crushing strain. It is important to note that the UHP-FRC prototype sample does not have any prestressing tendons or reinforcing longitudinal bars. Thus, it is normal that the concrete crushing under the flexural

compressive stress does not occur. Hence, it is confirmed that the flexural tensile strength of the UHP-FRC material dominates the strength of the UHP-FRC sleepers (as stated in Section 3.3).
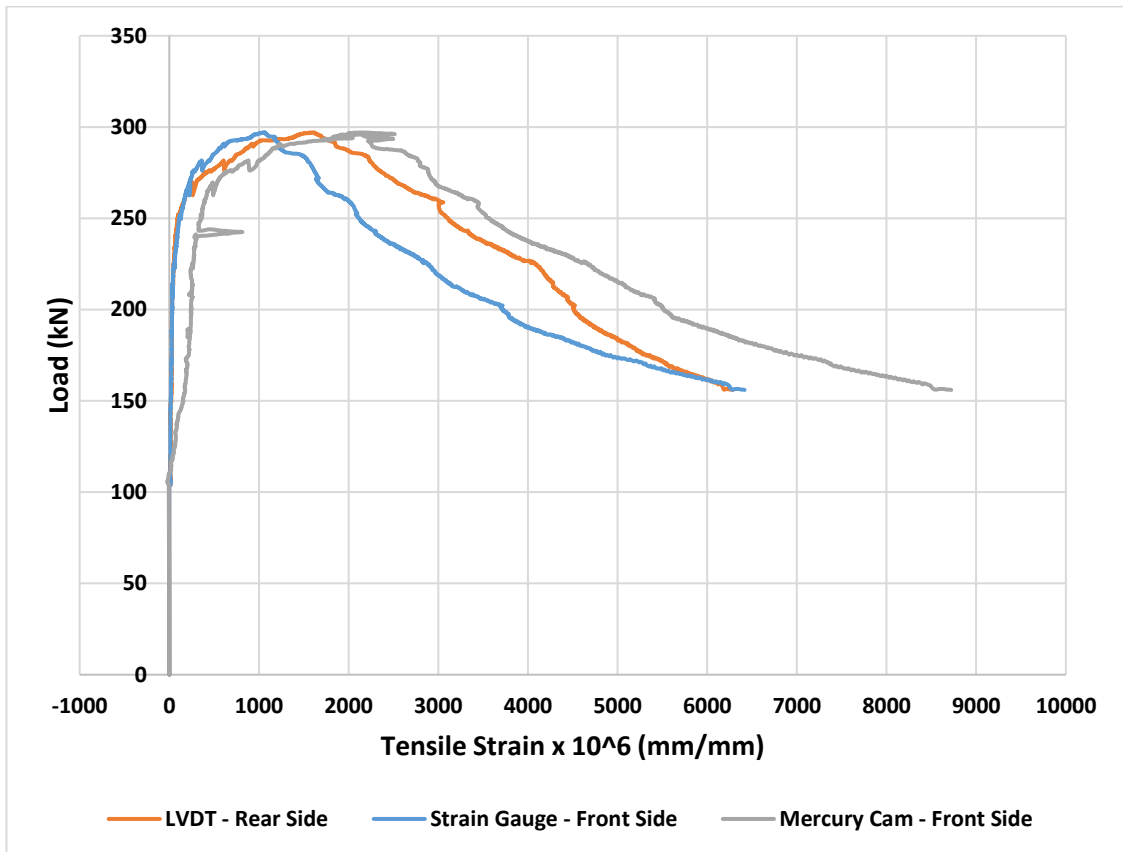
Figure 4.8 Load vs. tensile strain curves of sample S2-S2
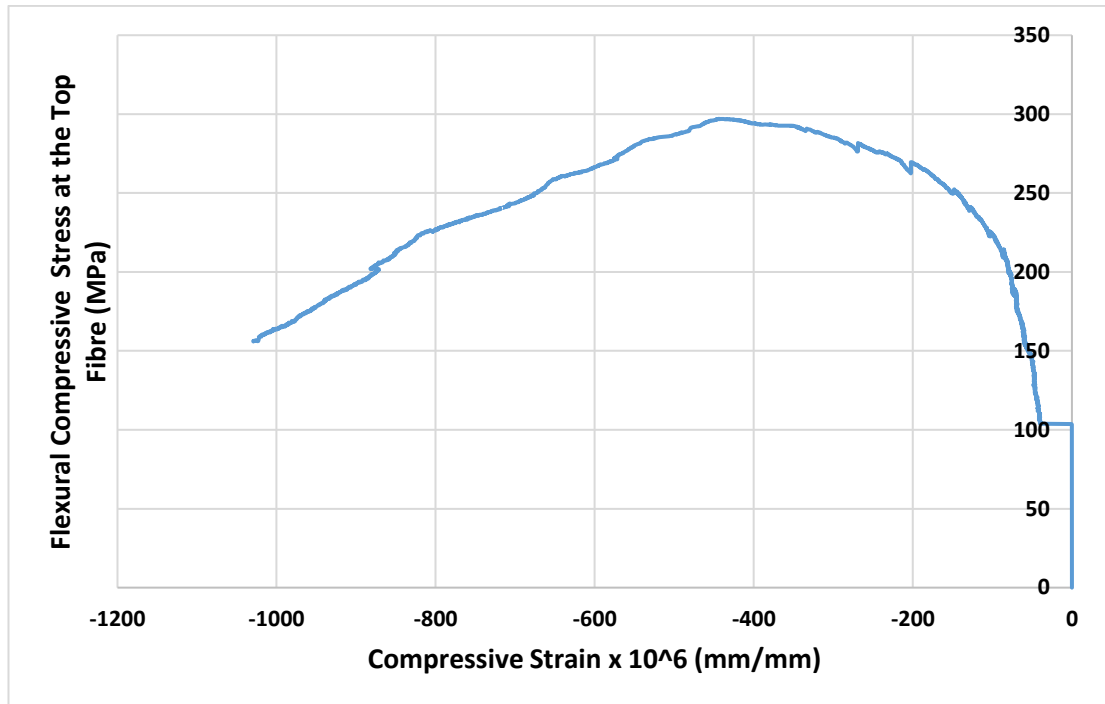
Figure 4.9 Load vs. compressive strain curve of sample S2-S2

4.4 Fatigue (Cyclic) Testing

Figure 4.10 shows the details of the fatigue test set-up developed for investigating the performance of the non-prestressed UHP-FRC prototype sleeper samples under cyclic (fatigue) loading. In this research, the fatigue test set-up is slightly different from the one recommended by the Australian Standard (AS1085.14, 2019), as shown in Figure 4.1. The main difference is that the two loading bars are replaced with a 60 kg (60 kg/m) rail segment.

It can also be seen that four LVDT gauges are installed at the mid-span of the UHP-FRC sleeper sample, with a 200 mm distance between their two points (200 mm gauge distance). These LVDT gauges are installed on the rear side of the sample, whereas the front side will be kept free of LVDT gauges for visual inspections and monitoring of the crack initiations and propagations. A strain gauge is also attached to the bottom face of the sample at the mid-span and close to the front face in order to record the maximum tensile strain magnitudes on the front side of the sample. A laser displacement gauge is utilized to capture the vertical deflection of the sample at the mid-span.
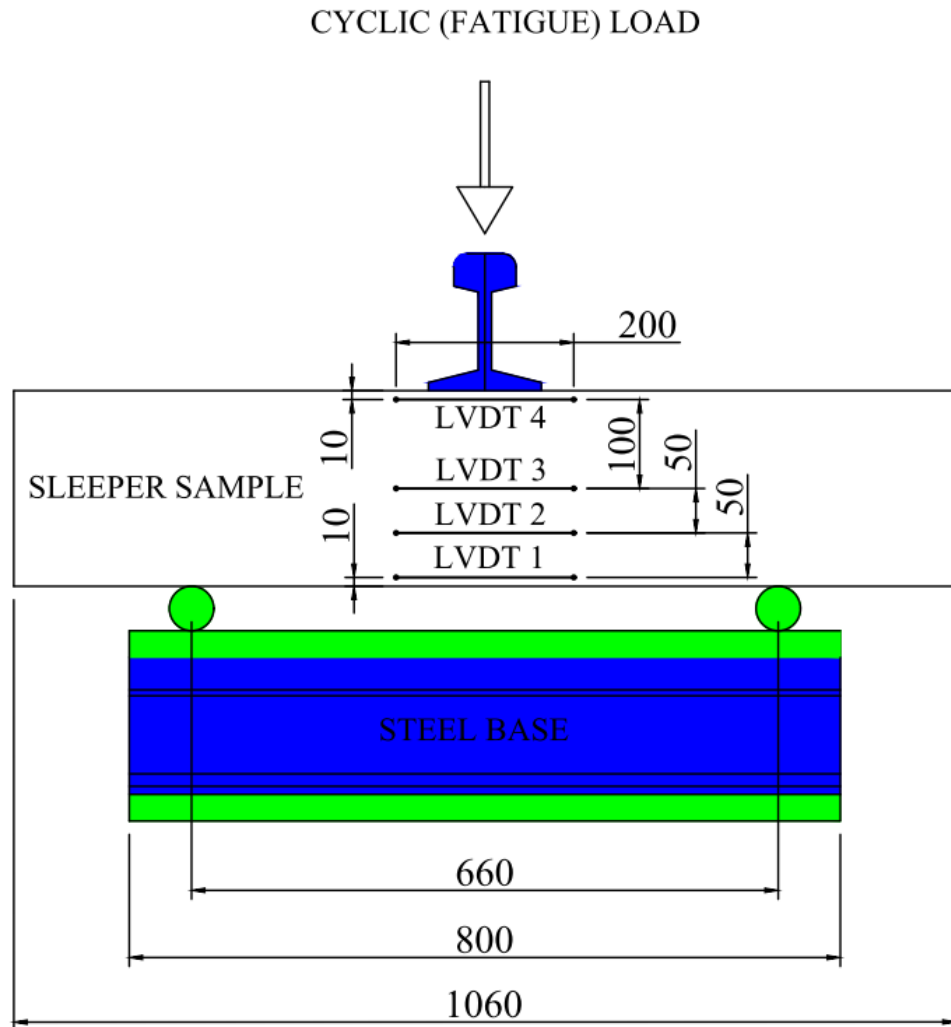
Figure 4.10 Details of the fatigue test set-up (dimensions in millimetres)

The cyclic loading is performed ranging between a minimum and maximum downward vertical load, i.e. there is no change in the sign (direction) of the vertical load. The minimum load is always constant and equal to 15 kN as recommended by the Australian Standard (AS1085.14, 2019). The maximum load magnitude is either 30 kN or 60% or 100% of the target maximum cyclic load, as shown in Figure 4.11. The target maximum cyclic load is selected such that it generates the same positive rail-seat moment within the prototype sleeper sample as 22.6 kN.m that was calculated for the design rail load according to the Australian Standard (refer to Table 3.2). Since the fatigue test set-up developed in this study is a type of three-point beam test, the maximum cyclic load can be calculated as follows:

$$P_{cyclic\_target} = \frac{2M_{R+}}{0.33} = \frac{2 * 22.6}{0.33} = 137 \ kN \qquad\qquad (4.5)$$
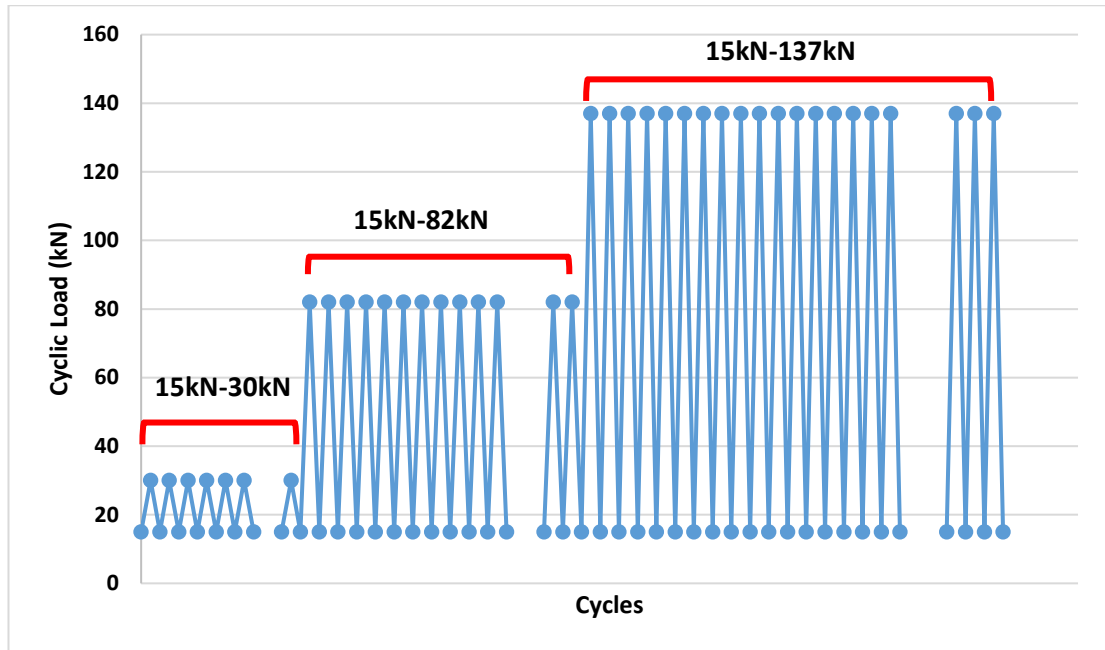
Figure 4.11 The Cyclic load levels

Herein, two non-prestressed UHP-FRC sleeper samples, S1-F1 and S2-F2, made from the first and the second UHP-FRC batches, respectively, with material properties demonstrated in Table 4.2, are tested. In the following section, the detailed cyclic (fatigue) testing procedures of samples S1-F1 and S2-F2 and their test results are reported separately.

4.4.1 Design of the Steel Supporting Frame

In order to perform the cyclic tests, a strong and rigid steel base is designed and constructed at the workshop of the University of Wollongong. Figure 4.12 shows the 3D view of the steel base. The support frame consists of two thick steel plates of 800 x 400 x 30 (mm) on top and bottom and two AS60 KG rail pieces with a length of 800 mm in between. The frame is engaged with the 250 kN Instron testing machine via the

metal pin (shown in dark blue), and the prototype sleeper sample is supported on top
of the steel frame.
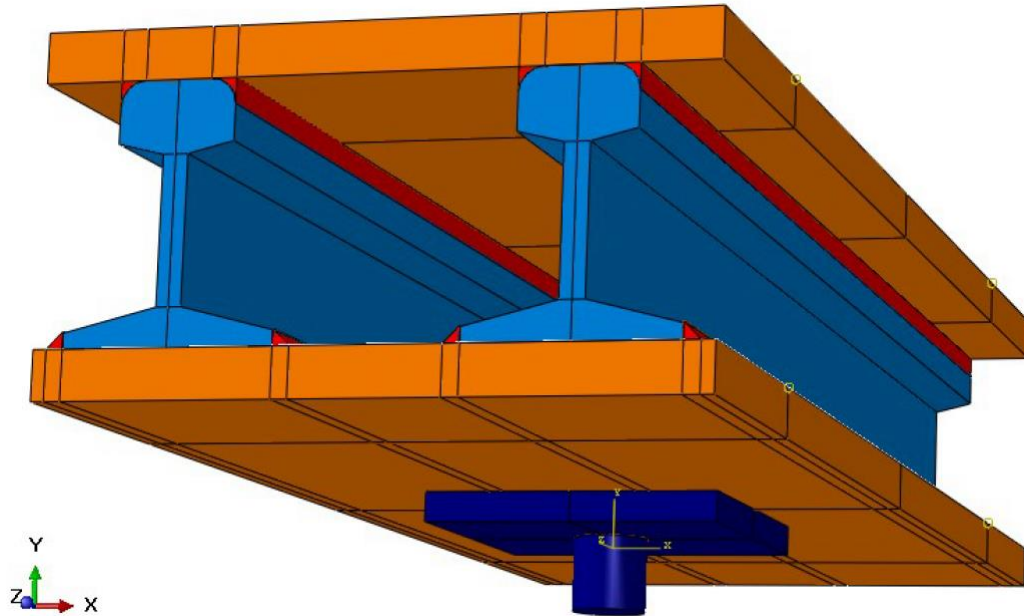
Figure 4.12 3D view of the steel frame for the fatigue testing of the UHP-FRC prototype
samples

In order to investigate the deflection and the stress magnitudes of the supporting steel
frame under the target load, 137 kN, a linear-elastic finite element analysis is
performed using the commercial finite element package, ABAQUS (ABAQUS, 2013).
It should be noted that the supporting frame is designed to remain elastic under cyclic
loads with relatively marginal deformations. Therefore, a linear-elastic FE analysis is
sufficient herein.

The elastic modulus and Poisson's ratio for all the elements are assumed 200 GPa and
0.3, respectively. The solid elements with reduced integration named C3D8R have
been used for all the elements. The total number of solid elements is 11,990. The load
is applied to the bottom rod (shown in dark blue in Figure 4.12), and the boundary
conditions are defined on top of the steel base at a distance of 660 mm from each other,
where the simple supports of the prototype samples will be installed (as shown in
Figure 4.10). The boundary conditions are shown in Figure 4.13.
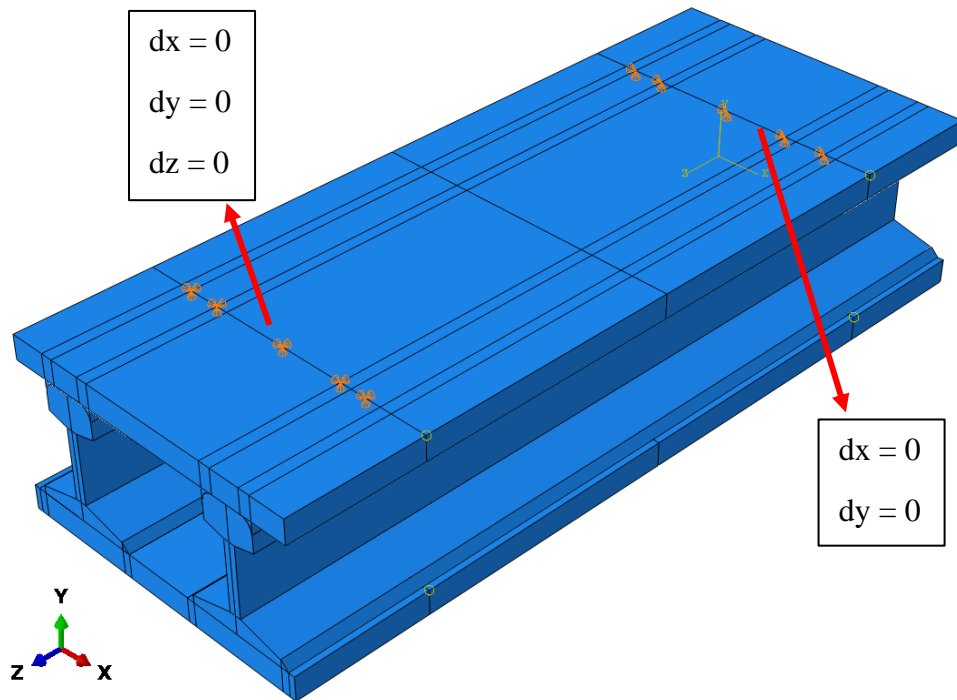
Figure 4.13 The boundary conditions on top of the steel at the location of the sleeper supports

Figure 4.14 shows the vertical deflection contour of the steel frame under 137 kN. It can be seen that the maximum deflection of the steel frame is 0.254 mm under the maximum cyclic load, which is acceptable because it provides sufficient rigidity and the ratio of deflection to the support span length is marginal (0.254 / 660 = 0.0004). Also, Figure 4.15 shows the contour of the Von Mises stress magnitudes generated within the steel frame under the maximum cyclic load. It is observed that the maximum magnitude of stress is 124.3 MPa, which is less than 50% of the yield point of the steel elements (f_y = 250 MPa). Hence, it is concluded that the designed steel supporting frame is adequate for the fatigue testing of the UHP-FRC prototype sleeper samples.
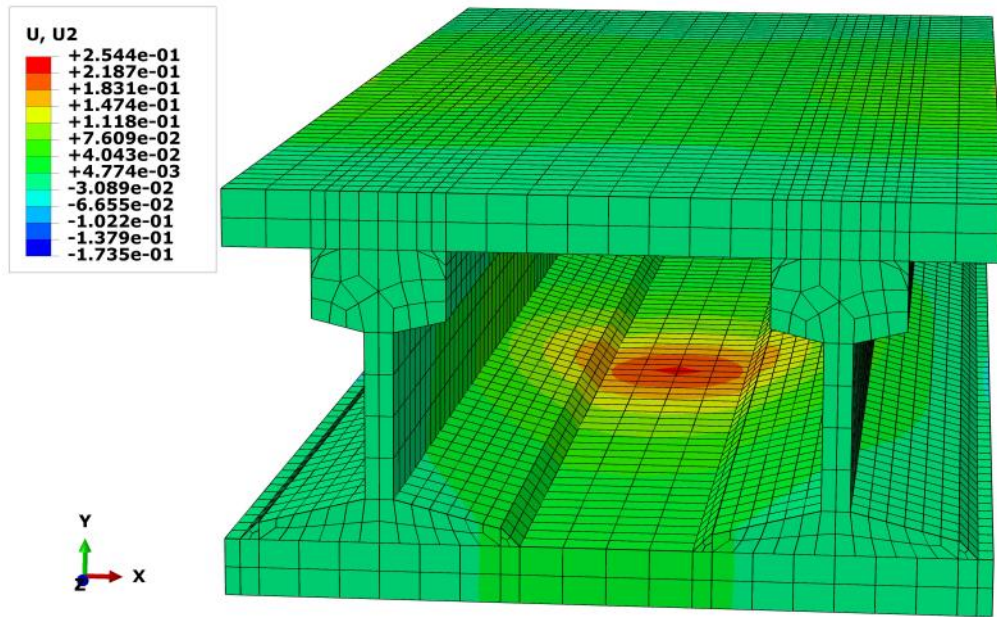
Figure 4.14 Contour of the vertical deflections (U2) of the steel frame
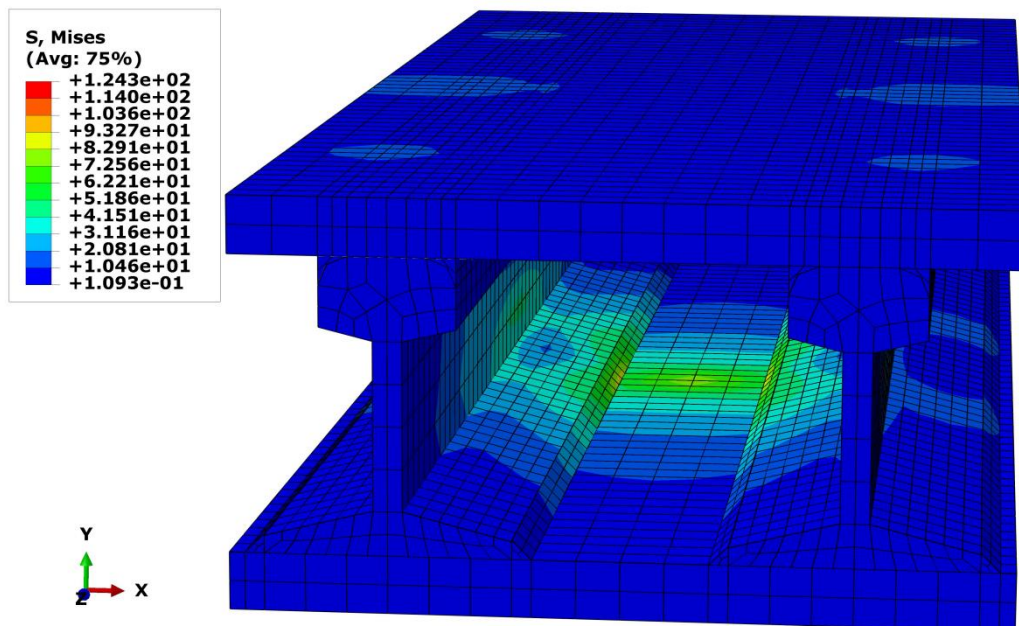
Figure 4.15 Contour of the Mises stress of the steel frame

4.4.2 Test Results of the Prototype Sleeper Sample S1-F1

The test set-up of the prototype UHP-FRC sample S1-F1 is shown in Figure 4.16. It is observed that on the front face, only the laser displacement gauge has been installed at

the mid-height mid-span of S1-F1. Thus, the front face is clear enough to observe and mark the cracks during the cyclic testing. As previously illustrated in Figure 4.10, four LVDT gauges are installed on the rear face of the sample.
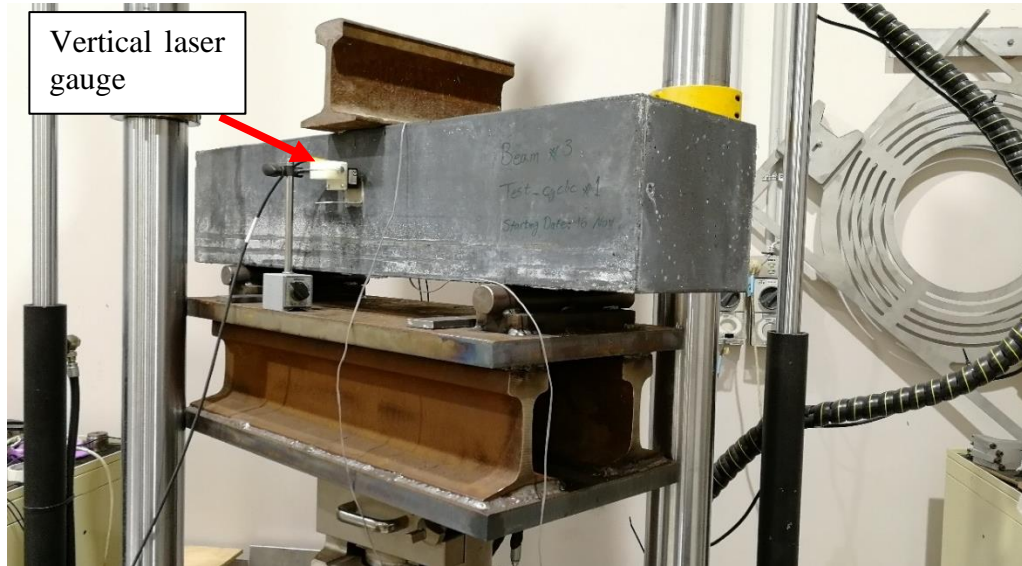
(a) front side

(b) rear side

Figure 4.16 The set-up for the fatigue testing of the UHP-FRC sample S1-F1

As explained in Section 4.2 and Section 4.3.1, it is expected that the prototype sleeper sample made with batch 1 of the UHP-FRC mix, i.e., S1-F1 shows significantly lower strength compared with sample S2-F2. The cyclic load ranging between the 15 kN and the maximum target load, 137 kN (obtained from Equation 4.5), is applied to S1-F1 to investigate the fatigue resistance of the sample under the maximum target load. The cyclic load diagram of sample S1-F1 is shown in Figure 4.17. It can be seen that, as was expected, the sample has failed prematurely at the 18th cycle. Although the load controller was adjusted to apply a cyclic load between 15 and 137 kN, it can be seen that the sample sustained maximum loads just below 100 kN. This issue is attributed to the fact that the sample has started failing under the cyclic loads with progressively increasing deflections after each cycle, as shown in Figure 4.18. Thus, the loading machine was only able to attain the maximum load of around 100 kN instead of the maximum target load of 137 kN. The maximum deflection in the first cycle is around 0.9 mm, rising to around 1.6 mm by the 17th cycle, while in the 18th cycle, the beam collapsed.

Figure 4.19 shows the surface strain magnitudes at the mid-span of sample S1-F1 obtained from the four LVDT gauges. The precise locations of these LVDT gauges can be seen in Figure 4.10. Overall, the gradual increase in the strain magnitudes and in residual strains through the cycles are observed. The maximum tensile strain close to the bottom fibre of the sample, captured by "LVDT 1" in the first cycle, is around 0.0038. This strain magnitude is significantly higher than the flexural cracking strain of a concrete beam under tension, which is around 0.0002. Hence, it is found that the beam incurred flexural tensile cracking at the first load cycle, which is in good agreement with the visual inspection outcome, as shown in Figure 4.20. The magnitude of the maximum flexural tensile strain at the mid-span of the sample has significantly risen from 0.0038 in the first cycle to 0.0093 in the 17th cycle. On the other hand, the maximum compressive strain close to the top fibre of the sample, recorded by "LVDT 4", increases from 0.0022 to 0.0077. The high compressive strain of 0.0077 is around two times the crushing strain of concrete under compression (0.003-0.0035). This result shows that the crushing of concrete under compression has occurred under the cyclic loading, as well as the tensile failure, which is not normal. Indeed, since the prototype sample is under-reinforced (it has no longitudinal reinforcements), concrete crushing in compression was not expected to occur.

104

Figure 4.20 shows the pattern of the cracks after 10 load cycles. The cracks after the first cycle are marked with "S". It is observed that only one crack appeared during the first load cycle, followed by further propagations until the 10th cycle. Figure 4.21 shows the ultimate failure of the prototype sample under the cyclic load (at the 18th cycle). It can be seen that the single initial crack has propagated and eventually resulted in the ultimate failure of the sample.

In general, it is found that the performance of sleeper sample S1-F1 is unacceptable as the sample is expected to resist far more load cycles to be approved in terms of fatigue strength. The weak performance of the sleeper sample S1-F1 is attributed to the poor mixing quality of Batch 1 of the UHP-FRC mix from which the prototype sample was made. This result was expected, as the first sample from this batch, S1-S1, has also failed to satisfy the requirements under the standard rail-seat static loading (refer to Section 4.3.1).

The important lesson learned from the static and cyclic test results obtained from the samples of the first batch, S1-S1 and S1-F1, respectively, is the great sensitivity of the UHP-FRC mix to the quality of mixing. Moreover, it is found through the mixing of the second UHP-FRC batch that the issue of the mixing quality can be simply prevented by precisely following the steps mentioned in Chapter 3. It should also be noted that the capacity of the mixer (in terms of mix volume) should be at least two times the final UHP-FRC mix to avoid losing the dry components, cement, silica fume, and sand, during the dry mixing. Indeed, these dry components have a large volume before the addition of the liquid components (water and superplasticizer).
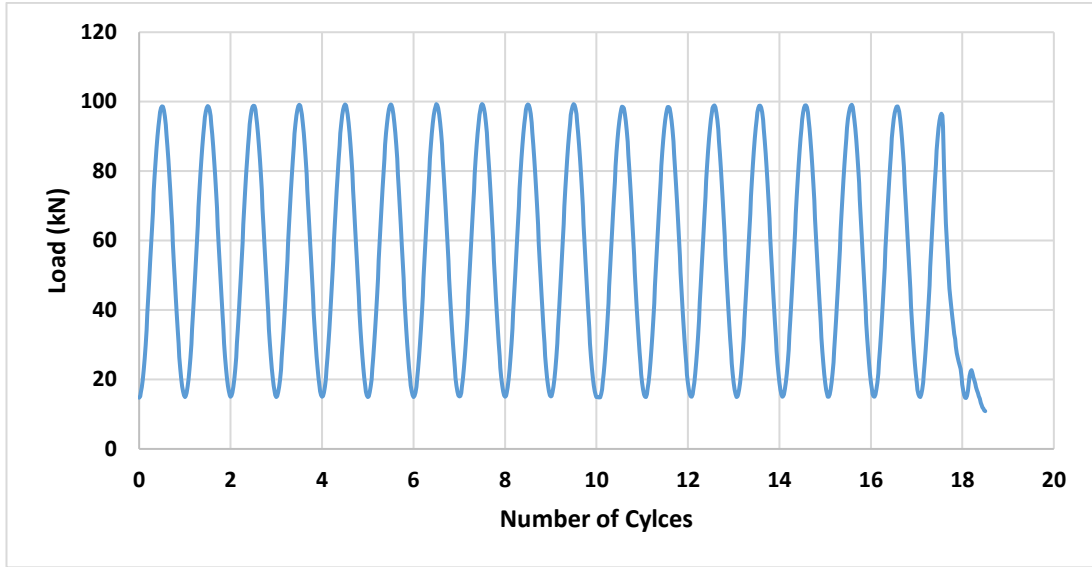
Figure 4.17 Cyclic rail-seat load pattern of sample S1-F1
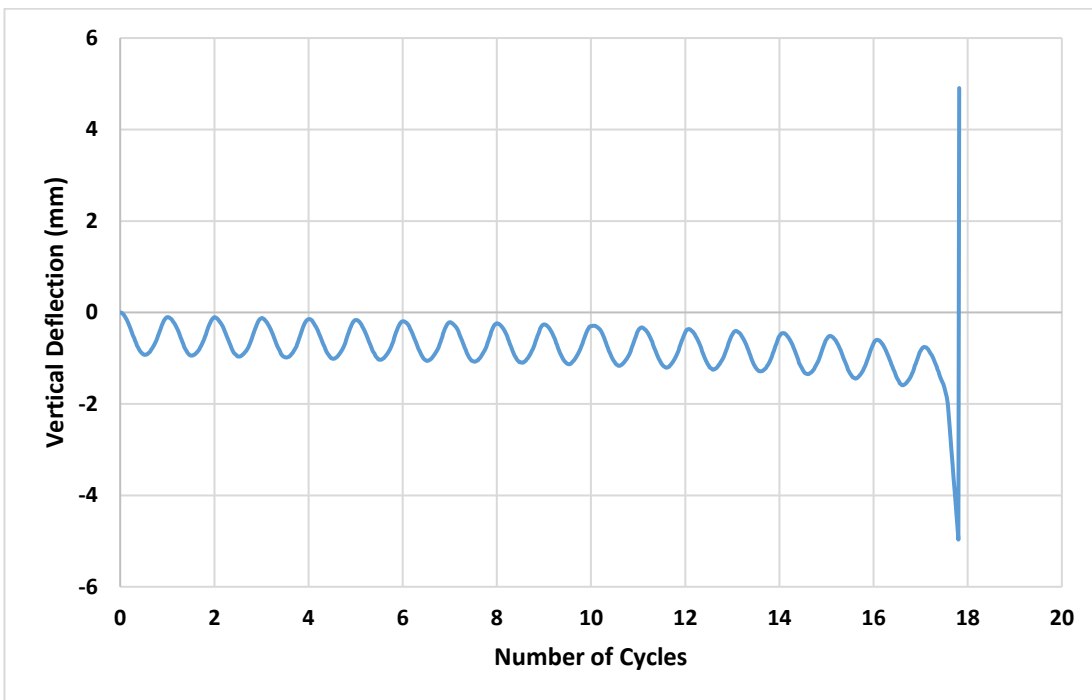
Figure 4.18 Relative vertical deflection at the mid-span of Sample S1-F1
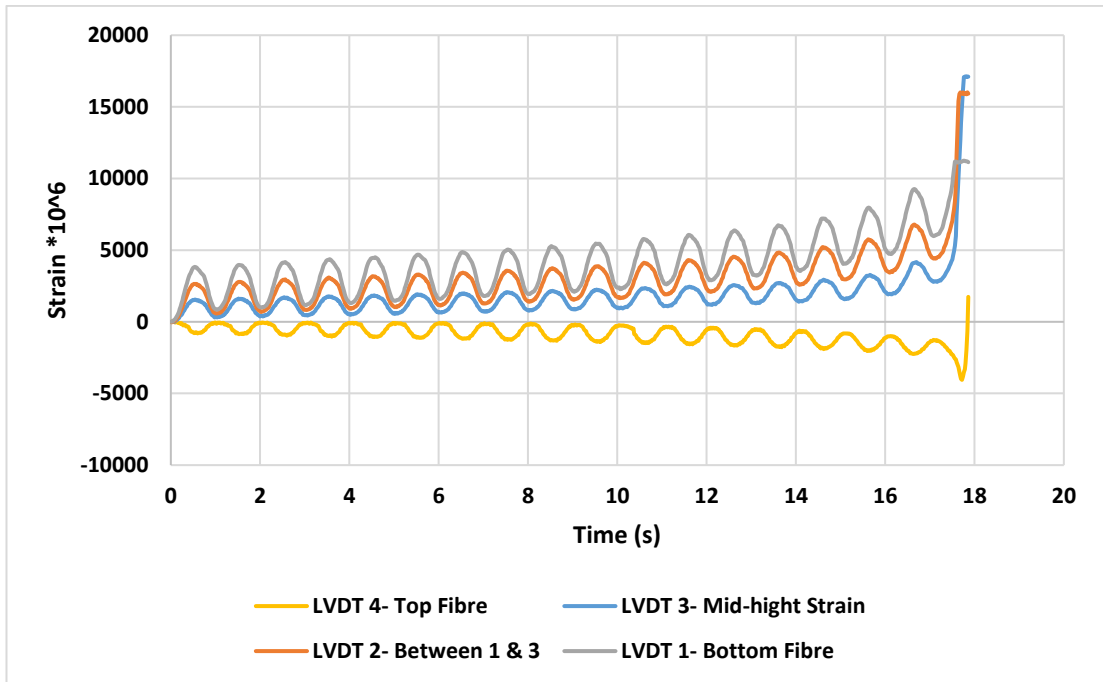
Figure 4.19 Relative surface strains at the mid-span of sample S1-F1

Figure 4.20 The cracking pattern of sample S1-F1 after 10 Cycles
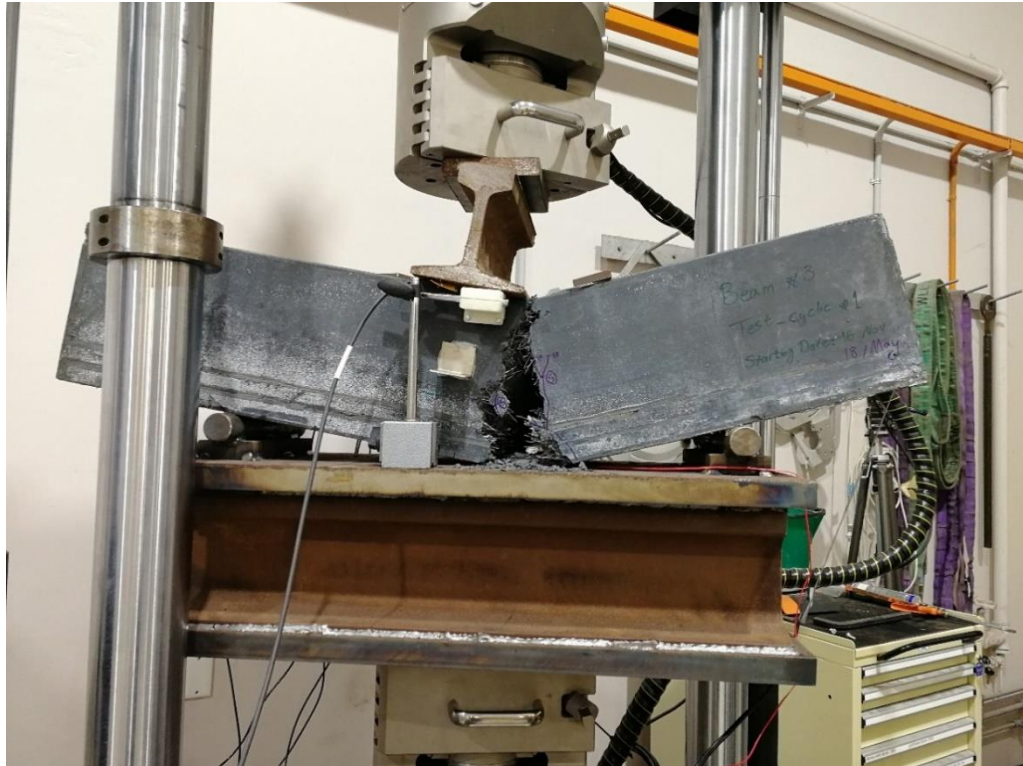
Figure 4.21 The ultimate failure of sample S1-F1 at the 18th load cycle

4.4.3 Test Results of the Prototype Sample S2-F2

Figure 4.22 shows the fatigue test set-up of the second prototype non-prestressed UHP-FRC sleeper sample, S2-F2. It can be seen that the laser deflection sensor is now mounted on the rear side. Hence, the front side is completely clear and painted in white for observing and marking the cracks and tracking their propagations during the fatigue testing.
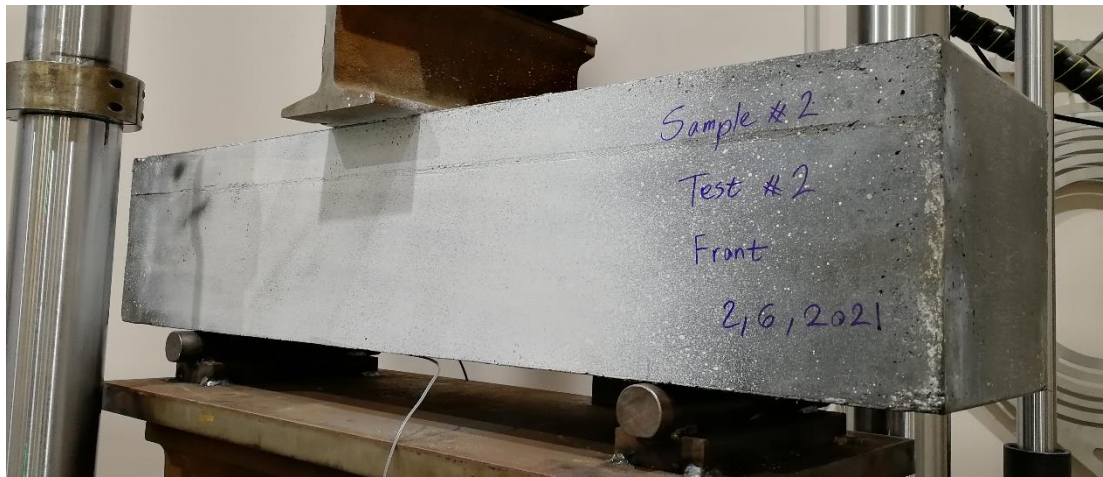
(a) front side

(b) rear side

Figure 4.22 The set-up for the fatigue testing of the UHP-FRC sample S2-F2

The cyclic load for sample S2-F2 has been applied at three different levels (load ranges), as summarised in Table 4.3. The first load level, 15 to 30 (kN), is for the observation of the elastic cyclic performance of the sample. The second cyclic load range is between 15 kN and 60% of the target load (0.6 * 137 kN = 82 kN). Field measurements have revealed that the wheel loads in Australian rail tracks rarely exceed 70-80 kN (Nairn and Stevens, 2010). The third load range is between 15 kN and the target design load, 137 kN (refer to Equation 4.5), to consider the less frequent cyclic loads of higher magnitudes. The latter load range continues until the total cycle number of 196,877, at which the complete failure of sample S2-F2 occurred. The frequency of the cyclic loading is retained within the range of 1 to 3 Hz.

Table 4.3 Cyclic load plan of the prototype sample S2-F2

Level No.	Minimum load	Maximum load	No of Cycles	From Cycle	To Cycle
Level 1		30 kN	1000	1	1000
Level 2	15 kN	82 kN	100,000	1001	101000
Level 3		137 kN	96,877	101001	197887

Figure 4.23 shows the growth of the maximum and minimum magnitudes of vertical deflections at the mid-span of sample S2-F2 during the cyclic loading. Also, Figure 4.24 shows the maximum and minimum magnitudes of horizontal deformations recorded by LVDT 1. Indeed, LVDT 1 captures the horizontal deformations within a gauge distance of 200 mm at the bottom mid-span of the sample (as shown in Figure 4.10). In other words, LVDT 1 records the total sum of the crack widths of the prototype sample during the cyclic loading.

As can be seen in Figure 4.23, the maximum and minimum vertical deflections of S2-F2 are marginal in the first 1000 cycles (under the first cyclic load level). This is due to the fact that the sample is in the elastic zone with no cracks during the first 1000 cycles, which is in good agreement with Figure 4.24. However, at the beginning of the second cyclic load level (15 kN to 82 kN), a significant jump occurs in the magnitudes of both the maximum and minimum vertical deflections due to cracking. The jump at the initiation of the second cyclic load level is also observed in Figure 4.24, which shows the total maximum crack width of 0.12 mm at the cycle number of 1001. Subsequently, the mid-span vertical deflection and total crack width increase steadily at marginal slopes until the end of the second cyclic load level, where the maximum crack width reaches 0.47 mm by the 100.000th cycle. Afterwards, the second jump occurs in both the vertical deflections and the crack widths at the initiation of the third load level (15 kN to 137 kN), where the maximum total crack width climbs to 0.96 mm. Then, after a short period of stabilization (for about 10,000 cycles), both the vertical deflections and the total crack width start growing rapidly until the ultimate failure of the sample by the total cycle number of 197,877, where the sample falls down under the cyclic load.
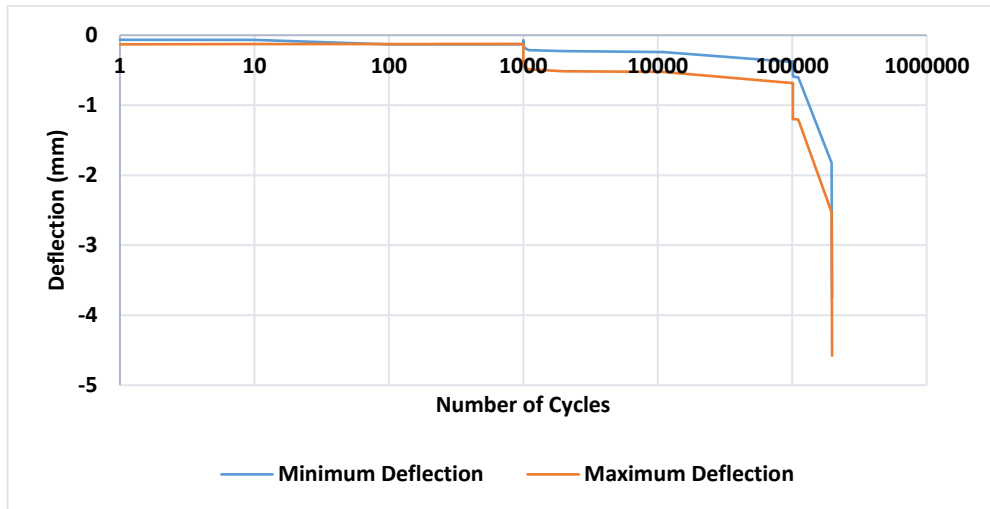
Figure 4.23 Deflection versus the number of cycles for sample S2-F2
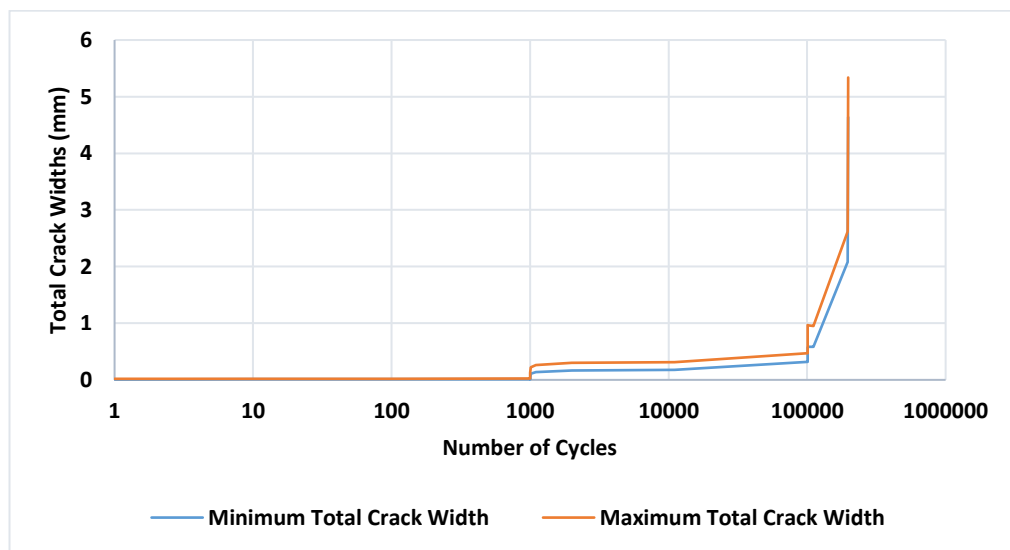
Figure 4.24 Total crack growth (obtained from "LVDT 1") versus the number of cycles for sample S2-F2

The jump between the first and the second cyclic load levels (after 1000 cycles) and between the second and third load levels (after 100,000 cycles) can be observed in the surface strain magnitudes at different mid-span section heights of S2-F2, as shown in Figure 4.25. The surface strain magnitudes are obtained from the horizontal deflections recorded by the four LVDT gauges divided by their gauge distance (200 mm). As expected, the tensile strain's magnitude at the bottom of S2-F2 (recorded by "LVDT

1") reaches 0.00011 by the end of the first cyclic load level, i.e., the 1000th cycle, which is below the tensile cracking strain of concrete. Then, at the first cycle of the second load level (cycle number of 1001), this strain magnitude jumps to 0.00062, indicating cracking at the beginning of the second load level (15 kN to 82 kN). On the other hand, the extent of the maximum compressive strain, recoded by "LVDT 4" at the last cycle (ultimate failure of S2-F2), reaches 0.001, which is below the crushing strain of concrete in compression (0.003-0.0035). Hence, it is concluded that the concrete crushing in compression does not occur at the failure of the prototype UHP-FRC sample under fatigue loading. Merely the material failure in tension is the mode of failure that agrees with the drastic jumps in the values of tensile strains recorded by the LVDT gauges 1 to 3, as shown in Figure 4.25.
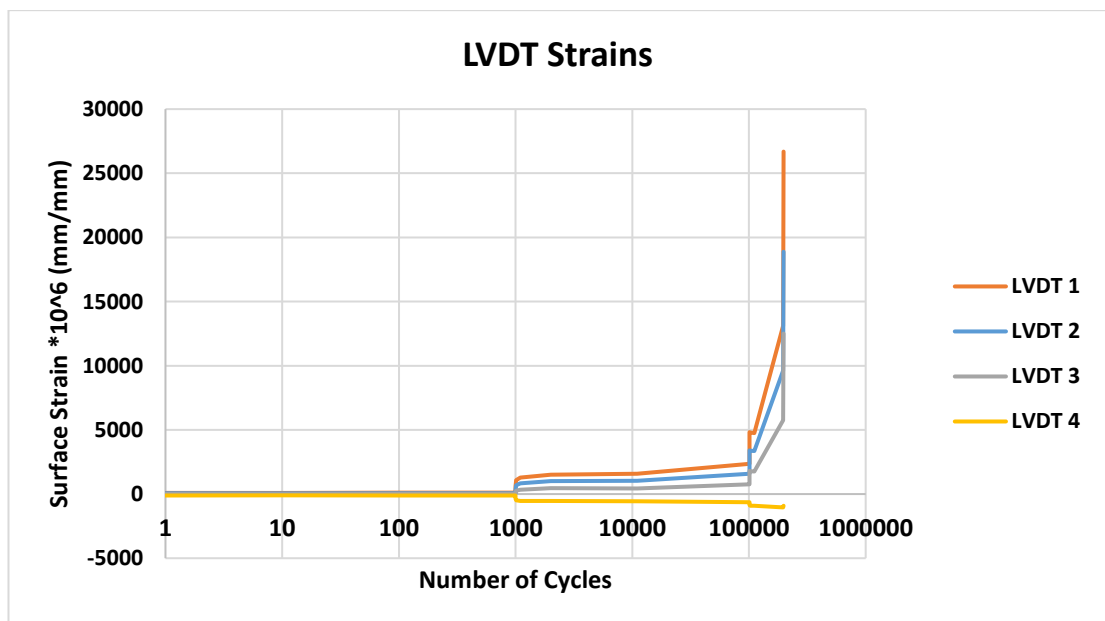
Figure 4.25 Surface strains versus the number of cycles for sample S2-F2

Figure 4.26 compares the maximum magnitudes of surface strains over the height of the prototype sample, S2-F2, at selected load cycles. The differences in the strain magnitudes from the cycle number 1000 to 1001 (from load level 1 to 2) and from 101,000 to 101,001 (from load level 2 to 3), can be seen in Figure 4.26. It can also be observed that the values of strains vary over the height of the prototype UHP-FRC sample nearly in a linear manner, even at the last load cycle.

112
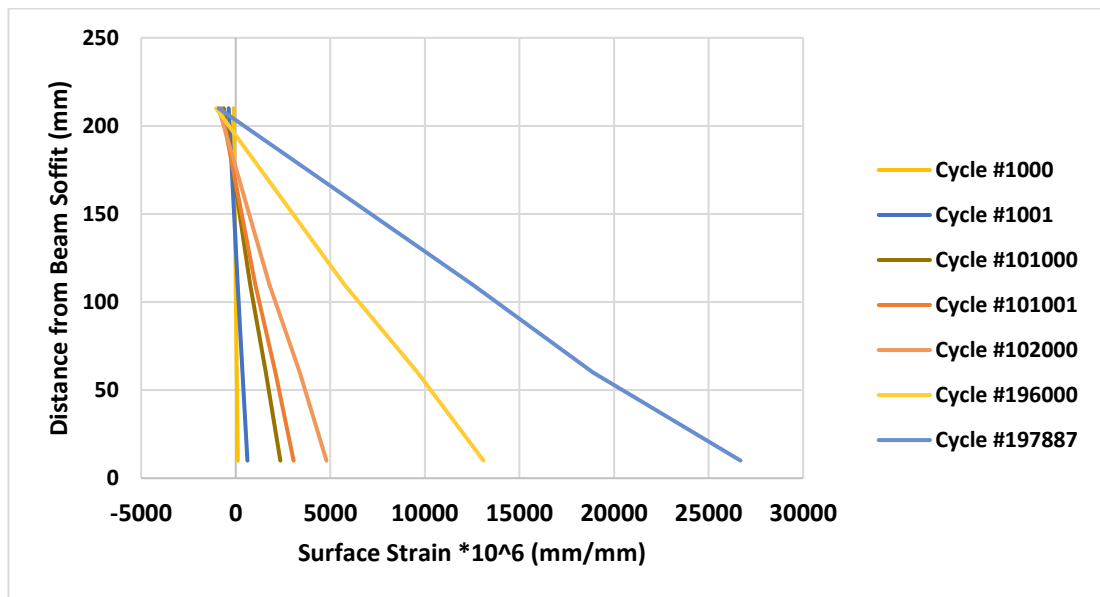
Figure 4.26 Growth of the surface strain over the height of sample S2-F2

Figure 4.27 shows the cracking pattern of S2-F2 under cyclic loading at the cycle number of 196,000 (before the ultimate failure). The blue marks show the crack propagation occurred during the second cyclic load level (15 kN to 82 kN) and the red marks show the crack propagation during the third load level (15 kN to 137 kN). It is found that after the first 1000 load cycles (15 kN to 30 kN), no cracks appear on S2-F2, which is in good agreement with the diagrams of deflection, total crack width and strain versus cycle number shown in Figure 4.23, Figure 4.24, and Figure 4.25, respectively. It can also be seen that the cracks do not experience further propagations after 1000 cycles of load level 3 (the total cycle number of 101,000), while the whole width of the cracks and the surface strains (measured by the LVDT gauges) continued increasing. Furthermore, it is observed that all the cracks are concentrated under the rail, with the deepest one under the centre line of the rail. As shown in Figure 4.27, at the ultimate failure of the non-prestressed prototype UHP-FRC sleeper sample, S2-F2, this middle crack widens rapidly until the sample becomes unstable. It is observed that (as it was also found through the analysis of the strain diagrams, shown in Figure 4.25) the UHP-FRC sample fails in tension while no crushing under compression is observed at the top mid-span area of the sample.
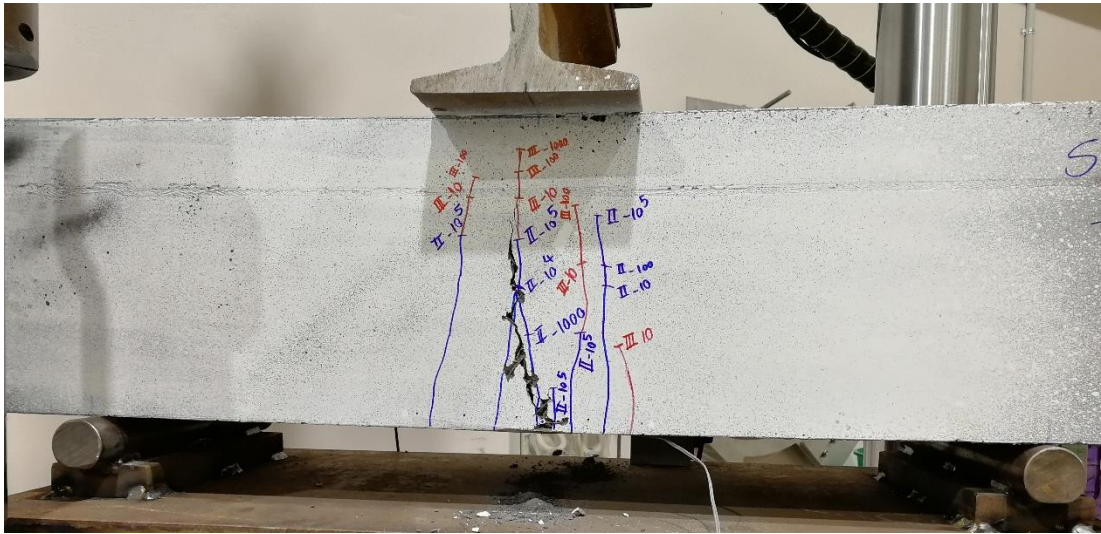
Figure 4.27 Crack pattern of sample S2-F2

Figure 4.28 Ultimate failure of sample S2-F2

4.5 Discussion of the Results and Conclusions

In this chapter, the behaviour of the prototype non-prestressed UHP-FRC sleeper samples under static and cyclic loads was investigated. For this purpose, four prototype sleeper samples were produced from two batches of the UHP-FRC mix (developed in Chapter 3), prepared with a mobile 300-litre pan mixer. One sample from batch 1 and one from batch 2 were selected for the standard rail-seat positive moment testing (static

testing) according to the Australian Standard (AS1085.14, 2019). The remaining two samples were used for the rail-seat fatigue testing, as shown in Table 4.4.

Both samples from the first batch, i.e. S1-S1 and S1-F1, showed unacceptable performance under the standard rail-seat positive moment and the cyclic rail-seat tests, respectively, as reported in Table 4.4. This undesirable performance is attributed to the problems during the mixing process of the first batch of the UHP-FRC mix, as the mixer paddles stopped working several times during the mixing process. Hence, it should be noted that UHP-FRC is considerably sensitive to the quality of the mixing process, which must be taken into account, especially in the case of preparing greater quantities of UHP-FRC mixes.

Table 4.4 General performance of the prototype UHP-FRC sleeper samples under static and fatigue testing

Sample name	Batch No.	Test type and number	Performance
S1-S1	Batch 1	Static Test #1	Failed
S1-F1		Fatigue Test #1	Failed
S2-S2	Batch 2	Static Test #2	Passed
S2-F2		Fatigue Test #2	Promising

In contrast to the samples made from the first batch of the UHP-FRC mix, the samples made from the second batch (that was mixed carefully), S2-S2 and S2-F2, showed significantly improved performances under static and fatigue (cyclic) loads, respectively, as reported in Table 4.4. The main results obtained from these two samples are as follows:

- The prototype non-prestressed UHP-FRC sample, S2-S2, passed the standard rail-seat positive moment test (static test). Based on the visual inspection during the testing and the load-deflection diagram, the first crack occurred under 189 kN. This cracking load is higher than the minimum required load to produce the required

rail seat positive moment in accordance with the Australian Standard (AS1085.14, 2019), i.e. 161 kN, and therefore the UHP-FRC sample has passed the tests.

- The analysis of the Load-strain curves showed that at the maximum load, the compressive strain is 0.00044, which is below the concrete crushing strain. Hence, concrete crashing does not occur at the peak load. Even after the peak load (in the post-failure zone), the compressive strain reached 0.001 until the loading stopped, which is around one-third of the concrete crushing strain.

- Sample S2-F2 proved elastic under the cyclic load level 1. However, it showed a jump by the first cycle of the second cyclic load level (15 kN to 82 kN) in the deflection and strain magnitudes. The second jump in the deflection and surface strain magnitudes was observed at the third cyclic load level (15 kN to 137 kN). Eventually, the prototype sample experienced the ultimate failure after 97,877 cycles under the third load level (the total of 197,877 cycles).

- The study of the strain curves showed that the compressive strain at the top of S2-F2 at the last (ultimate failure) cycle was around 0.0001, proving that the sample did not incur the concrete crushing in compression at the ultimate failure. Hence, as was expected, the sample's compressive strength does not dominate the ultimate fatigue resistance of the non-prestressed prototype UHP-FRC sample. However, the tensile strains at the bottom of the cross-section showed that S2-F2 experienced flexural tensile cracking at the first cycle of the second load level when the strains increased from 0.00011 to 0.00062.

In the end, it is important to note that the fatigue strength of the non-prestressed UHP-FRC sample is promising but not satisfactory. Railway sleepers are expected to resist a few million rail load cycles within their service life. For example, according to the Australian Standard (AS1085.14, 2019), prestressed concrete sleepers must resist three million load cycles to be approved. As it was explained in Section 4.4, the test set-up developed for the fatigue (cyclic) testing in this research is slightly different from the one recommended by the Australian Standard. However, the fatigue strength of the non-prestressed UHP-FRC sleeper samples needs further improvements in future studies.

It should be noted that there are comprehensive investigations on the fatigue performance of prestressed thin-web UHP-FRC beams without stirrups (e.g. (Fang

et al., 2020, Hu et al., 2021)). In such research projects, the focus has been mostly dedicated to the shear failure of the thin-web beams under fatigue loads when stirrups are not utilised. Thus, further investigations are needed to acquire a better understanding of the non-prestressed UHP-FRC sleeper samples under fatigue loading and to improve the performance of the samples.

A solution to mitigate the fatigue failure in the proposed non-prestressed UHP-FRC sleeper samples can be the application of these sleepers in rail tracks with lighter wheel loads and/or lighter train traffics. For example, as described in Section 4.4.3, the prototype sleeper F2-F2 did not show signs of failure under the second fatigue load level, i.e. 15-82 kN, which is equivalent to 15 tonne axle load. Another potential solution to improve the fatigue resistance of non-prestressed UHP-FRC sleepers would be the application of longitudinal reinforcements. As a trial, in Chapter 6, the influence of GFRP longitudinal reinforcing bars in improving the cracking and the ultimate strength of the non-prestressed UHP-FRC prototype samples under static rail-seat loading is investigated.

CHAPTER 5

IMPACT RESISTANCE OF NON-PRESTRESSED UHP-FRC SLEEPERS

5.1 Introduction

High-frequency dynamic loads that are well-known as impact loads are of large magnitudes and short durations and occur so infrequently during the service life of a concrete sleeper. This type of load normally occurs due to the abnormalities of rails, wheels, or rail track, such as wheel flat, bad welds, etc. In this chapter, to better understand the performance of the developed non-prestressed UHP-FRC sleepers under impact loads in a rail track system, impact testing is performed for the UHP-FRC prototype samples on different types of ballasted foundations. Varying magnitudes of impact loads and three different types of ballasted tracks, very hard, hard, and very soft tracks (with track modulus magnitudes of around 200 MPa, 150 MPa, and 2.0 MPa, respectively), are considered in this experimental study. A drop hammer machine at the University of Wollongong with high loading capacity has been used for applying the impact loads of desired magnitudes and duration (Remennikov and Kaewunruen, 2014b). Only one rail-seat area is simulated and tested in this study.

First, two UHP-FRC prototype sleeper samples without the fastening systems are tested on a very hard ballasted track. Subsequently, four prototype UHP-FRC samples with the cast-in shoulders for anchoring the rail-sleeper fastening systems are manufactured for further impact testing. Two samples are tested on a hard railway track foundation. The other two are tested on a very soft one to investigate the influence of different track conditions on the impact performance of the non-prestressed UHP-FRC sleepers.

5.2 Impact Test Set-up

5.2.1 Drop Hammer Machine

Figure 5.1 shows the drop-hammer impact testing machine built at the structural lab of the University of Wollongong (UOW). The drop hammer machine produces impact loads by dropping a hammer (impactor) from a prescribed height. The mass of the hammer is constant and equal to 600 kg, while the height is adjustable, with the maximum available drop height of 5.5 m. Hence, the drop height must be adjusted accordingly to adjust the impact load. The drop hammer machine has high efficiency with only a 2% loss of the total energy due to the friction of the running guides (Kaewunruen and Remennikov, 2009c).

Figure 5.1 The drop-hammer impact testing machine at the University of Wollongong

5.2.2 Impact Test Set-up

The impact test set-up developed in this research is illustrated in Figure 5.2. As can be seen in Figure 5.2, the prototype non-prestressed UHP-FRC samples have identical sections to the prototype samples tested in Chapter 4, i.e. 250 mm x 220 mm (width x height). The length of the prototype sample is selected as 700 mm to investigate the performance of the prototype sample over an effective area around the rail-seat section.

On each side of the prototype sample (front and rear side), two strain gauges are attached at the centre of the sample, on the top and bottom, with 10 mm distance from the top and bottom faces, respectively, as can be seen in Figure 5.2. It is important to note that the strain gauges are only helpful in the initial drops and, after that, will fail. However, they give valuable information about the elastic performance of the prototype UHP-FRC samples under the initial impact loads (it will be explained in Section 5.3 and Section 5.4 that in this research, the impact tests start with minor initial impact loads). It can also be seen that a number of dots are marked on one side of the prototype sample. A high-speed camera with a recording speed of 2000 frames per second is used to record the dynamic response of the sleeper samples during each drop. By analysing the frame sequences, the changes in the location of the samples and thereby the deflection of the system can be monitored over time. On the other hand, the applied impact load is recorded using a load cell installed underneath the dropping hammer with a maximum capacity of 1600 kN.
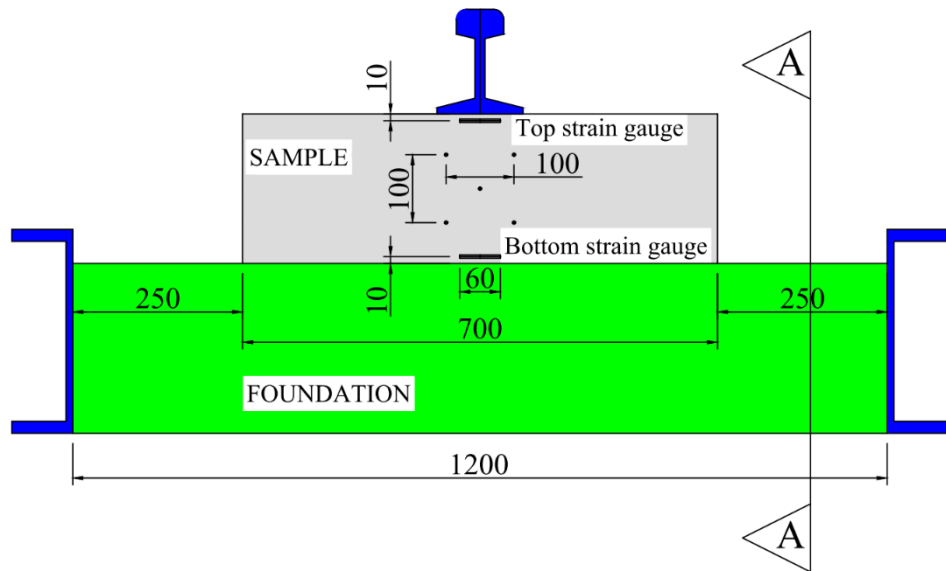
(a) side view
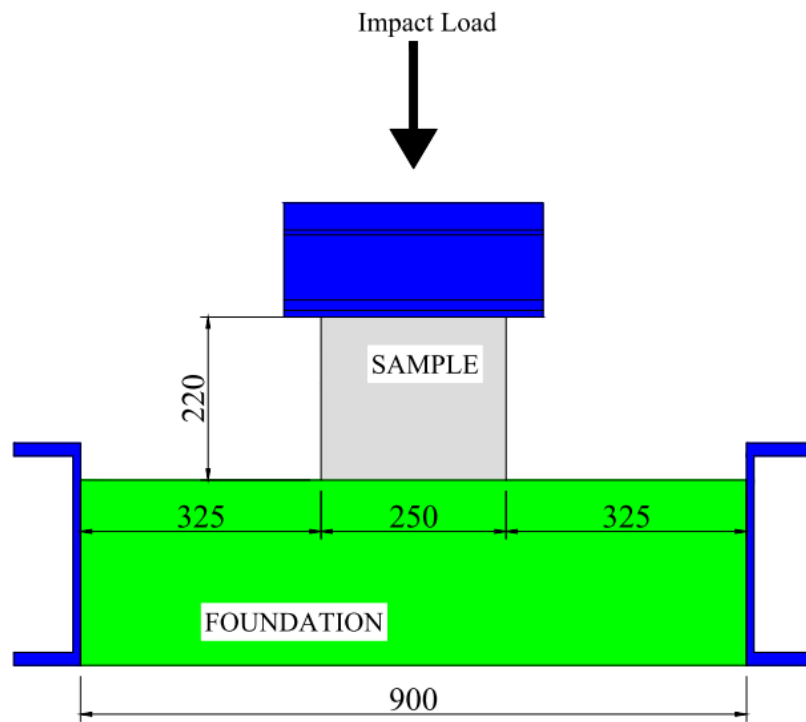
(b) section view (section A-A)

Figure 5.2 Details of the impact testing set-up installed on the strong concrete floor

The impact load is applied to the sample through a 60 kg/m rail segment to make the loading method realistic. It should be noted that the duration of the impact wheel loads in ballasted tracks due to the wheel/rail abnormalities is normally within 5-10 ms

(milliseconds). However, the impact load applied from the impact test rig to the railhead due to the 600-kg falling weight is considerably shorter than the real impact wheel loads (1-2 ms) (Kaewunruen and Remennikov, 2009c, Remennikov and Kaewunruen, 2014b). Hence, according to the literature (Kaewunruen and Remennikov, 2009c, Kaewunruen and Remennikov, 2010), to increase the duration of the impact load and protect the impact load-cell, a 3-mm rubber sheet is placed on top of the railhead before applying the impact loads. It is also seen that the prototype sample rests on a foundation. Three foundation configurations considered in this study are explained in the following section. To simulate the hard ballasted track foundation, a steel box with an area of 1200 mm x 900 mm is used to confine the gravel particles.

5.2.3 Production of UHP-FRC Samples for Impact Testing

In this chapter, three pairs of samples are cast with 3 batches of UHP-FRC mix. Each of these batches are prepared to cast two prototype samples for impact testing plus three compression and three flexural material samples. The mass per unit volume, compressive strength, and flexural strength (modulus of rupture) magnitudes are determined in accordance with the Australian Standards (AS-1012.9, 1999, AS-1012.11, 2000, AS-1012.12.1, 2014), as explained in Chapters 3 and 4. The mechanical properties of these samples are shown in Table 5.1. As can be seen, batch 2 is slightly stronger than the other two batches. However, the mechanical characteristics of the three batches are adequately close to each other.

Table 5.1 Mechanical characteristics of the UHP-FRC batches for making the impact test prototype samples

Results	Mass per unit volume (kg/m^3)	Compressive Strength (MPa)	Modulus of Rupture (MPa)
Batch 1	2349	115	18.6
Batch 2	2354	124	19.2
Batch 3	2365	119	20.1

The configurations of the six non-prestressed UHP-FRC prototype samples and their track foundations are presented in Table 5.2. As can be seen, the first pair of samples (which are preliminary impact test samples) do not have rail-sleeper fastenings, and the rail pieces are glued to the prototype samples. However, the other four samples are equipped with Pandrol fastening systems. Each prototype sample pair is tested on a specific track foundation configuration. These samples are named based on their batch number (B1, B2, or B3), track foundation configuration, i.e., Very Hard (VH), Hard (H), or Very Soft (VS), and their number (1 or 2). The track foundations, considered in this research, will be defined in Section 5.2.4. For example, samples B1-VH-1 & 2 are from the first batch with the very hard track type, whereas samples B3-VS-1 & 2 are from batch 3 with the very soft track type.

Table 5.2 Configurations of the samples and foundations

Sample Name	Batch No.	Rail Attachment	Track Type
B1-VH-1	Batch 1	Glued	Very Hard Track
B1-VH-2			
B2-H-1	Batch 2	Actual Fastening	Hard Track
B2-H-2			
B3-VS-1	Batch 3		Very Soft Track
B3-VS-2			

5.2.4 Configuration of the Track Foundations

The detailed configuration of the three track types, considered in this research study, i.e., Very Hard (VH), Hard (H) and Very Soft (VS), are shown in Figure 5.3. The very hard rail track foundation can simulate special cases such as the ballast on concrete slabs or on top of the deck of a railway bridge. On the other hand, the very soft track is expected to simulate extreme case scenarios where the rail-track foundation is highly damaged without maintenance measures, such as mud pumping. This research is based on an approximate estimation of the two case scenarios, while an extensive study may be needed in future research to determine the precise track modulus magnitudes of the extreme cases and simulate them in a more accurate manner for further experimental investigations.

It is observed that ballast particles are used for both the Very Hard (VH) and Hard (H) types of tracks. The VH type consists of 250 mm depth of ballast, while the H track type consists of 150 mm of ballast with a layer of stiff rubber belt (rubber belt 1). In contrast, the very soft (VS) track foundation consists of 6 layers of rubber belts (without ballast gravels). As shown in Figure 5.3, four types of rubber belts are used to simulate the very soft track configuration, i.e. rubber belts 1 to 4. All three types of track foundations lay on the strong concrete floor of the test rig (drop-hammer machine), which has a considerable depth of 1.5 m.
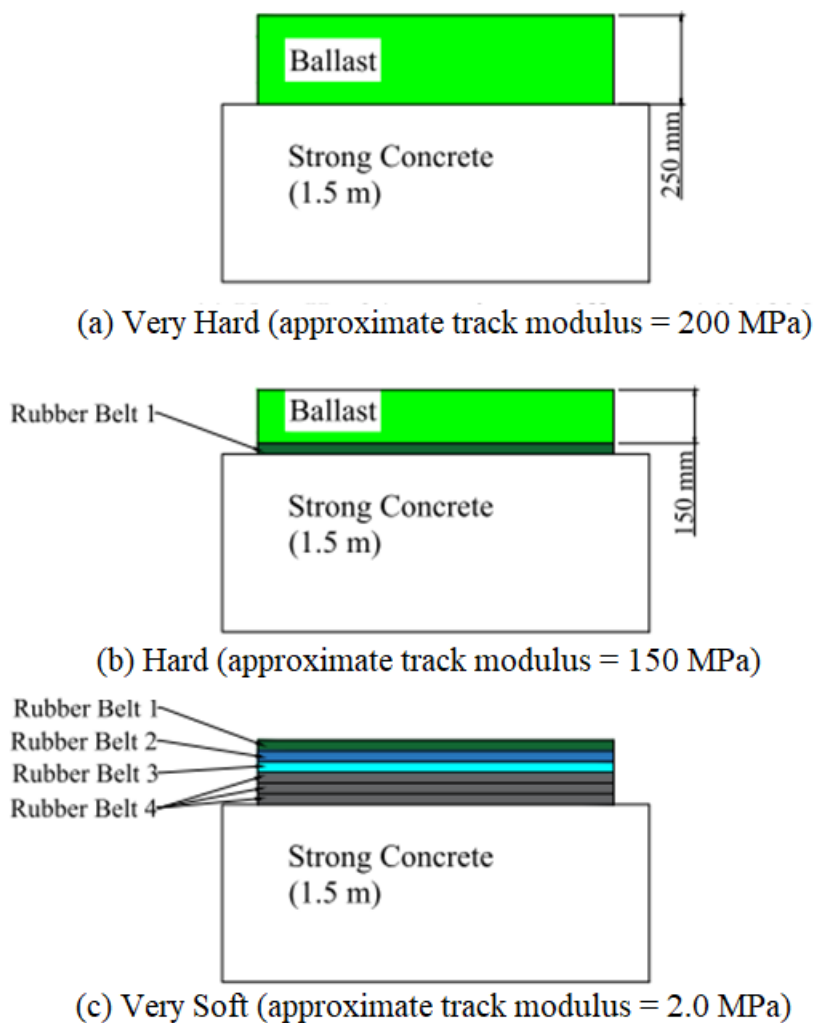
Figure 5.3 Detail configuration of the track foundations

In order to determine the mechanical characteristic of these rubber belts, square samples of 100 mm x 100 mm are cut from each of the rubber sheets using a water jet

cutting machine, as shown in Figure 5.4. The samples are marked as R.B.1 to 4, where R.B. is the abbreviation of "rubber belt" and the latter digit is the sample number (refer to Figure 5.3 for the location of these rubber belts in the simulated track foundations). Subsequently, these square rubber samples are tested under compression using a 350 kN Instron universal testing machine to find their elastic modulus magnitudes. Since these rubber belts are expected to remain elastic during the impact tests, their elastic modulus magnitudes are of the main interest. The compressive load is applied to the samples for a few cycles in a displacement-control manner with 1 mm/min speed, as shown in Figure 5.5. The magnitudes of elastic modulus are determined from the second load cycle, except for R.B.3, which exceeds the linear-elastic zone within the first cycle. Hence, the elastic modulus of sample R.B.3 is obtained from its first loading cycle. The properties of the rubber belt samples are presented in Table 5.3. Overall, it is observed that the rubber belts are ordered from the highest stiffness to the lowest stiffness. While the R.B.1 and R.B.2 samples have high stiffness values of 114.3 MPa and 98.42 MPa, respectively, R.B.4 has a low elastic modulus of 1.134 MPa.
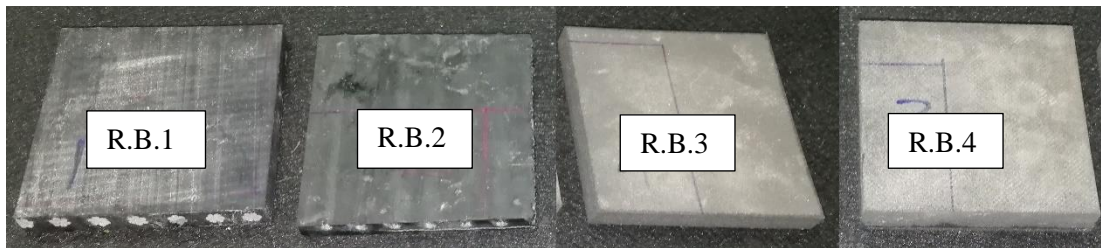
Figure 5.4 Samples of the rubber belts for material testing
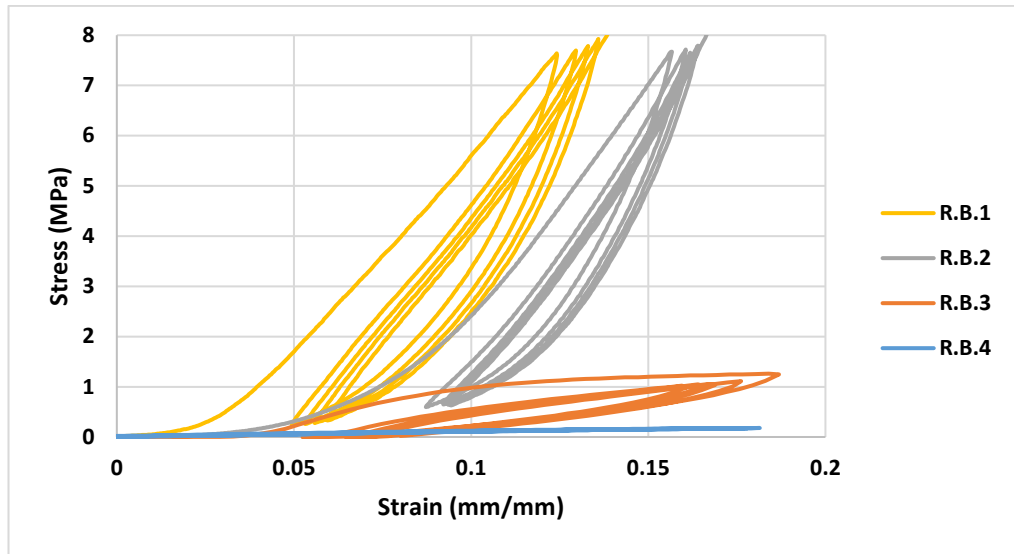
Figure 5.5 Compressive stress-strain curves of the rubber belt samples

Table 5.3 Properties of the rubber belts used in the track foundations

Sample name	Width (mm)	Length (mm)	Thickness (mm)	Weight (gr)	Mass per unit volume (kg/m3)	Elastic modulus (MPa)
R.B.1	99.96	99.41	12.49	267.1	2152	114.3
R.B.2	99.65	99.51	9.83	176.9	1815	98.42
R.B.3	98.94	99.2	11.31	45.7	412	20.63
R.B.4	99.68	98.88	18.29	73.2	406	1.134

5.2.5 Manufacturing Prototype Samples with the Rail-Sleeper Fastening System

As reported in Table 5.2, the two preliminary prototype UHP-FRC samples (B1-VH-1 and B1-VH-2) are tested under impact loads without the actual rail-sleeper fastening system. Indeed, a type of adhesive with elastic and shockproof performance, with the commercial name of "Selleys Liquid Nails Landscape" (SELLEYS, accessed on 27/12/2021) as shown in Figure 5.6, is applied to attach the rail to the preliminary prototype samples. Subsequently, a type of rail-sleeper fastening system with cast-in shoulders and e-clips, provided by Pandrol, Australia (Pandrol, accessed on 20/12/2021), is used for the remaining prototype samples B2-H-1, B2-H-2, B3-VS-1, and B3-VS-2. Different components of this type of fastening system are shown in

Figure 5.7. This type of e-Clip fastening system is suitable for the standard 60 kg/m rail profile and the 25 tonne axle load (TAL), the main axle load target in this research. The shoulders must be installed inside the moulds before pouring the UHP-FRC material, which requires cutting square holes at the bottom of the moulds at precise locations. The square holes are cut using a water jet cutting machine, and then the shoulders are installed at the holes. Subsequently, the corners are sealed with glue. The ready-to-cast moulds and the manufactured UHP-FRC sample are shown in Figure 5.8.
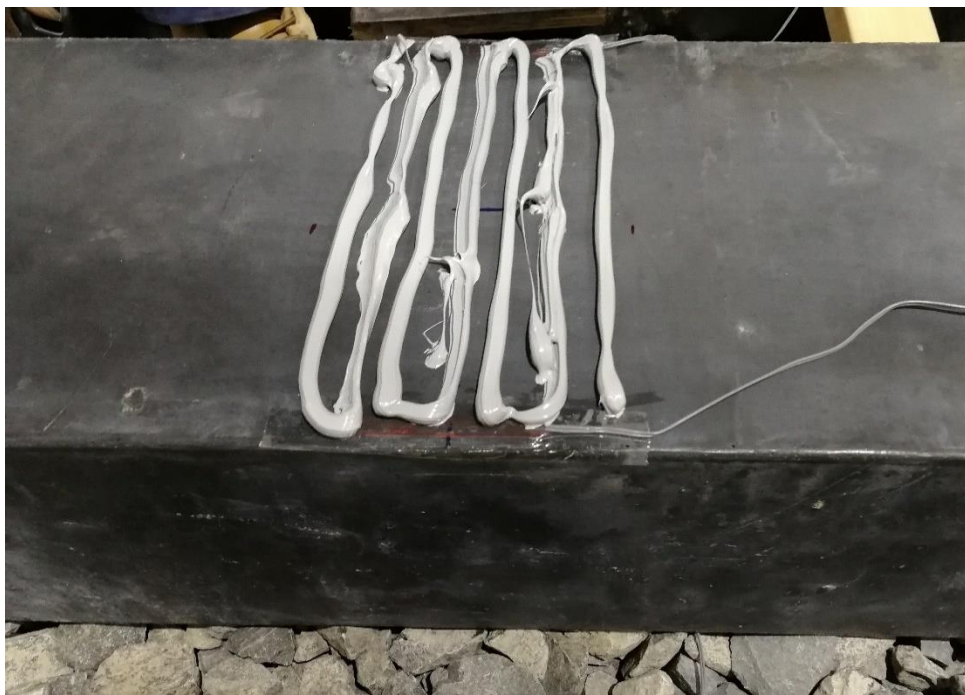
Figure 5.6 The elastic adhesive used to attach the rail piece to the preliminary prototype UHP-FRC sample
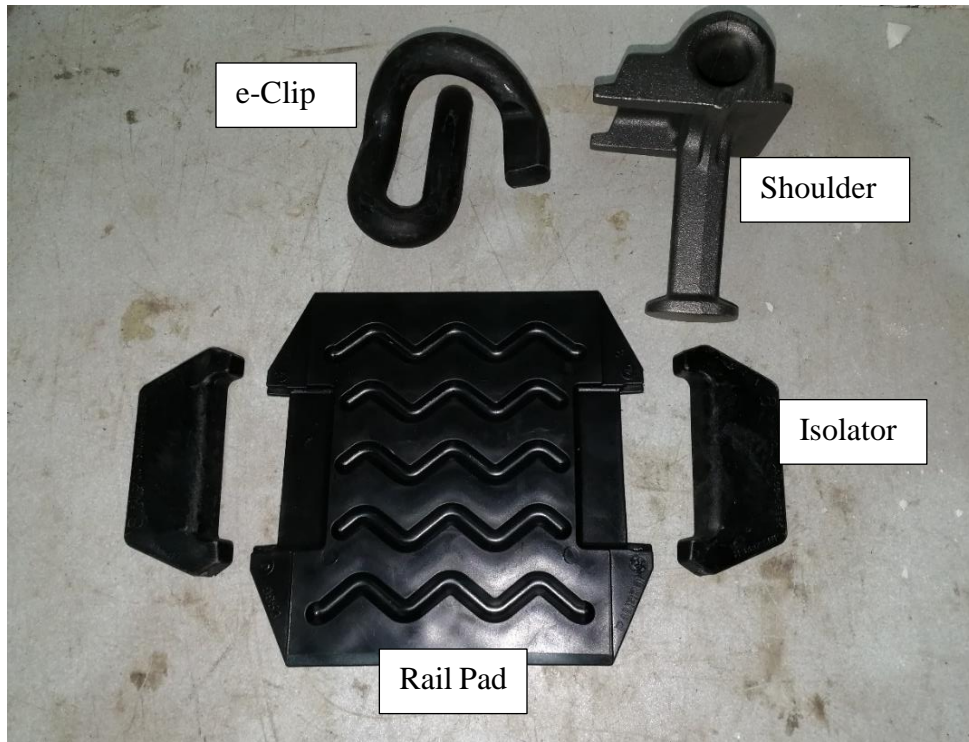
Figure 5.7 Different components of the Pandrol e-Clip fastening system

(a) moulds with shoulders   (b) the view of the final product

Figure 5.8 Production of the UHP-FRC prototype samples with actual rail-sleeper fastening system

5.3 Preliminary Impact Testing

Herein, the preliminary impact testing process and the important results are demonstrated. The main purpose of the preliminary tests is to have an overall understanding of the impact performance of the non-prestressed prototype UHP-FRC samples under impact loads. In the following, the impact testing of the two samples, B1-VH-1 and B1-VH-2, are described.

5.3.1 Impact Testing of Sample B1-VH-1

The test set-up of the first preliminary prototype UHP-FRC sample with the very hard track, i.e. B1-VH-1, is shown in Figure 5.9. As illustrated in Figure 5.3-a, the ballasted foundation has a depth of 250 mm. Four pieces of parallel flange channel profile PFC 300x90 are used to provide the confinement for the ballast. The main objectives of this test are to find the cracking impact load and the performance of B1-VH-1 under multiple impact loads, as well as the remaining strength of the sample after the cracks approach the compression zone of the sample.

As stated in section 5.2.2, on both the front and rear sides of the prototype sleeper sample, 60-mm electro-resistive strain gauges are attached to monitor the flexural compressive and tensile strains of the sample. These strain gauges are mainly used to monitor the occurrence of cracks and are expected to fail after the cracks initiate.

(a) front side

(b) rear side

Figure 5.9 The test set-up view of B1-VH-1

The load vs time curves of the impact loads applied to the prototype sleeper sample B1-VH-1 are shown in Figure 5.10. As can be seen in the figure, a total of eight drops (impact loads) are applied to the first preliminary prototype sleeper, B1-VH-1. The drop height increases gradually between 200 mm and 800 mm. The first three impact loads are of practically small heights, to monitor the elastic performance of the prototype sleeper sample and to assure the sample and foundation are set properly. Subsequently, the drop height is increased to 350 mm and then to 500 mm, until the crack is observed. Then, two more drops (impact loads) are applied with the same

height of 500 mm to observe the crack propagation. Then, the last drop is applied with a greater height of 800 mm, to assure the sample is fully cracked before performing the static rail-seat test to determine the remaining rail-seat moment capacity of the preliminary sleeper.

The first and second peak loads, called P1 and P2, respectively, are amongst the key results of the impact tests that represent the magnitudes of the impact loads. The first peak load (P1) is mainly related to the equivalent track mass and due to the inertial force generated at the contact area between the railhead and the impactor, while the second peak (P2) load is mainly related to the track stiffness. The second peak load is expected to represent the flexural strength of the sleeper (Kaewunruen, 2007), and therefore is more important in this study.

The first and the second peak loads, P1 and P2, obtained from the load vs time curves shown in Figure 5.10, are presented in Table 5.4. It can be found that except for Drop 1, which is the initial impact, P1 is always higher than P2. No cracks are observed by Drop 4, with a height of 350 mm and a P2 magnitude of 385 kN. However, at Drop 5, with the height and P2 magnitudes of 500 mm and 421 kN, three hairline cracks are observed on the front side and one minor crack on the rear side, as depicted in Figure 5.11-a. After that, during the 6th and 7th drops with the similar height of 500 mm, the cracks on the front side do not propagate considerably, while the only crack on the rear side propagates. Eventually, during the 8th drop, considerable crack propagations are observed on both sides, and cracks reach the top (compression) area of the sample, as depicted in Figure 5.11-b.

As shown in Figure 5.11, despite the considerable depths of the cracks, the sample does not show significant deformation after the 8th drop. Hence, it is expected that the sample has substantial remaining bending moment resistance. In order to determine the remaining strength of B1-VH-1, the static rail-seat testing is performed for this sample according to the Australian Standard (AS1085.14, 2019), as reported in Section 5.3.1.1.
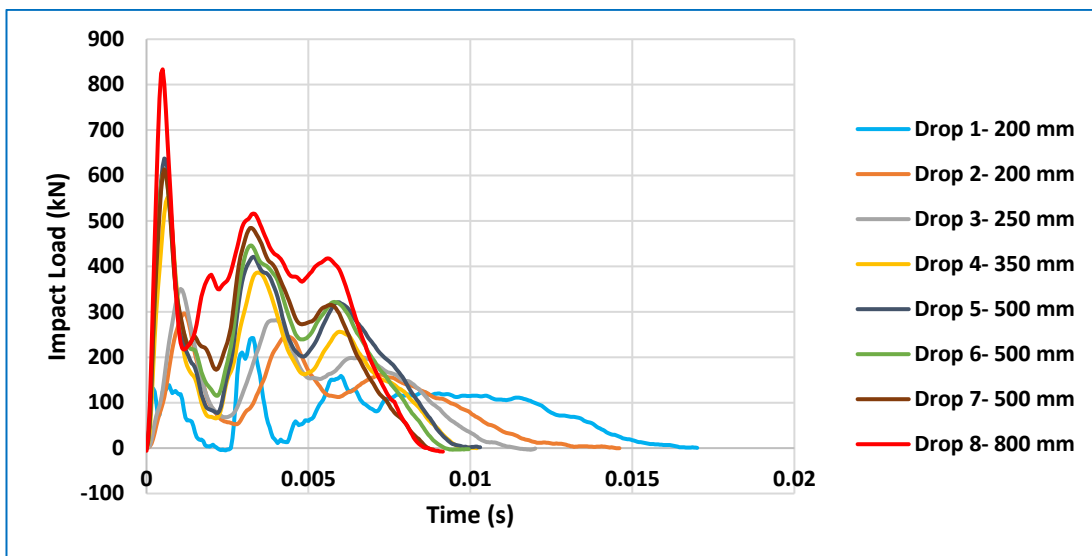
Figure 5.10 Load versus time duration of B1-VH-1

Table 5.4 The impact test summary of B1-VH-1

Drop No.	Drop height (mm)	P1 (kN)	P2 (kN)	Total Load Duration (ms)	Status
1	200	138	242	17	No cracks
2	200	297	246	15	No cracks
3	250	350	282	12	No cracks
4	350	552	385	10	No cracks
5	500	638	421	10	Bending cracks on the rear side and one minor crack on the front side
6	500	608	446	10	Cracks propagated slightly
7	500	614	484	9	Cracks propagated slightly
8	800	834	516	9	Bending cracks propagated toward the top (compression) area on both sides

(a) after Drop 5 (the first cracks)
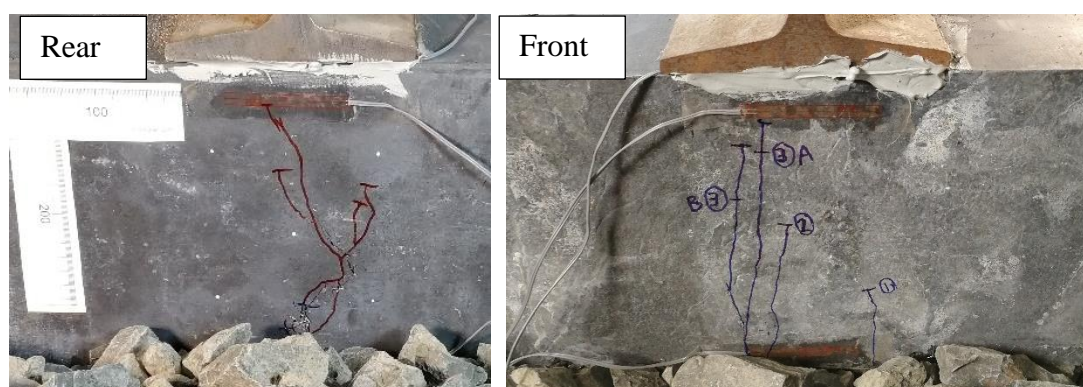
(b) after Drop 8 (the last drop)

Figure 5.11 Crack propagation of B1-VH-1 under impact loads

5.3.1.1 Remaining strength of B1-VH-1

Herein, the remaining strength of B1-VH-1 is determined by the standard rail-seat positive moment testing according to the Australian Standard (AS1085.14, 2019), as demonstrated in Section 4.3. As depicted in Figure 5.12, two LVDT gauges are used to measure the vertical deflections of the sample at the mid-span on both front and rear sides. Similarly, two horizontal LVDT gauges are used with a gauge distance of 200 mm to monitor the flexural tensile deformations of the bottom of the sample on both front and rear sides.

The static load-deflection diagram of B1-VH-1 is shown in Figure 5.13. For comparison with an undamaged UHP-FRC prototype sample, the load-deflection curve of the prototype sample, S2-S2 (reported in Section 4.3.1), is also included in Figure 5.13. It is observed that the load-deflection curves of B1-VH-1 with the deflections obtained from the front and rear sides of the sample match each other well.

(a) front face

(b) rear face

Figure 5.12 The rail-seat positive moment test set-up for determining the remaining strength
of B1-VH-1

Comparing the load-deflection curves of B1-VH-1 and S2-S2, it is found that S2-S2
(with no initial damage) has a steeper slope and thereby a higher stiffness and lower
deformations under the static rail-seat load, especially within its linear response part.

However, B1-VH-1, which has been cracked during the impact testing, reaches a relatively high peak load of 192 kN, which is 65% of the undamaged UHP-FRC prototype sample S2-S2 (with the peak load of 297 kN). In other words, the UHP-FRC sample can approximately retain around 65% of its initial strength while it is significantly cracked under impact loads.
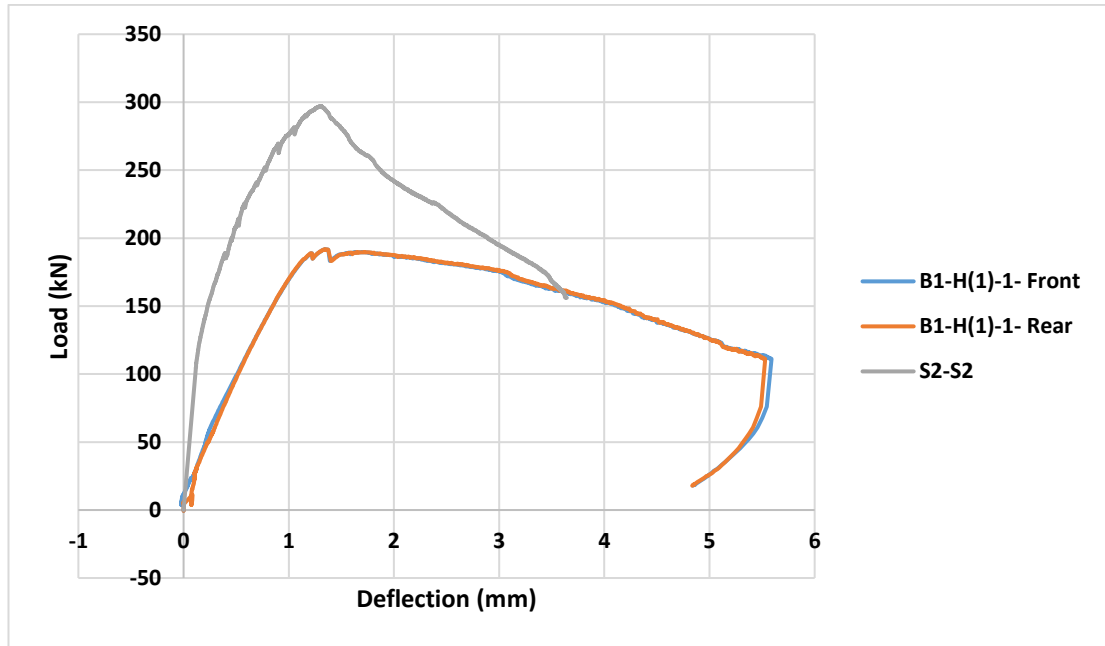
Figure 5.13 A comparison between the load-deflection diagram of B1-VH-1 and S2-S2

5.3.2 Impact Testing of Sample B1-VH-2

The main purpose of the second preliminary impact testing, B1-VH-2, is to understand the performance of the prototype non-prestressed UHP-FRC sample under extreme impact loads. Hence, the second preliminary UHP-FRC sample, B1-VH-2, which has the same configuration and track foundation configuration as the first preliminary sample (B1-VH-1), is tested under a few impact loads with larger magnitudes. The test set-up of sample B1-VH-2 is depicted in Figure 5.14. It can be seen that both the front and rear sides of the sample are painted in white to observe and mark the cracks more clearly.

(a) front side

(b) rear side

Figure 5.14 The test set-up view of B1-VH-2

A summary of the impact testing results of the second preliminary UHP-FRC sample, B1-VH-2, is presented in Table 5.5. Three drops are applied to the sample. The magnitudes of the peak loads, P1 and P2, and the load durations are determined from

the "load vs time" diagrams, shown in Figure 5.15. The first drop is of a moderate height of 400 mm, with the first (P1) and second (P2) peak impact loads of 462 kN and 378 kN, respectively. Two hairline cracks appear only on the rear side of the sample, while no cracks are found on the front side, as shown in Figure 5.16-a.

Subsequently, the second drop with the height of 2,500 mm, produces large peak loads of 784 kN (P1) and 422 kN (P2). As can be seen in Figure 5.16-b, during this impact load, one of the two cracks on the rear side (appeared during Drop 1) propagates toward the top (compression) zone of the sample. In addition, a cluster of cracks appears close to the propagated crack. On the other (front) side of the sample that had no cracks during Drop 1, two joint cracks appear, with one of them reaching the top area of the sample. Although the sample has several cracks, it is expected that the sample can sustain a higher impact load.

Eventually, the third impact load with the drop height of 3,000 mm, causes an extreme impact load with P1=1,358 kN and P2= 554 kN. Indeed, cracks significantly widen and reach the top of the sample such that the sample is almost departed at the centre, as shown in Figure 5.16-c.

It should be noted that as explained in Section 5.5, the latter P2 magnitude (554 kN) is suitable for railway tracks with limited traffic and train speeds, with return period of 100 years. Hence, it can be concluded from the second preliminary prototype sleeper test results that the UHP-FRC prototype sleepers have acceptable ultimate impact load resistance. In the next section, four prototype UHP-FRC sleepers with the actual fastening systems are produced for testing under impact loads with two different track foundation types to reach a better understanding of the prototype non-prestressed samples with more realistic configurations.

Table 5.5 The impact test summary of B1-VH-2

Drop No.	Drop height (mm)	P1 (kN)	P2 (kN)	Total Load Duration (ms)	Status
1	400	462	378	15	Two bending cracks on the rear side and no cracks on the front side
2	2,500	784	422	15	Several bending cracks on both sides reaching the top (compression) zone of the sample
3	3,000	1358	554	22	Ultimate failure of the sample as the cracks largely widen and reach the top face of the sample.
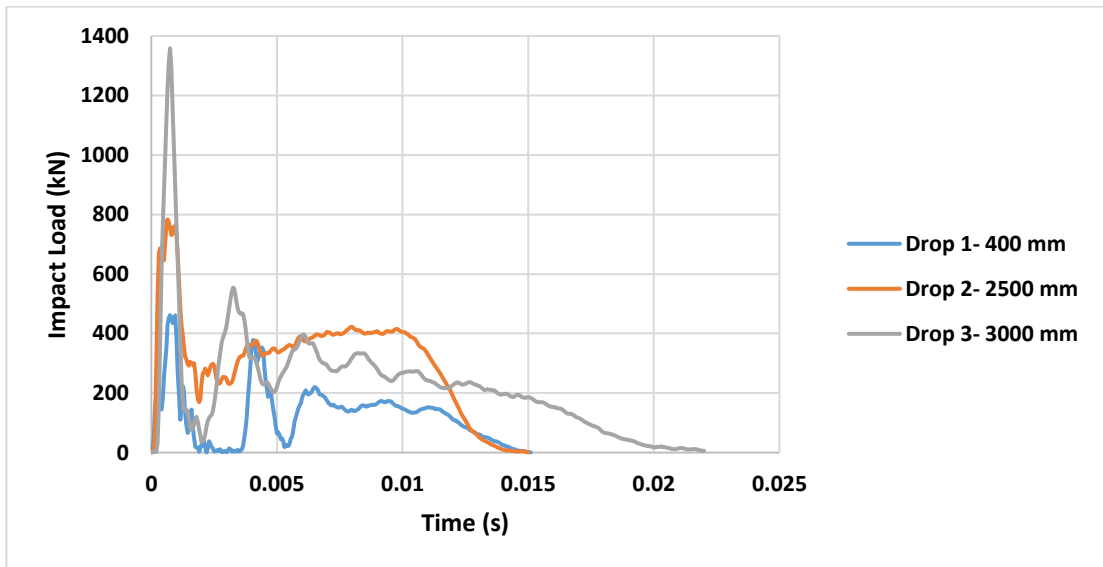
Figure 5.15 Load versus time duration of B1-VH-1
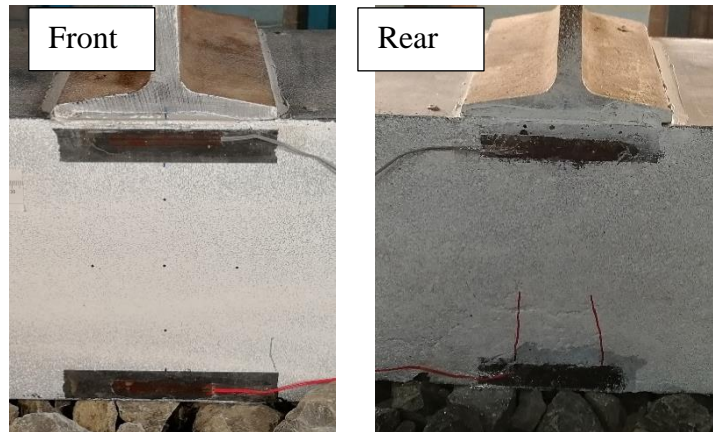
(a) after Drop 1 (drop height = 400 mm)
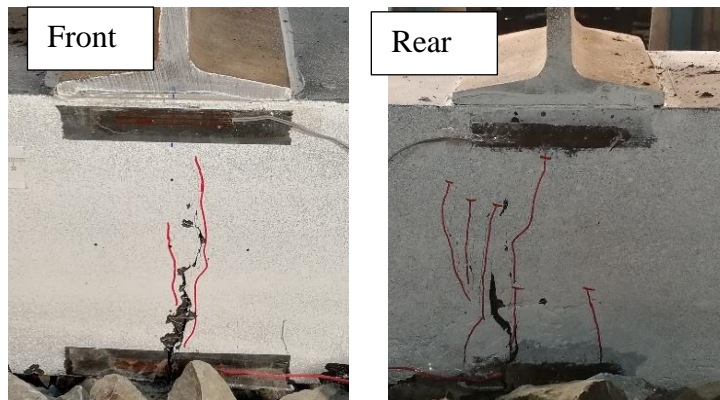
(b) after Drop 2 (drop height = 2,500 mm
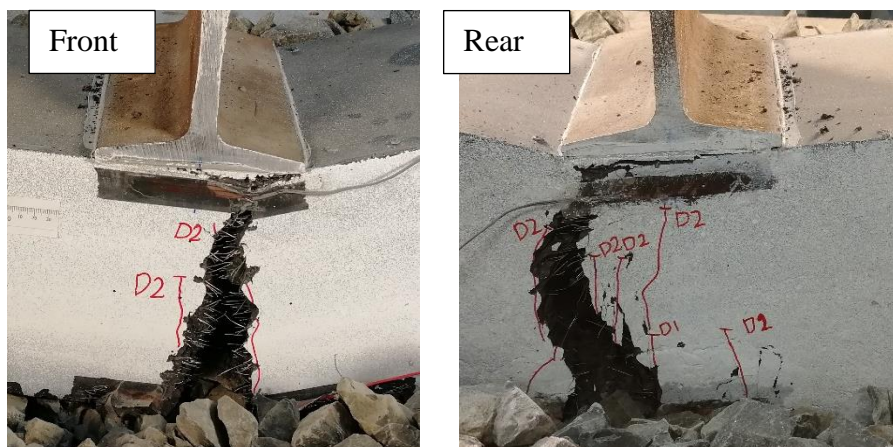
(c) after Drop 3 (drop height = 3,000 mm)

Figure 5.16 Crack propagation of B1-VH-1 under impact loads

5.4 Impact Testing of Sleepers with the Fastening Systems

In Section 5.3, the preliminary non-prestressed UHP-FRC samples with no actual rail-sleeper fastening systems (B1-VH-1 and B1-VH-2) under various impact loads were studied. It has been found from B1-VH-1 that the prototype UHP-FRC sleeper retains about 65% of its initial rail-seat moment capacity after sustaining several cracks under multiple impact loads. On the other hand, it was deduced from the second preliminary sample, B1-VH-2, that the prototype UHP-FRC sleeper can resist high impact loads with a return period beyond 50 years (the normal service life of a concrete sleeper).In this section, the performance of samples with actual rail-sleeper fastening systems is studied. Two types of track foundations, hard and very soft, are considered herein. For each track type, two samples are tested with a similar impact loading protocol (similar drop heights). The main objective of this investigation is to study the impact resistance of the non-prestressed UHP-FRC samples with cast-in fastenings and the effects of foundation types (hard and very soft) on their performance.

5.4.1 Sleepers with Fastening Systems on the Hard Track

The test set-up of the sleeper prototypes with the fastening systems and the hard track, B2-H-1 and B2-H-2, are similar to the preliminary samples (refer to Section 5.3) except for their foundations. The foundation of the samples consists of a layer of ballast with a height of 150 mm and a layer of the stiffest rubber belt (R.B.1), as illustrated in Figure 5.3-b. In order to confine the ballast particles, a confining wall is made from 200 PFC steel section profiles with a plan area of 1200 mm x 900 mm. Since the test set-up of B2-H-1 and B2-H-2 are identical, only the test set-up of B2-H-1 is shown in Figure 5.17.

(a) front side
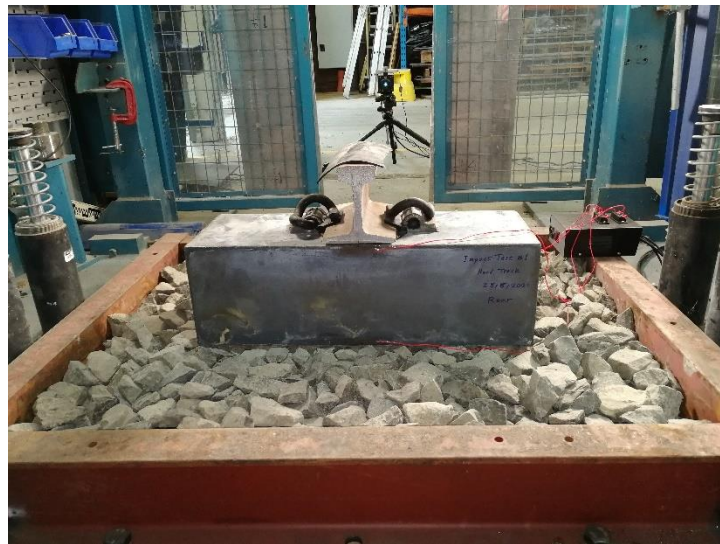
(b) rear face

Figure 5.17 The test set-up view of B2-H-1

The impact testing results of sample B2-H-1 and B2-H-2 and the main outcomes are presented in Table 5.6. A similar testing plan is considered for both of the UHP-FRC samples. First, three drops with the height of 200 mm are applied to each sample and then the major impact load, i.e. a drop from a height of 3,000 mm, is applied. The peak loads (P1 and P2) and the load duration magnitudes are determined from the load-time diagrams shown in Figure 5.18. It is shown in Table 5.6 that in all impact loads (drops), the first peak loads (P1) are higher than the second peak loads (P2). Also, it is found

that for both B2-H-1 and B2-H-2 (except for "Drop 3" of sample B2-H-2), the P2 magnitudes increase from Drop 1 to Drop 3. This increase is attributed to the fact that after each drop, the ballast particles are more compacted (stiffened) while the samples do not experience any considerable strength reduction (even with the hairline bending cracks). The total load durations of the two samples in the first three drops are similar and reduced to 17 ms from Drop 2. This reduction can also relate to the better compaction of ballast particles, which increases the stiffness of the whole system (sample + foundation).

Under the ultimate impact loads, i.e., Drop 4, the P1 magnitudes of the samples are almost similar (860 kN for B2-H-1 and 874 kN for B2-H-2). However, the P2 values of B2-H-1 and B2-H-2 are 439 kN and 569 kN, with a considerable difference. Considering the P2 magnitude of 554 kN obtained from the preliminary sample, B1-VH-2, under the extreme impact with a similar drop height (3,000 mm) (as reported in Table 5.5), it can be concluded that B2-H-2 (P2 = 569 kN) gives a more realistic representation of the UHP-FRC performance than B2-H-1 (P2 = 439 kN). Also, the ultimate load duration of B2-H-1 is considerably high (26 ms) compared with 18 ms for B2-H-2. Further information from the visual inspection is needed to attain a judgement about B2-H-1, as given in the following.

The cracking and damage status of the samples B2-H-1 and B2-H-2 after the initial three drops and the main (ultimate) drop are shown in Figure 5.19 and Figure 5.20, respectively. It is observed that both of the two UHP-FRC samples incurred two hairline bending cracks on their front and rear sides during the three initial drops. As was expected from the above statements, the two samples show different levels of damage after the last drop. Sample B2-H-1 shows the ultimate failure, including severe cracks reaching the top face of the sample and leading to the significant deflection of the sample. Indeed, it is supposed that B2-H-1 cannot maintain the track gauge after the final drop. However, sample B2-H-2 shows less damage after the last drop. Although several cracks are visible on both sides of the sample and approaching the top area of the sample section, these cracks have not attained the top face. Also, the sample does not show considerable deflections. Hence, it is believed that the sample is capable of maintaining the track gauge and is not entirely failed. Further studies may be needed for both the conventional PSC and the non-prestressed UHP-FRC sleepers

to define specific residual rail-seat deflection limits under dynamic rail loads for the ultimate failure of the sleepers.

Table 5.6 The impact test summary of B2-H-1 and B2-H-2

Drop No.	Drop height (mm)	P1 (kN)	P2 (kN)	Total Load Duration (ms)	Status
For Sample B2-H-1					
1	200	334	224	19	Two hairline bending cracks appeared on both the front and rear sides of the sample.
2	200	343	284	17	
3	200	332	286	17	
4	3,000	860	439	26	Sever cracking of the sample; the cracks reached the top face of the sample; the sample shows huge deflection at the mid span
For Sample B2-H-2					
1	200	298	174	20	Two hairline bending cracks similar to sample B2-H-1
2	200	306	259	17	
3	200	286	245	17	
4	3,000	874	569	18	Sever cracking of the sample; cracks reached the vicinity of the top face of the sample; the sample can hold the rail gauge
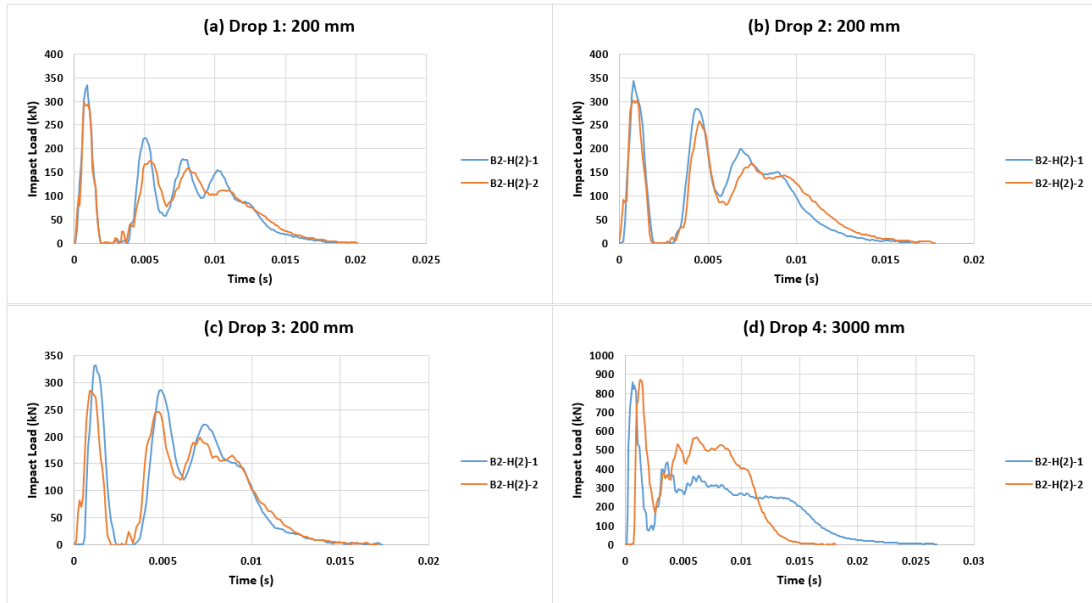
Figure 5.18 Load versus time diagrams of B1-VH-1 and B1-VH-2
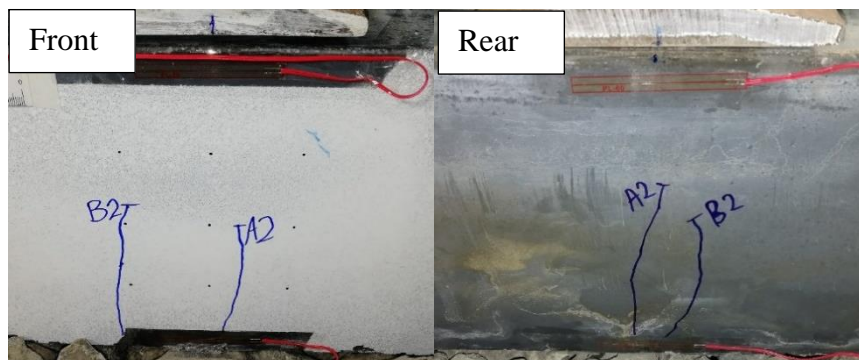
(a) after the initial three impacts (drop height = 200 mm)
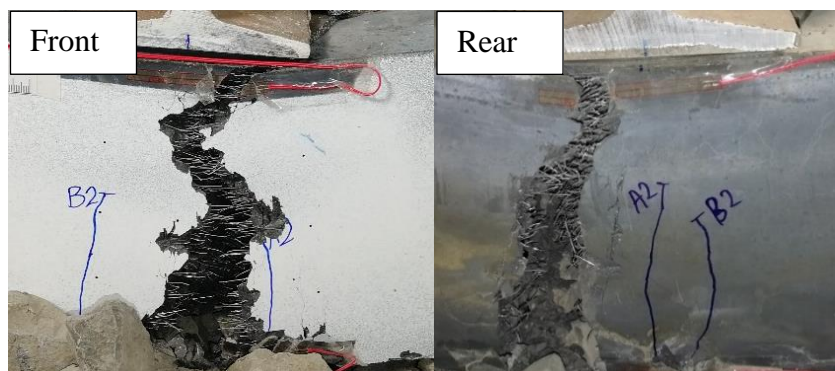
(b) after the ultimate impact (drop height = 3,000 mm)

Figure 5.19 Crack propagation of B2-H-1 between the initial and the main drops

144
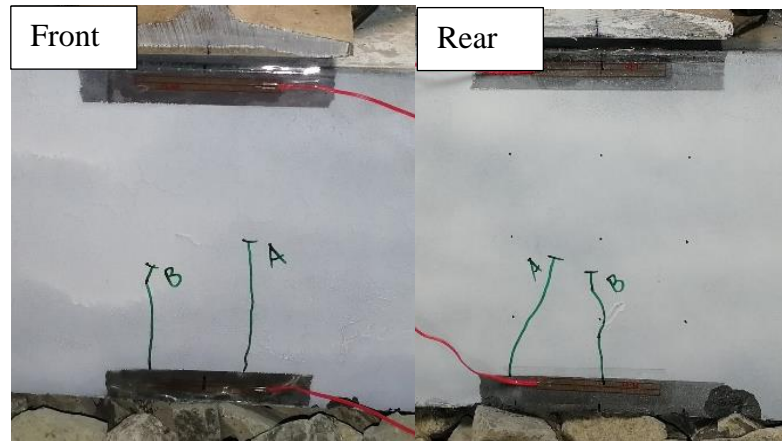
(a) after the initial three impacts with the drop height of 200
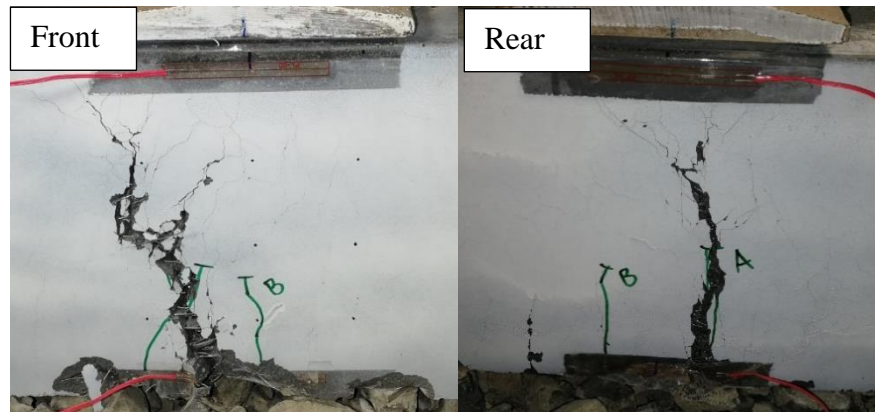
(b) after the ultimate impact with the drop height of 3,000 mm

Figure 5.20 Crack propagation of B2-H-2 between the initial and the main drops

5.4.2 Sleepers with Fastening Systems on the Soft Track

As explained in Section 5.2.4, six layers of rubber belts are used to simulate a very soft track foundation (with the approximate stiffness of 3-8 MN/m). The configuration (position) of the rubber belts and their mechanical characteristics can be found in Figure 5.3-c and Table 5.3, respectively. Figure 5.21 shows a view of the rubber belts placed together in the lab. The order of these rubber belts is according to their stiffness with the R.B.1 layer, which has the highest elastic modulus of 114.3 MPa, on the top and the three layers of R.B.4, which have the lowest elastic modulus of 1.134 MPa underneath the other layers. This arrangement is in good agreement with the structure of the rail tracks, where the top layer (ballast) is stiffer than the bottom layers (sub-ballast and formation layers). The test set-up of samples B3-VS-1 and B3-VS-2 are

identical. Hence, only the front and rear side views of the test set-up of sample B3-VS-1 are shown in Figure 5.22. The confining steel walls are not needed herein as ballast particles are not used. However, the walls are installed to protect the UHP-FRC samples and the test rig in the case that the samples incur unexpected bounce back after the impact loads (due to the elastic performance of rubber belts).
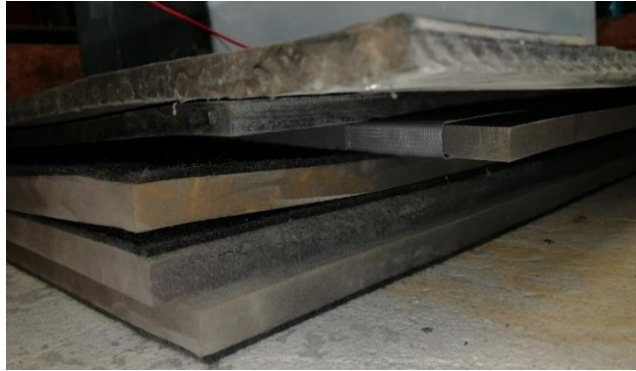
Figure 5.21 The six layers of rubber sheets make the very soft track foundation (with an approximate stiffness of 3-8 MN/m) for samples B3-VS-1 and B3-VS-2

(a) front side

(b) rear side

Figure 5.22 The test set-up view of B3-VS-1 with the very soft foundation

The impact testing procedures of B3-VS-1 and B3-VS-2 and the significant results obtained from the tests are shown in Table 5.7. A similar testing procedure is considered for both of the UHP-FRC samples. Since a ballast layer has not been used in the very soft track foundation and rubber belts perform elastically, only one initial impact load is needed to investigate the elastic behaviour of each sample. Hence, the first drop is applied from the small height of 200 mm, before the main (ultimate) impact loading, for each sample. Due to the safety issues regarding the bounce back of the samples due to the elastic performace of the rubber belts, the main drops are limited to 1,500 mm. Overall, one initial drop from the height of 200 mm and two main drops with the same height of 1,500 mm are applied to each sample. The first drop is for monitoring the elastic performance of the prototype sleepers and the two main drops (from 1.5 m height) are applied to investigate the ultimate impact load resistance of the sleepers on the very soft track. The peak loads (P1 and P2) and the total impact load durations are obtained from the load-time diagrams shown in Figure 5.23 and summarised in Table 5.7. It should be noted that the ultimate peak loads (P2 magnitudes) obtained from the four samples with fastening systems, are compared and analysed in Section 5.5. Overall, B3-VS-1 has a higher strength than B3-VS-2, as it has higher P1 and P2 magnitudes under the impact loads. For example, under Drop 2, B3-VS-1 reaches the higher P2 magnitude of 640 kN than B3-VS-2 with the P2 magnitude of 556 kN. Under Drop 3, samples B3-VS-1 and B3-VS-2 reach close P2 magnitudes, i.e. 546 kN and 548 kN, respectively.

Interestingly, the total load duration of the two samples is identical to each other. Under the first drop, both samples have a very long load duration equal to 41 ms. From Figure 5.23-a, both of the samples show elastic performances with low damping. However, sample B3-VS-1 has higher fluctuations. Under the second and third drops, the two samples have similar load durations of 28 ms and 29 ms, which are still high compared with the load duration of the samples B2-H-1 and B2-H-2 with the hard track foundation. The longer load durations of B3-VS-1 and B3-VS-2 are due to the elastic performance of the rubber belts and their lower damping ratio compared with the hard (ballasted) tracks.

Table 5.7 The impact test summary of B3-VS-1 and B3-VS-2

Drop No.	Drop height (mm)	P1 (kN)	P2 (kN)	Load Duration (ms)	Status
For Sample B3-VS-1					
1	200	406	364	41	Two hairline bending cracks appeared on both sides of the sample
2	1500	875	640	28	Several hairline cracks appeared around the rail-seat area on both sides
3	1500	708	546	29	A few hair-line cracks join together, and a wide crack appears on both sides
For Sample B3-VS-2					
1	200	353	179	41	Two bending cracks (similar to Sample 1) appeared on both sides of the sample
2	1500	679	556	28	Several hairline cracks appeared around the rail-seat area; one of the two cracks from the initial drop (crack A) shows considerable propagation and widening
3	1500	695	548	29	Crack "A" shows extreme widening and propagates to the top face of the sample
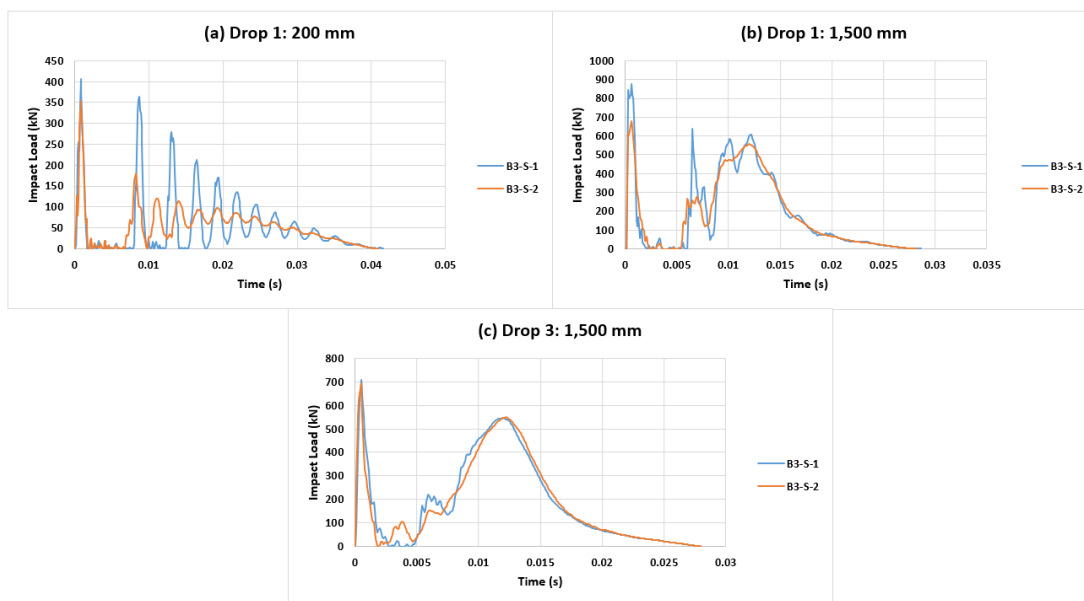
Figure 5.23 Load versus time diagrams of B3-VS-1 and B3-VS-2

Figure 5.24 and Figure 5.25 show the damages (cracks) of samples B3-VS-1 and B3-VS-2 under Drops 1 to 3. It can be seen that under the 1st drop, both samples incur two bending cracks under the rail seat. However, under the 2nd drop (with the drop height of 1,500 mm), both samples have several hairline cracks on both sides. Some of the cracks reach the vicinity of the top surface but do not grasp it. One of the two initial bending cracks (crack B in sample B3-VS-1 and crack A in sample B3-VS-2) shows more growth than the other cracks in propagation and widening. Under the 3rd drop, in addition to the several cracks, the same bending crack with bigger growth under the 2nd drop shows extreme opening on both sides of the two samples. However, sample B3-VS-2 shows more severe damages (crack widening) under Drop 3. Interestingly, both of the samples do not show apparent residual deflections and are expected to be able to maintain the track gauge in real situations. This is in contrast to the samples with the hard track foundations where one of the samples, i.e., B2-H-2, shows significant residual rail-seat deflection under the ultimate impact load and is expected not to be capable of retaining the track gauge.
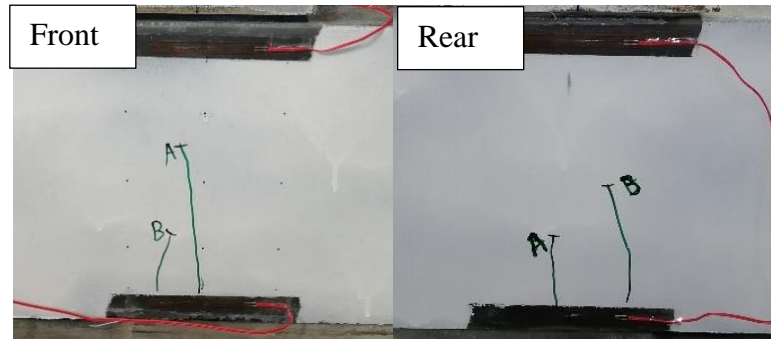
(a) after the initial drop (drop height = 200 mm)
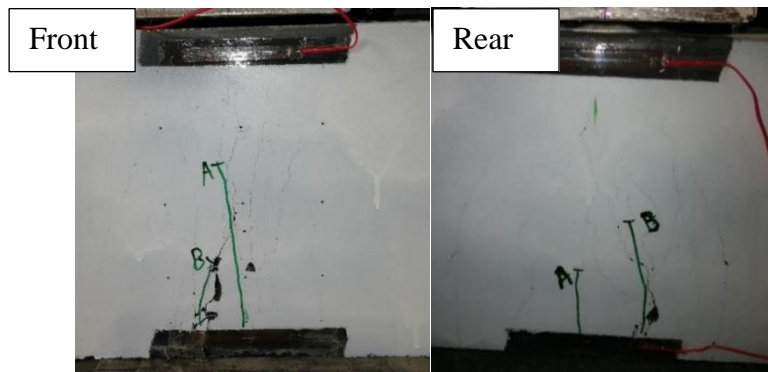
(b) after the 2nd drop (drop height = 1,500 mm)
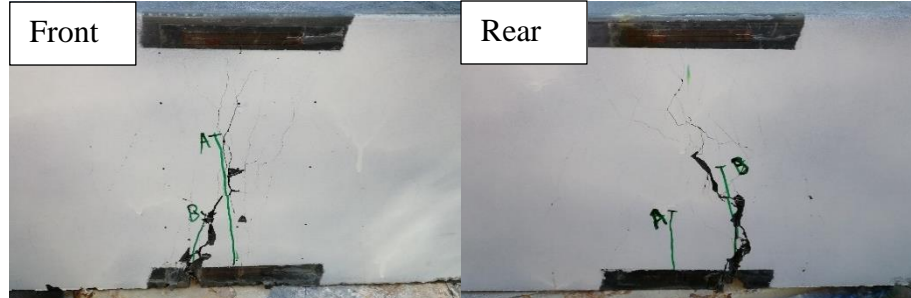
(c) after the 3rd drop (drop height = 1,500 mm)

Figure 5.24 Crack propagation of B3-VS-1 under the impact loads
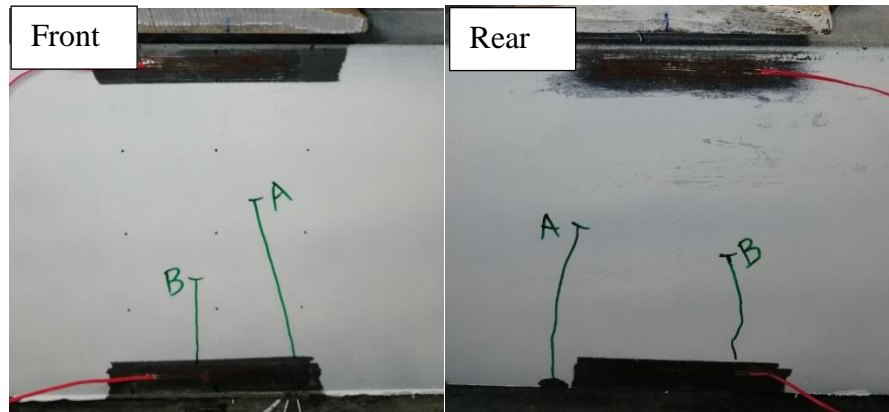
(a) after the initial drop with the drop height of 200 mm
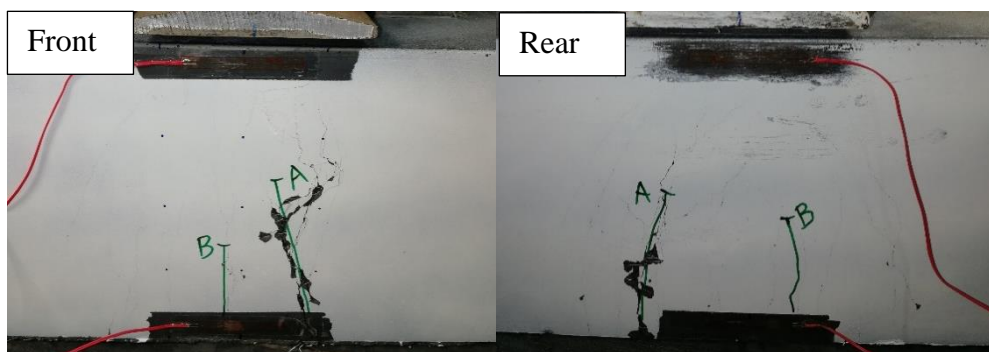
(b) after the 2nd drop with the drop height of 1,500 mm
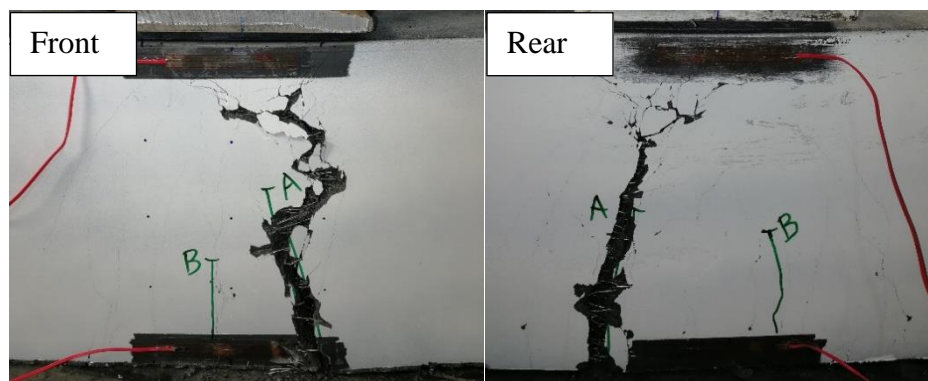
(c) after the 3rd drop with the drop height of 1,500 mm

Figure 5.25 Crack propagation of B3-VS-2 under the impact loads

5.5 Comparison of the Results

This section compares the main impact peak loads sustained by the non-prestressed UHP-FRC prototype samples with the actual rail-sleeper fastening systems. In the first step, it is needed to have an estimation of the impact wheel loads that may occur in the

wheel/rail interface in railway tracks. For this purpose, the magnitudes of the impact loads expected to occur within the service life of concrete railway sleepers are estimated according to a study conducted by Leong (2007). A review of the high-frequency dynamic (impact) wheel-rail loads was demonstrated in Chapter 2, Section 2.3.2. Herein, Equations 2.5 to 2.7 proposed by Leong (2007), based on the field investigation performed on Braeside railway track with the train speed ranging between 30 and 90 km/h, are utilised for calculating the impact load magnitudes corresponding to a return period of the impact loads (R) and the train speed. Hence, Equations 2.5 to 2.7 are repeated and briefly explained in the following. As demonstrated in Equation 2.5, the expected total impact load ($F_{t,w}$) is equal to 1.2 times the static wheel load (F_s) plus the wheel impact load ($F_{i,w}$). The wheel impact load can be calculated using Equation (2.6).

$$F_{t,w} = 1.2F_s + F_{i,w} \qquad\qquad (2.5)\ (5.1)$$

$$F_{i,w} = F_{imp}k_{wm}k_I k_{IFF} \qquad\qquad (2.6)\ (5.2)$$

where F_{imp} denotes the wheel impact force which is normally selected as 230 kN in congruence with the interstate network in Australia (Australasian Railway Association, 2002). k_{wm} is called the wheel maintenance factor that takes a magnitude of 1.0 for the moderate track wheel maintenance Group 2. Also, k_I is called the track importance factor that represents the defined commercial risk level of the railway track and takes a value between 0.85 and 1.0, corresponding to the track importance category. In this study, the magnitudes of k_{wm} and k_I are assumed as 1.0. K_{IFF} is called the impact force factor which is dependent on the defined return period (R) and the train speed (V) of the railway track, as demonstrated in the following equation.

$$k_{IFF} = 0.00278R + 0.029V - 0.73 \qquad\qquad (2.7)\ (5.3)$$

For the 25 TAL considered in this study, the static wheel load is equal to 123 kN (F_s = 25 * 9.81 / 2 = 123 kN). It is worthy of notice that the load coefficient of 1.2 in Equation 2.5 considers the possibility of the overload of the train, as recommended by Leong (Leong, 2007). Using the above equations, the expected total impact load ($F_{t,w}$) for the desired return period and train speed, can be estimated. The return period for a concrete sleeper with a service life of 50-100 years, should be considered as 100, 500, and 2000 years, for the railway tracks of Category 1, 2, and 3, respectively. Category 1 is attributed to the infrequent traffic and interstate tracks, Category 2 is attributed to the regular traffic or freight tracks, and Category 3 is attributed to the inner city and heavy-haul rail tracks (ABCB, 2009).

Figure 5.26 illustrates the magnitudes of the expected total impact loads for a variety of train speeds, ranging between 60 and 120 km/h, and return periods of 100, 500, and 2000 years. Although the estimated impact magnitudes are only based on a field investigation performed by Leong (Leong, 2007) at Braeside, they provide a rough estimation of the real wheel impact magnitudes. It can be deduced from Figure 5.26, the calculated wheel impact load increases linearly with the train speed or return the return period.
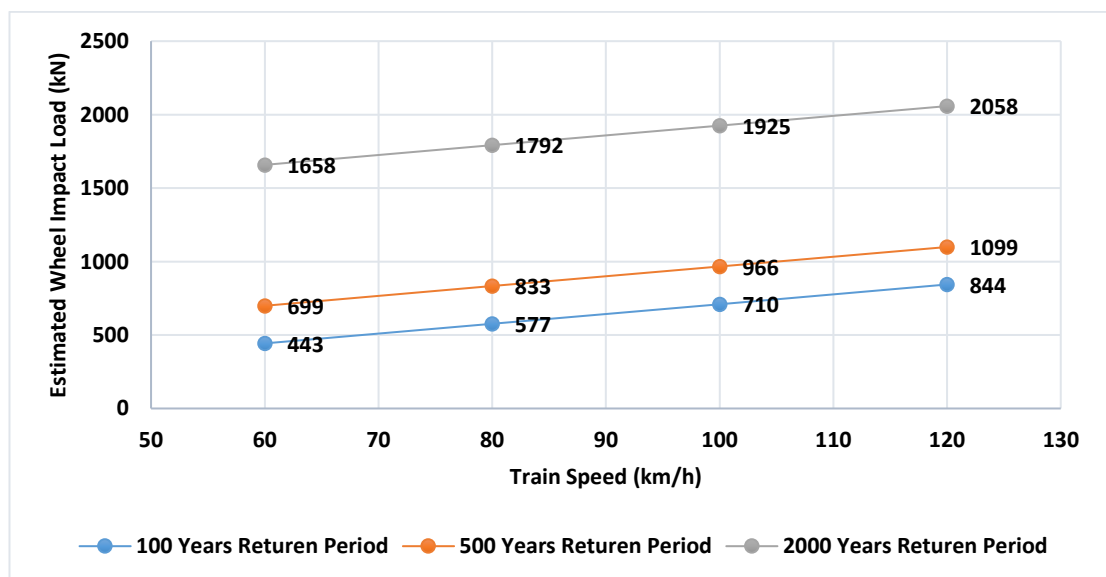
Figure 5.26 Estimated magnitudes of the wheel impact load for various train speeds and return periods

The main impact loads (P2 magnitudes) applied to the prototype UHP-FRC samples are summarised in Table 5.8. According to the main applied impact loads, it can be deduced that the UHP-FRC prototype samples can perform significantly better on soft track foundations compared with the hard tracks. Both samples on the very soft track, B3-VS-1 and B3-VS-2, could resist two main drops, whereas the samples on the hard track, B2-H-1 and B2-H-2, could resist merely one main drop.

Except for B2-H-1 which reached the considerably low P2 magnitude of 439 kN, the P2 loads of the prototype sleepers are within the range of 546 kN and 640 kN. The better performance of the samples with the soft track (B3-VS-1 and B3-VS-2) can be attributed to the fact that the soft track can better absorb the applied impact loads compared with the hard track. Hence, according to the estimated wheel impact load magnitudes shown in Figure 5.26, it can be deduced that the prototype non-prestressed UHP-FRC sleepers are only suitable for railway tracks of Category 1 (infrequent traffic or interstate tracks) with 100 years return period and train speeds not higher than 80 km/h. It should be noted that the conclusion is based on the study of a specific railway field, with a variety of train speeds between 30 km/hr and 90 km/hr. Further field investigations may be needed in the future to assure the safety of the prototype UHP-FRC samples under extreme impact loads. The low consistency between the results reported in Table 5.8 for similar samples (with the same track type) can be attributed to the complexity of the dynamic performance due to the interactions between the prototype samples and the foundation. In future research, it is recommended that at least three identical prototype samples (for each track type) be tested so that the average results can be reported.

Table 5.8 The main impact loads (drops) for the UHP-FRC samples with actual fastening

Sample	Track Type	Drop No.	Main Impact (kN)
B2-H-1	Hard	4	439
B2-H-2		4	569
B3-VS-1	Very Soft	2	640
		3	546
B3-VS-2		2	556
		3	548

In the end, it should be noted that the impact load resistance of the prototype non-prestressed UHP-FRC sleepers is significantly less than the impact resistance of their counterparts, i.e. conventional PSC sleepers with comparable cross-section dimensions. For instance, the impact tests performed by Kaewunruen (2007) for conventional PSC sleepers with the rail-seat soffit width and height of 250 mm and 227 mm, respectively, revealed that these PSC sleepers can sustain up to 1150 kN impact loads (P2 magnitudes). Such a high impact load is around two times the prototype UHP-FRC sleepers. Hence, it can be concluded that although the impact resistance of the prototype sleepers can be satisfactory for infrequent traffic railway tracks with limited train speeds, their impact resistance needs further improvements to be comparable with the conventional PSC sleepers.

5.6 Summary

In this chapter, the performance of the non-prestressed UHP-FRC prototype sleepers under impact loads was studied. For this purpose, a drop hammer impact testing machine at the University of Wollongong was utilised. First, two preliminary prototype samples are made with no rail/sleeper fastenings, named B1-VH-1 and B1-VH-2. The samples were placed on a very hard track foundation model with 250 mm of ballast on the strong concrete floor. One sample was tested under eight impact loads with the successive increase, from a short drop height of 200 mm to a drop height of 800 mm. Subsequently, the cracked sample was tested under rail-seat static loading in order to determine the remaining strength of the sample. Comparing the maximum static load of the cracked sample B1-VH-1 with the sample reported in Chapter 4, S2-S2, it was found that B1-VH-1 has around 65% of its initial strength under static rail-seat testing despite its several cracks from the impact testing.

The second preliminary prototype sample (without the actual rail/sleeper fastening system), B1-VH-2, was tested to determine the ultimate impact resistance of the UHP-FRC prototype sample under extreme impact loads. After an initial impact load, two main impact loads with drop heights of 2,500 mm and 3,000 mm were applied to the sample. Under the latter drop, the high peak load (P2) of 554 kN was obtained.

Subsequently, four prototype samples with the actual rail/sleeper fastening system were produced. Two samples were selected to be tested on a simulated hard track foundation made of 150 mm of ballast and a layer of "Rubber Belt 1" underneath the ballast layer. The other two samples were placed on a very soft rail track foundation made with six layers of rubber belts. The test results showed that the UHP-FRC samples on the very soft track foundation perform better than those on the very hard track. In the future, thorough experiments containing various rail track foundations are needed to determine the influence of the rail track type (stiffness) on the non-prestressed UHP-RC samples.

Afterwards, the ultimate wheel impact loads corresponding to various train speeds and return periods were estimated using the relations proposed by Leong (2007) based on a field investigation. Comparing the estimated impact loads with the ultimate impact loads resisted by the prototype sleepers with the actual rail/sleeper fastening system, it was found that the prototype UHP-FRC sleepers which can be only suitable for railway track systems with infrequent traffic and interstate rail tracks with limited train speeds (up to 80 km/h). However, further field investigations may be needed to gather more field data from various rail tracks to confirm the latter statement.

CHAPTER 6
LOW-HEIGHT UHP-FRC SLEEPERS REINFORCED WITH GFRP LONGITUDINAL BARS

6.1 Introduction

In Chapter 4, it was shown that the prototype non-prestressed UHP-FRC sleeper passed the standard rail-seat positive moment test (which is a type of static testing). However, the prototype sleeper did not show a satisfactory fatigue resistance. It is expected that adding longitudinal reinforcing bars to the UHP-FRC sleepers can improve the static and fatigue resistance of these sleepers. Hence, in this chapter, the influence of glass fibre reinforced polymer (GFRP) bars on the enhancement of the strength of the UHP-FRC prototype sleepers is investigated. The main reason for using the GFRP bars instead of the traditional steel bars is their non-corrosiveness of GFRP bars which can lead to higher durability and serviceability of the non-prestressed sleepers. For this purpose, four prototype sleepers are designed and produced with reinforcement ratios varying from 0.00 to 0.0272. Two different nominal GFRP bar diameters of 10 mm and 14 mm are used in this research. Subsequently, the standard rail-seat positive moment testing is carried out for these sleepers, and the results are compared.

6.2 Design of the Prototype Low-height UHP-FRC Sleeper

The dimensions of the UHP-FRC sleepers studied in this chapter are similar to the prototype sleepers investigated in Chapter 4 (refer to Table 4.1) except for the height. Indeed, the low-height cross-section of 250 mm x 150 mm (width x height) is selected for the UHP-FRC sleepers, to investigate the enhancing influence of the GFRP reinforcing bars on the flexural strengths of the UHP-FRC prototype sleepers. The length of the prototype low-height sleepers is identical to the prototype sleepers studied in Chapter 4 (length = 1060 mm). This is due to the standard support span of 660 mm according to the Australian Standard (AS1085.14, 2019) plus the hangover length of 200 mm from each side (200 + 660 + 200 = 1060 mm).

According to ACI 440 (ACI-440, 2003), the balanced reinforcement ratio (ρ_b) of FRP-reinforced concrete beams can be calculated using the following equation:

$$\rho_{fb} = 0.85 \times \beta_1 \times \frac{f_c'}{f_{fu}} \times \frac{E_f \varepsilon_{cu}}{E_f \varepsilon_{cu} + f_{fu}} \qquad (6.1)$$

where f'_c and f_{fu} are the characteristic 28-day compressive strength of the concrete and the ultimate tensile strength of the FRP bars, respectively. Also, E_f is the modulus of elasticity of the FRP bars, and ε_{cu} is the compressive strain of concrete at the maximum compressive stress. β_1 is the compressive stress block parameter and can be calculated as follows:

$$\beta_1 = 0.85 - 0.05 \times \left(\frac{f_c' - 28}{7} \right) \geq 0.65 \qquad (6.2)$$

The mean compressive strength (f'_c) of the UHP-FRC mix is selected as 115 MPa, which is the average of the mean compressive strengths of the first and the second UHP-FRC batches reported in Chapter 4 (113 MPa and 117 MPa), and thereby, the magnitude of β_1 is equal to 0.65. It should be noted that although the ACI 440 (ACI-440, 2003) is basically suitable for the normal-strength and high-strength concrete beams, it is expected that Equations (6.1) and (6.2) can give an acceptable approximation of the balanced reinforcement ratio for the UHP-FRC prototype sleepers, investigated in this research. Also, the ultimate strength and elastic modulus of the GFRP reinforcing bars are equal to 930 MPa and 59 GPa, respectively, according to a previous research (Elchalakani et al., 2019). Then, taking the peak-point strain of the UHP-FRC (ε_{cu}) as 0.003 as recommended by AS3600 (AS-3600, 2018), the balance reinforcement ratio will be found as 0.0109 according to Equation 6.1. It is important to note that in order to have a ductile failure, the reinforcement ratio must be higher than 0.0109 (ρ_b) to ensure that concrete crushing in compression occurs instead of the rupture of the FRP reinforcing bars in tension. This is due to the fact that

the FRP rupture is brittle. Hence, in this study, except for the reference UHP-FRC prototype sleeper (without GFRP reinforcements), the other sleepers must have reinforcement ratios equal to or higher than 0.0109.

The configuration details of the four low-height UHP-FRC sleepers considered in this study are summarised in Table 6.1. It can be seen that in all the GFRP-reinforced sleepers, the bottom, top, and side concrete covers are identical. Two nominal GFRP diameters of 10 mm and 14 mm are selected in this study. The naming system of the prototype sleepers consists of two parts. The first part shows the sleeper number (S1 to S4), and the second part shows the rounded reinforcement ratio. For example, S1-00 is the first sleeper and has no reinforcing GFRP bars (reinforcement ratio = 0.00), whereas S4-03 is sleeper number 4 with the rounded reinforcement ratio of 0.03 (reinforcement ratio = 0.0272). Overall, three different reinforcement ratios are considered in this study, including 0.00, 0.0109, and 0.0272. Two of the sleepers, i.e. S2-01 and S3-01, have an identical reinforcement ratio (0.0109), while the diameter and number of the reinforcing bars are different for these sleepers. S2-01 sleeper has two reinforcing bars of 14 mm diameter, whereas S3-01 has four bars of 10 mm diameter. The effects of the GFRP bar diameter, and thereby, the bond between the UHP-FRC matrix and the GFRP bars, on the performance of the prototype sleepers can be roughly found by comparing sleepers S2-01 and S3-01. The details of the cross-sections of the UHP-FRC sleepers are shown in Figure 6.1.

Table 6.1 Details of the low-height UHP-FRC sleepers with GFRP reinforcements

Sleeper	Width (mm)	Height (mm)	Vertical cover (mm)	Horizontal cover (mm)	d (mm)	Diameter (mm)	No of bars	Reinforcement ratio (As/bd)
S1-00	250	150	30	20	---	---	---	---
S2-01	250	150	30	20	113	14	2	0.0109
S3-01	250	150	30	20	115	10	4	0.0109
S4-03	250	150	30	20	113	14	5	0.0272
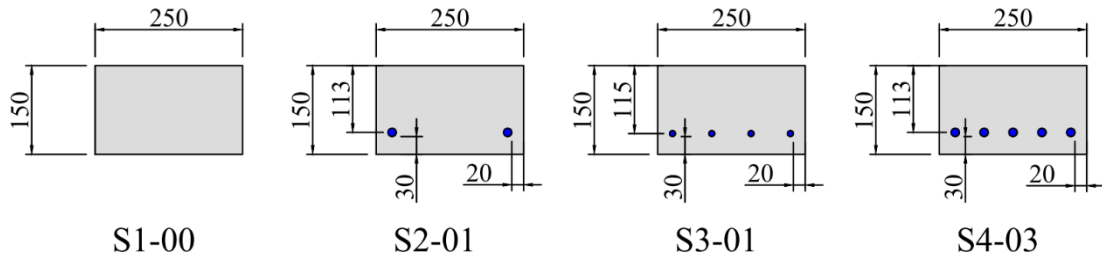
Figure 6.1 Detailed cross-section configurations of the low-height UHP-FRC sleepers

6.3 Manufacturing the Prototype Low-height UHP-FRC sleepers

Four low-height prototype non-prestressed UHP-FRC sleepers with various GFRP reinforcement ratios are manufactured and investigated in this chapter. Like in previous chapters, each pair of samples is cast by one batch of UHP-FRC mix. Hence, two batches of UHP-FRC mix are needed for the four samples. Herein, the mixing, casting, and curing procedures are similar to Chapter 4. A 300-litre mobile pan mixer is used for mixing the UHP-FRC mix. The moulds are made with plywood, as shown in Figure 6.2. To install the GFRP bars, holes with precise diameters and locations (according to Figure 6.1) are cut into the end plates of the moulds, such that the GFRP bars can be tightly inserted and fixed in their positions. Around 2 hours after mixing and pouring, the UHP-FRC prototype sleeper are covered with plastic sheets for one day until they are set, as shown in Figure 6.3. Subsequently, the prototype sleepers are covered with wet hessian and plastic sheets on the top while kept in their moulds, as shown in Figure 6.4. After 28 days from pouring, the prototype UHP-FRC sleepers are uncovered and unmoulded for being tested.

Figure 6.2 A view of the moulds and the GFRP bars for making the low-height UHP-FRC sleepers

Figure 6.3 The low-height UHP-FRC sleepers, 24 hours after pouring

Figure 6.4 Covering the UHP-FRC prototype sleepers with wet hessian and plastic sheets

6.4 Material Properties

The curing and testing procedures of the material samples are identical to Chapter 4. From each of the two batches of UHP-FRC, three cylinder samples with a height of 200 mm and a diameter of 100 mm for compression testing and two prismatic samples with dimensions of 100x100x350 (mm) for bending (modulus of rupture) tests are taken. The compression testing is performed according to AS 1012.9 (AS-1012.9, 1999) and the bending testing according to AS 1012.11 (AS-1012.11, 2000). Also, the mass per unit volume is determined using the rapid method recommended by (AS-1012.12.1, 2014). The results of the UHP-FRC material testing are presented in Table 6.2. It can be seen that the mass per unit volume of the two batches is approximately similar, while the compressive strength and the modulus of rupture of batch 2 are slightly higher than those of batch 1. It is expected that these relatively minor differences will not affect the outcome of this investigation and, therefore, are neglected.

As aforementioned, two diameters of GFRP reinforcing bars with nominal diameters of 10 mm and 14 mm are utilised in this research. As shown in Figure 6.5, the two bars have similar surface patterns. The mechanical characteristics of the GFRP bars are summarised in Table 6.3.

Table 6.2 Mechanical properties of the UHP-FRC mixes

Batch No.	Samples	Mass per Unit Volume (kg/m3)	Compressive Strength (MPa)	Flexural Strength (MPa)
Batch 1	S1-00	2362	103.2	18.83
	S2-01			
Batch 2	S3-01	2367	113.08	21.79
	S4-03			
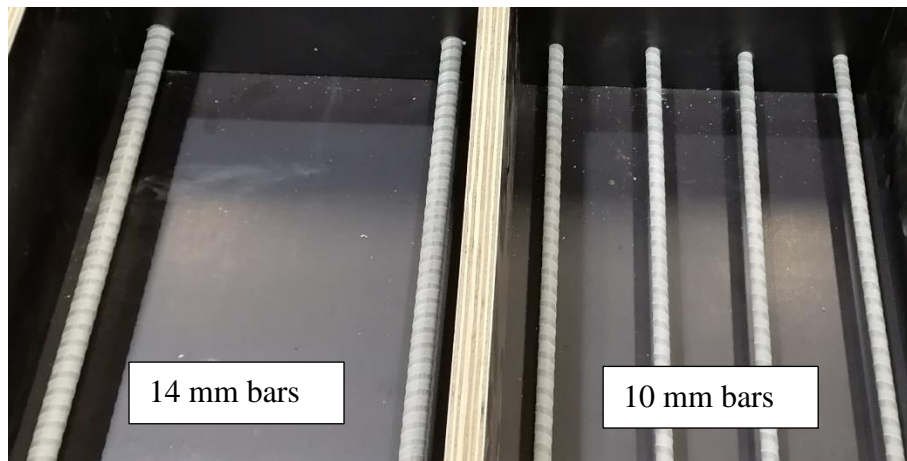
Figure 6.5 Surface ribs of the GFRP bars used in manufacturing the low-profile UHP-FRC sleepers

Table 6.3 Mechanical properties of the GFRP reinforcing bars

GFRP bar Diameter	Elastic Modulus (GPa)	Ultimate Tensile Strength (MPa)	Reference
10 mm	58	1219	(Hadi et al., 2021)
14 mm	59	930	(Elchalakani et al., 2019)

6.5 Rail-seat Positive Moment Test Set-up

The positive moment testing procedure is performed according to the Australian Standard (AS1085.14, 2019). The test set-up of the low-height UHP-FRC sleepers is shown in Figure 6.6. The same steel frame used for fatigue testing (reported in Section

4.4.1) is utilised in this experiment to support the low-height UHP-FRC sleepers. The figure shows that two steel plates are placed between the supporting steel bars and the prototype sleeper. Two thin rubber pieces are placed between the top (loading) bars and the prototype sleeper. Also, two LVDT gauges with the same gauge distance of 200 mm are installed on the front face of the prototype sleeper, with a 10 mm distance from the top and bottom of the prototype sleeper. Furthermore, a vertical LVDT is installed at the mid-span of the sleeper to measure its vertical deflections. The static rail-seat load is applied as displacement-control such that the load rate does not surpass 10 kN/min. The other side (rear side) of the sleeper is kept clear of attachments in order to observe and mark the cracks that appear during the rail-seat loading.
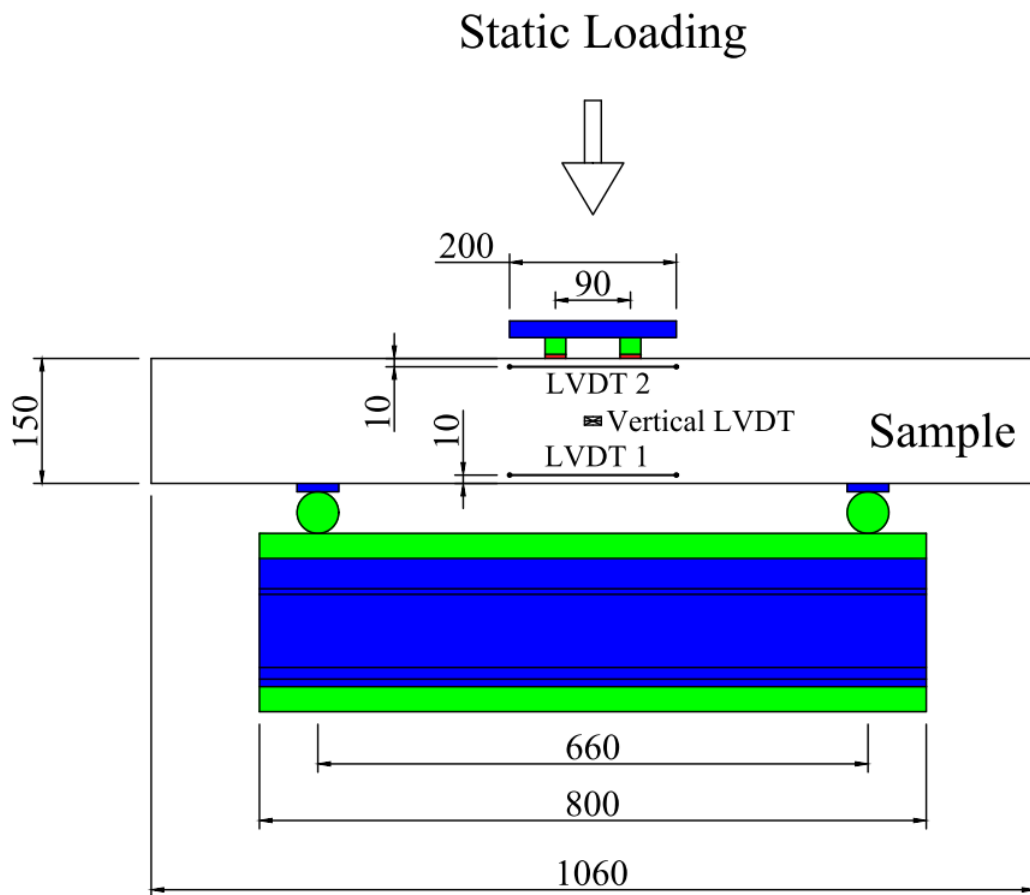
Figure 6.6 The rail-seat test set-up for the low-height UHP-FRC sleepers (front side) (all dimensions in mm)

6.6 Rail-seat Positive Moment Tests Results

Herein, the positive moment testing results of the four low-height non-prestressed UHP-FRC sleepers are presented. A view of the sleepers and their set-ups are shown in Figure 6.7. An identical test set-up and testing procedure are selected for all the sleepers. In this manner, the results obtained from the sleepers can be comparable. Therefore, the influences of the GFRP bars on the performance of the UHP-FRC prototype sleepers can be identified.

(a) Sleeper Sample S1-00   (b) Sleeper Sample S2-01

(a) Sleeper Sample S3-01   (b) Sleeper Sample S4-03

Figure 6.7 The view of the low-height UHP-FRC prototype sleepers

6.6.1 Visual Inspection, Failure Modes, and Load-Deflection Performance

The cracking patterns of the low-height UHP-FRC sleepers are depicted in Figure 6.8. The first cracking load is critical data to extract from the prototype sleeper visual inspection. The first cracks are marked with red lines in Figure 6.8, and the magnitudes of the first crack and peak loads are summarised in Table 6.4. It is observed that the

165

first cracks in all the prototype sleepers occur due to bending. As was expected, the lowest cracking load occurs in S1-00 at 68 kN, followed by two other bending cracks at 72 kN. After the peak load, two post-peak bending cracks appeared at 35 kN namely AP-35 where AP denotes "after peak". It is deduced from the inspection that the ultimate failure of the sleeper occurs in bending. The bending failure mode agrees with the smooth and ductile post-peak performance observed in the load-deflection diagram, as shown in Figure 6.9.

Sleeper S2-01 experiences the first crack at 95 kN of load. Subsequently, a number of bending cracks appear on the sleeper, followed by several shear cracks. The last two shear cracks appear at 220 kN. Interestingly, the shear cracks do not open widely as a typical ultimate failure mode of the reinforced concrete beams due to shear (such as what happens for S3-01 and S4-03). Instead of the shear failure mode, it is found in the inspection that sleeper S2-01 experiences multiple stepwise slippages of the GFRP reinforcing bars around the mid-span region with noticeable sounds. Such a stepwise slippage causes the post-peak fluctuations of the load-deflection curve of the sleeper, as shown in Figure 6.9.

Sleepers S3-01 and S4-03 have similar failure modes. In sleeper S3-01, the first crack appears at 130 kN of load, while in S4-03, the first crack appears at 100 kN. The higher cracking load of sleeper S3-01 compared to S2-01 and S4-03 is attributed to the better bond between the UHP-FRC material and the 10 mm GFRP reinforcing bars in S3-01 while the other two samples have 14 mm GFRP reinforcing bars. Previous research works have proved the better bond strengths of 8-10 mm GFRP bars with concrete compared to GFRP bars of the same types with greater diameters (e.g. (Baena et al., 2009)). Subsequently, more bending cracks appear on the two sleepers, and then the shear cracks start appearing on the sleepers. The typical ultimate failure mode due to shear occurs for both sleepers, where a shear crack widens and propagates towards the top face of the sleeper. Comparing the load-deflection curves of S3-01 and S4-03 (refer to Figure 6.9), it can also be found that in both cases, the load-deflection curves have a dramatic drop which is due to the shear failure of the sleepers.

(a) S1-00
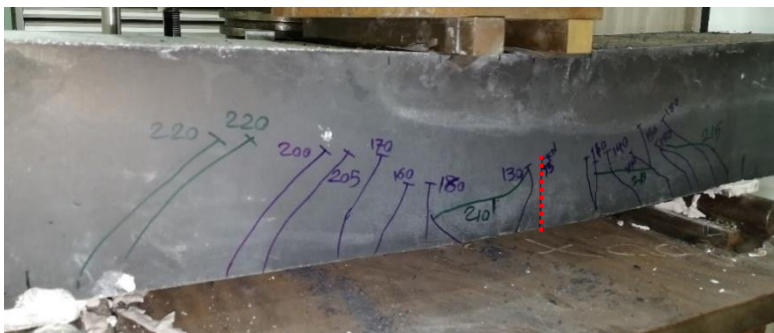
(b) S2-01

(c) S3-01

(d) S4-03

Figure 6.8 Crack patterns of the low-height UHP-FRC sleepers

Table 6.4 Summary of the strength and failure behaviour of the low-height UHP-FRC sleepers

Sleeper	Cracking load (kN)	Peak Load (kN)	Failure Mode	Load-deflection post-peak shape
S1-00	68	75.6	Bending failure	Smooth decrease
S2-01	95	225	Bar slippage	fluctuation
S3-01	130	266	Shear failure	Sharp drop
S4-03	100	321	Shear failure	Sharp drop

The load-deflection diagram of the non-prestressed low-height UHP-FRC samples is shown in Figure 6.9. It can be seen that all the sleepers reinforced with GFRP bars have stiffer (greater slope) and stronger performance compared with the sleeper without GFRP reinforcement (S1-00). Indeed, S1-00 has the softest linear portion and the smallest first cracking load, whereas S3-01, with 4 bars of 10 mm diameter, has the stiffest and longest liner part and the highest first cracking load. The other sleepers, S2-01 and S4-03, with 2 and 5 bars of 14 mm diameter, respectively, have slightly softer linear performance than S2-01. The smaller initial load-deflection curve slope of the sleepers with 14 mm GFRP bars than the sleeper with 10 mm reinforcing bars is attributed to the stronger bond between the 10 mm GFRP bars and the UHP-FRC matrix.

The ultimate (peak) strengths of the UHP-FRC sleepers are also affected by the inclusion of the GFRP bars. It is observed in Figure 6.9 that sleeper S1-00 attains 75.6 kN of peak load, while S4-03, with the greatest reinforcement ratio, reaches the highest peak load of 320 kN. The second and third highest peak loads were attained by S3-01 (with 10 mm GFRP bars) and S2-01 (with 14 mm bars) with 266 kN and 225 kN, respectively. Hence, for a constant reinforcement ratio of 0.011, the sleeper with a thinner GFRP bar reaches a considerably higher peak load.
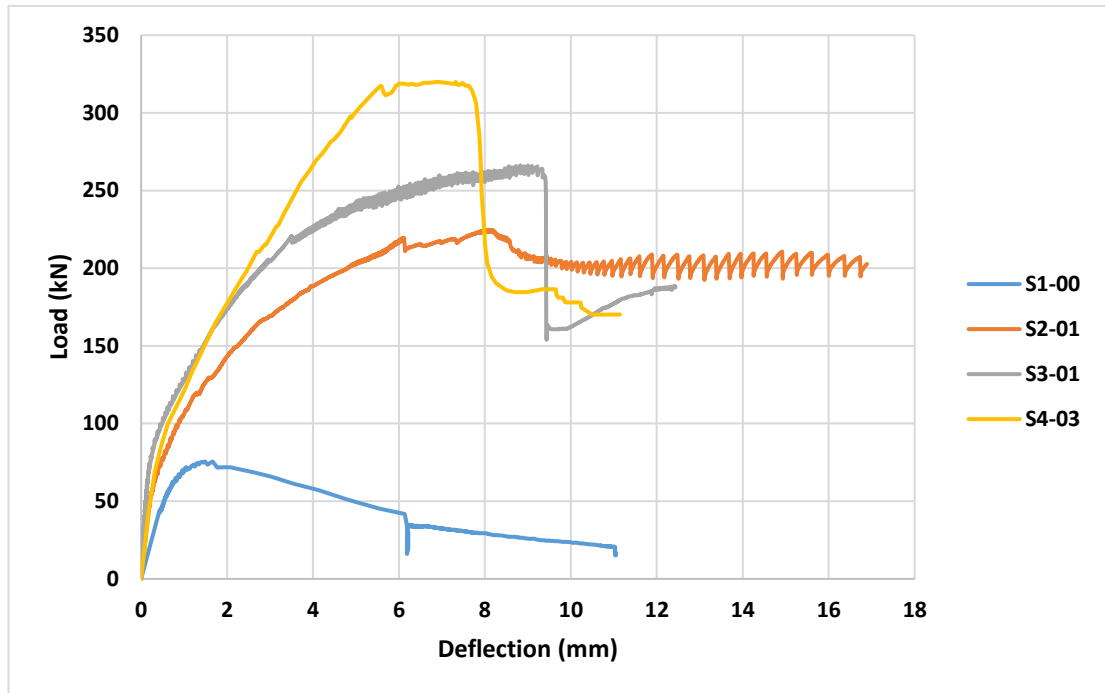
Figure 6.9 The load-deflection curves of the low-height UHP-FRC sleepers

6.6.2 Load-Strain Relationship

In this section, the relationships between the rail seat load and the compressive and tensile flexural strain magnitudes of the UHP-FRC sleepers at the rail-seat section are studied. The tensile and compressive strains are recorded by the 5-mm LVDT gauges with the gauge distance of 200 mm, called LVDT1 and LVDT2, on bottom and top of the front sleeper face, respectively (refer to Figure 6.6).

The load versus compressive strain curves of the prototype low-height UHP-FRC sleepers, are shown in Figure 6.10. It is seen that the compressive strain curve of sleeper S3-01 has several drastic jumps that may be due to the software error. Hence, the compressive strain values extracted from this sleeper are not reliable. However, as explained in Section 6.6.2 (refer to Table 6.4), the general performance and ultimate failure mode of S3-01 is similar to S4-03. Therefore, the same conclusions made for S4-03 can also apply to S3-01.

The maximum compressive strains of the sleepers at the peak load are listed in Table 6.5. As expected, the strain of sleeper S1-00 (without GFRP reinforcing bars) at the peak load is considerably less than the typical concrete crushing strain (0.003), which

indicates that the concrete crushing in compression does not occur at the peak load. However, sleepers S2-01 and S4-03 (and most probably sleeper S3-01), surpass the compressive strain of 0.003, which shows that the sleepers reinforced with the GFRP bars incur concrete crushing at the top of their mid-span sections.

The flexural tensile strains of the low-height UHP-FRC sleepers at the mid-span sections (recorded by LVDT 1 in Figure 6.6), are shown in Figure 6.11. Overall, the curves are similar to the load-deflection curves shown in Figure 6.9. The tensile strains of the sleepers at the peak load points are presented in Table 6.5. As was expected, S1-00 has the lowest strain at the peak point, while the other three sleepers (with GFRP reinforcing bars) have substantially higher strains at the peak load. Sleeper S2-01, which is expected to experience reinforcing bar slippage, has the highest tensile strain at the peak load.
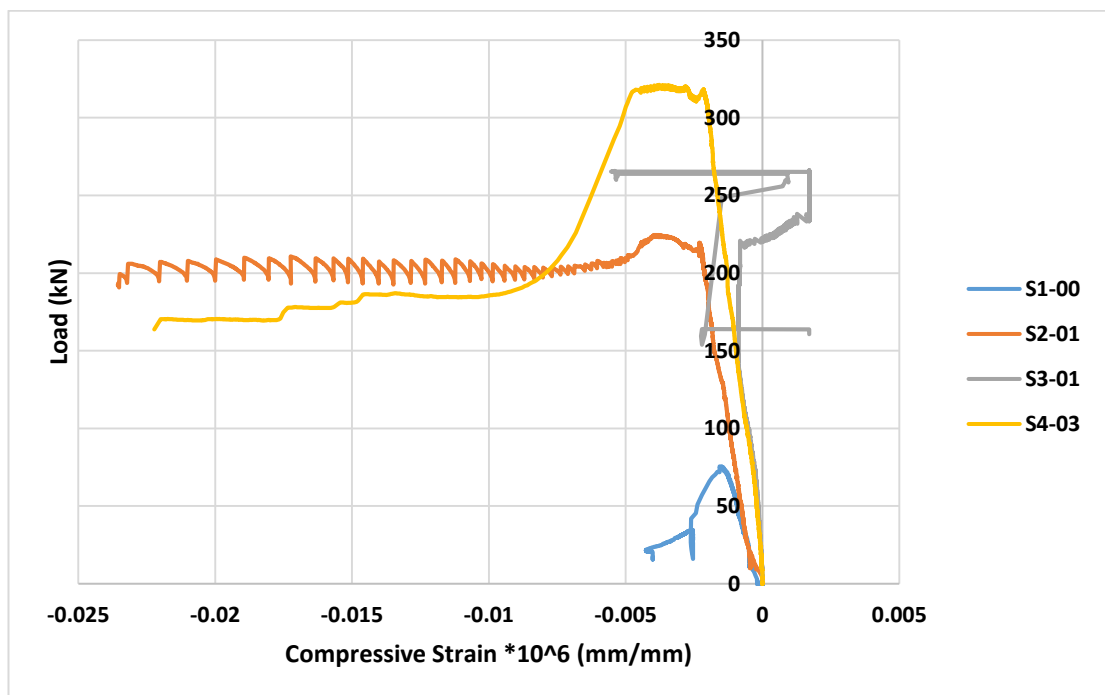
Figure 6.10 Load vs. compressive strain curves of the low-height UHP-FRC sleepers
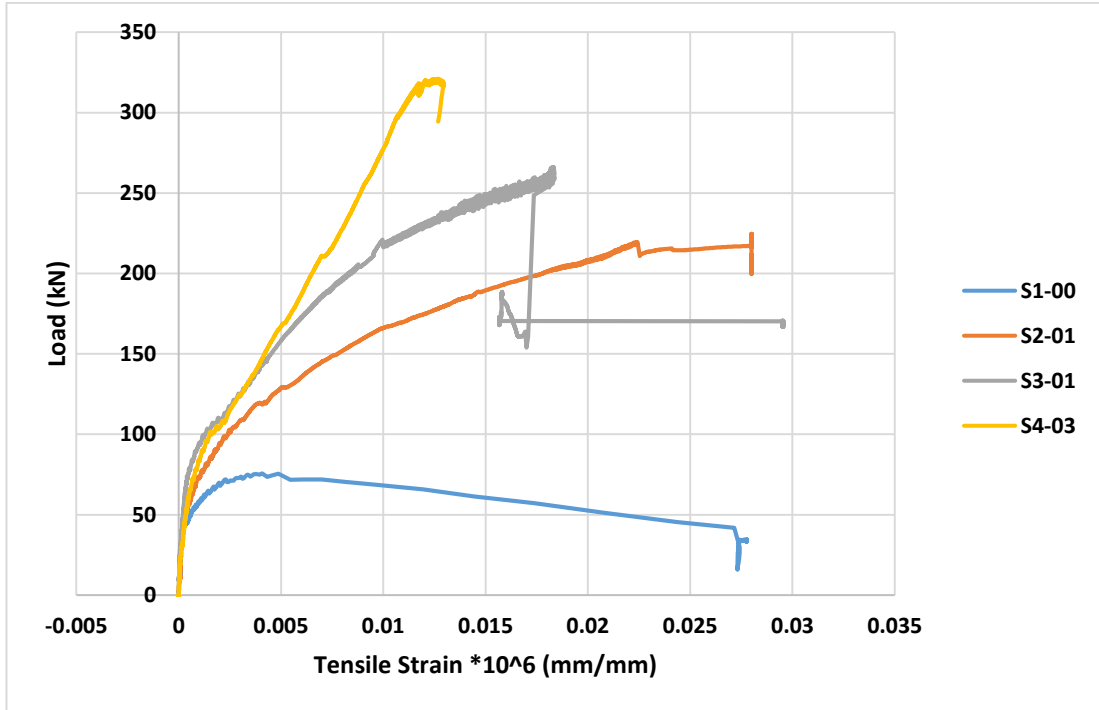
Figure 6.11 Load vs. tensile strain curves of the low-height UHP-FRC sleepers

Table 6.5 Maximum compressive and tensile strains of the low-height sleepers at the mid-span section

Sleeper	Compressive Strain at peak point	Tensile Strain at peak point
S1-00	- 0.00140	0.00408
S2-01	- 0.00386	0.0280
S3-01	----------	0.0183
S4-03	- 0.00378	0.0127

6.7 Estimation of the Cracking Moment (M_{cr})

According to the Australian Standard (AS1085.14, 2019), concrete sleepers must be designed to withstand the wheel loads without cracking. Hence, the cracking moment, M_{cr}, is a key parameter in the design of concrete sleepers rather than the ultimate moment (M_u). In this section, a simple section analysis process is proposed to determine the positive cracking moment of the UHP-FRC section reinforced with FRP

bars in congruence with the Australian Standard (AS-3600, 2018). The analysis steps are demonstrated below.

Step 1: Determine the transformed section as shown in the following figure. In Figure 6.12, n is the ratio of the elastic modulus of the FRP reinforcement to the elastic modulus of the UHP-FRC material. Also, $A_{FRP,t}$ and $A_{FRP,c}$ are the total section areas of the tension and compression FRP reinforcements, respectively. It should be noted that the UHP-FRC sleepers do not need top reinforcement as the UHP-FRC material has a high compressive strength, and the only reason for the inclusion of top reinforcement in Figure 6.12 is to consider the general case in the analysis.
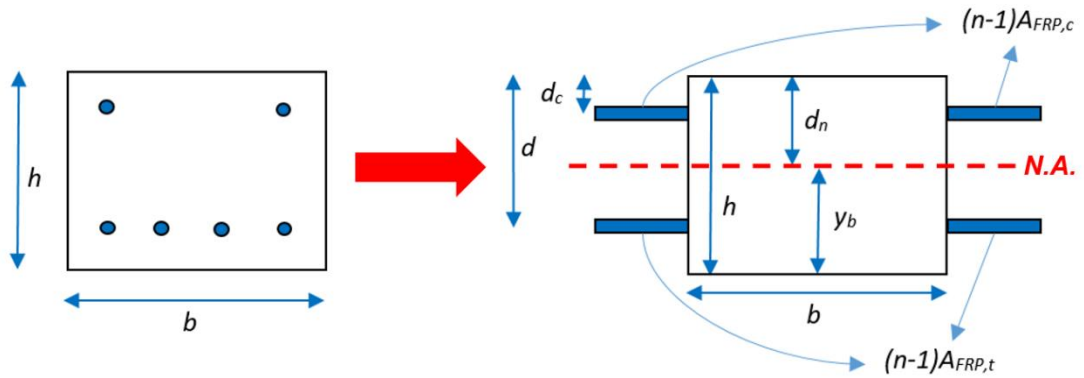
Figure 6.12 Transformed cross-section of the UHP-FRC sleeper reinforced with the FRP bars

Step 2: Determine the distance between the top fibre and the neutral axis (d_n) by solving Equation (6.3).

$$\frac{bd_n^2}{2} = \frac{b(h - d_n)^2}{2} + (n - 1)A_{FRP,t}(d - d_n) -$$
$$(n - 1)A_{FRP,c}(d_n - d_c)$$

(6.3)

Step 3: Calculate the gross moment of inertia of the transformed section (I_g) using Equation (6.4).

172

$$I_g = \frac{bh^3}{12} + bh(\frac{b}{2} - d_n)^2 + (n-1)A_{FRP,t}(d - d_n)^2 +$$

$$(n-1)A_{FRP,c}(d_n - d_c)^2$$

(6.4)

Step 4: Determine the cracking moment using Equation (6.5).

$$M_{cr} = \frac{(f'_{ct,f} - \sigma_{cs})I_g}{y_b}$$

(6.5)

where $f'_{ct,f}$ is the flexural cracking strength of the UHP-FRC material and can be obtained from the material bending tests or conservatively obtained using Equation (6.6) in congruence with the Australian Standard (AS-3600, 2018). In Chapter 3, it was shown that the flexural cracking strength of the UHP-FRC mix proposed in this research is around 13.2 MPa, while the ultimate flexural strength (modulus of rupture) of the UHP-FRC mix is normally around or above 20 MPa.

$$f'_{ct,f} = 0.6\sqrt{f'_c}$$

(6.6)

Also, σ_{cs} is the stress due to the shrinkage of the concrete. In the case of steel reinforcements, the magnitude of σ_{cs} can be obtained using Equation (6.7) according to AS 3600 (AS-3600, 2018).

$$\sigma_{cs} = \frac{(2.5\rho - 0.8\rho_c)}{1 + 50\rho}E_s\varepsilon^*_{cs}$$

(6.7)

where ε^*_{cs} is the shrinkage strain of the concrete that can be calculated according to Section 3 of AS3600 (AS-3600, 2018). Also, ρ and ρ_c are the tension and compression reinforcement ratios, respectively, and can be calculated using Equations (6.8) and (6.9).

$$\rho = \frac{A_{FRP,t}}{bd} \tag{6.8}$$

$$\rho_c = \frac{A_{FRP,c}}{bd} \tag{6.9}$$

It should be noted that as the elastic modulus of the GFRP bars (58-59 GPa) is considerably less than that of the steel reinforcements (200 GPa), the magnitude of σ_{cs} obtained from Equation (6.7) is considerably smaller when the GFRP bars are used instead of steel bars. Thus, in the case of UHP-FRC sleeper reinforced with GFRP bars, the influence of shrinkage in the magnitude of cracking moment can be neglected in comparison with the flexural cracking strength ($\sigma_{cs} << f'_{ct,f}$).

A comparison between the calculated and the experimental cracking moments of the low-height UHP-FRC sleepers is presented in the following table. It observed that except for the reference sample (S1-00), the analytical method according to AS 3600 (AS-3600, 2018) gives conservative results. As can be seen, the inclusion of the GFRP reinforcing bars theoretically does not have significant effects on the cracking moment of the low-profile UHP-FRC sleepers. However, the experimental results have proved the considerable enhancing effects of the GFRP reinforcements on the performance of the sleepers, especially in terms of the cracking and ultimate moment capacities.

Table 6.6 Comparison between the experimental and analytical cracking moment capacities of the low-profile UHP-FRC sleepers

Sleeper	M_{cr} (Experimental) (MPa)	M_{cr} (analytical) (MPa)
S1-00	9.69	12.4
S2-01	13.54	12.44
S3-01	18.53	12.45
S4-03	14.25	12.54

6.8 Design of Non-prestressed UHP-FRC Sleepers

The following procedure can be proposed in order to design a UHP-FRC sleeper with FRP bars:

1. Determine the design wheel load (R) and the design moments at the rail-seat and mid-span of the sleeper according to the Australian Standard (AS1085.14, 2019) as demonstrated in Section 3.3.
2. Choose the typical cross-section width and height of the sleeper.
3. Determine the minimum GFRP reinforcement ratio (using Equations (6.1) and (6.2)) and the number of GFRP bars accordingly. It should be noted that according to the experimental results reported in this Chapter, GFRP bars of 10 mm diameter are recommended.
4. Calculate the section cracking moment (M_{cr}) magnitudes by performing the section analysis at the rail-seat and the mid-span sections, according to the Australian Standard (AS-3600, 2018), as demonstrated in Section 6.7.
5. If the M_{cr} magnitudes calculated for the rail-seat and mid-span sections of the sleeper are less than the corresponding design moments, the cross-section dimensions and/or the number of GFRP bars must be increased and Steps 2 to 4 must be repeated.
6. If the M_{cr} magnitudes at the rail-seat and mid-span sections are higher than the design moment magnitudes, the designed sleeper is approved.

6.9 Discussion of the Results and Summary

In this chapter, the influence of the GFRP longitudinal reinforcing bars on the performance enhancement of low-height UHP-FRC sleepers under rail-seat positive moment loading was investigated. Four low-height UHP-FRC sleepers with the cross-section dimensions of 250 mm x 150 mm (width x height) and threereinforcement ratios, i.e. 0.00, 0.011, and 0.027, were produced. Two diameters of GFRP bars, 10 mm and 14 mm, were used in this investigation, and every two sleepers were made with a batch of UHP-FRC mix (two batches in total).

Overall, the experimental results proved that the application of the GFRP reinforcing bars could considerably improve the performance of the low-profile UHP-FRC

prototype sleepers. Especially, the cracking load (and thereby the cracking moment), which is a key characteristic in the design of concrete sleepers, has shown significant enhancement when GFRP reinforcing bars are used in the non-prestressed UHP-FRC prototype sleepers. It should be noted that according to the Australian Standard (AS1085.14, 2019), concrete sleepers are expected to withstand the design wheel loads without incurring structural cracks. The following main conclusions can be made as a results of adding the GFRP reinforcing bars:

- The cracking load increased from 68 to 130 kN (91% increase) and the peak load from 75.6 to 321 kN (325% increase).
- The sleepers reinforced with GFRP reinforcing bars experienced concrete crushing in compression at the rail-seat section at the peak load, which indicates that the compressive strength of the UHP-FRC material is fully used.

Sleepers S2-01 and S3-01 had an identical reinforcement ratio of 0.011 but were different in the number and diameter of the reinforcing GFRP bars. Indeed, S2-01 had two bars of 14 mm diameter, whereas S3-01 had four bars of 10 mm diameter. Comparing the test results of these two sleepers, it can be concluded that for the same reinforcement ratio, the UHP-FRC sleeper reinforced with GFRP bars of smaller diameters perform better than the UHP-FRC with fewer bars of bigger diameters. This difference is attributed to the better bond between the UHP-FRC material and the thinner GFRP bars. Indeed, according to the load-deflection diagram (refer to Figure 6.9), S2-01 with two 14 mm GFRP bars incurred multiple stepwise bar slippage that led to the fluctuating post-peak load-deflection curve.

Eventually, a simple step-by-step section-analysis process was presented to estimate the craking moment (M_{cr}) of the developed non-prestressed UHP-FRC sleepers reinforced with GFRP bars. Subsequently, a stepwise process was proposed to design the non-prestressed UHP-FRC sleepers, in compliance with the Australian Standards (AS1085.14, 2019, AS-3600, 2018).

Further studies considering wider ranges of reinforcement ratios and GFRP bar diameters are needed to determine the relationships between the bond strength of the reinforcing bars and the UHP-FRC matrix and the bar diameter and the reinforcement ratio of the GFRP bars.

CHAPTER 7
FINITE ELEMENT MODELLING OF CONCRETE SLEEPERS

7.1 Introduction

In this chapter, the performance of concrete sleepers under static rail-seat loading is simulated using the FEM. For this purpose, ABAQUS, which is well-known commercial finite element software, is utilised. It is expected that the concrete material model used by ABAQUS, called concrete damage plasticity (CDP), be suitable for the static modelling of concrete sleepers. The finite element modelling process is performed in two steps.

In the first step, the conventional prestressed concrete (PSC) sleeper is simulated and verified against the experimental results. The reason for starting with the of modelling of the PSC sleeper is that this type of sleeper is made with the conventional high-performance concrete which is considerably simpler than the UHP-FRC material in regard to the material modelling process. For this purpose, the standard rail-seat test results of a number of heavy-haul PSC sleepers tested at the structural lab of the UOW are reported. The material test results carried out on the core samples extracted from these sleepers are used for the concrete material modelling. Also, the prestressing forces of the sleepers are measured and applied to the prestressing wires in the FE model. Eventually, the load-deflection curves obtained from the experiments and the FE modelling are compared in order to verify the accuracy of the FE modelling technique.

After confirming that the CDP material model works well for conventional prestressed concrete, in the second step, the non-prestressed UHP-FRC prototype sample is simulated and verified against the experimental rail-seat static test result obtained from the prototype sample S2-2. The material model is created based on the standard material test results except for the direct tensile behaviour of the UHP FRC sample. The direct tensile behaviour is determined using the direct tensile test results presented in this chapter, as well as the reverse engineering method (such that the load-deflection curve obtained from the rail-seat test agrees well with the FE load-deflection curve).

7.2 Modelling of the Prestressed Concrete Sleepers

In this section, the finite element modelling of PSC sleepers using ABAQUS is investigated. For this purpose, the PSC sleepers, provided by BHP Iron Ore Pty Ltd., and the experimental test results are reported in Appendix A. Then, the FE model is developed in ABAQUS. Eventually, the experimental and the FE results (the load-deflection curves) are compared with each other to validate the finite element modelling technique.

7.2.1 Finite Element Modelling

In this section, the numerical modelling process of the heavy-haul PSC sleepers demonstrated in the previous section is presented. The well-known commercial finite element code, ABAQUS is utilised in this research for the modelling. Since the loading rate is slow, the static implicit solving technique is expected to be adequate for the analysis of the sleeper model, as recommended by several researchers (e.g. (You et al., 2019)).

7.2.1.1 Geometry of the Heavy Haul PSC Sleeper

The Geometry of the sleeper is shown in Figure 7.1. It is observed that the soffit of the sleeper has a constant width of 300 mm while the top width of the sleeper cross-section varies over the sleeper length. The centre to centre distance between the two rail seats is 1510, which is normal for a standard gauge sleeper (with a standard gauge distance of 1435 mm). Figure 7.2 shows the full 3D model of the heavy-haul sleeper created in ABAQUS.
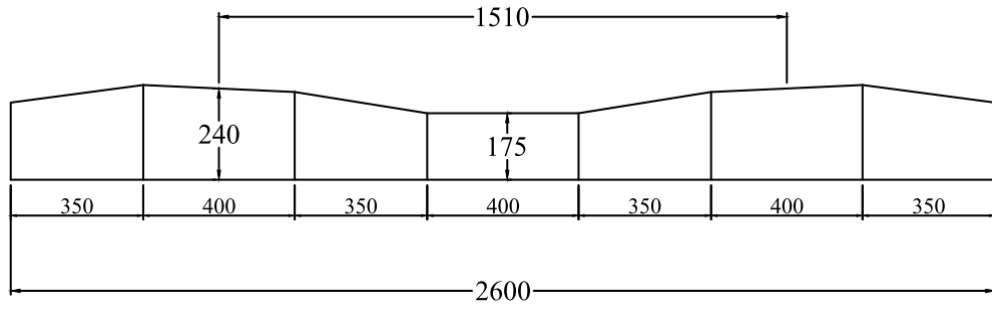
(a) Elevation view
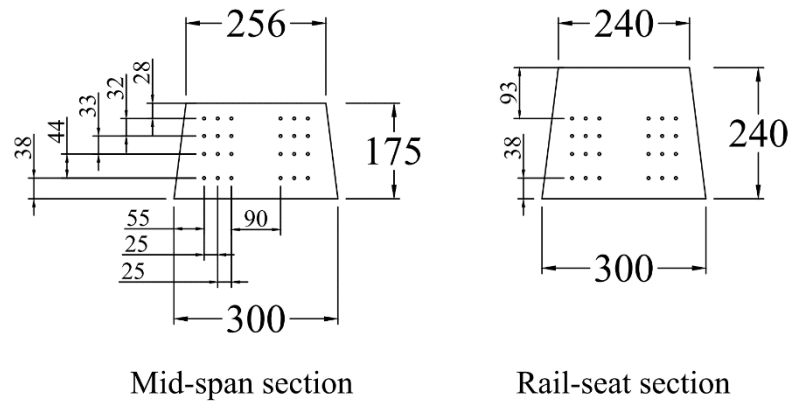
Mid-span section   Rail-seat section

(b) Rail-seat and Mid-span sections

Figure 7.1 Detailed dimensions of the heavy-haul PSC sleeper (dimensions in millimetres)
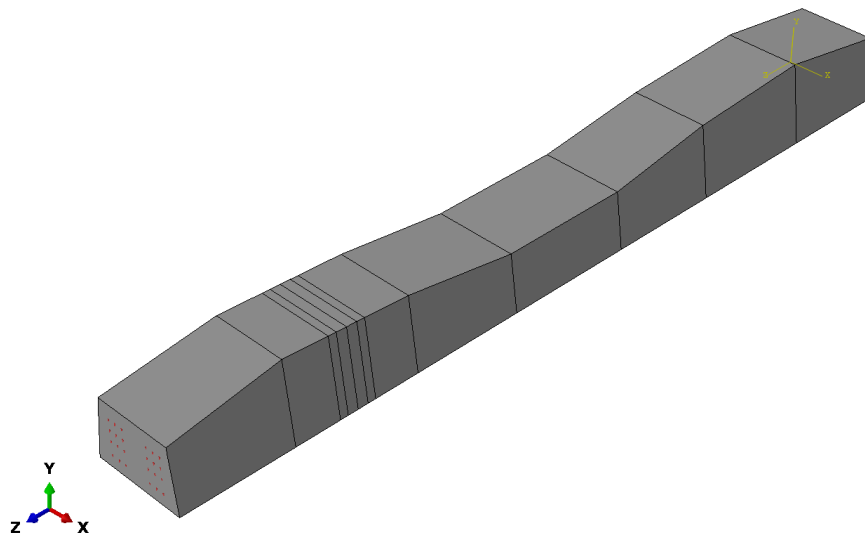
Figure 7.2 The 3D model of the heavy-haul PSC sleeper

7.2.1.2 Material Model

The average of the corrected compressive strengths determined for the sleepers, P4, P5, and P6 through the core tests are 64.93, 66.65, and 66.82 (MPa), respectively (refer to Table A.4). The average of these values, i.e. 66.13 MPa, is selected for the FE modelling. According to AS 3600 (AS-3600, 2018), the elastic modulus of a concrete material (E_c) with the compressive strength higher than 40 MPa can be determined based on its mass per unit volume (ρ) and the mean compressive strength (f_{cmi}), using Equation (7.1):

$$E_c = (\rho^{1.5}) \times (0.024\sqrt{f_{cmi}} + 0.12) \tag{7.1}$$

Also, the tensile strength of the concrete material (f_{ct}) can be determined according to its mean compressive strength using Equation (7.2) (AS-3600, 2018):

$$f_{ct} = 0.36 \times \sqrt{f_{cmi}} \tag{7.2}$$

According to Voo and Foster (2006), the magnitude of the fracture energy of concrete (G_f) can also be estimated based on the mean compressive strength, using Equation (7.3):

$$G_f = 1.92 \times f_{cmi} \tag{7.3}$$

In this manner, the mechanical characteristics of the concrete material are summarised in Table 7.1. It should be noted that the mass per unit volume of concrete (ρ) and the Poisson's ratio (v) are assumed as 2400 kg/m3 and 0.2, respectively, which are typical values for concrete materials.

Table 7.1 Mechanical properties of the concrete material of the heavy-haul sleeper

ρ (kg/m3)	ν	f_{cmi} (MPa)	E_c (MPa)	f_{ct} (MPa)	G_f (N/m)
2400	0.2	66.13	37056	2.93	127

The concrete damage plasticity (CDP) material model developed for ABAQUS (ABAQUS, 2013) is used for modelling the concrete component of the heavy-haul PSC sleeper. The tensile behaviour of the concrete material can be defined by the tensile strength (f_{ct}) and the fracture energy (G_f) of the concrete material. On the other hand, the behaviour of concrete in unidirectional compression can be defined in ABAQUS as compressive stress vs strain data. For this purpose, the relationship between stress (f_c) and strain (ε) can be determined using the well-known model proposed by Popovics (Popovics, 1973), as demonstrated in Equation (7.4):

$$f = E_c \varepsilon \, \frac{n-1}{n-1+\left(\frac{\varepsilon}{\varepsilon_0}\right)^n}$$

(7.4)

Where ε_0 can be determined using Equation (7.5):

$$f = 2.7 \times 10^{-4} \times \sqrt[4]{f_0}$$

(7.5)

Where f_0 can be calculated using Equation (7.6):

$$f_0 = 145.038 \times f_{cmi}$$

(7.6)

Also, the value of n can be calibrated for every concrete material such that the amount of the peak compressive strength of the stress-strain diagram is equal to the mean compressive strength (f_{cmi}). In this study, the value of n is found to be equal to 3.038,

and the stress-strain diagram is shown in Figure 7.3. The compressive stress-strain data points can be directly inserted into ABAQUS.
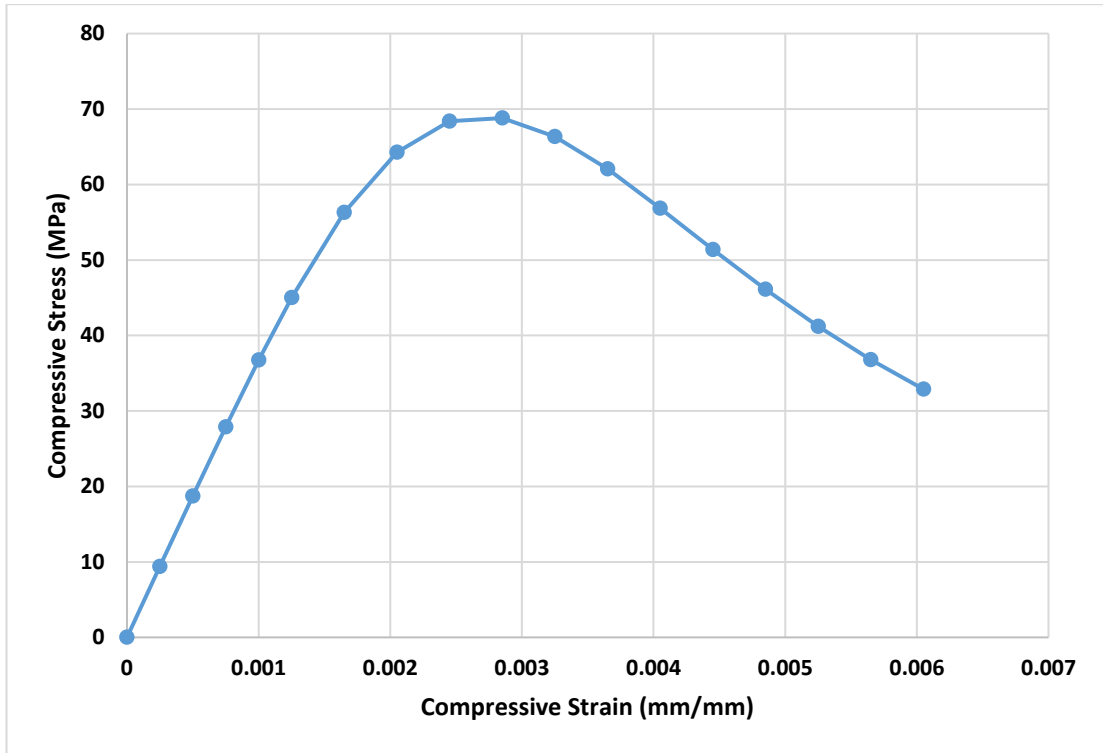
Figure 7.3 The unidirectional stress-strain data points of the concrete material for FE modelling of the heavy-haul PSC sleepers

The typical mechanical properties of the prestressing tendons are presented in Table 7.2. These values are directly inserted in ABAQUS to develop a bilinear material model for the prestressing tendons.

Table 7.2 Mechanical properties of the prestressing tendons of the heavy-haul PSC sleepers

Elastic modulus (GPa)	Poisson's ratio	Yield stress (MPa)	Ultimate tensile strength (MPa)
200	0.3	1535.5	1850

7.2.1.3 Interaction Properties, Boundary Conditions and Loading

In this study, due to the symmetry of the cross-section, only half of the sleeper is analysed to save the analysis time. So, it is important to define the correct boundary conditions for the half-model to obtain correct results from the FE analysis. The boundary conditions of the half model are shown in Figure 7.4. The defined boundary conditions to model the supported condition of the actual rail-seat positive moment test set-up are shown in Figure 7.4-b. Also, the loading process is simulated with a downward displacement applied to the two areas that the loading bars are placed in the actual rail-seat positive moment testing.
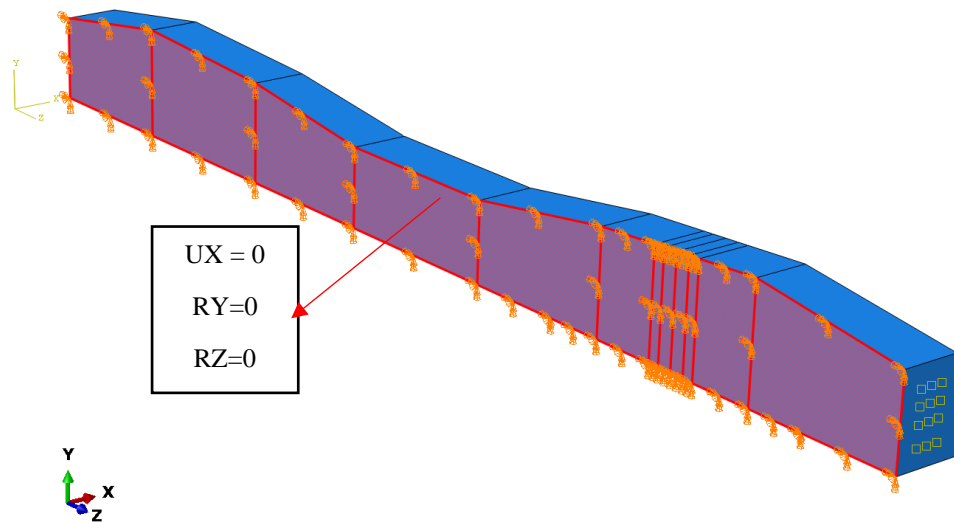
(a) symmetric boundary condition for half-model

Figure 7.4 Boundary conditions applied to the FE model
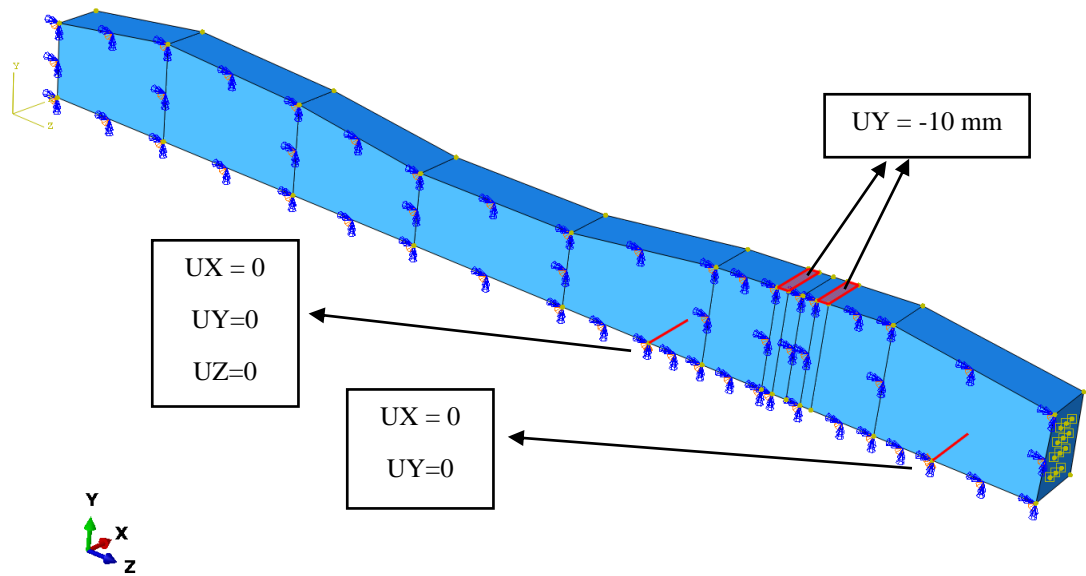
(b) boundary conditions at the supports and loading areas

Figure 7.4 Boundary conditions applied to the FE model

The Prestressing force is applied to the tendons using the keyword "Predefined Field", which enables the application of the desired prestress magnitude in the longitudinal direction of the tendons (ABAQUS, 2013). Herein, the average prestress loss of 13% (refer to Table A.3) has been considered. It should be noted that the 13% stress loss that has been found from the decompression testing of the heavy-haul PSC sleepers (refer to Appendix A) is in good agreement with the considered prestress loss in a previous research on the FE modelling of PSC sleepers, which was 12% (You et al., 2019). The initial prestressing force of each tendon is 23.75 kN which is equivalent to the prestress magnitude of 1195.2 MPa. Hence, the applied prestress in the FE model (after applying 13% of prestress loss) is 1039.8 MPa. The keyword "Embedded Region" (ABAQUS, 2013) is used to define the perfect bond (interaction) between the tendons and the concrete parts.

7.2.1.4 Elements and Mesh Properties

In this study, the 8-node linear solid element with reduced integration, named as C3D8R keyword in ABAQUS (ABAQUS, 2013), is selected for the concrete component of the heavy-haul PSC sleeper. This type of solid element has proved

adequate in the dynamic modelling of PSC sleepers in the previous research (Kaewunruen et al., 2018b), and it is expected that it leads to satisfactory results for the static/implicit analysis in this research. The linear 2-node truss element, named with the keyword of T3D2 in ABAQUS, is selected for modelling the prestressing tendons. The 3D meshed view of the half-model of the PSC sleeper is shown in Figure 7.5. As can be seen, the area around the front rail seat, where the rail-seat positive moment static load is applied, has a finer mesh to reach more accurate results. On the other hand, the other rail-seat area and the central part of the sleeper have coarser mesh as they have less influence on the final results. The half-sleeper FE model has a total of 25,728 linear hexahedral solid elements (C3D8R) and 3120 linear truss elements (T3D2).
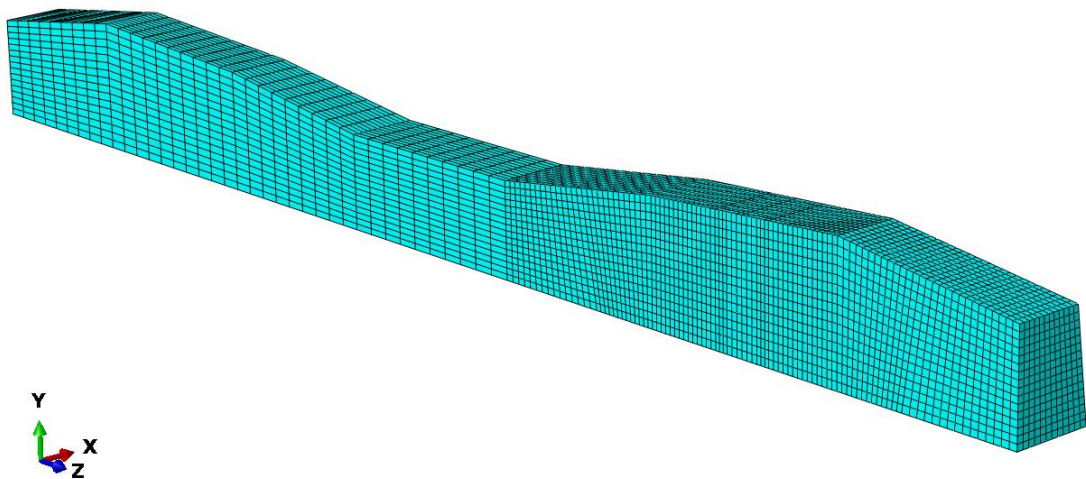
Figure 7.5 Mesh refinement of the heavy-haul PSC sleeper model

7.2.2 FE Analysis and Verification of the Results

In this research, the static/implicit analysis solving method, called with the keyword "Static, General" in ABAQUS, is applied for the FE analysis of the heavy-haul PSC sleeper model. A comparison between the load-deflection curves obtained from the standard rail-seat testing of the heavy-haul PSC sleepers, i.e. sleepers P4, P5 and P6 (refer to Figure A.3), and the one obtained from the analysis of the FE model, is given in Figure 7.6. It is observed that the linear-elastic parts of the experimental and FE curves have similar angles. As the non-linearity starts, the experimental and FE curves

186

show slightly different trends. However, the FE curve generally agrees with the experimental curves. A comparison between the cracking and ultimate rail-seat loads is presented in Table 7.3. It can be found that the cracking load obtained by the FE modelling is 15.5% higher than the average experimental one; however, the experimental and FE ultimate cracking loads have merely a slight difference (with 1.9% error). Hence, it can be concluded that the concrete damage plasticity model is adequate for the FE analysis of PSC sleepers under static loading.

It is important to note that although the concrete damage plasticity (CDP) material model takes into account the damages in concrete components both in compression and tension, it does not give a visual illustration of the cracks in concrete. Indeed, using the CDP material model, instead of the visible cracks, the damage contours in compression and tension are available and can represent the possible concrete cracks. The damage contours of the heavy-haul PSC sleeper in compression and tension are shown in Figure 7.7. The diagonal failure lines (due to shear) can be seen in the damage contours that agrees with the actual failed heavy-haul PSC sleepers (refer to Figure A.4). However, in experiments, the shear cracks appeared only on one side of the PSC sleeper, while in the FE model, the damage due to the shear forms on both sides. According to the discussion presented in Appendix A (Section A.2) about the variation of the prestressing force over the length of the PSC sleepers, further studies on the magnitudes of the prestressing force at different locations of the PSC sleeper over its length are needed to reach more accurate failure models. It should be noted that the previous numerical study carried out by You et al. (You et al., 2019) also showed a similar failure mode to the current FE analysis, i.e. shear cracks (failure) forming on both sides of the rail-seat area.
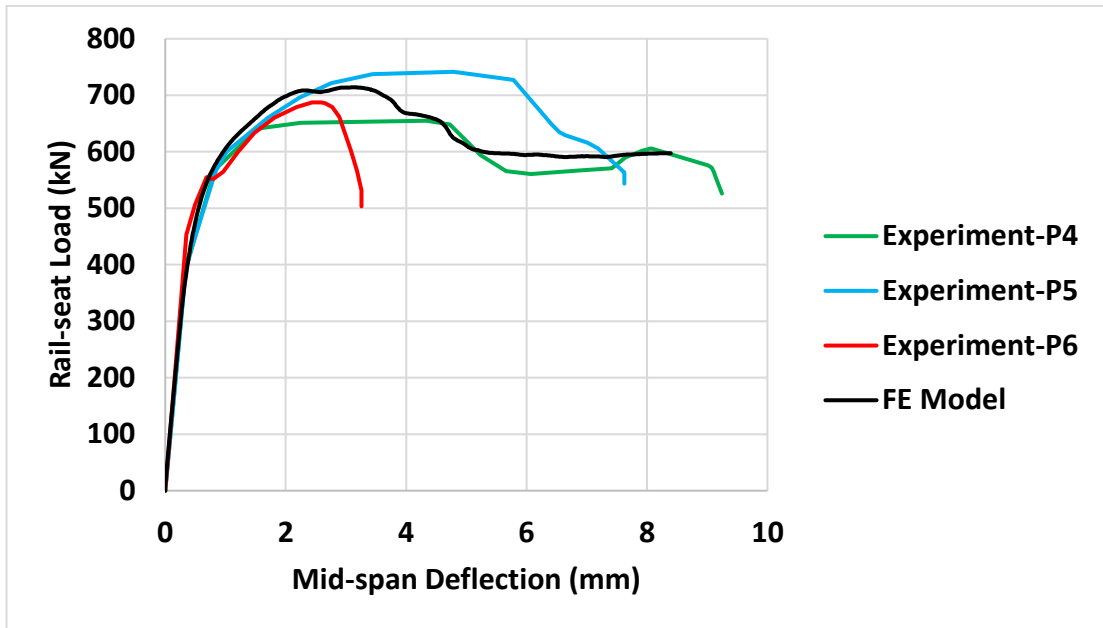
Figure 7.6 Comparison of the experimental and FE load-deflection curves

Table 7.3 Comparison of the cracking and ultimate rail-seat loads obtained by the experiment and the FE modelling

	Cracking Load (kN)	Ultimate Load (kN)
Experiment (average of three sleepers, P4, P5 and P6)	428.7	700.6
FE	495.2	714.0
Error (%)	15.5 %	1.9 %

DAMAGEC
(Avg: 75%)
+8.051e-01
+7.380e-01
+6.710e-01
+6.039e-01
+5.368e-01
+4.697e-01
+4.026e-01
+3.355e-01
+2.684e-01
+2.013e-01
+1.342e-01
+6.710e-02
+0.000e+00

(a) damage in compression

DAMAGET
(Avg: 75%)
+7.516e-01
+6.889e-01
+6.263e-01
+5.637e-01
+5.010e-01
+4.384e-01
+3.758e-01
+3.132e-01
+2.505e-01
+1.879e-01
+1.253e-01
+6.263e-02
+0.000e+00
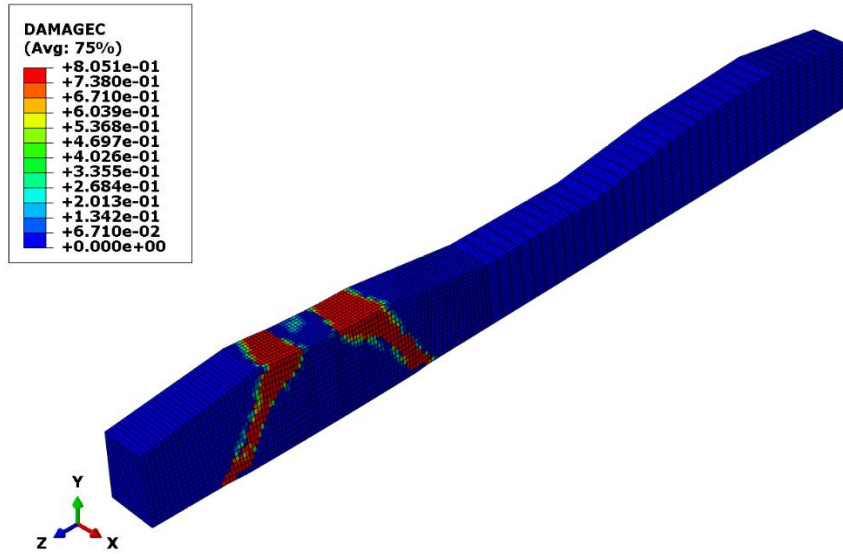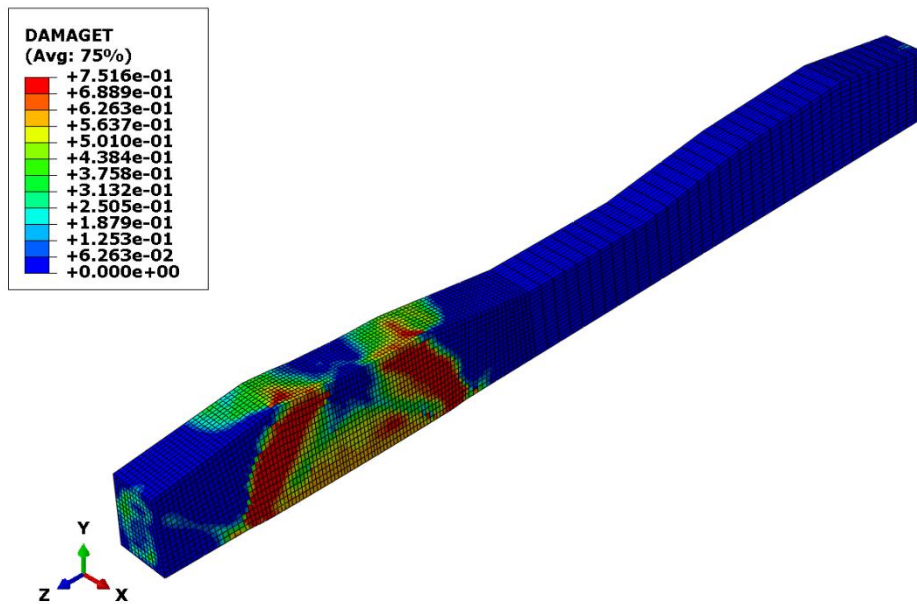
(b) damage in tension

Figure 7.7 Damage contours of the heavy-haul PSC sleeper

The heavy-haul PSC sleepers modelled in this section are made with the conventional high-performance concrete (HPC) without steel fibres, which is simpler than the UHP-FRC material in terms of the material model. Hence, as the first step, the FE model of this type of sleeper has been validated against the experimental rail-seat test results

before embarking on the UHP-FRC prototype sleepers. In the following section, the FE modelling of the UHP-FRC prototype sleeper is presented.

7.3 Modelling of the UHP-FRC Prototype Sleeper

In this section, the FE element modelling procedure of the non-prestressed prototype UHP-FRC sample, S2-S2, is presented. As demonstrated in Section 4.3, S2-2 is a prototype sample with a simple prismatic shape with the cross-section width and height of 250 mm and 220 mm, respectively, and the length of 1060 mm. Also, this sample does not contain prestressing tendons or reinforcing bars. In other words, S2-S2 merely consists of one component, which is the UHP-FRC material. Thus, the FE modelling and analysis of this sample seem simpler than the heavy-haul PSC sleepers reported in the previous section. However, the performance of the UHP-FRC material in compression and tension is more complicated than that of the high-performance concrete (HPS) material by which PSC sleepers are made. Hence, the main challenge of this simulation is to obtain adequate material properties input data such that the results of the FE analysis is of acceptable accuracy.

Indeed, except for the material input data, the FE modelling process of the UHP-FRC prototype sample (S2-S2) is similar to the PSC sleeper modelling process described in the previous section. The liner 8-node solid element with reduced integral, C3D8R, is used for the meshing process. Also, the same boundary conditions are exploited to simulate the supports and the loading method (refer to Figure 7.4). Similarly, the same concrete material model, i.e. CDP, is utilised in ABAQUS to simulate the performance of the UHP-FRC material performance. However, the challenge is to determine the correct material input data, as stated above. This problem is solved in two steps. Firstly, the input compressive stress-strain data obtained from the material testing is validated against the corresponding compressive material test result. After verifying the adequacy of the compressive stress-strain data, the tensile stress-strain data is determined according to the experimental results obtained from the standard static rail-seat testing of the prototype sample, S2-S2.

7.3.1 Compressive Stress-Strain Input Data

Herein, the input data for modelling the performance of the UHP-FRC material under compression is developed and validated against the compression material test results. The compressive stress-strain data obtained from the three cylindrical UHP-FRC material samples with a diameter of 100 mm and a height of 200 mm are shown in Figure 7.8. The compression testing process has been carried out according to AS1012-9 (AS-1012.9, 1999), as demonstrated in Section 3.5. The strains are obtained from the deflection recorded by the LVDT cage apparatus (similar to what was shown in Figure 3.13) divided by the gauge distance, which is 123 mm. Averaging the stress magnitudes, the stress-strain curve is obtained, which is shown with the black curve. The data points of these curves are inserted directly into ABAQUS as the input data for the unidirectional performance under compression.
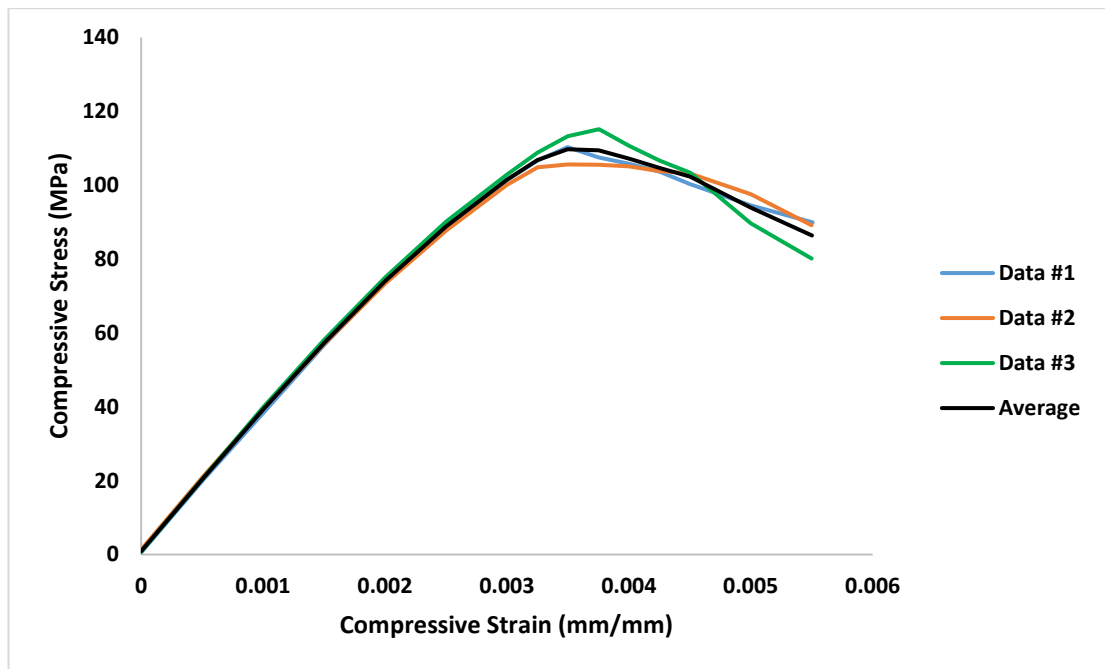
Figure 7.8 The compressive stress-strain curves obtained from the UHP-FRC compression tests

Other properties of the UHP-FRC material that can be inserted in ABAQUS as the input data for the CDP material model are given in Table 7.4. The Poisson ratio (ν) is assumed as 0.2. The values of mass per unit volume (ρ), mean compressive strength (f_{cmi}), and flexural tensile strength (f_{cf}), have been obtained from material tests,

reported in Table 4.2 (Batch 2). The elastic modulus is taken as 38.6 GPa according to the initial part of the average stress-strain curve shown in Figure 7.8. The magnitude of the (direct) tensile strength of the UHP-FRC material (f_{ct}), is obtained from its flexural strength as according to the Australian Standard (AS-3600, 2018), the ratio of f_{ct} / f_{cf} is equal to 0.6. Hence, the tensile strength (f_{ct}) is determined as 12.6 MPa (0.6 * 21 = 12.6). The magnitude of G_f is determined by Equation 7.3. It should be noted that at this step, only the compressive material model is studied. The more accurate tensile input data for the UHP-FRC material model is determined in the next section.

Table 7.4 Basic material input properties of the UHP-FRC mix

ρ (kg/m3)	ν	f_{cmi} (MPa)	f_{cf} (MPa)	E_c (GPa)	f_{ct} (MPa)	G_f (N/m)
2418	0.2	117	21	38.6	12.6	225

The FE model of the cylinder UHP-FRC sample with the defined boundary conditions is shown in Figure 7.9. It is observed that the bottom face of the model is fixed in all three directions, and the load is applied to the top face of the sample in the form of applied deflection in the downward direction (-UY). Also, two points are highlighted where the vertical deflections are recorded. These two points are at a distance of 123 mm from each other, similar to the gauge distance of the LVDT cage apparatus. Also, the mesh refinement of the sample is shown in Figure 7.10. It can be seen that wedge elements are generated at the centre (core) zone of the sample cross-section. In total, 2436 linear 6-node wedge elements, called with the keyword "C3D6", and 31,668 linear 8-node hexahedral elements, called with the keyword "C3D8R", are used in the FE cylinder model.
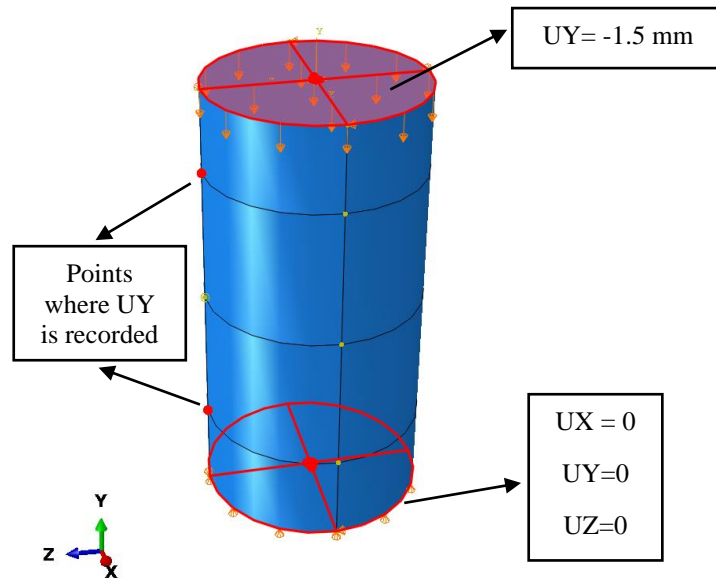
Figure 7.9 The FE model of the cylinder sample of the UHP-FRC material with the defined boundary conditions
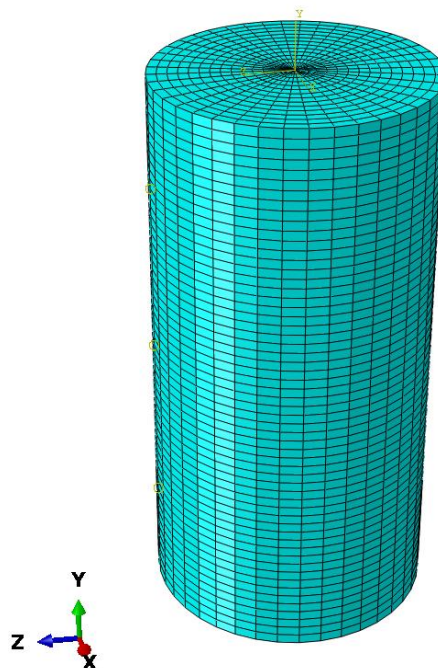
Figure 7.10 Mesh refinement view of the FE model of the UHP-FRC cylinder sample

A comparison between the unidirectional compressive load-deflection diagrams obtained from the material testing (the average curve) and the FE analysis is presented

in Figure 7.11. In both cases, the deflection is recorded as the relative displacement between the two points at a distance of 123 mm (see Figure 7.9). It is seen that the load-deflection curve obtained by the FE analysis is in good agreement with the material test result. Also, a comparison between the ultimate failure of the UHP-FRC material sample under the unidirectional compression test and the Von-Mises contour obtained from the FE modelling is given in Figure 7.12. The diagonal failure line obtained from the material testing is in good agreement with the Von-Mises contour. Hence, it can be deduced that the FE modelling using the CDP material model in ABAQUS is adequate for simulating the performance of the UHP-FRC material under universal compression.
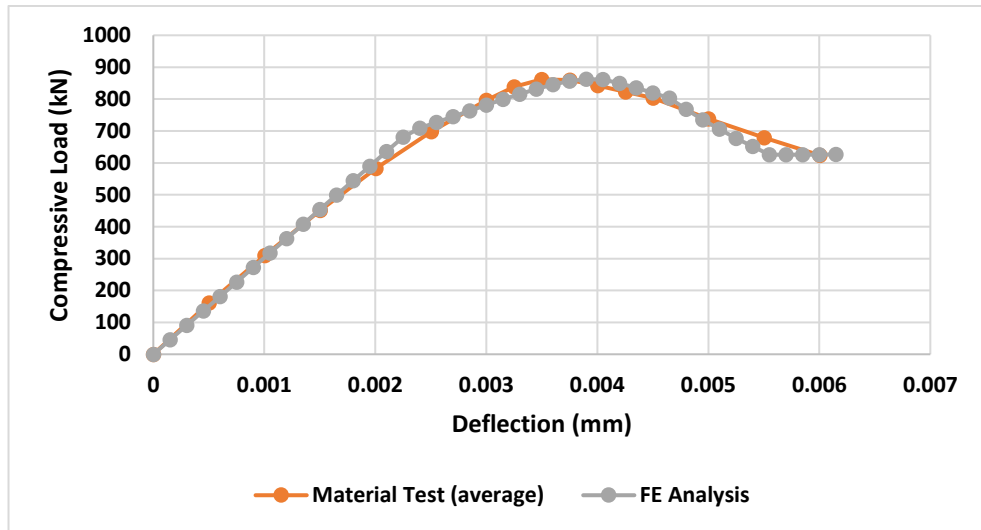
Figure 7.11 The compressive load-deflection curves obtained by the material testing and the FE analysis
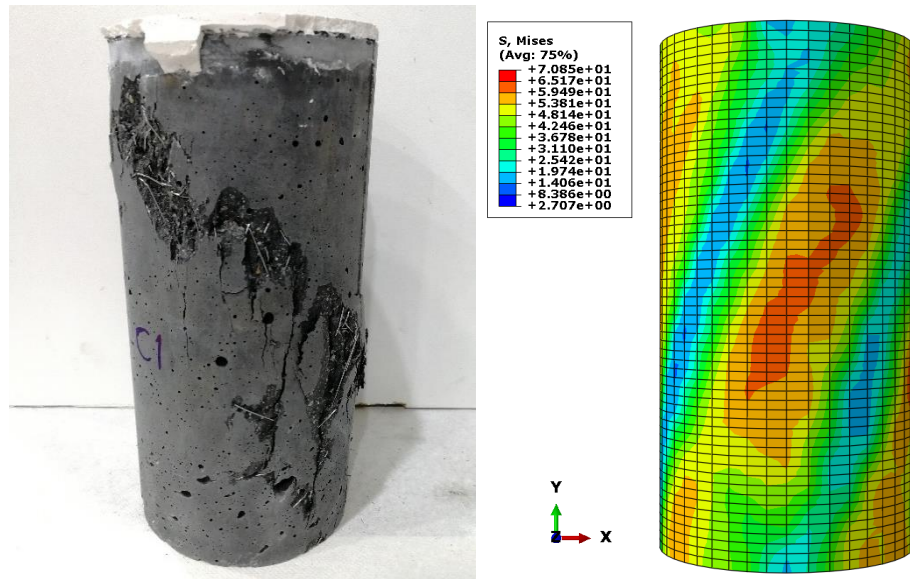
<center>(a) experimental failure   (b) FE Von-Mises contour</center>

<center>Figure 7.12 The failure mode of the cylinder UHP-FRC sample</center>

7.3.2 Tensile Stress-Strain Input Data

In this section, the performance of the UHP-FRC material under direct tension is studied. This investigation aims to determine adequate tensile stress-strain input data for the FE material modelling of the UHP-FRC prototype sample, S2-S2. The 3D view of the FE model of S1-S1 is shown in Figure 7.13. It can be found that the boundary conditions for modelling the supports and the rail-seat loading are similar to what was demonstrated in Section 7.2 for the PSC sleepers. In total, 17850 8-node linear solid elements, C3D8R, are used in the FE model.
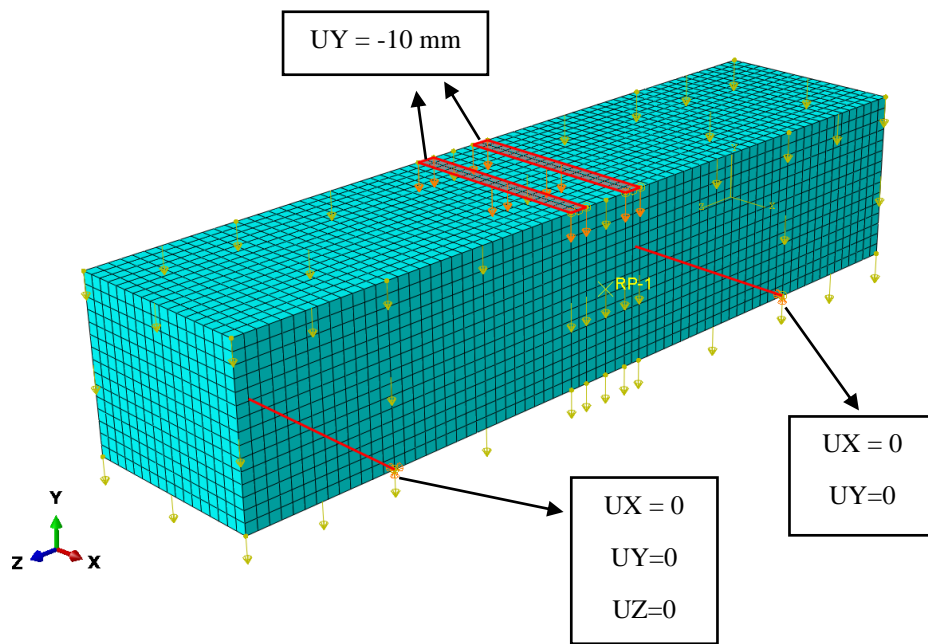
Figure 7.13 The FE model of the UHP-FRC prototype sample, S2-S2

As aforementioned, it is expected that the non-linear performance of the UHP-FRC material in tension is more complicated than the conventional high-performance concrete. Therefore, a type of direct tensile test (DTT) set-up is developed in this research to acquire a better understanding of the UHP-FRC material, as demonstrated in the following section.

7.3.2.1 Development of a Direct Tensile Test (DTT) Set-up

The designed shape and dimensions of the UHP-FRC sample for performing the DTT tests are shown in Figure 7.14-a. Overall, it is seen that the sample has a dog-bone shape (the middle area of the sample is narrower than the end parts) which was recommended by several researchers (e.g. (Hassan et al., 2012, Mahmud et al., 2013, Singh et al., 2017)). Indeed, the cross-section of the sample is of constant size in one direction (100 mm) while in the other direction is of varied dimensions of 110 mm at the two ends and 70 mm at the centre. It is observed that the smallest cross-section dimension is selected as 70 mm, which is two times the nominal length of the steel fibres used in the UHP-FRC mix design, according to Hassan et al. (Hassan et al.,

2012). At each end of the sample, an embedded metal bar with four welded anchors is placed, as suggested by Goaiz et al. (2019). The produced samples are shown in Figure 7.14-b.

The DTT set-up of the UHP-FRC samples is shown in Figure 7.15. It is shown that the universal tension is applied to the two built-in metal bars extending from the ends of the DTT sample through the universal joints. Also, the DIC camera, with the commercial name of Mercury Camera, is utilised to record the elongation of the sample. The 500 kN hydraulic testing machine, with the commercial name of Instron, is utilised to perform the static tensile loading at the slow rate of 0.2 mm/min to avoid any dynamic reactions. The failure modes of the direct tensile samples are shown in Figure 7.16. It is observed that the failure (tensile cracking) of the samples has been successfully directed to the reduced section area.
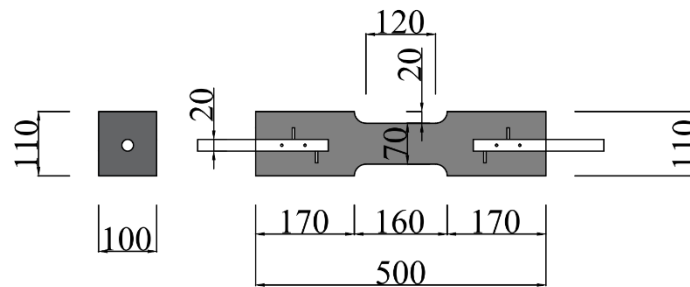
(a) detailed dimensions (all dimensions in mm)

(b) manufactured sample

Figure 7.14 Design and production of DTT samples

Figure 7.15 Direct tensile test (DTT) set-up
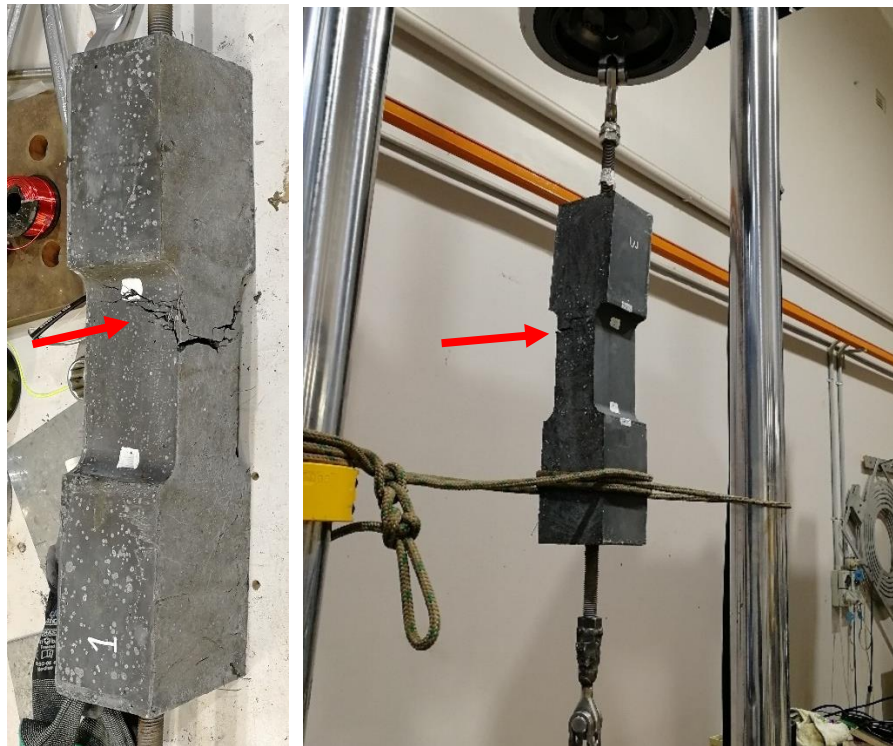
(a) sample DTT#1   (b) sample DTT#2

Figure 7.16 Failure modes of the direct tensile test (DTT) samples

The tensile stress versus the non-linear displacement curves obtained from testing the two UHP-FRC samples are shown in Figure 7.17. The average of the two curves is demonstrated with a black curve, and a simplified multi-linear curve is proposed to fit the average curve. As can be seen, in both of the tests, the non-linearity starts with a marginal drop in the stress-displacement curve. Then, the stress magnitudes increase until it reaches a flat line, followed by a downward trend. The tensile stress-displacement data points of the simplified diagram can be directly inserted in ABAQUS as the tabular input data for modelling the tensile behaviour of the UHP-FRC material. In the next section, the accuracy of the multi-linear input data determined based on the DTT test results is investigated.
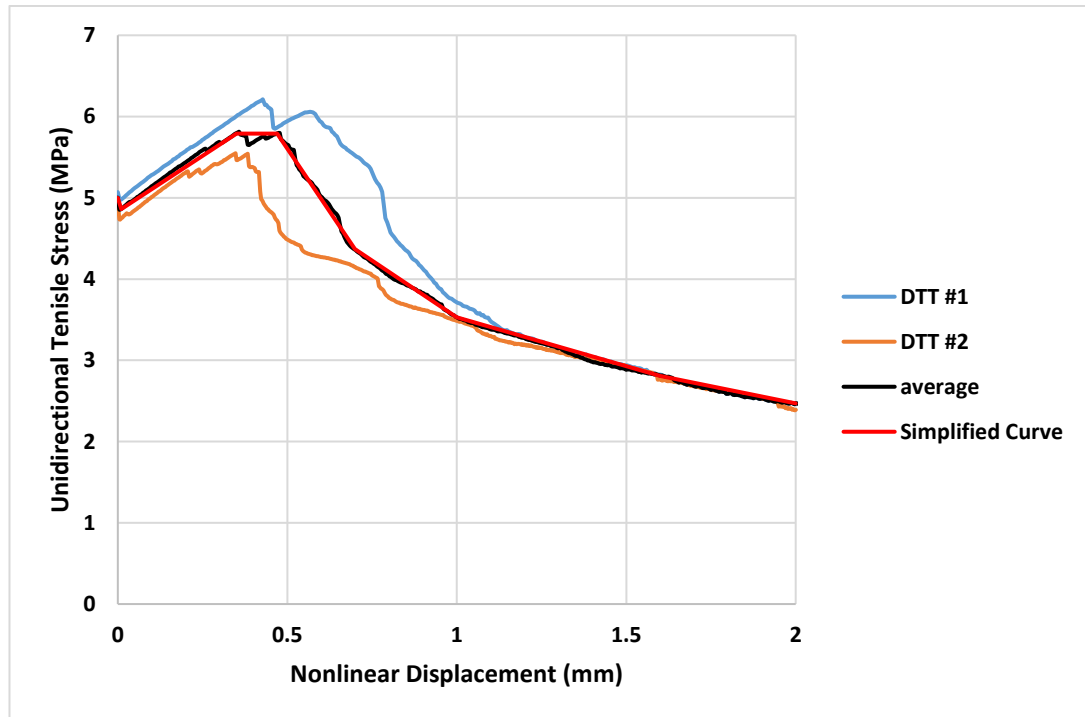
Figure 7.17 The direct tensile stress-strain curves of the UHP-FRC samples

7.3.2.2 Verification of the FE Analysis Results

Similar to the previous sections, static/implicit analysis is utilised for conducting the FE analyses in ABAQUS. Figure 7.18 compares the vertical load vs the deflection curves obtained from the FE analysis and the rail-seat positive moment testing of the prototype UHP-FRC sample, S2-S2. As was expected, the tensile behaviour input data

determined from the DTT test does not lead to an acceptable prediction of the load-deflection performance of the UHP-FRC sample, S2-S2, under static rail-seat load. Indeed, the maximum rail-seat load estimated by the DTT input data is significantly lower than the experimental one. Herein, a tensile material model proposed by Fujikake et al. (Fujikake et al., 2006a) for a UHP-FRC material is investigated. The material model consists of three parts, as shown in Figure 7.19. It can be seen in Figure 7.18 that in contrast to the tensile material model obtained from DTT, the material model proposed by Fujikake et al. leads to a substantial overestimation in the rail-seat load resistance of S2-S2.

In this research, in order to understand the UHP-FRC material behaviour in the unidirectional tension, another tensile material model is developed based on numerous trials to enhance the agreement between the FE and experimental load-deflection curves, as shown in Figure 7.19. The proposed stress-strain curve starts with a short flat part followed by an increase with the slope of the elastic modulus (38.6 GPa) to the peak tensile strength of 12.6 MPa (as presented in Table 7.4). Subsequently, a multi-linear reduction part is added to the curve. As shown in Figure 7.18, the proposed adjusted material model leads to a load-deflection that agrees well with the experimental curve. It should be noted that further investigations are needed to verify the preciseness of the adjusted model under various conditions, such as dynamic loads, and to apply further adjustments to improve it.
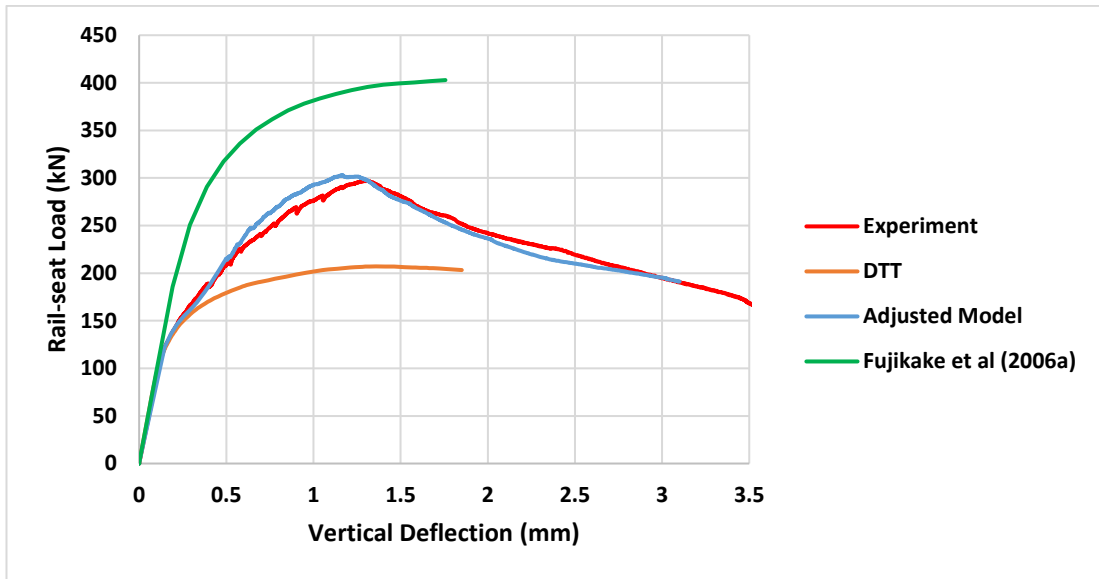
Figure 7.18 Comparison of the experimental and FE Load-deflection curves of S2-S2
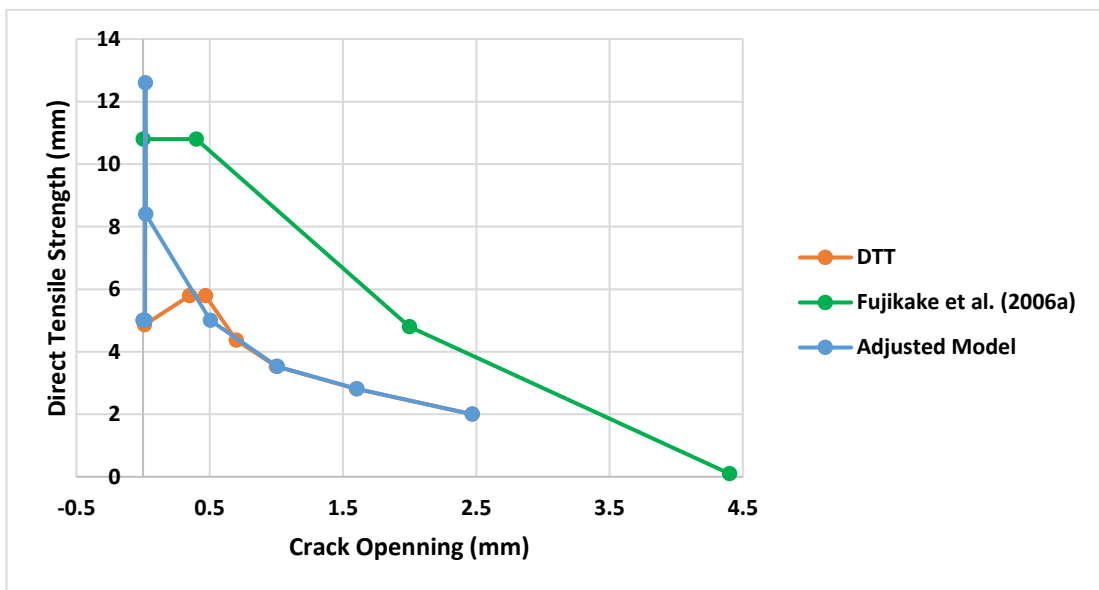
(a) entire stress-crack opening curves
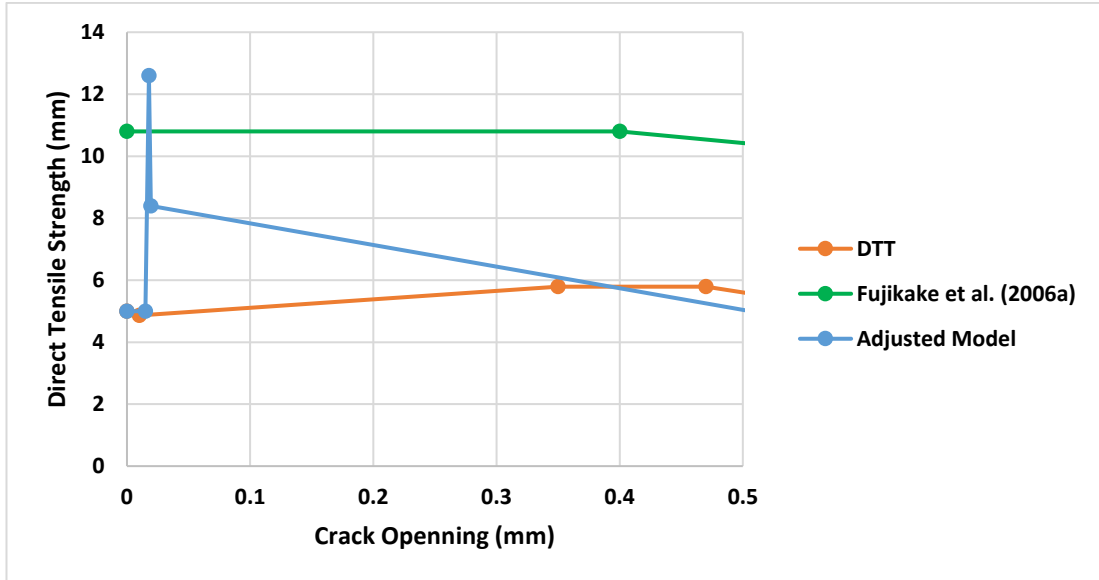
(b) close-up of the initial crack opening region

Figure 7.19 The tensile stress-crack opening material models for the UHP-FRC material

A comparison between the failure modes of the S2-S2 obtained from the static rail-seat loading and the FE analysis (using the proposed adjusted tensile model) is presented in Figure 7.20. The FE modelling shows the bending mode of failure, which agrees with the experimental failure mode. Hence it can be deduced that the FE model developed in ABAQUS with the CDP material model can adequately simulate the behaviour of the prototype UHP-FRC sample under static rail-seat loading.

(a) failure mode of S2-S2
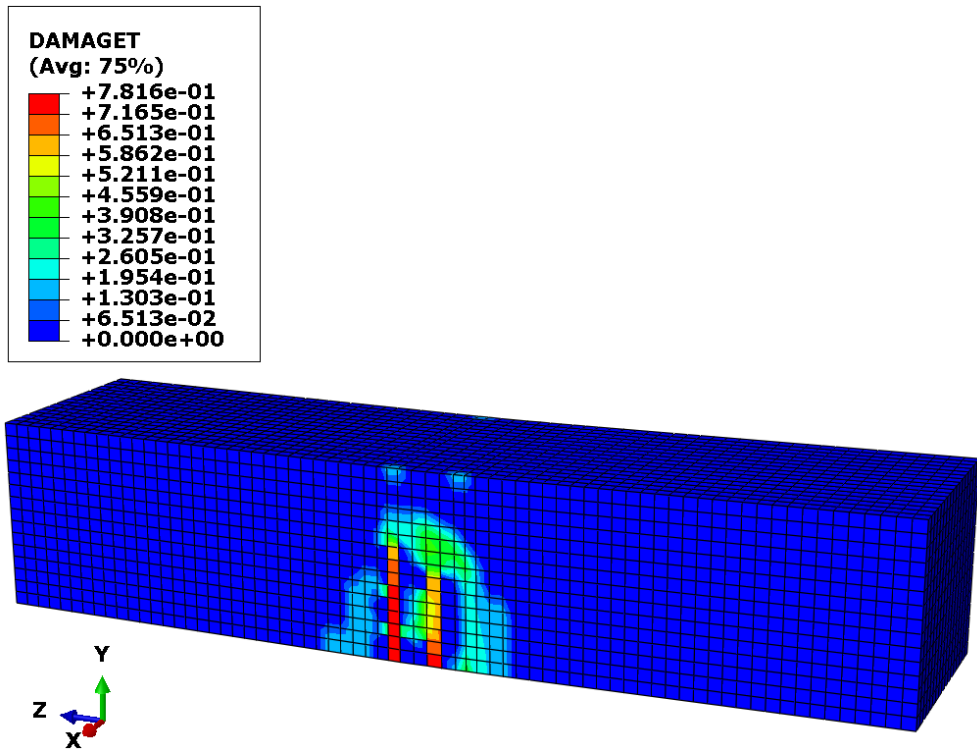
(b) tensile damage of the FE model of S2-S2

Figure 7.20 Comparison of the failure mode of S2-S2 obtained from the experiment and the
FE analysis

7.4 Discussion of Results and Summary

In this chapter, the application of the finite element method (FEM) using the
commercial software ABAQUS in the simulation of concrete sleepers and predicting

their performance was studied. The adequacy of the well-known concrete material model developed in ABAQUS, called concrete damage plasticity (CDP) was verified. Two types of concrete sleepers were modelled in this study, the conventional prestressed concrete (PSC) sleeper and the non-prestressed UHP-FRC prototype sleeper sample.

First, the PSC sleeper simulation was conducted. For this purpose, six heavy-haul PSC sleepers provided by BHP Iron Ore Pty Ltd. were used to extract the experimental data. Three sleepers (P4, P5, and P6) were selected for the rail-seat positive moment testing to extract the vertical (rail-seat) load vs vertical rail-seat deflection curves. Subsequently, to determine the concrete material characteristics of these sleepers, six cores were taken from each of the sleepers, three cores vertically taken from the centre area, and three cores were taken horizontally from the rail-seat area (the undamaged rail-seat area). After determining the compressive concrete strength by testing the concrete cores, the other characteristics of the high-performance concrete was determined based on the mean compressive strength of the concrete (f_{cmi} = 66.13 MPa) using the empirical formulae.

The other three heavy-haul PSC sleepers were used for decompression testing in order to find the remaining prestressing forces of the sleepers. It was found that the PSC sleepers lost an average of 13% of their initial prestressing force (570 kN). Eventually, the comparison of the experimental and FE load-deflection curves proved the adequacy of the FE modelling in ABAQUS using the CDP material model. Comparing the damages found in the tested sleepers and the FE model, it was found that there is a possibility that the prestressing force of the tendons near the two ends of the PSC sleepers is considerably lower than that of the central area. Further future investigations are needed to determine the variation of the prestressing force over the length of the PSC sleepers.

Subsequently, the FE modelling of the UHP-FRC prototype sample was carried out. Since the UHP-FRC material has higher compressive and tensile strength than the conventional high-performance concrete, determining suitable input data for the material behaviour in compression and tension was the most challenging part of the FE modelling. First, the unidirectional compressive material data was verified. For this purpose, a small cylinder sample of the UHP-FRC material was modelled in ABAQUS

and analysed under universal compression. The average experimental and the FE compressive load-deflection curves were close. Also, the stress contour of the FE model was in good agreement with the actual failure of the cylinder sample under the unidirectional compression test.

After that, the tensile behaviour of the UHP-FRC material was studied. For this purpose, a direct tensile test (DTT) sample configuration and the test set-up were designed to reach a better understanding of the UHP-FRC material behaviour under the unidirectional tension. The stress-displacement data points were inserted in ABAQUS as tabular data. The FE analysis was performed for the FE model of the UHP-FRC prototype sample, S2-S2, to verify the preciseness of the input material data obtained from the DTT. The comparison of the FE and the experimental rail-seat load-vertical deflection diagrams revealed that the DTT input data underestimates the flexural strength of S2-S2. Hence, adjustments were performed to the unidirectional tensile material model based on numerous trial analyses to reach a more accurate FE load-deflection curve. Also, the damage contour of the FE model with the adjusted material input data has a good agreement with the actual failure of S2-S2 under static rail-seat testing. However, the unidirectional tensile model of the UHP-FRC material requires further future studies and improvements.

CHAPTER 8
Conclusions and Design Recommendations

8.1 Concluding Remarks

8.1.1 Overall View

The main focus of this research was to the application of reactive powder concrete (RPC), which is also called ultra-high performance fibre-reinforced concrete (UHP-FRC), in manufacturing non-prestressed concrete sleepers. Although prestressed concrete (PSC) sleepers are of interest to the railway industry, the exclusion of the prestressing technique from the manufacturing process of concrete sleepers can reduce the manufacturing time, energy, and cost. Indeed, to manufacture PSC sleepers, a large indoor area and sophisticated equipment are required. Furthermore, the manufacturing process of the PSC sleepers, requires heat curing, which is energy consuming and leads to the emission of greenhouse gases into the atmosphere. Hence, this project investigated the viability of producing non-prestressed concrete sleepers.

8.1.2 Optimisation of the UHP-FRC Mix Design

The first challenge in manufacturing the non-prestressed concrete sleepers was to attain a concrete mix design that could attain the significant flexural tensile stresses generated within the sleeper under the design rail-seat load. In Chapter 3, the design moments and the generated stresses were estimated for 25 TAL and 40 TAL. Then, the material optimisation procedure was performed based on the well-known Taguchi method. It was found that using the Taguchi method and the L9 orthogonal arrays, the UHP-FRC mix design can be optimised with only 9 trial mixes. In this case, four main mix design parameters (ratios), including SF/C, Sand/C, SP/C, and W/Binder, were considered with three different proportions for each parameter.

It was found that the optimal UHP-FRC mixes with the maximum compressive and flexural tensile strengths had different proportions of the aforementioned parameters. Therefore, it was concluded that the optimisation process of the UHP-FRC mix design must be based on the trial test results relevant to the target characteristic. For instance, if the optimisation target is to reach the maximum possible flexural strength, the

optimisation procedure must be carried out based on the flexural test results of the trial mixes, not the compression test results, vice versa.

The experimental results showed that the optimal plain UHP-FRC mix, T10-F, with the W/Binder ratio of 0.2, SP/C ratio of 0.04, Sand/C ratio of 1.2, and SF/C ratio of 0.3 could satisfy the minimum required flexural tensile strength for manufacturing non-prestressed concrete sleepers. Subsequently, the optimal volume of macro steel fibres was found equal to 2%. Further material tests proved the adequacy of the UHP-FRC mix T10-F-02, and therefore, it was used for manufacturing all the UHP-FRC prototype samples in this research.

8.1.3 Verification of the Prototype UHP-FRC Samples

In Chapter 4, the static and cyclic (fatigue) behaviours of the prototype non-prestressed samples made with the optimal UHP-FRC mix were investigated. During the mixing process of the first batch, the mixer stopped working a few times. This issue is due to the fact that after adding the water and superplasticiser, the UHP-FRC material turns into a sticky plastic phase just before turning into its final fresh form, which is a homogenous soft mix. It was concluded that extra considerations are needed when mixing larger quantities of UHP-FRC. The second batch was mixed adequately with extra care.

As expected, the two samples from the first batch did not perform adequately in the static rail-seat positive moment testing and the cyclic/fatigue testing. Due to the issues in the mixing process, these samples were considered defective samples and, therefore, were excluded from the final conclusions.

By contrast, the two prototype samples cast with the second batch of the UHP-FRC mix showed better static and fatigue performance. Indeed, sample S2-S2 satisfied the static rail-seat positive moment test requirements and passed the test. The first cracking and the ultimate rail-seat loads of this sample were 189 kN and 297 kN, respectively. Also, sample S2-F2 resisted hundreds of thousands of load cycles before the ultimate failure. However, a railway sleeper is expected to sustain around 3-6 million cyclic rail loads over its service life. Hence, it was concluded that the cyclic/fatigue strength of the non-prestressed UHP-FRC samples needs further studies and enhancements.

Herein, the inclusion of the GFRP reinforcements can be a promising solution for enhancing fatigue strength.

8.1.4 Impact Testing

In actual ballasted rail track systems, railway sleepers are placed on a foundation and are expected to sustain infrequent extreme transient dynamic (impact) loads during their service lives. Hence, in Chapter 5, in order to understand the impact performance of the prototype samples placed on different track foundations, 6 prototype UHP-FRC samples were tested under various impact loads. For this purpose, a drop-hammer impact loading test rig was utilised.

First, two preliminary prototype samples (without rail-sleeper fastening systems) placed on a hard track (called type 1), i.e. B1-VH-1 and B1-VH-2, were investigated. It was shown that after incurring several cracks under 8 impact loads (drops), B1-VH-1 could still resist around 65% of the ultimate load of a healthy sample under standard static rail-seat loading. Also, B1-VH-2 resisted two extreme loads with the drop heights of 2.5 m and 3.0 m, with the P2 (second peak load) magnitudes of 422 kN and 554 kN, respectively. The latter results proved the considerable impact load resistance of the UHP-FRC prototype samples.

Secondly, four prototype samples with the actual rail-sleeper fastening system were investigated. Two samples were tested on a hard (H) track, and the other two were tested on a very soft track (made with 6 layers of rubber belts). The samples were tested under extreme impact loads. Eventually, these extreme impact loads (P2 magnitudes) were compared and analysed. It was found that the prototype samples sustained the required impact loads for interstate rail lines with infrequent passage traffic and train speeds not higher than 80km/hr. To confirm the latter conclusion, further field investigations (statistic data) are required to extract more data about the significance and frequency of these dynamic/impact rail loads.

8.1.5 Inclusion of GFRP Bars

As mentioned above, the application of longitudinal GFRP reinforcements can be an effective approach to enhance the fatigue performance of the UHP-FRC prototype sleeper samples. As an initial trial for future research, in Chapter 6, four low-height UHP-FRC prototype samples are designed with various ratios of GFRP reinforcement to be tested under standard static rail-seat loading. The main purpose of this investigation was to find the enhancing effects of the GFRP bars on the static performance of the UHP-FRC samples.

By adding the GFRP bars to the low-height prototype UHP-FRC sample, the first cracking and the ultimate positive moment rail-seat loads had up to 91% and 325% increase, respectively. Furthermore, using the GFRP reinforcements, concrete compression crushing was detected by the LVDT gauges, which shows that the excessive compressive capacity of the UHP-FRC material was utilised.

It was observed that two samples with the equal reinforcement ratio of 0.011, S2-01 and S3-01, had different failure modes. Sample S2-01, with two GRFP bars of 14 mm diameter, showed sharp fluctuations in its post-peak load-deflection diagram, hovering around a nearly horizontal line, attributed to the stepwise bar slippages. In contrast, sample S3-01 reached a considerably higher peak load followed by a drop in the load-deflection diagram, which is normal for reinforced beams with the ultimate shear failure mode. The bond strength between the UHP-FRC and the GFRP bars and the effects of the bar diameter on the bond strength is recommended as another area for future research.

Also, a simplified section analysis approach in congruence with the Australian Standard was demonstrated to calculate the cracking moment capacity (M_{cr}) of the UHP-FRC sleepers reinforced with FRP bars. A comparison between the analytical and experimental values of M_{cr} showed that the analytical approach gives a conservative estimation, and therefore, it can lead to a safe design. Eventually, a stepwise approach was presented for the design of the UHP-FRC sleepers with FRP reinforcements.

8.1.6 Finite Element Modelling

In Chapter 7, finite element modelling was carried out for both the prestressed concrete sleeper and the non-prestressed UHP-FRC prototype sample. The FE results were validated against the experimental results. First, six heavy-haul PSC sleepers provided by BHP Iron Ore Pty Ltd. were tested in order to extract the required experimental data. Three sleepers were selected for the rail-seat positive moment testing. Subsequently, three core samples were taken vertically from the centre part and three cores from the undamaged rail-set of these sleepers. The average compressive strength of 66.13 MPa obtained from the core sample testing was used for determining other mechanical properties of the high-performance concrete of the PSC sleepers. Also, a 3-point decompression bending test was conducted for the other three PSC sleepers to obtain their remaining prestressing force. An average of 13% prestress loss was obtained while the initial prestressing force was 570 kN. Comparing the FE and the experimental load-deflection diagrams, it was concluded that the FE modelling technique using the concrete damage plasticity (CDP) material model in ABAQUS is capable of simulating the PSC sleepers. However, comparing the failure modes of the FE model and the PSC sleepers, it was found that the PSC sleeper tended to incur the shear failure only in the vicinity of the support, which was close to the end of the sleeper. This phenomenon was attributed to the possibility of a lower prestressing force at the ends of the PSC sleeper than the centre part. This conclusion needs further studies to quantify the precise remaining prestressing force magnitudes over the length of the PSC sleeper.

In the next step, the non-prestressed UHP-FRC sample, S2-S2, was modelled using the same material model (CDP) in ABAQUS. In contrast to the PSC sleepers, S2-S2 was not prestressed and had a simple prismatic shape. However, the performance of UHP-FRC material under unidirectional compression and tension was expected to be more complicated than the conventional high-performance concrete. First, the unidirectional compression stress-strain data obtained from the compression material testing was validated against the experimental result. Subsequently, the tensile unidirectional stress-strain data was extracted from a direct tensile test method developed in this research. Comparing the rail-seat load-deflection diagrams obtained from the FE analysis and the rail-seat testing of S2-S2, it was found that the DTT input data significantly underestimated the rail-seat load resistance capacity of the sample.

Hence, an adjusted model was proposed based on several trial analyses, such that the FE and experimental load-deflection curves were close to each other. It was also shown that the adjusted unidirectional tensile stress-strain data leads to the adequate prediction of the failure mode. In the end, it was noted that further studies are needed to ensure the adequacy of the proposed adjusted tensile model under various conditions, and further modifications may be applied to the model.

8.2 Design Recommendation

One of the advantages of the proposed non-prestressed UHP-FRC sleepers compared to the conventional PSC sleepers is the simple design process of these sleepers. The design procedure of the UHP-FRC sleeper can be summarised as the following steps:

1) The magnitude of R (design rail-seat load) and thereby, the design moments are calculated according to the Australian Standard (AS1085.14, 2019), as demonstrated in Table 3.2;

2) The flexural compressive and tensile stress magnitudes generated inside the sleeper due to the design moments are calculated at critical cross-sections of the UHP-FRC sleeper (e.g. the rail-seat and the centre sections). For this purpose, a simple elastic section analysis can be applied, i.e. the stress is equal to M*y/I, where y is the distance from the neutral axis of the section, I is the moment of inertia of the section, and M is the corresponding design moment;

3) The calculated acting compressive and tensile stresses are compared with the permissible compressive and tensile stresses of the UHP-FRC material, respectively;

4) If the acting compressive or tensile stresses surpass the permissible strengths of the UHP-FRC material, the relevant section dimensions must be increased, and steps 1 to 4 must be repeated. Otherwise, the designed non-prestressed UHP-FRC sleeper is acceptable.

8.3 Future Studies

In chapter 5, only two extreme types of track foundations, i.e. very hard and very soft, were studied. A more comprehensive study considering a variety of track foundation types can better understand the influence of the rail track foundation on the impact (transient dynamic) performance of the non-prestressed UHP-FRC sleepers.

In chapter 4, it was shown that the fatigue load resistance of the non-prestressed UHP-FRC samples is not satisfactory. Hence, further studies are needed to improve the fatigue resistance of the non-prestressed prototype samples. Thus, the use of GFRP reinforcing bars was studied in Chapter 6, and the results showed a great improvement in the static performance of the low-height UHP-FRC samples. Therefore, it is expected that a similar enhancement will be reached by using the GFRP reinforcements under cyclic loading. Hence, further studies on the influence of GFRP reinforcements on the fatigue performance of the UHP-FRC samples is recommended.

Besides, in Chapter 6, it was perceived helpful to investigate the influence of the GFRP reinforcement ratio and the bond strength between the UHP-FRC matrix and the GFRP bars on the static and cyclic behaviours of the non-prestressed prototype samples. In such research, the influence of the bar diameter and the rib shape and size on the UHP-FRC/GFRP bond strength can also be investigated.

In Chapter 7, the possibility of a variety of prestress loss over the length of the sleeper was perceived. Hence, further investigations about the amounts of the remaining prestress forces of the tendons through the length of the PSC sleepers can lead to more accurate FE models. Also, the proposed unidirectional stress-strain data (in tension) has been developed merely based on the load-deflection curve of the prototype sample, S2-S2. Further studies are needed to verify the accuracy of the proposed tensile material model under different scenarios, such as dynamic loads.

In the end, it is important to note that in this study, only prototype non-prestressed UHP-FRC samples with simple prismatic shapes and short lengths were studied. Shape optimisation of the non-prestressed UHP-FRC samples using FEM and experiments is another area of research to continue the current project.

APPENDIX A
EXPERIMENTAL TESTING OF THE HEAVY-HAUL PSC SLEEPERS

Introduction

The heavy-haul prestressed concrete (PSC) sleepers, tested in this research according to the Australian Standard (AS1085.14, 2019), are shown in Figure A.1. These six used sleepers were provided by BHP Iron Ore Pty Ltd, and have similar number of prestressing tendons and nominal dimensions. The dimensions of these PSC sleepers and the cross-section details are shown in Chapter 7 (see Figure 7.1). Three of the samples are selected for the positive moment rail-seat testing and the remaining three samples are selected for determining the remaining prestressing force applied to the sleepers from the tendons, as listed in Table A.1.

Figure A.1 A view of the heavy-haul PSC sleepers

Table A.1 Summary of the heavy-haul sleeper tests

Sleeper No.	Test Type	Test Number
P1	3-point mid-span bending test (determination of the remaining prestressing force)	1
P2		2
P3		3
P4	Rail-seat Positive Moment Test	1
P5		2

P6		3

Standard Rail-Seat Positive Moment Testing

The process of static rail-seat testing has been demonstrated in Chapter 4 (refer to Section 4.3). The test set-up developed for the heavy-haul PSC sleepers is depicted in Figure A.2. The load versus the rail-seat deflection of the three samples are shown in Figure A.3. A summary of the cracking and the ultimate loads is presented in Table A.2.

The ultimate failure mode of the three heavy-haul PSC sleepers under standard rail-seat testing is depicted in Figure A.4. It can be seen that in all cases, the ultimate failure occurs due to the shear cracks (shear failure). In all cases, the shear cracks propagated from the vicinity of the support close to the end of the sleeper rather than the other (internal) support, as shown with red lines in Figure A.4. The tendency to experience shear cracking close to the sleeper end is attributed to the fact that the prestressing force of the tendons close to the ends of the PSC sleepers is slightly less than the internal part. Also, concrete crushing around the rail-seat areas (especially under the loading bars) are observed.

Figure A.2 The positive moment rail-seat test set-up of the heavy-haul PSC sleepers
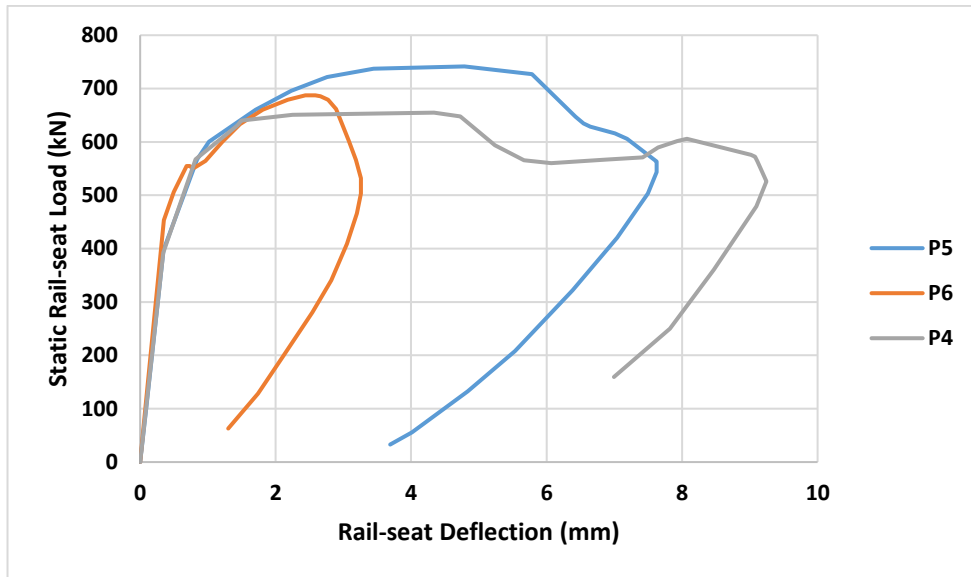
Figure A.3 Load versus rail-seat deflection diagram of the heavy-haul PSC sleepers

Table A.2 The cracking and ultimate (maximum) loads sustained by the heavy-haul PSC
sleepers under the standard rail-seat testing

Sleeper No.	Test No.	Cracking Load (kN)	Ultimate Load (kN)
P4	#1	441	668.1
P5	#2	420	742.8
P6	#3	425	691.0

(a) sample P4

(b) sample P5

(c) sample P6

Figure A.4 The ultimate failure of the heavy-haul PSC sleepers

Determination of the Remaining Prestressing Force

The prestressing force applied from the steel wires to the concrete component of the PSC sleeper can be obtained from an indirect (decompression) method proposed by Barr et al. (Barr et al., 2013). For this purpose, a number of 3-point bending tests are needed to be performed. Three heavy-haul sleepers, i.e. P1, P2, and P3, are selected for the 3-point mid-span bending tests with the support span of 1000 mm. Figure A.5 shows the test set-up used for bending tests. Two steel bars with the square cross-sections of 50 mm x 50 mm are used as supports at a distance of 1000 mm, and another bar with similar dimensions is placed on top at the mid-span for applying the static load. Thin rubber bearings are placed between the steel bars and the sleeper for better stress distribution.

First, the static load is applied to the sleeper until a crack is observed on both sides (front and rear sides) of the sleeper. The crack is marked, and then the load is released. Subsequently, two dots are marked around the crack on one side of the sleeper at a 10 mm distance from the bottom of the sleeper. The DIC-based extensometer camera with the commercial name of Mercury Camera can measure the horizontal deflection of the sleeper can be measured by capturing the extension between the two dots. After that, the static loading is applied again up to 135% of the cracking load, while the load is recoded by the hydraulic 5000 kN testing machine, and the extension between the two dots (surrounding the crack) is recoded by the DIC extensometer. Then, the decompression load can be obtained from the load-deflection diagram, as shown in Figure A.6.

Figure A.5 The 3-point bending test set-up for determining the prestressing force
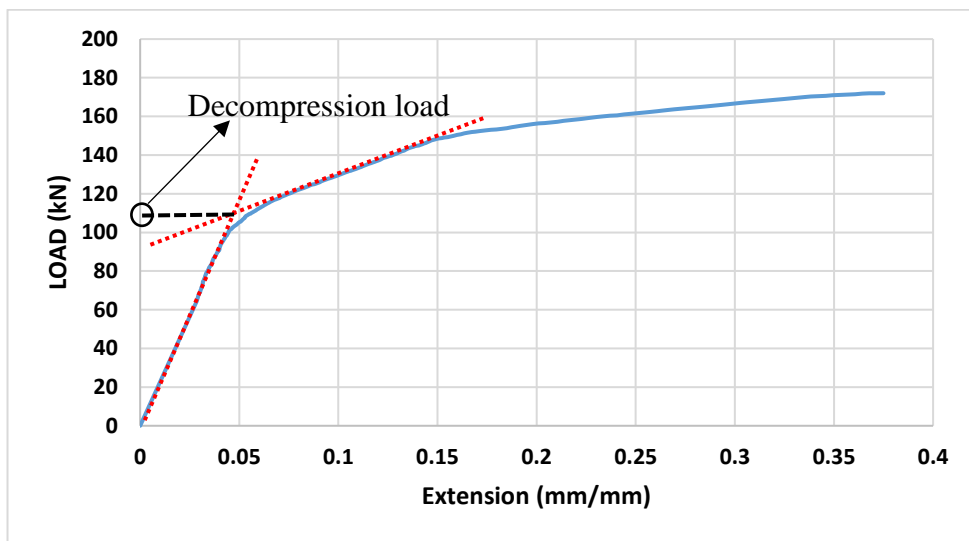
Figure A.6 Obtaining the decompression load from the load-deflection diagram

Afterwards, the remaining prestressing force (P) can be calculated using the following equation:

$$P = \dfrac{\dfrac{M_{ext}C + M_{sw}C}{I_g}}{\dfrac{1}{A} + \dfrac{e_p C}{I}} \qquad (A.1)$$

Where the parameters are as follows:

- A: Cross-section area of the sleeper (at the mid-span);
- e_p: Eccentricity of the total prestressing force (distance between the prestressing force and the centroid of the sleeper cross-section);
- C: the height of the neutral axis from the soffit;
- M_{sw}: moment caused by the self-weight at the crack location;
- M_{app}: moment due to the decompression load at the location of the crack;
- I_g: the gross inertial moment of the sleeper section at the mid-span;
- I: the moment of inertia of the transformed section.

In this manner, the remaining prestressing magnitudes can be determined as presented in Table A.3. It is seen that the percentages of the prestress loss obtained from the three sleepers are close to each other, between 11.4% and 14.4%. The average of these values, i.e. the prestress loss of 13%, is used in the FE modelling.

Table A.3 The remaining prestressing force of the heavy-haul PSC sleepers

Sleeper No.	Test No.	Initial Prestressing Force (kN)	Remaining Prestressing Force (kN)	Prestress Loss (%)
P1	1		487.95	14.4
P2	2	570	505.05	11.4
P3	3		500.12	12.3

Material Testing of the Core Samples

In order to find the material characteristics of the heavy-haul PSC sleepers, six core samples are taken from each sleeper for the compression tests according to AS 1012.14

(AS-1012.14, 2018). For each sleeper, three samples are cored vertically from the mid-span area of the sleeper and three samples horizontally from the rail-seat area, as shown in Figure A.7. A 77mm core drill with an outer diameter of 77 mm and an inner diameter of 73 mm has been used for the coring procedure.

Figure A.7 A view of the horizontal and vertical core holes

Once the samples are cored, they are checked for any considerable flaws, ridges, or breakage. In case a sample is not acceptable due to flaws, it is excluded, and another sample will be extracted from the same area of the sleeper. The two ends of the approved core samples are cut and grinded to have smooth ends for the universal compression testing, as shown in Figure A.8. The ratio of the height to diameter of the samples after grinding is around 2, as recommended by the AS 1012.14 (AS-1012.14, 2018).

Figure A.8 The universal compression testing of the core samples

According to the Australian Standard (AS-1012.14, 2018), the core samples with diameters less than 100 mm show lower compressive strengths compared to those with 100 mm diameter. Therefore, for samples with a diameter of around 75 mm, a correction factor of 1.06 needs to be applied to adjust the compressive strengths of these samples. In this study, the core diameters are around 70 mm, and it is assumed that the same correction factor of 1.06 leads to acceptable results. Also, according to AS 1012.14 (AS-1012.14, 2018), the core samples incur damages due to the coring process, and another correction coefficient must be applied to adjust the compressive test results. This coefficient is recommended to be about 1.06. The other correction factor recommended by AS 1012.14 (AS-1012.14, 2018) is to consider the influence of the coring direction. It is expected that the samples obtained from the horizontal cores have less strength compared with those taken from vertical coring. Hence, in the case of the cores drilled horizontally, another coefficient factor of 1.07 is

recommended to be applied to these samples. Hence, the final magnitudes of the adjustment coefficients for the horizontal and vertical samples are as follows:

- Coefficient for horizontal core samples = 1.06 x 1.06 x 1.07 = 1.2
- Coefficient for vertical core samples = 1.06 x 1.06 = 1.12

A summary of the corrected compressive strength test results of the core samples is shown in Table A.4. It is observed that the average corrected compressive strengths of the sleepers are close to each other. It will be shown in the following that the other characteristics of the concrete material can be estimated using the empirical formulae based on the compressive strength of the concrete.

Table A.4 The compressive test results of the core samples

Sleeper No.	Location/ Direction	Corrected compressive strength (MPa)	Average corrected compressive strength (MPa)	Coefficient of Variation (CoV) %
P4	Rail-seat/ Horizontal	68.43	64.93	7.3
		73.98		
		64		
	Mid-span/ Vertical	63.48		
		61.62		
		58.06		
P5	Rail-seat/ Horizontal	65.5	66.65	4.9
		59.46		
		61.53		
	Mid-span/ Vertical	69.84		
		72.86		
		70.73		
P6	Rail-seat/ Horizontal	61.85	66.82	12.1
		73.09		
		58.12		
	Mid-span/ Vertical	70.37		
		71.42		
		66.04		

References:

13230-1, E. 2009. Railway applications. Track. Concrete sleepers and bearers. Part 1: General requirements. British Standard London.

ABADI, T., PEN, L. L., ZERVOS, A. & POWRIE, W. 2019. Effect of Sleeper Interventions on Railway Track Performance. *Journal of Geotechnical and Geoenvironmental Engineering,* 145**,** 04019009.

ABAQUS, V. 2013. 6.14-2. *Simulia, Dassault Systemes, Providence RI, USA*.

ABCB 2009. The Australian Building Codes Board. *Retrieved February/08*.

ABDULRAHEEM, M. S. & KADHUM, M. M. 2018. Experimental and numerical study on post-fire behaviour of concentrically loaded reinforced reactive powder concrete columns. *Construction and Building Materials,* 168**,** 877-892.

ACI-440. Guide for the Design and Construction of Concrete Reinforced with FRP Bars: ACI 440.1 R-03. 2003. American Concrete Institute.

AHLBECK, D. & HADDEN, J. 1985. Measurement and prediction of impact loads from worn railroad wheel and rail surface profiles. *Journal of Engineering for Industry,* 107**,** 197-205.

AITCIN, P. C. & RICHARD, P. The pedestrian/bikeway bridge of Sherbrooke. Proceedings 4th International Symposium on Utilization of High-Strength/High-Performance Concrete, Paris, 1996. 1399-1406.

AL-TIKRITE, A. & HADI, M. N. S. 2017. Mechanical properties of reactive powder concrete containing industrial and waste steel fibres at different ratios under compression. *Construction and Building Materials,* 154**,** 1024-1034.

ALGBURI, A. H. M., SHEIKH, M. N. & HADI, M. N. S. 2019. Mechanical properties of steel, glass, and hybrid fiber reinforced reactive powder concrete. *Frontiers of Structural and Civil Engineering,* 13**,** 998-1006.

ALTUN, F., HAKTANIR, T. & ARI, K. 2007. Effects of steel fiber addition on mechanical properties of concrete and RC beams. *Construction and Building Materials,* 21**,** 654-661.

ANWAR, M., SOGHAIR, H. & AHMED, M. 1993. 1209 New Aspects Affecting the Mutual Relation between Strength and Permeability of Concrete. *コンクリート工学年次論文報告集,* 15**,** 1229-1234.

AREMA, L. 2013. American railway engineering and maintenance-of-way association. *Manual for railway engineering*.

ASTM. C1856/C1856M-17. 2017. standard practice for fabricating and testing specimens of ultra-high performance concrete. Philadelphia: American Society for Testing and Materials.

AS1085.14 2019. *Railway track material-prestressed concrete sleeper,* Australia, Standard Australia.

AS-1012.9 1999. Methods of testing concrete. Method 9: Determination of the compresive strength of concrete specimens. Standards Australia Sydney, NSW, Australia.

AS-1012.11 2000. Methods of testing concrete. Method 11: Determination of the modulus of rupture. Standards Australia Sydney, NSW, Australia.

AS-1012.12.1 2014. Methods of testing concrete. Method 12.1: Determination of mass per unit volume of hardened concrete-Rapid measuring method. Standards Australia Sydney, NSW, Australia.

AS-1012.14 2018. Methods of testing concrete. Method 14: Method for securing and testing cores from hardened concrete for compressive strength and mass per unit volume. Standards Australia Sydney, NSW, Australia.

AS-1012.17 1997. Methods of testing concrete. Method 17: Determination of the static chord modulus of elasticity and Poisson's ratio of concrete specimens. Standards Australia Sydney, NSW, Australia.

AS-3600 2018. Australian Standard: Concrete Structures. Standards Australia Sydney, NSW, Australia.

AUERSCH, L., SAID, S., KNOTHE, E. & RÜCKER, W. The dynamic behavior of railway tracks with under sleeper pads, finite-element boundary-element model calculations, laboratory tests and field measurements. Proc. 9th European Conference on Structural Dynamics (EURODYN 2014), Porto, 2014. 805-812.

AUSTRALASIAN RAILWAY ASSOCIATION, A. 2002. *Volume 5: Rollingstock (Draft), Part 2: Common Requirements, Section 2: Commissioning and recommissioning, RCP-2201: Performance Acceptance Requirements, Code of Practice for the Defined Interstate Rail Network, Version 1,* Australia, Australasian Railway Association.

BAENA, M., TORRES, L., TURON, A. & BARRIS, C. 2009. Experimental study of bond behaviour between concrete and FRP bars using a pull-out test. *Composites Part B: Engineering,* 40**,** 784-797.

BAKHAREV, T. 1994. *Microstructural features of railseat deterioration in concrete railroad ties.* University of Illinois at Urbana-Champaign.

BANTHIA, N., YAN, C. & SAKAI, K. 1998. Impact resistance of fiber reinforced concrete at subnorma temperatures. *Cement and Concrete Composites,* 20**,** 393-404.

BARNES, R. & GARDEN, H. 1999. Time-dependent behaviour and fatigue. *Strengthening of reinforced concrete structures using externally bonded FRP composites in structural and civil engineering", edited LC Hollaway and MB Leeming, Woodhead Publishing Limitied, Cambridge***,** 83-134.

BARR, P., HALLING, M. & HIGGS, A. 2013. Forensic Testing of Prestress Concrete Girders After Forty Years of Service.

BASTION accessed on 04/04/2021. General Purpose Cement: https://dingocement.com.au/wp-content/uploads/2017/05/900500-Bastion-General-Purpose-Cement-201705.pdf.

BEZGIN, N. Ö. 2014. Design Evaluations for the Time Dependent Contractions of Prestressed Concrete High Speed Railway Sleepers.

BEZGIN, N. Ö. 2015. Climate effects on the shoulder width measurements of prestressed concrete high speed railway sleepers of ballasted tracks. *Measurement,* 75**,** 201-209.

BEZGIN, N. Ö. 2017. High performance concrete requirements for prefabricated high speed railway sleepers. *Construction and Building Materials,* 138**,** 340-351.

BIAN, J., GU, Y. & MURRAY, M. 2013. Numerical study of impact forces on railway sleepers under wheel flat. *Advances in Structural Engineering,* 16**,** 127-134.

BIAN, J., GU, Y. & MURRAY, M. H. 2012. A dynamic wheel–rail impact analysis of railway track under wheel flat by finite element analysis. *Vehicle System Dynamics,* 51**,** 784-797.

BIRMANN, F. Paper 5: Track Parameters, Static and Dynamic. Proceedings of the Institution of Mechanical Engineers, Conference Proceedings, 1965. SAGE Publications Sage UK: London, England, 73-85.

C230/C230M, A. 1998. Standard specification for flow table for use in tests of hydraulic cement. ASTM International West Conshohocken, Pa.

CAI, X., ZHONG, Y., HAO, X., ZHANG, Y. & CUI, R. 2019. Dynamic behavior of a polyurethane foam solidified ballasted track in a heavy haul railway tunnel. *Advances in Structural Engineering,* 22**,** 751-764.

CAI, Z. 1992. *Modelling of rail track dynamics and wheel/rail interaction*.

CHEEMA, D. Low calcium fly ash geopolymer concrete–a promising sustainable alternative for rigid concrete road furniture. 25th ARRB conference–shaping the future: Linking policy, research and outcomes, Perth, Australia, 2012.

CHOI, S., LEE, C.-W., KIM, J.-C. & CHO, J.-H. Interior noise of a korean high-speed train in tunnels. Proceedings of Acoustics, 2004. 415-9.

COMMITTEE, A. 2002. ASTM C109/C109M-02 Standard Test Method for Compressive Strength of Hydraulic Cement Mortars. *Annu. B. ASTM Stand,* 4**,** 1-6.

COPE, D. & ELLIS, J. 2001. Plain line maintenance. *British railway track. England: The permanent way, institution*.

CWIRZEN, A., PENTTALA, V. & VORNANEN, C. 2008. Reactive powder based concretes: Mechanical properties, durability and hybrid use with OPC. *Cement and Concrete Research,* 38**,** 1217-1226.

DOYLE, N. F. 1980. Railway track design: a review of current practice.

DRAMIX4D-65/35 accessed on 04/04/2021. https://www.bekaert.com/en/product-catalog/content/dop/~//-/media/Files/ImportFiles/DRAMIX-4D/Dramix-4D-6535BG-6535BG.pdf?sc_lang=en-US.

DUKKIPATI, R. V. & DONG, R. 1999. Impact loads due to wheel flats and shells. *Vehicle System Dynamics,* 31**,** 1-22.

EC2 2005. Design of Concrete Structures—Part 2: Concrete Bridges Design and Detailing Rules. United Kingdom: British Standard.

ELCHALAKANI, M., DONG, M., KARRECH, A., LI, G., ALI, M. S. M. & YANG, B. 2019. Experimental Investigation of Rectangular Air-Cured Geopolymer Concrete Columns Reinforced with GFRP Bars and Stirrups. *Journal of Composites for Construction,* 23**,** 04019011.

EN, T. 2005. 196-1. Methods of testing cement–Part 1: Determination of strength. *European Committee for standardization,* 26.

ESVELD, C. 2001. Modern Railway Track, 2nd Editon. *Delft university of Technology*.

FANG, Z., HU, R., JIANG, R., XIANG, Y. & LIU, C. 2020. Fatigue Behavior of Stirrup Free Reactive Powder Concrete Beams Prestressed with CFRP Tendons. *Journal of Composites for Construction,* 24.

FERDOUS, M., KHENNANE, A. & KAYALI, O. 2013. Hybrid FRP-concrete railway sleeper. *Advanced Composites in Construction***,** 67-77.

FERDOUS, W. & MANALO, A. 2014. Failures of mainline railway sleepers and suggested remedies – Review of current practice. *Engineering Failure Analysis,* 44**,** 17-35.

FERDOUS, W., MANALO, A., KHENNANE, A. & KAYALI, O. 2015a. Geopolymer concrete-filled pultruded composite beams – Concrete mix design and application. *Cement and Concrete Composites,* 58**,** 1-13.

FERDOUS, W., MANALO, A., VAN ERP, G., ARAVINTHAN, T., KAEWUNRUEN, S. & REMENNIKOV, A. 2015b. Composite railway sleepers – Recent developments, challenges and future prospects. *Composite Structures,* 134**,** 158-168.

FERMÉR, M. & NIELSEN, J. 1994. Wheel/rail contact forces for flexible versus solid wheels due to tread irregularities. *Vehicle System Dynamics,* 23**,** 142-157.

FERTIG, R., JONES, A., KIMBLE, M., HACKER, D., TOKER, S. & TANNER, J. E. 2013. Evaluation of ASR potential in Wyoming aggregates. Wyoming. Dept. of Transportation.

FOWLKES, W. & CREVELING, C. 1995. Engineering Methods for Robust Product Development—Using Taguchi Methods in Technology and Product Development. Reading, MA: Addison-Wesley Longman.

FU, Q. & ZHENG, C. 2014. Three-dimensional dynamic analyses of track-embankment-ground system subjected to high speed train loads. *The Scientific World Journal,* 2014.

FUJIKAKE, K., SENGA, T., UEDA, N., OHNO, T. & KATAGIRI, M. 2006a. Effects of strain rate on tensile behavior of reactive powder concrete. *Journal of Advanced Concrete Technology,* 4**,** 79-84.

FUJIKAKE, K., SENGA, T., UEDA, N., OHNO, T. & KATAGIRI, M. 2006b. Study on impact response of reactive powder concrete beam and its analytical model. *Journal of advanced concrete technology,* 4**,** 99-108.

GALLERY, W. S. R. 2010. *Low profile concrete sleepers at Hawksburn* [Online]. Melbourne-Australia: Wongm's Rail Gallery. Available: https://railgallery.wongm.com/mtm-trackwork/E103_9722.jpg.html [Accessed 26/06/2019].

GAO, R., LIU, Z. M., ZHANG, L. Q. & STROEVEN, P. Static properties of plain reactive powder concrete beams. Key Engineering Materials, 2006. Trans Tech Publ, 521-527.

GIANNAKOS, K. & LOIZOS, A. 2010. Evaluation of actions on concrete sleepers as design loads–Influence of fastenings. *International Journal of Pavement Engineering,* 11**,** 197-213.

GOAIZ, H. A., FARHAN, N. A., SHEIKH, M. N., YU, T. & HADI, M. N. 2019. Experimental evaluation of tensile strength test methods for steel fibre-reinforced concrete. *Magazine of Concrete Research,* 71**,** 385-394.

GONZÁLEZ-NICIEZA, C., ÁLVAREZ-FERNÁNDEZ, M. I., MENÉNDEZ-DÍAZ, A., ÁLVAREZ-VIGIL, A. E. & ARIZNAVARRETA-FERNÁNDEZ, F. 2008. Failure analysis of concrete sleepers in heavy haul railway tracks. *Engineering Failure Analysis,* 15**,** 90-117.

GOURLEY, J. & JOHNSON, G. Developments in geopolymer precast concrete. World Congress Geopolymer, 2005. Geopolymer Institute Saint-Quentin, France, 139-143.

GRASSIE, S., NILSSON, P., BJURSTROM, K., FRICK, A. & HANSSON, L. G. 2002. Alleviation of rolling contact fatigue on Sweden's heavy haul railway. *Wear,* 253**,** 42-53.

GRASSIE, S. L. 1984. Dynamic modelling of railway track and wheelsets. CAMBRIDGE UNIV (ENGLAND) DEPT OF ENGINEERING.

GRAYBEAL, B., BRÜHWILER, E., KIM, B.-S., TOUTLEMONDE, F., VOO YEN, L. & ZAGHI, A. 2020. International Perspective on UHPC in Bridge Engineering. *Journal of Bridge Engineering,* 25**,** 04020094.

GUSTAVSON, R. 2002. Structural behaviour of concrete railway sleepers (PhD Thesis). *Göteborg, Sweden: Chalmers University of Technology*.

GYLLTOFT, K. 1983. *Fracture mechanics models for fatigue in concrete structures.* Luleå tekniska universitet.

HADI, M. N. S., AHMAD, H. & SHEIKH, M. N. 2021. Effect of Using GFRP Reinforcement on the Behavior of Hollow-Core Circular Concrete Columns. *Journal of Composites for Construction,* 25**,** 06020003.

HADI, M. N. S., FARHAN, N. A. & SHEIKH, M. N. 2017. Design of geopolymer concrete with GGBFS at ambient curing condition using Taguchi method. *Construction and Building Materials,* 140**,** 424-431.

HAMEED, A. S. & SHASHIKALA, A. P. 2016. Suitability of rubber concrete for railway sleepers. *Perspectives in Science,* 8**,** 32-35.

HASSAN, A. M. T., JONES, S. W. & MAHMUD, G. H. 2012. Experimental test methods to determine the uniaxial tensile and compressive behaviour of ultra high performance fibre reinforced concrete (UHPFRC). *Construction and Building Materials,* 37**,** 874-882.

HAWKINS, N. & SHAH, S. 1982. American concrete institute considerations for fatigue. *International Assoc. for Bridge and Structural Engineering***,** 41-50.

HAY, W. W. 1982. *Railroad engineering*, John Wiley & Sons.

HEINZ, D. & LUDWIG, U. Mechanism of subsequent ettringite formation in mortars and concretes after heat treatment. Proceeding of the 8th Int. Congr. on the Chem. of Cem., 1986.

HIME, W. G. 1996. Delayed ettringite formation: A concern for precast concrete? *PCI journal,* 41**,** 26-30.

HOBBS, D. W. 2001. Concrete deterioration: causes, diagnosis, and minimising risk. *International Materials Reviews,* 46**,** 117-144.

HU, R., FANG, Z., JIANG, R., XIANG, Y. & LIU, C. 2021. Fatigue prediction model of ultra-high-performance concrete beams prestressed with CFRP tendons. *Advances in Structural Engineering,* 25**,** 611-624.

INDRARATNA, B. & SALIM, W. 2005. *Mechanics of ballasted rail tracks: a geotechnical perspective*, CRC Press.

IPEK, M., YILMAZ, K., SÜMER, M. & SARIBIYIK, M. 2011. Effect of pre-setting pressure applied to mechanical behaviours of reactive powder concrete during setting phase. *Construction and Building Materials,* 25**,** 61-68.

JEFFS, T. Towards ballast life cycle costing. Fourth International Heavy Haul Railway Conference 1989: Railways in Action; Preprints of Papers, The, 1989. Institution of Engineers, Australia, 439.

JIAO, C. & SUN, W. 2015. Impact resistance of reactive powder concrete. *Journal of Wuhan University of Technology-Mater. Sci. Ed.,* 30**,** 752-757.

JOHANSSON, A. & NIELSEN, J. C. 2003. Out-of-round railway wheels—wheel-rail contact forces and track response derived from field tests and numerical simulations. *Proceedings of the Institution of Mechanical Engineers, Part F: Journal of Rail and Rapid Transit,* 217**,** 135-146.

JOOSS, M. & REINHARDT, H. W. 2002. Permeability and diffusivity of concrete as function of temperature. *Cement and Concrete Research,* 32**,** 1497-1504.

JU, Y., LIU, H., SHENG, G. & WANG, H. 2010. Experimental study of dynamic mechanical properties of reactive powder concrete under high-strain-rate impacts. *Science China Technological Sciences,* 53**,** 2435-2449.

KAEWUNRUEN, S. 2007. Experimental and numerical studies for evaluating dynamic behaviour of prestressed concrete sleepers subject to severe impact loading. Doctoral Thesis, University of Wollongong.

KAEWUNRUEN, S. 2010. Sleepers and fastenings. *Track design fundamentals, Rail engineering course, Rail corporation*.

KAEWUNRUEN, S., LI, D., CHEN, Y. & XIANG, Z. 2018a. Enhancement of dynamic damping in eco-friendly railway concrete sleepers using waste-tyre crumb rubber. *Materials,* 11**,** 1169.

KAEWUNRUEN, S., NGAMKHANONG, C. & LIM, C. H. 2018b. Damage and failure modes of railway prestressed concrete sleepers with holes/web openings subject to impact loading conditions. *Engineering Structures,* 176**,** 840-848.

KAEWUNRUEN, S. & REMENNIKOV, A. 2007. Incorporating contact mechanisms into free vibration analysis of an in-situ railway concrete sleeper in track system. *Proceedings of the Institution of Mechanical Engineers Part F: Journal of Rail and Rapid Transit.*

KAEWUNRUEN, S. & REMENNIKOV, A. 2013. On the residual energy toughness of prestressed concrete sleepers in railway track structures subjected to repeated impact loads. University of Wollongong.

KAEWUNRUEN, S., REMENNIKOV, A. & MURRAY, M. H. 2012. Limit states design of railway concrete sleepers. University of Wollongong.

KAEWUNRUEN, S. & REMENNIKOV, A. M. 2008. Effect of a large asymmetrical wheel burden on flexural response and failure of railway concrete sleepers in track systems. *Engineering Failure Analysis,* 15**,** 1065-1075.

KAEWUNRUEN, S. & REMENNIKOV, A. M. 2009a. Dynamic flexural influence on a railway concrete sleeper in track system due to a single wheel impact. *Engineering Failure Analysis,* 16**,** 705-712.

KAEWUNRUEN, S. & REMENNIKOV, A. M. 2009b. Impact capacity of railway prestressed concrete sleepers. *Engineering Failure Analysis,* 16**,** 1520-1532.

KAEWUNRUEN, S. & REMENNIKOV, A. M. 2009c. Progressive failure of prestressed concrete sleepers under multiple high-intensity impact loads. *Engineering Structures,* 31**,** 2460-2473.

KAEWUNRUEN, S. & REMENNIKOV, A. M. 2010. Dynamic Crack Propagations in Prestressed Concrete Sleepers in Railway Track Systems Subjected to Severe Impact Loads. *Journal of Structural Engineering,* 136**,** 749-754.

KAEWUNRUEN, S. & REMENNIKOV, A. M. 2011. Experiments into impact behaviour of railway prestressed concrete sleepers. *Engineering Failure Analysis,* 18**,** 2305-2315.

KAEWUNRUEN, S., REMENNIKOV, A. M. & MURRAY, M. H. 2014. Introducing a new limit states design concept to railway concrete sleepers: an Australian experience. *Frontiers in Materials,* 1**,** 8.

KERNES, R. G., EDWARDS, J. R., DERSCH, M. S., LANGE, D. A. & BARKAN, C. P. Investigation of the dynamic frictional properties of a concrete crosstie rail seat and pad and its effect on rail seat deterioration (RSD). Transportation Research Board 91st Annual Meeting, 2011.

KIM, D. J., PARK, S. H., RYU, G. S. & KOH, K. T. 2011. Comparative flexural behavior of Hybrid Ultra High Performance Fiber Reinforced Concrete with different macro fibers. *Construction and Building Materials,* 25**,** 4144-4155.

KIM, M.-J., CHOI, H.-J., SHIN, W., OH, T. & YOO, D.-Y. 2021. Development of impact resistant high-strength strain-hardening cementitious composites (HS-SHCC) superior to reactive powder concrete (RPC) under flexure. *Journal of Building Engineering,* 44.

KNOTHE, K. & GRASSIE, S. 1993. Modelling of railway track and vehicle/track interaction at high frequencies. *Vehicle system dynamics,* 22**,** 209-262.

KOHOUTEK, R. Dynamic and static performance of interspersed railway track. Conference on Railway Engineering 1991: Demand Management of Assets; Preprints of Papers, 1991. Institution of Engineers, Australia, 153.

KOVÁCS, I. & BALÁZS, G. 2003. Structural behaviour of steel fibre reinforced concrete. *Structural Concrete,* 4**,** 57-63.

KUMARAN, G., MENON, D. & KRISHNAN NAIR, K. 2002. Evaluation of dynamic load on railtrack sleepers based on vehicle-track modeling and analysis. *International Journal of Structural Stability and Dynamics,* 2**,** 355-374.

LE PEN, L. & POWRIE, W. 2011. Contribution of base, crib, and shoulder ballast to the lateral sliding resistance of railway track: a geotechnical perspective. *Proceedings of the Institution of Mechanical Engineers, Part F: Journal of Rail and Rapid Transit,* 225**,** 113-128.

LEE, M.-G., WANG, Y.-C. & CHIU, C.-T. 2007. A preliminary study of reactive powder concrete as a new repair material. *Construction and Building Materials,* 21**,** 182-189.

LEE, M., CHIU, W. & KOSS, L. 2005. A numerical study into the reconstruction of impact forces on railway track-like structures. *Structural Health Monitoring,* 4**,** 19-45.

LEI, J. V. Y. 2006. Shear strength of 160 MPa steel fibre reinforced reactive powder concrete bridge girders without stirrups.

LEONG, J. 2007. *Development of a limit state design methodology for railway track.* Doctoral Thesis, Queensland University of Technology.

LUNDQVIST, A. & DAHLBERG, T. 2005. Load impact on railway track due to unsupported sleepers. *Proceedings of the Institution of Mechanical Engineers, Part F: Journal of Rail and Rapid Transit,* 219**,** 67-77.

MA, C., LI, X. & BU, J. 2010. Cause and modification measures of longitudinal cracks from bolt hole of the PC sleepers II. *ICCTP 2010: Integrated Transportation Systems: Green, Intelligent, Reliable.*

MAHMUD, G. H., YANG, Z. & HASSAN, A. M. T. 2013. Experimental and numerical studies of size effects of Ultra High Performance Steel Fibre Reinforced Concrete (UHPFRC) beams. *Construction and Building Materials,* 48**,** 1027-1034.

MANALO, A., ARAVINTHAN, T., KARUNASENA, W. & TICOALU, A. 2010. A review of alternative materials for replacing existing timber sleepers. *Composite Structures,* 92**,** 603-611.

MIURA, S., TAKAI, H., UCHIDA, M. & FUKADA, Y. 1998. The mechanism of railway tracks. *Japan Railway & Transport Review,* 3**,** 38-45.

MOHAMMADZADEH, S. & VAHABI, E. 2011. Time-dependent reliability analysis of B70 pre-stressed concrete sleeper subject to deterioration. *Engineering Failure Analysis,* 18**,** 421-432.

MURRAY, M. & CAI, Z. 1998. Prestressed concrete sleeper: Literature review. *Report ARA Project Ref,* 15250.

NAIRN, J. & STEVENS, N. 2010. Rational design method for prestressed concrete sleepers. *CORE 2010: Rail, Rejuvenation and Renaissance***,** 174.

NARAYANAN, R. & BEEBY, A. 2005. *Designers' Guide to EN 1992-1-1 and EN 1992-1-2. Eurocode 2: Design of Concrete Structures: General Rules and Rules for Buildings and Structural Fire Design*, Thomas Telford London, UK.

NEWTON, S. & CLARK, R. 1979. An investigation into the dynamic effects on the track of wheelflats on railway vehicles. *Journal of Mechanical Engineering Science,* 21**,** 287-297.

NGAMKHANONG, C., KAEWUNRUEN, S. & REMENNIKOV, A. M. Static and dynamic behaviours of railway prestressed concrete sleepers with longitudinal through hole. IOP Conference Series: Materials Science and Engineering, 2017a. IOP Publishing, 012099.

NGAMKHANONG, C., LI, D. & KAEWUNRUEN, S. Impact capacity reduction in railway prestressed concrete sleepers with surface abrasions. IOP Conference Series: Materials Science and Engineering, 2017b. IOP Publishing, 032048.

NGAMKHANONG, C., LI, D. & KAEWUNRUEN, S. Impact capacity reduction in railway prestressed concrete sleepers with vertical holes. IOP Conference Series: Materials Science and Engineering, 2017c. IOP Publishing, 012041.

NIELSEN, J. C. & IGELAND, A. 1995. Vertical dynamic interaction between train and track influence of wheel and track imperfections. *Journal of sound and vibration,* 187**,** 825-839.

OKAY, F. & ENGIN, S. 2012. Torsional behavior of steel fiber reinforced concrete beams. *Construction and Building Materials,* 28**,** 269-275.

OZBAY, E., OZTAS, A., BAYKASOGLU, A. & OZBEBEK, H. 2009. Investigating mix proportions of high strength self compacting concrete by using Taguchi method. *Construction and Building Materials,* 23**,** 694-702.

PALOMO, A. & FERNÁNDEZ-JIMÉNEZ, A. Alkaline activation, procedure for transforming fly ash into new materials. Part I: Applications. World of Coal Ash (WOCA) Conference, 2011. 1-14.

PALOMO, A., FERNÁNDEZ-JIMÉNEZ, A., LÓPEZ-HOMBRADOS, C. & LLEYDA, J. L. 2007. Railway sleepers made of alkali activated fly ash concrete. *Revista Ingenieria de Construccion,* 22**,** 75-80.

PANDROL accessed on 20/12/2021. Pandrol e-Clip

PARVEZ, A. 2015. Fatigue behaviour of steel-fibre-reinforced concrete beams and prestressed sleepers. Sydney: The University of New South Wales.

PARVEZ, A. & FOSTER, S. J. 2017. Fatigue of steel-fibre-reinforced concrete prestressed railway sleepers. *Engineering Structures,* 141**,** 241-250.

PETERS, N. & MATTSON, S. CN 60E concrete tie development. AREMA Conference Proc, 2004.

PETERS, S. 2007. Abrasion Testing of Epoxy-Coated Concrete Ties (Using Symons Product No. 301 Epoxy), JA Cesare & Associates. Inc.

PHADKE, M. S. 1989. Quality Engineering Using Robust Design, PTR Prentice-Hall. *Inc., Englewood Cliffs, NJ*.

PITA, A. L. 2006. *Infraestructuras ferroviarias*, Universitat Politecnica de Catalunya. Iniciativa Digital Politecnica.

POPOVICS, S. 1973. A numerical approach to the complete stress-strain curve of concrete. *Cement and Concrete Research,* 3**,** 583-599.

PRAUSE, R., MEACHAM, H., HARRISON, H., JOHN, T. & GLAESER, W. 1974. Assessment of Design Tools and Criteria for Urban Rail Track Structures, Vol. 1. Report No. UMTA-MA-06-0025-74-3. Urban Mass Transit Administration.

Q/CR-9130 2015. Q/CR 9130-2015-Provisional Code for Limit State Design Method of Railway Track. China: Chinese Railway.

QINHUA, J., MIN, D. & SUFEN, H. 1996. Investigation of deteriorated concrete railway ties. *Cement and concrete research,* 26**,** 999-1006.

REMENNIKOV, A. & KAEWUNRUEN, S. 2005. Investigation of vibration characteristics of prestressed concrete sleepers in free-free and in-situ conditions. University of Wollongong.

REMENNIKOV, A. & KAEWUNRUEN, S. 2007. Resistance of railway concrete sleepers to impact loading. University of Wollongong.

REMENNIKOV, A., MURRAY, M. H. & KAEWUNRUEN, S. 2012. Reliability-based conversion of a structural design code for railway prestressed concrete sleepers. *Proceedings of the Institution of Mechanical Engineers, Part F: Journal of Rail and Rapid Transit,* 226**,** 155-173.

REMENNIKOV, A. M. & KAEWUNRUEN, S. 2008a. A review of loading conditions for railway track structures due to train and track vertical interaction. *Structural Control and Health Monitoring: The Official Journal of the International Association for Structural Control and Monitoring and of the European Association for the Control of Structures,* 15**,** 207-234.

REMENNIKOV, A. M. & KAEWUNRUEN, S. 2008b. A review of loading conditions for railway track structures due to train and track vertical interaction. *Structural Control and Health Monitoring,* 15**,** 207-234.

REMENNIKOV, A. M. & KAEWUNRUEN, S. 2014a. Determination of prestressing force in railway concrete sleepers using dynamic relaxation technique. *Journal of Performance of Constructed Facilities,* 29**,** 04014134.

REMENNIKOV, A. M. & KAEWUNRUEN, S. 2014b. Experimental load rating of aged railway concrete sleepers. *Engineering Structures,* 76**,** 147-162.

REZAIE, F., SHIRI, M. R. & FARNAM, S. M. 2012. Experimental and numerical studies of longitudinal crack control for pre-stressed concrete sleepers. *Engineering Failure Analysis,* 26**,** 21-30.

RICHARD, P. & CHEYREZY, M. 1995. Composition of reactive powder concretes. *Cement and concrete research,* 25**,** 1501-1511.

ROCHARD, B. & SCHMID, F. Benefits of lower-mass trains for high speed rail operations. Proceedings of the Institution of Civil Engineers-Transport, 2004. Thomas Telford Ltd, 51-64.

ROSS, P. J. 1996. *Taguchi techniques for quality engineering: loss function, orthogonal experiments, parameter and tolerance design*.

ROY, R. K. 1996. Qualitek-4 Software for Automatic Design of Experiment Using Taguchi Approach, IBM or Compatible computer, Nutek, Inc.

SADEGHI, J. 1997. Investigation of characteristics and modelling of railway track system.

SADEGHI, J. & BARATI, P. 2010. Evaluation of conventional methods in Analysis and Design of Railway Track System. *International Journal of Civil Engineering,* 8**,** 44-56.

SADEGHI, J., TOLOU KIAN, A. R. & SHATER KHABBAZI, A. 2016. Improvement of mechanical properties of railway track concrete sleepers using steel fibers. *Journal of Materials in Civil Engineering,* 28**,** 04016131.

SADEGHI, J. & YOULDASHKHAN, M. 2005. Investigation on the accuracy of the current practices in analysis of railway track concrete sleepers. *International Journal of Civil Engineering,* 3**,** 31.

SAHU, S. & THAULOW, N. 2004. Delayed ettringite formation in Swedish concrete railroad ties. *Cement and Concrete Research,* 34**,** 1675-1681.

SCHRAMM, G. 1961. *Permanent way technique and permanent way economy: with 23 tables*, Elsner.

SELIG, E. T. & LI, D. 1994. Track modulus: Its meaning and factors influencing it. *Transportation Research Record*.

SELIG, E. T. & WATERS, J. M. 1994. *Track geotechnology and substructure management*, Thomas Telford.

SELLEYS accessed on 27/12/2021. https://go.lupinsys.com/duluxgroup/harms/public/materials/35f7010af1be44e6a8669efe4106e2df-published/attachments_api/1bcc97ccb5e3b0c89a7320b8acff2ebc/individual_api/SELLEYS_LIQUID_NAILS_LANDSCAPE-AUS_GHS.pdf.

SHAHEEN, E. & SHRIVE, N. G. 2007. Cyclic loading and fracture mechanics of Ductal® concrete. *International Journal of Fracture,* 148**,** 251-260.

SHAYAN, A. & QUICK, G. 1992. Microscopic features of cracked and uncracked concrete railway sleepers. *Materials Journal,* 89**,** 348-361.

SHI, Z., WANG, K., ZHANG, D., CHEN, Z., ZHAI, G. & HUANG, D. 2019. Experimental investigation on dynamic behaviour of heavy-haul railway track induced by heavy axle load. *Transport,* 34**,** 351-362.

SHOKRIEH, M. M. & RAHMAT, M. 2006. On the reinforcement of concrete sleepers by composite materials. *Composite Structures,* 76**,** 326-337.

SHU, X. & HUANG, B. 2014. Recycling of waste tire rubber in asphalt and portland cement concrete: An overview. *Construction and Building Materials,* 67**,** 217-224.

SHURPALI, A. A., KERNES, R. G., EDWARDS, J. R., DERSCH, M. S., LANGE, D. A. & BARKAN, C. P. Investigation of the mechanics of rail seat deterioration (RSD) and methods to improve the abrasion resistance of concrete sleeper rail seats. 10th International heavy haul association conference, New Delhi, India, 2013. 4-6.

SIKA-VISCOCRETE-HRF-1 accessed on 04/04/2021. https://aus.sika.com/content/dam/dms/au01/h/sika_viscocrete_pchrf-1.pdf.

SIKAFUME accessed on 04/04/2021. https://aus.sika.com/content/dam/dms/au01/e/Sika%20Fume.pdf".

SINGH, M., SHEIKH, A. H., MOHAMED ALI, M. S., VISINTIN, P. & GRIFFITH, M. C. 2017. Experimental and numerical study of the flexural behaviour of ultra-high performance fibre reinforced concrete beams. *Construction and Building Materials,* 138**,** 12-25.

SRINIVASAN, M. 1969. Modern permanent way.

STEVENS, N. & DUX, P. 2008. Case study: design of new prestressed concrete railway sleepers. Viewed.

SU, H., YANG, J., LING, T.-C., GHATAORA, G. S. & DIRAR, S. 2015. Properties of concrete prepared with waste tyre rubber particles of uniform and varying sizes. *Journal of Cleaner Production,* 91**,** 288-296.

SUN, Y. Q., SPIRYAGIN, M., WU, Q., COLE, C. & MA, W. H. 2018. Feasibility in assessing the dipped rail joint defects through dynamic response of heavy haul locomotive. *Journal of Modern Transportation,* 26**,** 96-106.

TAGUCHI, G. 1987. System of experimental design, vols. 1 and 2. *White Plains, New York: UNIPUB/Krauss International*.

TAGUCHI, G., CHOWDHURY, S. & WU, Y. 2005. *Taguchi's quality engineering handbook*, Wiley.

TAKAHASHI, T., SEKINE, E., HORIIKE, T., MATSUOKA, S. & HOSHIRO, H. 2008. Study on the Applicability of Short Fiber Reinforced Concrete to Precast Concrete Slabs for Slab Track. *Quarterly Report of RTRI,* 49**,** 40-46.

TAM, C. M., TAM, V. W. Y. & NG, K. M. 2012. Assessing drying shrinkage and water permeability of reactive powder concrete produced in Hong Kong. *Construction and Building Materials,* 26**,** 79-89.

TEPPONEN, P. & ERIKSSON, B.-E. 1987. DAMAGES IN CONCRETE RAILWAY SLEEPERS IN FINLAND. *Nordic concrete research*, 199-209.

THOMAS, J. & RAMASWAMY, A. 2007. Mechanical properties of steel fiber-reinforced concrete. *Journal of materials in civil engineering,* 19, 385-392.

THOMPSON, M. & TAYABJI, D. 1976. Track support system parameter study, Report No. *FRA/OR & D-78-256, Federal railroad Administration, Department of Transportation, Washington, USA,* 232-231.

THUN, H. 2006. *Assessment of fatigue resistance and strength in existing concrete structures.* Luleå tekniska universitet.

TRUE, G. 1993. Durable concrete structures design guide: Comité Euro-international du Beton Thomas Telford, 1992 112 pp,£ 45 (Hardback) ISBN 0-7277-1620-4. Elsevier.

TUAMA, W. K., KADHUM, M. M., ALWASH, N. A., AL-KHAFAJI, Z. S. & ABDULRAHEEM, M. S. 2020. RPC effect of crude oil products on the mechanical characteristics of reactive-powder and normal-strength concrete. *Periodica Polytechnica Civil Engineering,* 64, 422-429.

UEHARA, M. 2010. New Concrete with Low Environmental Load Using the Geopolymer Method. *Quarterly Report of RTRI,* 51, 1-7.

UIC-713R 2004. Design of Monoblock Concrete Sleepers. Paris: UIC Leaflet.

UNAL, R. & DEAN, E. B. Taguchi approach to design optimization for quality and cost: an overview. 1991 Annual Conference of the International Society of Parametric Analysts, 1990.

VAN DYK, B. J., EDWARDS, J. R., DERSCH, M. S., RUPPERT JR, C. J. & BARKAN, C. P. 2017. Evaluation of dynamic and impact wheel load factors and their application in design processes. *Proceedings of the Institution of Mechanical Engineers, Part F: Journal of Rail and Rapid Transit,* 231, 33-43.

VISINTIN, P., STURM, A. B., MOHAMED ALI, M. S. & OEHLERS, D. J. 2018. Blending macro- and micro-fibres to enhance the serviceability behaviour of UHPFRC. *Australian Journal of Civil Engineering,* 16, 106-121.

VOO, Y. L., FOSTER, S. J. & GILBERT, R. I. 2006. Shear strength of fiber reinforced reactive powder concrete prestressed girders without stirrups. *Journal of Advanced Concrete Technology,* 4, 123-132.

WAKUI, H. & OKUDA, H. 1997. A study on limit state design method for prestressed concrete sleepers. *Doboku Gakkai Ronbunshu,* 1997, 35-54.

WANG, D., SHI, C., WU, Z., XIAO, J., HUANG, Z. & FANG, Z. 2015. A review on ultra high performance concrete: Part II. Hydration, microstructure and properties. *Construction and Building Materials,* 96, 368-377.

WANG, N. 1996. *Resistance of concrete railroad ties to impact loading.* University of British Columbia.

WANG, Y., AN, M.-Z., YU, Z.-R., HAN, S. & JI, W.-Y. 2017. Durability of reactive powder concrete under chloride-salt freeze–thaw cycling. *Materials and Structures,* 50, 18.

WU, T. & THOMPSON, D. 2001. A hybrid model for wheel/track dynamic interaction and noise generation due to wheel flats.

WU, T. & THOMPSON, D. 2004. The effects of track non-linearity on wheel/rail impact. *Proceedings of the Institution of Mechanical Engineers, Part F: Journal of Rail and Rapid Transit,* 218, 1-15.

XU, S., ZHOU, F., LI, Q. & WU, P. 2021. A novel dynamic cavity expansion model to predict the resistance of reactive powder concrete (RPC) against projectile impact. *Composites Part B: Engineering,* 223.

YAZıCı, H., YARDıMCı, M. Y., AYDıN, S. & KARABULUT, A. Ş. 2009. Mechanical properties of reactive powder concrete containing mineral admixtures under different curing regimes. *Construction and Building Materials,* 23**,** 1223-1231.

YAZıCı, H., YARDıMCı, M. Y., YIĞITER, H., AYDıN, S. & TÜRKEL, S. 2010. Mechanical properties of reactive powder concrete containing high volumes of ground granulated blast furnace slag. *Cement and Concrete Composites,* 32**,** 639-648.

YAZıCı, H., YIĞITER, H., KARABULUT, A. Ş. & BARADAN, B. 2008. Utilization of fly ash and ground granulated blast furnace slag as an alternative silica source in reactive powder concrete. *Fuel,* 87**,** 2401-2407.

YOO, D.-Y., BANTHIA, N., KIM, S.-W. & YOON, Y.-S. 2015. Response of ultra-high-performance fiber-reinforced concrete beams with continuous steel reinforcement subjected to low-velocity impact loading. *Composite Structures,* 126**,** 233-245.

YOU, R., GOTO, K., NGAMKHANONG, C. & KAEWUNRUEN, S. 2019. Nonlinear finite element analysis for structural capacity of railway prestressed concrete sleepers with rail seat abrasion. *Engineering Failure Analysis,* 95**,** 47-65.

YOU, R. & KAEWUNRUEN, S. 2019. Evaluation of remaining fatigue life of concrete sleeper based on field loading conditions. *Engineering Failure Analysis,* 105**,** 70-86.

YOU, R., LI, D., NGAMKHANONG, C., JANELIUKSTIS, R. & KAEWUNRUEN, S. 2017. Fatigue life assessment method for prestressed concrete sleepers. *Frontiers in built environment,* 3**,** 68.

ZAKERI, J. & ABBASI, R. Field investigation on distribution of contact pressure between sleeper and saturated ballast with flowing sand. 11th International Conference of Railway Engineering, 2011.

ZAKERI, J. A. & REZVANI, F. H. 2012. Failures of railway concrete sleepers during service life. *Int J Constr Eng Manage,* 1**,** 1-5.

ZANUY, C., ALBAJAR, L. & DE LA FUENTE, P. 2009. Sectional Analysis of Concrete Structures under Fatique Loading. *ACI Structural Journal,* 106.

ZARAGÜETA, F. R. 2013. Análisis de una vía con traviesas cuadro Analysis of a track with frame sleepers. *Revista Vía Libre-Técnica/número***,** 53.

ZEMAN, J. C., EDWARDS, J. R., BARKAN, C. P. & LANGE, D. A. Failure mode and effect analysis of concrete ties in North America. Proc. of the 9th International Heavy Haul Conference, 2009. 270-278.

ZHAI, W. & CAI, Z. 1997. Dynamic interaction between a lumped mass vehicle and a discretely supported continuous rail track. *Computers & structures,* 63**,** 987-997.

ZHANG, J., LI, V. C. & STANG, H. 2001. Size effect on fatigue in bending of concrete. *Journal of materials in civil engineering,* 13**,** 446-453.

ZHAO, J., CHAN, A. H. C. & BURROW, M. P. N. 2007. Reliability analysis and maintenance decision for railway sleepers using track condition information. *Journal of the Operational Research Society,* 58**,** 1047-1055.

ZHONG, W., HU, J. J., SHEN, P., WANG, C. Y. & LIUS, Q. Y. 2011. Experimental investigation between rolling contact fatigue and wear of high-speed and heavy-haul railway and selection of rail material. *Wear,* 271**,** 2485-2493.

ZHU, J. 2006. On the effect of varying stiffness under the switch rail on the wheel—rail dynamic characteristics of a high-speed turnout. *Proceedings of the*

Institution of Mechanical Engineers, Part F: Journal of Rail and Rapid Transit, 220**,** 69-75.

ZI, G., MOON, D. Y., LEE, S.-J., JANG, S. Y., YANG, S. C. & KIM, S.-S. 2012. Investigation of a concrete railway sleeper failed by ice expansion. *Engineering Failure Analysis,* 26**,** 151-163.